

New Applications of Nanomaterials

Noi aplicatii ale unor nanomateriale

New Applications of Nanomaterials

EDITORS:

**Alina Catrinel Ion, Dan Dascalu,
Gabriela Carja, Magdalena Lidia Cirea**



EDITURA ACADEMIEI ROMÂNE

București, 2014

Copyright © Editura Academiei Române, 2014.
All rights reserved.

The responsibility for originality and the contents of the
articles lies exclusively with the authors.

Address: EDITURA ACADEMIEI ROMÂNE
Calea 13 Septembrie nr. 13, sector 5,
050 711, București, România,
Tel. 4021-3188146, 4021-3188106
Fax: 4021-3182444
E-mail: edacad@ear.ro
Internet: <http://www.ear.ro>

Peer reviewers:
Prof. Gheorghe Brezeanu, Dr. Mihai Mihailă, m.c. al Academiei României

Descrierea CIP a Bibliotecii Naționale a României

New applications of nanomaterials / editors:

Alina Catrinel Ion, Dan Dascalu, Gabriela Carja,
Magdalena Lidia Cirea - București : Editura Academiei Române,
2014

ISBN 978-973-27-2311-1

- I. Alina Catrinel Ion (ed.)
- II. Dan Dascalu (ed.)
- III. Gabriela Carja (ed.)
- IV. Magdalena Lidia Cirea (ed.)

621.3.049.77

Editorial assistant: Mihaela Marian

Computer operator: Elena Trică

Cover: Elena Trică

Passed for press: 03.2014. Size: 16 / 70 × 100.

Printed sheets: 9

D.L.C. for large libraries: 621.3.049.77

D.L.C. for small libraries: 621.3

CONTENTS

FOREWORD	7
AuNPs/LDHS ASSEMBLIES AS NANOARCHITECTURES: FABRICATION, PROPERTIES AND SPECIFIC APPLICATION AS PHOTOCATALYSTS <i>M. BIRSANU, D. MARDARE, M. PUSCASU, K. OKADA, G. CARJA</i>	9
A NEW NANOMATERIAL FOR THE STUDY OF PROTEIN INTERACTIONS <i>A. VASILESCU, I. MIHAIA, A. VEZEANU, V. ANDREI, G. NEDELICU</i> <i>E. POPA, C. PURCAREA, P. SUBRAMANIAN, Y. COFFINIER,</i> <i>R. BOUKHEROUB, S. SZUNERITS</i>	19
ENVIRONMENTAL APPLICATIONS OF CARBON-BASED NANOMATERIALS. ACETYLCHOLINESTERASE BIOSENSORS FOR ORGANOPHOSPHATE PESTICIDE ANALYSIS <i>I. ION, A. CULETUA, D. GHERASE, F. SIRBU, A. C. ION</i>	33
THE EFFECTS OF CALCINED AND DOPED SILICA NANOSTRUCTURES ON HALOTOLERANT MICROORGANISMS ISOLATED FROM ROCK SALT CRYSTAL <i>M. ENACHE, S. NEAGU, C. ANASTASESCU, R. COJOC, M. ZAHARESCU</i>	51
PULSED LASER ABLATION SYNTHESIS OF CARBON NANO-STRUCTURES: EFFECT OF TARGET COMPOSITION AND LASER ABLATION CONDITION ON THEIR YIELD AND MORPHOLOGY <i>I. BOERASU, M. ENACHESCU</i>	61
STRATEGIES FOR THE STRUCTURE AND MORPHOLOGY CONTROL OF BaTiO₃ NANOPARTICLES <i>F. MAXIM, P. FERREIRA, P. VILARINHO</i>	83
NANOMATERIALS FOR RESTORATION AND CONSERVATION OF HISTORICAL MONUMENTS <i>R.M. ION</i>	99
NANOSCALE DIODES WITHOUT p-n JUNCTIONS <i>M. DRAGOMAN</i>	113
PREPARATION OF POROUS CALCIUM ALGINATE BEADS AND THEIR USE FOR ADSORPTION OF O-NITROPHENOL FROM AQUEOUS SOLUTIONS <i>S. PERETZ, M. FLOREA-SPIROIU, D.F. ANGHEL, D. BALA,</i> <i>C. STOIAN, Ghe. ZGHEREA</i>	123

**COMPARATIVE THERMODYNAMIC STUDY ON EXFOLIATED GRAPHITE
NANOPLATELETS SYSTEMS DISPERSED IN DIMETHYLFORMAMIDE
AND WATER AT T= (293.15, 298.15 and 303.15) K**

F. SIRBU, I. ION, A.C. ION 137

**NANOSTRUCTURED TITANOSILICATE MICROSPHERES WITH
GALLIUM AND LANTHANUM BASED NANOCRYSTALS**

O. PONTA, S. SIMON 153

FOREWORD

The new volume “**New applications of nanomaterials**” belongs to the “**Micro and nano engineering**” series, edited by the Publishing House of the Romanian Academy. This volume consists of the extended versions of the most relevant papers selected from the 12th edition of the Annual National Seminar for Nanoscience and Nanotechnology (Bucharest, May 13th, 2013).

The manuscripts published in this volume address a large area of very interesting applications among which there can be emphasized the environmental ones: AuNPs/LDHS assemblies as nanoarchitectures for environmental photocatalysts; possible environmental applications of graphene-based nanomaterials; functionalized porous alginate beads for environmental decontamination. Some medical applications are also present, the effect of titanate nanotubes against moderately halophilic bacteria being one of them. Applications of nanomaterials in electronics include nanoscale diodes without p-n junctions and last but not at least, nanomaterials for restoration and conservation of historical monuments offer new solutions for obeying to the principle of preserving the authenticity of historical heritage.

From this very short summary of the contributions it results a broad area of applications, but not enough for another group of researchers at the Seminar who presented new routes of synthesis and characterization of nanomaterials which can be the seeds for new applications in the near future. This first sub-set of manuscripts presents studies on carbon-based nanomaterials such as: boron-doped diamond nanowires (BDD NWs) for the sensitive detection of amino acids in binary mixtures and in proteins, conditions for carbon nano-onions deposition, using excimer laser to ablate a commercial pure graphite, further characterized by transmission electron microscopy (TEM) analyses and thermodynamic studies on exfoliated graphite nanoplatelets dispersed in water, and N,N-dimethylformamide, respectively, at different concentrations of solvate and at different temperatures.

The second sub-set of manuscripts of this group containing synthetic routes and characterization refers to inorganic nanomaterials strategies for simultaneous control of tetragonality, size and shape in barium titanate, the effect of lanthanum and gallium

and of the thermal treatment on the surface composition and structure of titanosilicate systems and the major interest of these systems in different applications.

The volume “**New applications of nanomaterials**” contains eleven papers (170 pages) and it might help the experienced researchers in this field to find new motivations to continue and the new comers to gain the enthusiasm to make the first steps in the magic nano world.

The Editors
March 2014

AuNPs/LDHS Assemblies as Nanoarchitectures: Fabrication, Properties and Specific Application as Photocatalysts

Mihaela BIRSANU¹, Dragos MARDARE¹, Magda PUSCASU¹,
Kiyoshi OKADA² and Gabriela CARJA²

¹Department of Chemical Engineering, Faculty of Chemical Engineering and
Environmental Protection, Technical University "Gh. Asachi" of Iasi,
Bd. Mangeron no.71, Iasi 700554, Romania
e-mail: carja@uaic.ro

²Materials and Structures Laboratory, Tokyo Institute of Technology,
4259 Nagatsuta, Midori, Yokohama, 226-8503, Japan

Abstract. Nanostructured formulations based on nanoparticles of gold supported on zinc-cerium substituted anionic clays (denoted as Au/LDHs) and their derived solid solutions were reported for the investigation of photocatalytic performances in the process of Methylene Blue degradation from aqueous solutions with Vis light. The fabrication of Au/LDHs nano-photocatalysts is simple and cost effective based on the structural "memory effect" of the clay matrix in aqueous solution of AuCl₃. XRD, N₂ adsorption-desorption and UV-Vis analysis were used to investigate the structure, size morphologies characteristics and the photoresponsive properties of the samples. The results presented in our work open new perspectives for fabrication of nano-photoresponsive formulations for degradation of toxic organic pollutants from aqueous solutions.

Keywords: gold substituted anionic clay, layered double hydroxides; Methylene blue; photodegradation

1. Introduction

In the last years have been increasing demands for catalysts that can eliminate the polluting materials from the environmental, because the environmental deterioration has become a major obstacle [1]. Photocatalytic degradations of the pollutants represent the most extensive solution for removal of organic dyes and toxic contaminants from wastewater. The degradations of dyes by photocatalytic phenomena, where a semiconductor is activated by light irradiation, can release

harmless products in wastewater [1, 2]. The photodegradation of the dyes from aqueous solution can be performed by oxidizing agents produced by photo – Fenton based reactions under visible light using oxidants such as H₂O₂, ozone or transitional metals [2]. A wide range of semiconductors, that can take action as sensitizers for light reduced redox process, have been used in photocatalytic reactions type ZnO, SnO₂, but the most applied was TiO₂ due to high oxidative power, photostability and nontoxicity [3, 4]. The degradation of the dyes under different lights is largely depend on the types of catalysts and composition, light intensity, catalyst loading, solution pH, calcinations temperature [5].

Many investigations were oriented to layered double hydroxides, also known as hydrotalcite like compounds (HTLcs), that can be a great extend as environmental-friendly materials, in incipient or derived form, used as photocatalysts or photocatalyst supports for a variety of anion species or pollutants such as synthetic dyes, pesticides [1, 3, 6, 7].

Nanostructured materials type LDHs are characterized by a lamellar layered structure, which enables specific properties such as redox or acid-base properties, developed surface area, mesoporosity, ion exchange capability. Their layered structure is derived from the isomorphic substitution of a fraction of divalent cations by trivalent cations in a brucite – like lattice (Mg (OH)₂) and the positive charge is compensated by the intercalation of anions in the interlayer, with the most common CO₃²⁻. These materials are a class of synthetic two dimensional nanostructured anionic clays, with favorable textural and acid base properties, as well as anion exchange [1].

The positively charged cationic layers are bound together by the inter-layer anions, as well as hydration water molecules [8, 9]. The majority of anionic clays type layered double hydroxides (LDHs) are described by the general formula [M(II)_{1-x}M(III)_x·(OH)₂^{x+}(Aⁿ⁻)_{x/n}·mH₂O, where M(II) represents divalent metal ions, M(III) trivalent metal ions, Aⁿ⁻ intercalated anions, n is the amount of water in the crystal and x represents the molar ratio of trivalent metal ions to all metal ions, x being the ratio between M(III) and total metal amount M(III) + M(II) [1, 10, 11].

The most attractive features of the nanostructured materials type LDHs is “so-called” structural “memory effect”. Thermal treatment of LDHs leads to the collapse of the layered structure and the formation of highly active metal mixed oxides with high surface area and thermal stability. Based on the manifestation of the LDHs structural “memory effect”, have been reported a simple procedure for obtaining nanoparticles of metal oxides – LDHs (Me_xO_y/LDHs) as self-assemblies [12,13]. These calcined layered double hydroxides have the capability to restore the original layered structure by treatment with aqueous solutions containing anions and also to adsorb the metal cations of the aqueous solution [9, 13, 14].

Considering the advantage of characteristic memory effect of LDHs materials, this work has been focused to synthesize new nanostructured photo-responsive catalytic formulations of ZnCeAILDH clay reconstructed in AuCl₃ aqueous

solutions and because highly dispersed gold nanoparticles supported on different metal oxides have been demonstrated to be active in many reactions [15]. The obtained materials were characterized by X-ray diffraction (XRD), transmission electron microscopy (TEM) and UV–Vis spectroscopy.

The photocatalytic performances of nanostructured formulations based on gold substituted hydrotalcite type anionic clays supporting on cerium oxides was investigated for the degradation of heterocyclic aromatic chemical compound like Methylene Blue (MB) under visible light irradiation.

2. Experimental

2.1. Catalyst Synthesis

The hydrotalcite like clay denoted ZnCeAILDH1 and ZnCeAILDH2 were obtained by coprecipitation method following the procedure described elsewhere [16, 17]. The difference between the samples consists in molar ratio of cerium in the hydrotalcite like clay. Au/ZnCeAILDH1 and Au/ZnCeAILDH2: 1g of “freshly” calcined clays (the anionic clays were calcined at 550°C for 9 h) was added, under vigorous stirring in 150 mL of a 0.1 M aqueous solution of AuCl₃. Cl⁻ was used as an anion source for the structural reconstruction of the clay interlayer. The obtained samples were aged at room temperature for 1h, washed with double deionized water, dried in air and were denoted as Au/ZnCeAILDH1 and Au/ZnCeAILDH2. After calcinations at 600°C for 8h the samples were denoted as Au/ZnCeAILDH1 600 and Au/ZnCeAILDH2 600, respectively.

2.2. Instruments and Techniques

Structural characteristics, crystallinity and purity information were recorded by power X-ray diffraction (XRD) using a Philips Cubix Pro with Cu K α radiation at 45 kV and 40 mA in the range from 5° to 70°. Transmission electron microscopy (TEM) observation was performed on the Philips CM 10 transmission electron microscope operating at an accelerating voltage of 100 kV. Also the surface morphology was probed with field emission scanning electron microscopy FESEM Mira II LMU Tescan. UV-Vis absorption spectra were recorded on a Jasco V 550 spectrophotometer with integration sphere. Elemental analysis was performed by ICP emission spectroscopy using solution prepared by dissolving the samples in dilute H₂SO₄. Specific surface areas (S_{BET}) were determined using the Brunauer –Emmett-Teller method based on adsorption-desorption [13, 18].

2.3. Photocatalytic Activity Measurement

Photocatalytic activity for all the samples was tested by degradation of dye molecules of Methylene Blue (MB). Photocatalysis study was carried out by using

25 mg of catalyst in 25 mL of solution containing Methylene Blue (MB) with an initial concentration of dyes equal to 40 mg/L. Prior to the catalytic experiments the aqueous solution with the dye and the catalyst were stirred in the dark for about 1h to establish the adsorption – desorption equilibrium, until the dye concentration remained constant. The weight of the catalyst was always maintained the same (1g/L). A 200 W xenon doped mercury lamp (Hamamatsu Lightningcure LC8), with a cutoff filter for visible light irradiation ($\lambda > 420$ nm) was used as the light source for the photocatalytic reaction. The degradation of MB was conducted also using oxidizing agents in form of H_2O_2 with MB: H_2O_2 molar ratio of 1:1, 1:2 and 1:5. All the photocatalytic experiments were performed at room temperature. During the irradiation, at different time intervals, samples of the suspension were collected, centrifuged to remove the catalyst and then monitored by UV – Vis analysis following the intensity of the absorption peak at a wavelength 664 nm characteristic MB. The blank reaction was doing following the same procedure without the catalyst.

3. Results and discussion

3.1. Characterization of the Photocatalysts

The result of the quantitative analysis, carried out by ICP emission spectroscopy, surface areas and pore volume of the materials are presented in Table 1. The decrease of the surface area and the pore volume for the mixed oxides obtained from the reconstructed clays can suppose less emphasized porous property for clays matrices. The crystalline structure of the studied samples, in their as-synthesized form and after reconstruction process in $AuCl_3$ solution was characterized by XRD.

Table 1. Various physical-chemical properties of the catalysts

Sample	ICP Au Atomic ratio (%)	S_{BET} (m^2/g)	V_p (cm^3/g)
Au/ZnCeAILDH1	4.98	57	0.349
Au/ZnCeAILDH1 600	4.94	19	0.210
Au/ZnCeAILDH2	4.79	54	0.387
Au/ZnCeAILDH2 600	4.78	32	0.348

Figure 1A and B illustrates the power X-ray diffraction of the LDH like clays and the X-ray diffraction pattern for the calcined samples. It reveals the presence of a single crystalline phase with the reflections assigned to the layered structure, with sharp and symmetric basal reflection of (003), (006) and (009) planes, at low 2θ angles and broad, less intensive and asymmetric reflections for the non-basal (012), (015) and (018) planes, at high 2θ angle [19, 20]. Low intensity peaks, also observed, can be assigned to the presence of crystalline ZnO phase dispersed over the brucite like layers and also a second phase of cerium oxide, indicating that

cerium ions are not only in the lamellar structure [4, 21]. Calcination of the samples leads to the collapse of the layered structure and new diffraction peaks appear.

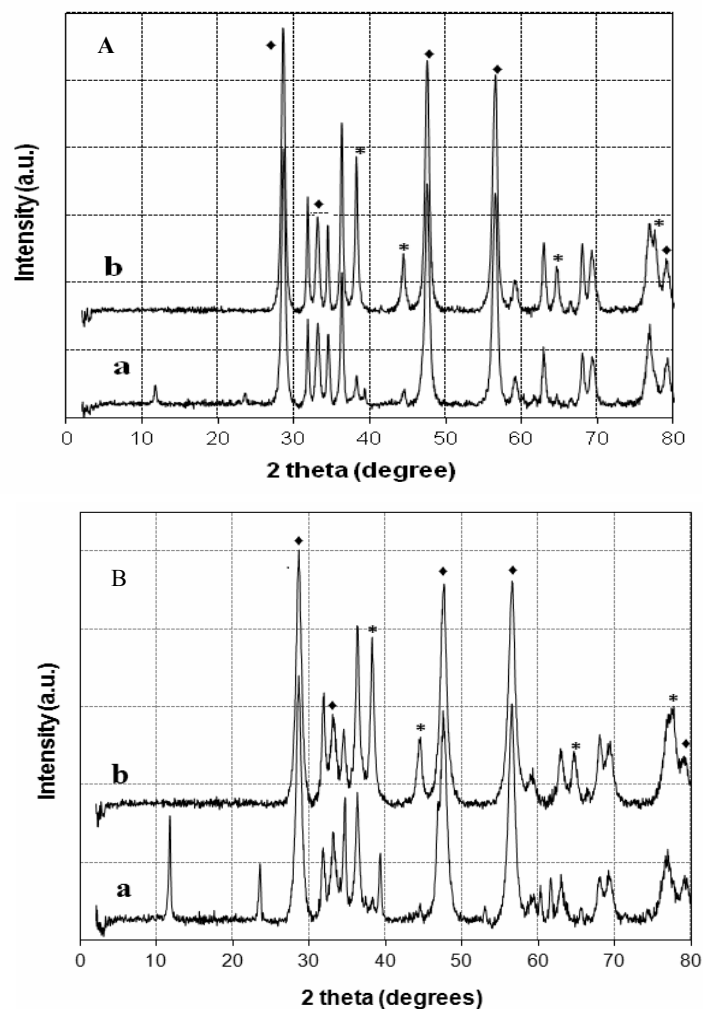


Fig. 1A. XRD patterns for Au/ZnCeAILDH1 (a) reconstructed clay and (b) calcined clay at 600°C; **B.** XRD patterns for Au/ZnCeAILDH2 (a) reconstructed clay and (b) calcined clay at 600°C; (◆) CeO₂; (*) Au.

The XRD diffractograms of the calcined samples reveals the decomposition of the LDHs phase leading to zincite ZnO (wurtzite JCPDS file No. 36-1451) phase and the spinel phase ZnAl₂O₄ (JCPDS file No. 5-0669) [13] and face centered cubic structure of CeO₂ with narrow two theta signals at 28.6°, 33.1°, 47.5°, 56.5° and 79.1°, which could be indexed to the (111), (200), (220), (311), (331)

[15]. Samples, typically violet-colored as expected for the gold deposited on LDHs, exhibits a surface plasmon band with the intensity proportional with gold particles size [26]. Also, the spectra show the existence of gold in the prepared nanoparticles system. The diffraction peaks at 2θ : 38.4° , 44.6° , 64.8° and 77.8° were indexed to the crystal planes (111), (200), (220), (311) of gold cubic phase (JCPDS Card No. 65-2870) [22].

In photocatalytic activity, important information about the photoresponsive properties of the materials can be supplied by the optical spectrum. The optical absorption of reconstructed samples and derived mixed oxides in the UV – Vis region is shown in Fig. 2.

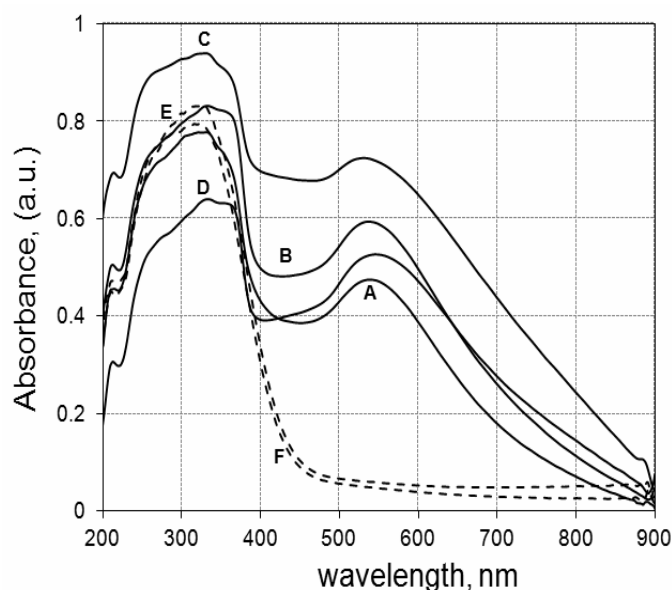


Fig. 2. UV-Vis absorption spectra of: (A) Au/ZnCeAlLDH1; (B) Au/ZnCeAlLDH2; (C) Au/ZnCeAlLDH1 600; (D) Au/ZnCeAlLDH2 600; (E) ZnCeAlLDH1; (F) ZnCeAlLDH2.

The addition of gold nanoparticles introduces a new band in the visible region around 550 nm attributed to the surface plasmon resonance [23, 24], absorption that is realized by the collective oscillation of the conduction band electron of gold nanoparticles as response to the optical excitation [25].

The XRD and UV-Vis results point out the formation of the nanoparticles of gold deposited on ZnCeAlLDH clay matrices and that the calcinations process transforms the hydrotalcite like anionic clays into $\text{CeO}_2/\text{ZnO}/\text{ZnAl}_2\text{O}_4$ phase with the increase of the gold nanoparticles size of dispersed on the larger nanoparticles of LDHs.

3.2. Photocatalytic Activity

The photocatalytic activity of as-synthesized and calcined samples was evaluated using the photocatalytic degradation of the aqueous solutions of the Methylene Blue dye under visible light. Temporal evolution of the spectral changes during the photodegradation of MB using is shown in Fig. 3A while the photocatalytic efficiency of the catalysts is presented in Fig. 3B. The derived solid solutions displayed lower photocatalytic efficiency, thus the removal efficiency of MB apparently decrease by almost 6% for the calcined samples over the entire range of wavelength. For the parent clay ZnCeAILDH1 and ZnCeAILDH2, the MB degradation efficiency is 10% and 16% respectively.

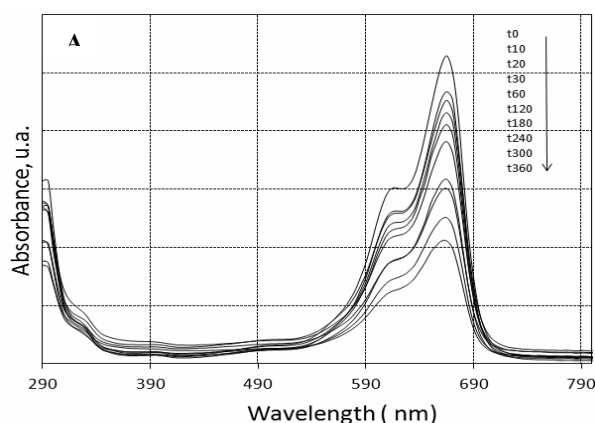


Fig. 3A. Temporal evolution of the UV Vis spectral changes taking place during the photodegradation of MB on Au/ZnCeAILDH2 600.

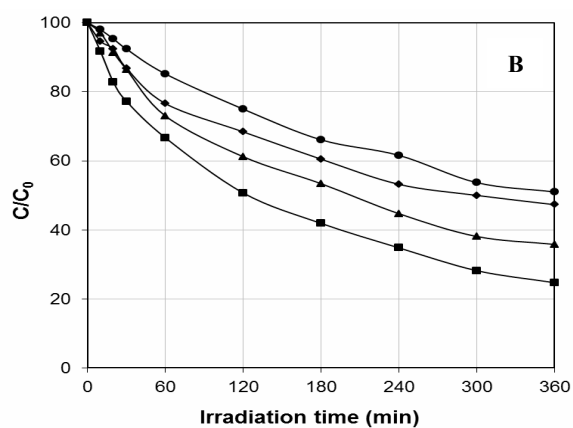


Fig. 3B. Comparison of the photocatalytic efficiency of the catalysts during the photodegradation process of MB over the entire range of wavelength; ● Au/ZnCeAILDH1 600; ◆ Au/ZnCeAILDH1; ▲ Au/ZnCeAILDH2; ■ Au/ZnCeAILDH2 600.

The experiments were carried out in presence of visible light also using an oxidizing agent H_2O_2 thus providing that the dye is decolorized by photo Fenton reaction. Figure 4A shows the temporal evolution of the spectral changes and Fig. 4B presents comparison of the rate of degradation of MB dye in presence of visible light and Au/ZnCeAILDH2 catalyst using different molar ratios of hydrogen peroxide and MB. Hydrogen peroxide concentration is an important parameter for the degradation of the dye in heterogeneous photo- Fenton reaction. H_2O_2 was decomposed at the surface of catalyst to generate hydroxyl radicals. The increase of hydrogen peroxide concentration would lead to more hydroxyl radicals produced.

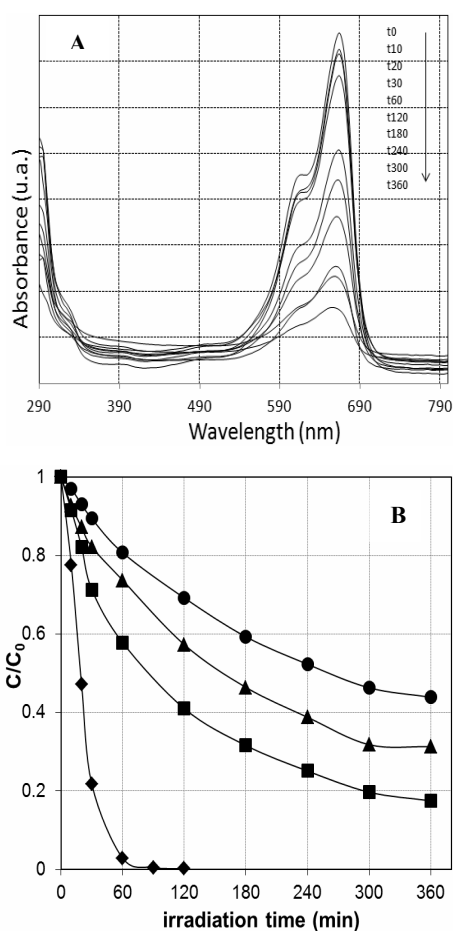


Fig. 4A. Temporal evolution of the UV Vis spectral changes taking place during the photodegradation of MB on Au/ZnCeAILDH2 600 using H_2O_2 ; **B.** Comparison of the photocatalytic efficiency of the catalysts during the photodegradation process of MB over the entire range of wavelength using different molar ratios MB: H_2O_2 ;
 ● without H_2O_2 ; ▲ 1 mol H_2O_2 ; ■ 2 moles H_2O_2 ; ◆ 5 moles H_2O_2 .

At low concentration, H₂O₂ could not generate enough hydroxyl radicals and the degradation efficiency was slow. It can be observed that using a lower concentration of hydrogen peroxides the degradation of the dye reached nearly 70% for 1M of H₂O₂ and 82% for 2M of H₂O₂ respectively, after 6h of irradiation. If we increase the amount of hydrogen peroxide at 5 M, the degradation of the dye solution is completely after 3h of irradiation with visible light; however the decolorization of Methylene blue increased significantly with the increase of amount of hydrogen peroxide. This is because the hydroperoxyl radicals (\bullet HO₂) are produced in presence of a local excess of H₂O₂ [27]. The degradation of MB dye likewise under the same conditions was studied by using the dye solution without the catalysts as reference sample. It was found that any degradation of the dye take place during the photodegradation process using visible light irradiation.

4. Conclusions

The results of the present work show the successful synthesis nanoparticles of gold deposited on the layered matrix of the anionic clays by using the structural reconstruction of the ZnCeAlLDH clays in AuCl₃ aqueous solutions. The calcinations process converts anionic clays type LDHs into mixture of mixed oxides and increase the size of gold nanoparticles. The morphology and structure of nanostructured materials have been analyzed by various methods. These nanostructured assemblies, especially Au/ZnCeAlLDH₂, showed an efficient photodegradation of the dye Methylene Blue under visible light irradiation. Also it was found that the samples had a highly catalytic activity for degradation of MB in presence of H₂O₂ and visible light. The new nanostructures Au/LDHs may contribute to open new perspective for the facile fabrication of cheap nano-photoresponsive formulations for removal of toxic pollutants from wastewater.

Acknowledgement. This work was supported by the grant of the Romanian National Authority for Scientific Research, CNCS-UEFISCDI, Project number PN-II-ID-PCE- 75/2013.

References

- [1] M.S. HADNADEV-KOSTIC, T.J. VULIC, D.B. ZORIC, R.P. MARINKOVIC-NEDUCIN, *Chem. Ind. Chem. Eng. Q.* **18**, pp. 295–303, 2012.
- [2] T. WARANG, N. PATEL, R. FERNANDEZ, N. BAZZANELLA, A. MIOTELLO, *Appl. Catal. B* **132-133**, pp. 204–211, 2013.
- [3] X. LIU, X. ZHAO, Y. ZHU, F. ZHANG, *Appl. Catal. B* **140-141**, 241–248, 2013.
- [4] M. HADNADJEV-KOSTIC, T. VULIC, J. RANOGAJEC, R. MARINKOVIC-NEDUCIN, A. RADOSAVLJEVIC-MIHAILOVIC, *J. Therm. Anal. Calorim.* **111**, pp. 1155–1162, 2013.
- [5] S. SHAKTIVEL, B. NEPPOLIAN, M.V. SHANKAR, B. ARABINDO, M. PALANICHAMY, V. MURUGESAN, *Sol. Energ. Mat. Sol. C* **77**, pp. 65–82, 2003.
- [6] F. ZHANG, X. XIANG, F. LI, X. DUAN, *Catal. Surv. Asia* **12**, pp. 253–265, 2008.

- [7] D.G. EVANS, R.C.T. SLADE, *Structure Bonding*, pp. 1191–1287, 2006.
- [8] P. BENITO, J. LABAJOS, J. ROCHA, V. RIVES, *Microporous Mesoporous Mat.* **94**, pp. 148–158, 2006.
- [9] G. CARJA, Y. KAMESHIMA, A. NAKAJIMA, K. OKADA, *Mesoporous Mat., Mesoporous Materials: Properties, preparation and applications* **9**, pp. 191–202, 2009.
- [10] A. MANTILLA, F. TZOMPANTZI, J.L. FERNANDEZ, J.A.I. DIAZ GONGORA, R. GOMEZ, *Catal Today*. **150**, pp. 353–357, 2010.
- [11] Z.P. XU, J. ZHANG, M.O. ADEBAJO, H. ZHANG, C. ZHOU, *Appl. Clay Sci.* **53**, pp. 139–150, 2011.
- [12] G. CARJA, A. NAKAJIMA, S. DRANCA, C. DRANCA, K.J. OKADA, *Phys. Chem. C* **114**, pp. 14722–14728, 2010.
- [13] G. CARJA, L. DARTU, K. OKADA, E. FORTUNATO, *Chem. Eng. J.* **222**, pp. 60–66, 2013.
- [14] S. YUAN, Y. LI, Q. ZHANG, H. WANG, *Colloids Surf. A Physicochem. Eng. Asp.* **348**, pp. 76–81, 2009.
- [15] E. SMOLENTSEVA, A. SIMAKOV, S. BELOSHAPKIN, M. ESTRADA, E. VARGAS, V. SOBOLEV, R. KENZHIN, S. FUENTES, *Appl. Catal. B* **115-116**, pp. 117–128, 2012.
- [16] G. CARJA, E. HUSANU, C. GHERASIM, H. IOVU, *Appl. Catal. B* **107**, pp. 253–259, 2011.
- [17] W.T. REICHLER, S.Y. KANG, D.S. EVERHARDT, *J. Catal.* **101**, pp. 352–359, 1986.
- [18] V. PREVOT, V. BRIOIS, J. CELLIER, C. FORANO, F. LEROUX, *J. Phys. Chem.* **69**, pp. 1091–1094, 2008.
- [19] F. CAVANI, F. TRIFIRO, A. VACCARI, *Catal. Today* **11**, pp. 173–301, 1991.
- [20] Y. KAMESHIMA, H. SASAKI, T. ISOBE, A. NAKAJIMA, K. OKADA, *Int. J. Pharm.* **381**, pp. 34–39, 2009.
- [21] C. GOMES SILVA, R. JUÁREZ, T. MARINO, R. MOLINARI, H. GARCÍA, *J. Am. Chem. Soc.* **133**, pp. 595–602, 2011.
- [22] E. NALBANT ESENTURK, A.R. HIGHT WALKER, *J. Nanopart. Res.* **15**, pp. 1364–1373, 2013.
- [23] I.M. ARABATZIS, T. STERGIPOULOS, D. ANDREEVA, S. KITOVA, S.G. NEOPHYTIDES, P. FALARAS, *J. Catal.*, **220**, pp. 127–135, 2003.
- [24] J. MATOS, T. MARINO, R. MOLINARI, H. GARCIA, *Appl. Catal. A.* **417-418**, pp. 262-272, 2012.
- [25] P.V. KAMAT, *J. Phys. Chem B.* **106**, pp. 7729–7744, 2002.
- [26] T. MARINO, R. MOLINARI, H. GARCIA, *Catal. Today* **206**, pp. 40–45, 2013.
- [27] F. JI, C. LI, J. ZHANG, L. DENG, *J. of Hazard. Mater.* **186**, pp. 1979–1984, 2011.

A New Nanomaterial for the Study of Protein Interactions

Alina VASILESCU^a, Iuliana MIHAI^a, Alis VEZEANU^a, Veronica ANDREI^a,
Georgian NEDELICU^a, Elena POPA^b, Cristina PURCAREA^b,
Palaniappan SUBRAMANIAN^c, Yannick COFFINIER^c,
Rabah BOUKHEROUB^c, Sabine SZUNERITS^c

^aInternational Centre of Biodynamics, 1 B Intrarea Portocalelor, sector 6,
060101, Bucharest, Romania

^bInstitute of Biology of the Romanian Academy, 296 Splaiul Independentei,
060031 Bucharest, Romania

^cInstitut de Recherche Interdisciplinaire (IRI, USR CNRS 3078), Université Lille 1,
Parc de la Haute Borne, 50 Avenue de Halley,
BP 70478, 59658 Villeneuve d'Ascq, France

Abstract. Selective determination of amino acids such as tyrosine and tryptophan is highly relevant when studying protein interactions. We investigated the efficacy of boron-doped diamond nanowires (BDD NWs) for the sensitive detection of the two amino acids in binary mixtures, and in a protein, lysozyme. BDD NWs allowed differentiating the individual electrochemical signals due to tyrosine and tryptophan oxidation in binary mixtures, and were used for monitoring lysozyme aggregation by Square Wave Voltammetry (SWV) and Electrochemical Impedance Spectroscopy (EIS). BDD NWs represent thus an interesting alternative nanostructured electrode for the electrochemical detection of these amino acids from biological samples.

1. Introduction

Selective determination of amino acids is very important for several transformations suffered by peptides and proteins, including phosphorylation [1, 2], nitration, unfolding [3], and aggregation [4, 5], as well as for monitoring their interactions with various compounds [6] for drug screening purposes. Changes in the exposure of tyrosine and tryptophan residues during protein unfolding and aggregation were emphasized by several electrochemical studies, mainly concerning the direct electrochemical oxidation

of these amino acid residues. However, the ability to capture snapshots of structural changes in proteins by electrochemical methods depends not only on the nature of the protein, but also on the electrode material [7]. Electrochemical oxidation of tyrosine and tryptophan occurs at very similar potential values on a variety of materials. Boron doped diamond (BDD) films raised high interest for applications in the field of electroanalytical chemistry, mostly due to their wide potential range for water stability as compared to other materials, their low background current and their biocompatibility [1, 8-14]. H-terminated BDD electrodes have been described as a hydrophobic, low-fouling substrate, ideal for electrochemical determinations in complex matrices. Oxidation of H-terminated BDD films by thermal, plasma, ozone treatment or electrochemical methods resulted in interfaces with applicative interest for electrochemistry, presenting different chemical reactivity and opening new avenues for functionalization [15]. BDD electrodes have been used for the detection of proteins [1], along with more classic carbon-based electrodes [7].

In the past decade, several reports have demonstrated the fabrication of nanostructured diamond interfaces [16-22]. The increase of the surface area of these interfaces resulted in higher sensitivities and selectivities when compared to planar BDD interfaces. Some of us have shown recently that BDD NWs can be prepared from polycrystalline BDD interfaces by reactive Ion Etching (RIE) with oxygen plasma in a maskless approach [18, 21-23]. These new interfaces allowed a sensitive detection of tryptophan with a detection limit of 5×10^{-7} M, representing a 20-fold improvement compared to planar electrodes from the same material [18].

These results prompted us to evaluate the utility of BDD NWs for the selective detection of tyrosine and tryptophan, both in binary mixtures and in a protein, represented by lysozyme, in a comparative study when using glassy carbon electrodes. The BDD NWs were used for monitoring the self-assembly of lysozyme in acidic media using Square Wave Voltammetry (SWV), and Electrochemical Impedance Spectroscopy (EIS). Fluorescence measurements using an amyloid indicator dye (Thioflavin T), Atomic Force Microscopy (AFM) and sodium dodecyl sulphate polyacrylamide gel electrophoresis (SDS-PAGE) were additionally performed in order to assess the degree of aggregation at various time points.

2. Material and Methods

Tryptophan was purchased from Fluka. Hen egg lysozyme, and tyrosine were from Sigma Aldrich. Britton-Robinson buffer, pH 2-11, and 0.2 M acetate, pH 5, were used in the electrochemical tests. Glassy carbon electrodes were from BAS.

BDD NWs electrodes were prepared from polycrystalline highly boron-doped

diamond electrodes (the boron concentration was $N_A = 8 \times 10^{19}$ B cm⁻² determined by SIMS measurements) by Reactive Ion Etching with oxygen plasma, without using any mask or template [18]. Reactive ion etching (RIE) of BDD was performed with oxygen plasma (Plasmalab 80 plus), with a radio frequency generator (13.56 MHz) for 10 min. Operating oxygen pressure, flow speed, and plasma power were: 150 mT, 20 sccm, and 300 W. The resulted BDD NWs were immersed for 15 min in an aqueous solution of HF (5% v/v) to dissolve the SiO₂ deposits. The dimensions of the obtained nanowires were 1.4 ± 0.1 μm long, with a tip and base radius of $r_{\text{tip}} = 10 \pm 5$ nm and $r_{\text{base}} = 40 \pm 5$ nm. Their density was $(14 \pm 3) \cdot 10^8$ nanowires cm⁻²[9].

2.1 Forced Aggregation of Lysozyme

A solution of 10 mg/mL lysozyme in 0.015 M at pH 2, containing 5 mg/mL NaCl was filtered through a 0.22 μm Nylon membrane and incubated at 60°C for up to 4 days. Aliquots were removed at various time intervals and diluted to 10-30 μg/mL with Britton-Robinson buffer pH 2 before analysis by electrochemical methods. The aggregation process was studied in detail by a variety of techniques as described elsewhere [24].

2.2 Electrochemical Studies

A VSP potentiostat/galvanostat from Bio-Logic S.A, France, equipped with EC-Lab software, was used for the electrochemical studies. Studies with BDD-NWs were performed in a flow-through cell of about 120 μL volume with BDD NWs as the working electrode, while the counter electrode was a platinum wire and the reference was a silver wire covered with silver chloride (Ag/AgCl). The geometric area of the BDD NWs exposed in the electrochemical cell was 4.1 mm².

The BDD NW electrodes were initially cleaned for 10 minutes in piranha (Hydrogen peroxide: sulphuric acid =1:3. *Warning: Piranha solution reacts violently with most organic materials and must be handled with extreme care!*) followed by a 15 minutes UV-ozone treatment (PSD-UV, NovaScan). After each measurement, the nanowires were cleaned in the presence of 0.2 M NaOH, by cycling the potential between -0.4 and 1.2 V vs Ag/AgCl, at 50 mV/s for 5-10 cycles.

In the case of glassy carbon electrodes, we used a classical setup, where the counter electrode was a Pt wire and the reference was Ag/AgCl, KCl (3M). The measurements were performed in 0.2 M acetate buffer pH 5, as described elsewhere [24]. The electrodes were cleaned by polishing with alumina slurry, followed by rinsing with water.

2.2.1 Tests with BDD NWs

Analysis of tyrosine and tryptophan

Solutions of 100 µg/mL tyrosine and 10 µg/mL tryptophan at pH ranging from 2 to 11 were prepared in Britton-Robinson buffer. For cyclic voltammetry experiments, the potential was scanned at 50 mV/s, from 0 to 1.3 V, vs. Ag/AgCl. SWV analysis was optimized by analyzing the amino acid solutions of various concentrations at a frequency of 5 Hz, step height of 10 mV, and peak amplitude of 25 mV. The potential was swept directly from -0.25 to 1.2 V without any pre-adsorption.

Analysis of lysozyme by square wave voltammetry (SWV)

The protein solution obtained in 20 mM Britton-Robinson buffer pH 2 was adsorbed on pseudo Ag/AgCl for 5 minutes at -0.25V in the flow-through cell, and the potential was further increased to +1.5 V at 200 Hz, with a step height of 5 mV and a peak amplitude of 25 mV. In the case of the glassy carbon electrodes, the square wave voltammetry measurements (SWV) were performed in the presence of 0.2 M acetate buffer containing 0.1 M NaCl, pH 5, after first pre-treating the electrodes by polarizing them at +1.4 V vs. Ag/AgCl for 30 s [24].

Analysis of lysozyme by Electrochemical Impedance Spectroscopy (EIS)

The EIS spectra were recorded within a frequency range of 0.1 -9.5 kHz, using an equimolar mixture of 1 mM potassium ferricyanide and potassium ferrocyanide in PBS pH 7.4 buffer, at the formal potential of the ferri/ferro redox couple. A sinusoidal signal with 10 mV amplitude was applied in addition of the formal potential. Data were fitted to an equivalent circuit (R1+Q2/(R2)), using Zview software. The variation of the resistance to the ion transfer, before and after lysozyme adsorption, was determined as a function of lysozyme concentration (calibration) and incubation time (aggregation studies).

2.3 Study of the lysozyme aggregation by Thioflavin T fluorescence, SDS-PAGE and Atomic Force Microscopy

Thioflavin T fluorescence and Atomic Force Microscopy experiments were conducted as previously described [24], using a Glomax 20/20 Luminometer (Promega) with a Fluorescent Blue Module (excitation at 465–485 nm, emission at 515–575nm). Samples of 10 µL protein solution were mixed with 1 mL of 28 mM thioflavin T in PBS pH 7.4 buffer, and the fluorescence was immediately measured. Results were expressed as the mean of five replicate measurements. AFM studies were carried on using a Nanowizard II AFM instrument (JPK, Germany) operating in

intermittent contact in air, and the protein structure was visualized with an RTESP cantilever (resonant frequency of ~ 300 kHz, force constant of ~ 40 N m⁻¹, (Veeco, USA). Aggregated lysozyme solutions (50 μ g/mL) were adsorbed on mica and dried for 30 minutes at room temperature under vacuum, and the resulted mica samples were thoroughly washed with ultrapure water and dried under nitrogen flow. A SDS-PAGE analysis of aggregated lysozyme was performed using an electrophoresis system with cooling (Biometra, Analytik Jena) to avoid decomposition of aggregates at high temperature in SDS, and the protein oligomers were separated on 10% polyacrylamide gels at 20 mA and 40 mA/cm gel. Protein fragments were stained with Coomassie Blue for visualizing their migration position.

3. Results and Discussion

3.1 Detection of Tyrosine and Tryptophan in Simple Mixtures

A 10:1 mixture of tyrosine: tryptophan was analyzed by cyclic voltammetry in Britton-Robinson buffer with pH ranging from 2 to 11. The electrochemical oxidation signals for tyrosine and tryptophan were well separated at pH 2, while, at alkaline pH, the peaks completely overlapped (Fig. 1a). The redox peaks corresponding to the oxidation of tyrosine and tryptophan shifted towards more negative values as the pH increased, in accordance with electrode reactions involving transfer of protons. When glassy carbon electrodes were used, the two amino-acids were oxidized at very similar potential values, exhibiting fully overlapped peaks (Fig. 1b). The peak intensity also decreases upon cycling due to passivation of the electrode surface with adsorbed oxidation products.

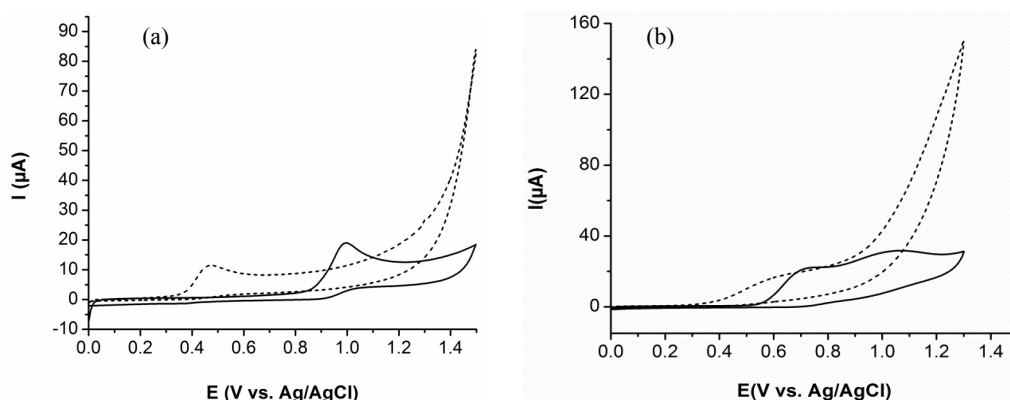


Fig. 1. Cyclic voltammograms of mixtures of tyrosine/tryptophan (100 μ g/mL tyrosine and 10 μ g/mL tryptophan) recorded on (a) BDD NWs and (b) glassy carbon electrodes in Britton-Robinson buffer pH 2 (full line) and pH 11 (dashed line) at a scan rate of 50 mV/s.

Our data, unraveling the ability of BDDNWs to discriminate between the electrochemical signature of tyrosine and tryptophan is a particularly important result, since very few materials that allow such separation have been described so far.

We further explored the potential of BDD NWs for the sensitive detection of amino- acids using SWV. In SWV, the contribution from the charging capacitive current to the electrochemical signal is minimized, which can lead to improvement of the sensitivity of the detection compared to cyclic voltammetry.

Typical voltammograms recorded for tyrosine and tryptophan (Fig. 2) emphasize the difference in the magnitude of the oxidation peak for the two aminoacids at the same concentration. Depending on the ratio between tyrosine and tryptophan, their accurate detection in binary mixtures would be hampered by the partial overlap of their electrochemical oxidation signals.

At pH 2, the tyrosine current intensity peak from the SWV profile showed a linear dependence with the amino-acid concentrations in the range 1-60 μM , according to: $I_{(\mu\text{A})} = 0.0526 \times [\text{tyrosine}]_{(\mu\text{M})} + 0.0779$ ($R^2 = 0.9972$), with a detection limit ($S/N=3$) of 0.86 μM . Under the same conditions, the current signal for tryptophan oxidation varied linearly with the protein concentration in the range 0.2-200 μM according to $I_{(\mu\text{A})} = 0.0705 \times [\text{tryptophan}]_{(\mu\text{M})} + 0.4557$ ($R^2=0.9947$) with a detection limit of 0.14 μM . When compared to similar experiments performed on screen-printed carbon electrodes, a lower detection limit of 10 nM and a linear range from 100 nM -200 μM were obtained for this aminoacid [2]. However, in this later case, the accumulation time on the surface of screen-printed electrodes prior to the voltammetric detection was of 10 minutes, while our tests with BDD NWs do not involve any pre-concentration of the electroactive species.

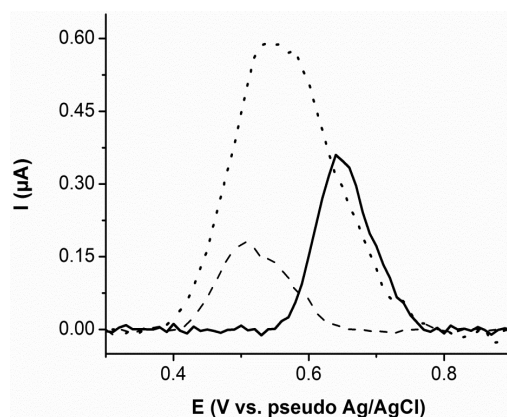


Fig. 2. SW voltammograms for 5 μM tyrosine (full line), 5 μM tryptophan (dotted line) and 0.5 μM tryptophan (dashed line) using BDD NWs in Britton Robinson buffer at pH 2.

The individual contributions of tyrosine and tryptophan to the electrochemical oxidation signal were previously studied when using carbon electrodes for the analysis of binary amino acid mixtures and small peptides [4]. In this case, a baseline separation was obtained between the oxidation signals of these two amino acids from the 393 amino acid cancer-related p53 protein.

In the following we investigated the electrochemical detection of the amino acids in lysozyme using BDDNWs electrodes. We further used the BDDNWs electrodes for the electrochemical monitoring of the aggregation process of this protein at pH 2.

3.2 Lysozyme Detection

Although lysozyme contains 3 tyrosine and 6 tryptophan residues, its electrochemical signal is determined by the exposed groups and influenced by the neighboring amino acids. SWV studies of lysozyme solutions using BDDNWs emphasized only one oxidation peak the signals of tyrosine and tryptophan overlapping completely at pH 2-11 (Fig. 3). The current intensity peak value increased linearly with the lysozyme concentration in the range between 0.140 μM and 1.4 μM , with a detection limit (S/N=3) of 70 nM (Figure 3 a and b) comparable to the analytical characteristics previously obtained with GC electrodes [24].

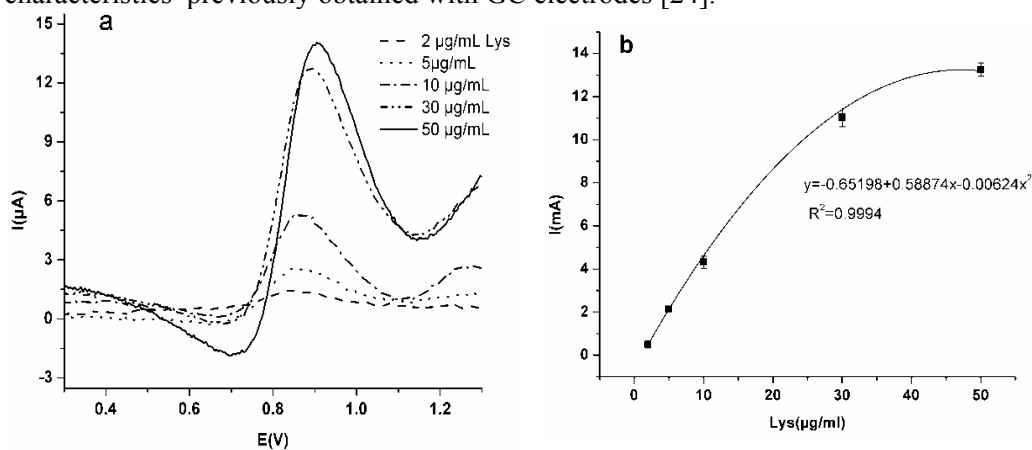


Fig. 3. SWV obtained on BDDNWs electrodes for different concentrations of lysozyme, after subtracting the base line (a), and the corresponding calibration curve (b).

When using EIS, similar results were obtained. The impedance spectra were fitted to a classic circuit (Fig. 4a and b), in order to determine the resistance to charge transfer (Rct). The charge transfer resistance showed a linear dependency with the

lysozyme concentration in the range of $0.140 - 1.4\mu\text{M}$ ($R^2=0.9901$), with a detection limit of 70 nM.

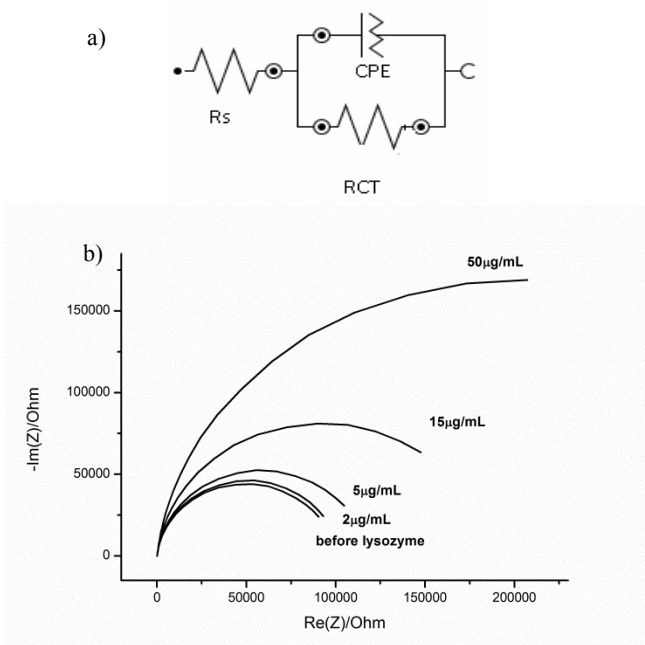


Fig. 4. Detection of lysozyme with BDD-NWs electrodes by EIS: Equivalent circuit used for fitting the data (a) and Nyquist plots for different concentrations of lysozyme (b).

3.3 Lysozyme Aggregation

The lysozyme aggregation process was also investigated by SWV and EIS. SWV showed an increase in the peak intensity during the initial 24 hours of the aggregation process, correlating with an increase in the charge transfer resistance to charge transfer using EIS. This was followed by a slow but continuous decrease of the signal thereafter (Fig. 5a). A similar profile was previously observed for the first 24 hours of the same aggregation process monitored on glassy carbon electrodes [24] (Fig. 5b). However, both BDD NWs and glassy carbon electrodes did not allow distinguishing between the individual contributions of tyrosine and tryptophan to the electrochemical signal recorded by SWV during the aggregation.

Our previous characterization of the lysozyme aggregation process using MALDI-TOF indicated that in the first 24 hours, the dominant processes were the lysozyme

acid hydrolysis and formation of small soluble oligomers up to homopentameric quaternary structure [24].

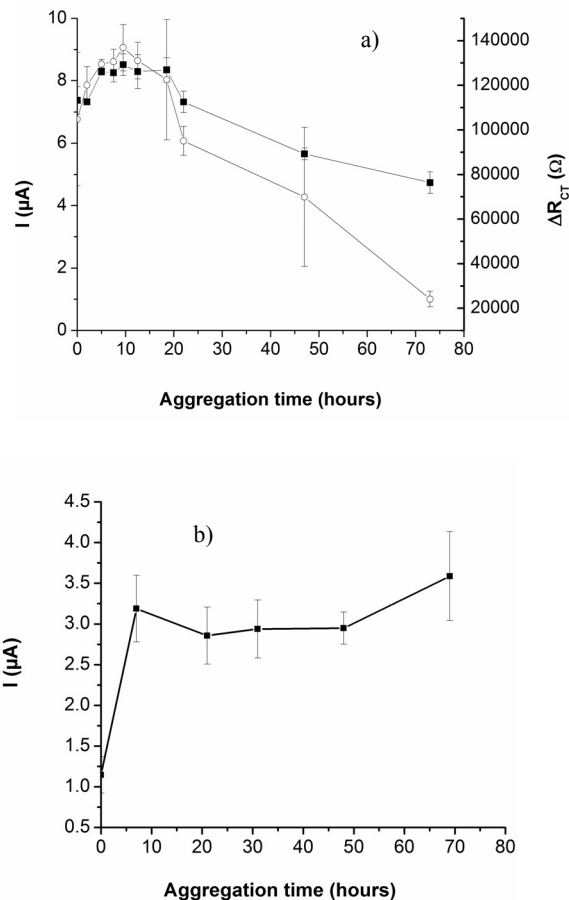


Fig. 5. Time course of lysozyme aggregation in the presence of (a) BDD -NWs using SWV (full squares) and EIS (open circles) and (b) in the presence of glassy carbon electrodes using SWV.

Moreover, the while oligomerization process from monomer to aggregates implies several probable pathways occurring in parallel [25], the population of protein species in solution at any given time is rather complex. In this context, the utilization of BDD NWs and electrochemical methods, such as SWV and EIS, allowed us to capture a snapshot of these transformations.

In order to correlate the electrochemical data with different stages of aggregation, we analyzed the aggregated lysozyme by not only by electrochemical methods but also by thioflavin T fluorescence, SDS-PAGE and AFM. Thioflavin T is widely used as an *in vitro* amyloid staining dye, based on the shift of its excitation maxima and enhanced fluorescence presented upon binding to β -sheets in protein fibrils. In our experiments, fluorescence measurements with thioflavin T were typical for aggregation studies leading to formation of amyloid fibrils and emphasized a lag period of about 24 hours, corresponding to a sharp increase in fluorescence and a plateau after 3-4 days (Fig. 6). Within corroboration with the AFM results (Fig. 6, insets) and SDS-PAGE data (Fig. 7), this observation supports the SWV profiles obtained. In this case, the most extensive shift in the electrochemical signal recorded with both BDD-NWs and glassy carbon electrodes occurred in the first 24 hours, as previously observed [24]. These signal changes are attributed to protein unfolding, exposing more electroactive tyrosine and tryptophan residues to the hydrophilic environment.

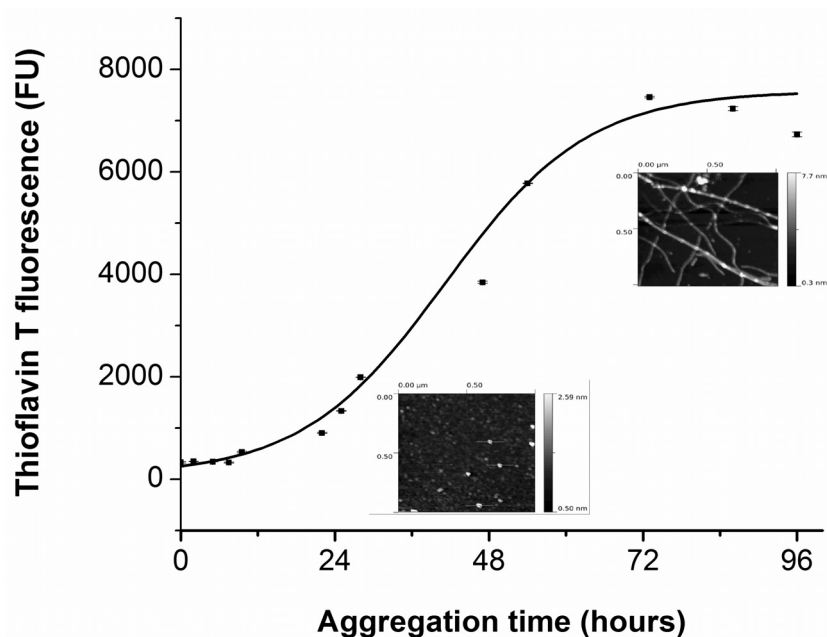


Fig. 6. Fluorescence of thioflavin T in solutions of lysozyme at different aggregation times. Insets: intermittent contact mode AFM images of fresh lysozyme (bottom inset; protein fibrils formed long, twisted protein fibrils (4 nm diameter) formed in lysozyme solutions kept for three days in the forced aggregation conditions (upper inset).

There was no increase in thioflavin T fluorescence in the first 24 hours, indicating that the fibrillation did not start after this period (Fig. 6). After 2-3 days of aggregation, the fibril formation determined by AFM (Fig. 6, insets) corresponded to the sharp increase in thioflavin T fluorescence (Fig. 6) due to its binding to amyloid fibrils [26].

Moreover, the fibrils formation leads to the decrease of the available electroactive amino-acid residues inducing an electrochemical signal decrease.

SDS-PAGE confirmed the results observed with the techniques detailed above. The concentration of monomers decreased after increasing aggregation time and in the presence of various NaCl concentrations, due to acidic hydrolysis, with the formation of increasing amounts of high molecular weight oligomers (around 80-120 kDa) (Fig. 7).

These results, together with data obtained with the complementary techniques presented above, substantiate our explanation of the trends observed with electrochemical methods during aggregation, both using BDD NWs or glassy carbon electrodes.

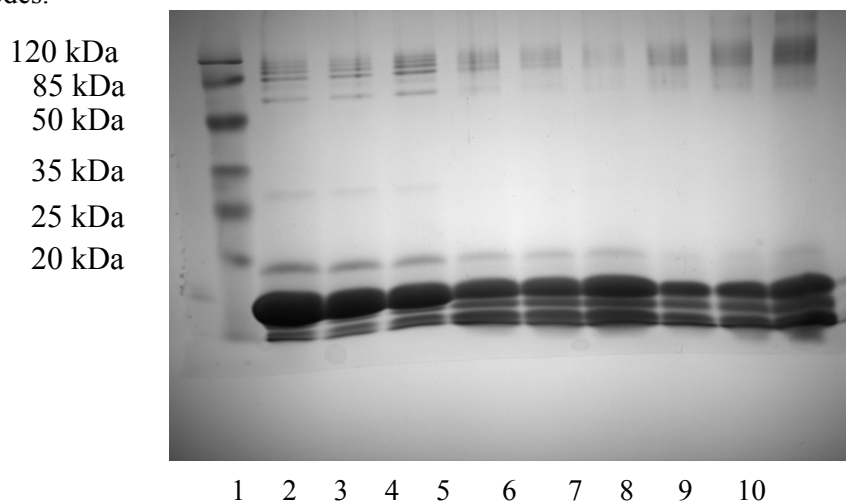


Fig. 7. SDS-PAGE analysis of lysozyme solutions. Samples of 10 mg/mL lysozyme solutions at pH 2 were incubated at 60°C for different periods of time and in the presence of various concentrations of NaCl: (1) MW Markers; (2) 2h, 3 mg/mL NaCl; (3) 2h, 5 mg/mL NaCl; (4) 4h, 5 mg/mL NaCl; (5) 18h, 5 mg/mL NaCl; (6) 20h, 5 mg/mL NaCl; (7) 24h, 5 mg/mL NaCl; (8) 28h, 5 mg/mL; (9) 41h, 3 mg/mL; (10); 41 h, 5 mg/mL NaCl.

Our results are in accordance with those obtained by the electrochemical monitoring of Alzheimer's disease (AD) amyloid beta peptides ($A\beta$ -40, $A\beta$ -42) aggregation process [5]. The present study also confirms that BDDNWs represent

an adequate material for studying protein interactions, suggesting that it could be used as a general tool for studying proteins that are prone to aggregation.

4. Conclusions

Our results demonstrated that utilization of BDDNWs allowed not only the sensitive detection of tyrosine and tryptophan, but also partially resolved the individual electrochemical oxidation signals for simple mixtures analyzed at pH 2. This procedure provides a simple way to analyze aminoacids that could be explored for analyzing biological samples. However, under these conditions, it was not possible to resolve the contributions due to the tyrosine and tryptophan residues in lysozyme, not in the fresh protein or in aggregated samples. Future investigations are required to further improve the resolution between the electrochemical oxidation signals for the two aromatic amino-acids, by using approaches based on chemometrics.

Electrochemical detection of lysozyme with BDD-NWs was equally sensitive by using SWV and EIS, with a detection limit of 1 $\mu\text{g/mL}$. Moreover, the lysozyme adsorbed on the nanowires could be easily removed electrochemically after each analysis. Therefore, BDD-NWs could be useful in the flow injection analysis of lysozyme and, potentially, of other electroactive proteins. This is the first report of using BDDNWs for monitoring the aggregation of lysozyme using a forced degradation protocol leading to amyloid fibrils. The data obtained was further underlined by fluorescence measurements using Thioflavin T, SDS-PAGE and AFM, respectively. Moreover, the analytical performances and the trends observed with BDDNWs and glassy carbon electrodes when monitoring lysozyme aggregation were similar.

Acknowledgments. This work was financially supported by the Marie Curie International Reintegration Grant FP7 PEOPLE-2010-RG-277126, PN-II-RU-TE-2011-3-0302 (ANCS UEFISCDI) and PN-II-PT-PCCA-2011-3.1-1809 (ANCS UEFISCDI). We would like to express our gratitude to Dr. Szilveszter Gaspar from the International Centre of Biodynamics for the AFM scans.

References

- [1] M. CHIKU, T.A. IVANDINI, A. KAMIYA, A. FUJISHIMA and Y. EINAGA, "Direct electrochemical oxidation of proteins at conductive diamond electrodes", *J. Electroanal. Chem.*, **612**(2), pp. 201–207, Jan. 2008.
- [2] K. KERMAN, M. VESTERGAARD, M. CHIKAE, S. YAMAMURA and E. TAMIYA, "Label-free electrochemical detection of the phosphorylated and non-phosphorylated forms of peptides based on tyrosine oxidation", *Electrochem. Commun.*, **9**(5), pp. 976–980, May 2007.

- [3] V. OSTATNÁ, B. USLU, B. DOGAN, S. OZKAN and E. PALEČEK, “Native and denatured bovine serum albumin. D.c. polarography, stripping voltammetry and constant current chronopotentiometry”, Spec. Issue Honour Petr Zuman Occas. His 80th Birthd., **593**(1–2), pp. 172–178, Aug. 2006.
- [4] D. POTESIL, R. MIKELOVA, V. ADAM, R. KIZEK and R. PRUSA, “Change of the protein p53 electrochemical signal according to its structural form - quick and sensitive distinguishing of native, denatured, and aggregated form of the ‘guardian of the genome’”, Protein J., **25**(1), pp. 23–32, Jan. 2006.
- [5] M. VESTERGAARD, K. KERMAN, M. SAITO, N. NAGATANI, Y. TAKAMURA and E. TAMIYA, “A rapid label-free electrochemical detection and kinetic study of Alzheimer’s amyloid beta aggregation”, J. Am. Chem. Soc., **127**(34), pp. 11892–11893, Aug. 2005.
- [6] T. CHAN, A.M. CHOW, D.W.F. TANG, Q. LI, X. WANG, I.R. BROWN and K. KERMAN, “Interaction of baicalein and copper with α -synuclein: Electrochemical approach to Parkinson’s Disease”, J. Electroanal. Chem., **648**(2), pp. 151–155, Oct. 2010.
- [7] V. OSTATNÁ, H. ČERNOCKÁ, K. KURZAŤKOWSKA and E. PALEČEK, “Native and denatured forms of proteins can be discriminated at edge plane carbon electrodes”, Anal. Chim. Acta, **735**, pp. 31–36, Jul. 2012.
- [8] E. FORTIN, J. CHANE-TUNE, P. MAILLEY, S. SZUNERITS, B. MARCUS, J.-P. PETIT, M. MERMOUX and E. VIEIL, “Nucleosides and ODN electrochemical detection onto boron doped diamond electrodes”, Bioelectrochemistry Amst. Neth., **63**(1–2), pp. 303–306, Jun. 2004.
- [9] S. SZUNERITS, J. NIEDZIOLKA-JÖNSSON, R. BOUKHERROUB, P. WOISEL, J.-S. BAUMANN and A. SIRIWARDENA, “Label-free detection of lectins on carbohydrate-modified boron-doped diamond surfaces”, Anal. Chem., **82**(19), pp. 8203–8210, Oct. 2010.
- [10] D. MEZIANE, A. BARRAS, A. KROMKA, J. HOUDKOVA, R. BOUKHERROUB and S. SZUNERITS, “Thiol-yne Reaction on Boron-Doped Diamond Electrodes: Application for the Electrochemical Detection of DNA–DNA Hybridization Events”, Anal. Chem., **84**(1), pp. 194–200, Jan. 2012.
- [11] D. DELABOUGLISE, B. MARCUS, M. MERMOUX, P. BOUVIER, J. CHANE-TUNE, J.-P. PETIT, P. MAILLEY and T. LIVACHE, “Biotin grafting on boron-doped diamond”, Chem. Commun., **21**, pp. 2698–2699, Oct. 2003.
- [12] T. KNICKERBOCKER, T. STROTHER, M. P. SCHWARTZ, JOHN N. RUSSELL, J. BUTLER, L. M. SMITH and R. J. HAMERS, “DNA-Modified Diamond Surfaces”, Langmuir, **19**(6), pp. 1938–1942, Mar. 2003.
- [13] A. HÄRTL, E. SCHMICH, J.A. GARRIDO, J. HERNANDO, S.C.R. CATHARINO, S. WALTER, P. FEULNER, A. KROMKA, D. STEINMÜLLER and M. STUTZMANN, “Protein-modified nanocrystalline diamond thin films for biosensor applications”, Nat. Mater., **3**(10), pp. 736–742, Oct. 2004.
- [14] J. ZHAO, L. WU and J. ZHI, “Non-enzymatic glucose detection using as-prepared boron-doped diamond thin-film electrodes”, Analyst, **134**(4), pp. 794–799, Mar. 2009.
- [15] S. SZUNERITS and R. BOUKHERROUB, “Different strategies for functionalization of diamond surfaces”, J. Solid State Electrochem., **12**(10), pp. 1205–1218, Oct. 2008.
- [16] D. LUO, L. WU and J. ZHI, “Fabrication of Boron-Doped Diamond Nanorod Forest Electrodes and Their Application in Nonenzymatic Amperometric Glucose Biosensing”, ACS Nano, **3**(8), pp. 2121–2128, Aug. 2009.
- [17] N. YANG, H. UETSUKA and C.E. NEBEL, “Biofunctionalization of Vertically Aligned Diamond Nanowires”, Adv. Funct. Mater., **19**(6), pp. 887–893, 2009.

- [18] S. SZUNERITS, Y. COFFINIER, E. GALOPIN, J. BRENNER and R. BOUKHERROUB, "Preparation of boron-doped diamond nanowires and their application for sensitive electrochemical detection of tryptophan", *Electrochem. Commun.*, **12**(3), pp. 438–441, Mar. 2010.
- [19] Y. COFFINIER, E. GALOPIN, S. SZUNERITS and R. BOUKHERROUB, "Preparation of superhydrophobic and oleophobic diamond nanograss array", *J. Mater. Chem.*, **20**(47), pp. 10671–10675, Nov. 2010.
- [20] C. TERASHIMA, K. ARIHARA, S. OKAZAKI, T. SHICHI, D. A. TRYK, T. SHIRAFUJI, N. SAITO, O. TAKAI and A. FUJISHIMA, "Fabrication of Vertically Aligned Diamond Whiskers from Highly Boron-Doped Diamond by Oxygen Plasma Etching", *ACS Appl. Mater. Interfaces*, **3**(2), pp. 177–182, Feb. 2011.
- [21] P. SUBRAMANIAN, Y. COFFINIER, D. STEINMÜLLER-NETHL, J. FOORD, R. BOUKHERROUB and S. SZUNERITS, "Diamond nanowires decorated with metallic nanoparticles: A novel electrical interface for the immobilization of histidinylated biomolecules", *Electrochem. Adv. Mater. Technol. Instrum. Sel. Pap. 63rd Annu. Meet. Int. Soc. Electrochem.* 19–24 August 2012 Prague Czech Repub., **110**, pp. 4–8, Nov. 2013.
- [22] N. YANG, H. UETSUKA, E. OSAWA and C.E. NEBEL, "Vertically Aligned Diamond Nanowires for DNA Sensing", *Angew. Chem. Int. Ed.*, **47**(28), pp. 5183–5185, 2008.
- [23] Q. WANG, A. VASILESCU, P. SUBRAMANIAN, A. VEZEANU, V. ANDREI, Y. COFFINIER, M. LI, R. BOUKHERROUB and S. SZUNERITS, "Simultaneous electrochemical detection of tryptophan and tyrosine using boron-doped diamond and diamond nanowire electrodes", *Electrochem. Commun.*, **35**, pp. 84–87, Oct. 2013.
- [24] A. VASILESCU, S. GASPAR, I. MIHAI, A. TACHE and S.C. LITESCU, "Development of a label-free aptasensor for monitoring the self-association of lysozyme", *Analyst*, **138**(12), pp. 3530–3537, May 2013.
- [25] S.E. RADFORD, C.M. DOBSON and P.A. EVANS, "The folding of hen lysozyme involves partially structured intermediates and multiple pathways", *Nature*, **358**(6384), pp. 302–307, Jul. 1992.
- [26] M.R.H. KREBS, E.H.C. BROMLEY and A.M. DONALD, "The binding of thioflavin-T to amyloid fibrils: localisation and implications", *J. Struct. Biol.*, **149**(1), pp. 30–37, Jan. 2005.

Environmental Applications of Carbon-Based Nanomaterials. Acetylcholinesterase Biosensors for Organophosphate Pesticide Analysis

Ion ION^a, Alina CULETU^a, Dragos GHERASE^b,
Florinela SIRBU^c and Alina Catrinel ION^a

^a“Politehnica” University of Bucharest, Faculty of Applied Chemistry and Material Science,
1-7 Polizu str., 011061, Bucharest, Romania
E-mail: i_ion@chim.upb.ro, alina.culetu@yahoo.com,
ac_ion@yahoo.com

^bCentre for Organic Chemistry “Costin D. Nenitescu”, Romanian Academy,
Bucharest 060023, Romania
E-mail: dragos_gherases@yahoo.com

^c“Ilie Murgulescu” Institute of Physical Chemistry of Romanian Academy, 202 Splaiul
Independentei str., 060021, Bucharest, Romania
E-mail: sflorinela@yahoo.com

Introduction

Natural resources of the world beginning to get exhausted, agriculture has to accomplish an important role in a sustainable world. Taking into account the limited availability of water and land resources, achievements in agriculture can be obtained using new technologies. Nanotechnologies can offer the ways to make crucial changes in the agricultural sector in environmental engineering and in water resources.

Improving air, water and soil quality represent an important challenge of the 21st century. Identifying and treating the environmental contaminants and preventing pollution are obligatory steps in environmental protection, each step involving important contributions of materials science. The progress in materials science increased exponentially in the last decade, arriving in our days at a large variety of nanomaterials, which can deliver new environment technologies, due to their

immensely powerful capacity.

Organophosphate pesticides (OPP) include parathion, malathion, methyl parathion, chlorpyrifos, diazinon, dichlorvos, phosmet, tetrachlorvinphos, triazophos, oxydemeton and azinphos methyl. OPP obtain their toxicity from the ability to inhibit cholinesterase, causing neurotoxicity, but apart from the toxic effects long term effects include their ability to disrupt the endocrine systems in organisms [1]. It must be noted that many pesticides are transformed in the environment through physical, chemical and biological processes, being sometimes transformed in much more toxic products [2]. At this moment, there are alternative methods of detection investigated, using enzymes for detection purposes seeming a very promising route. These enzymes are incorporated into biosensors, these miniaturized devices being very promising for monitoring pesticides in agriculture. Nanotechnology offers new solutions in pollution sensing and prevention by using adequate nanomaterials with unique properties. A multitude of applications of nanomaterials in environmental pollutions and pollution sensing in agriculture are already published, but nanotechnology has to move in a more practical regime, making its presence really felt in improved agricultural production and in environmental protection.

Types of Nanomaterials used in the Biosensor's Construction. In recent years, nanomaterials and their functional derivatives began to have environmental applications in treatment and remediation, pollution sensing, detection and pollution prevention, the most important ones being in sorption of environmental contaminants and in environmental sensing.

Environmental applications benefit from the unique properties of nanomaterials and in particular, their size, shape and surface area; molecular interactions and sorption properties; electronic, optical and thermal properties. Molecular manipulation implies control over the structure and conformation of a material. For carbon nanomaterials this includes size, length, chirality and number of layers.

Elucidating the molecular interactions, sorption and partitioning properties governing nanotubes, graphene and graphitic nanoplatelets is a joint effort between theorists and experimentalists [3].

There are a lot of criteria of classification of nanomaterials, function of their composition, crystalinity, dimensions, shapes and forms [4]. One of the mostly used classifications of the nanomaterials is based on their composition in Fig. 1.

Function of the number of characteristic dimensions, nanomaterials can be classified in 0-D (nanomaterials with spherical shape) [5], 1-D (nanowires, nanorods, nanotubes) [6], 2-D (nanocoatings and nanofilms) [7] and 3-D (nanocrystalline and nanocomposite materials with no bulk dimensions) (Fig. 2).

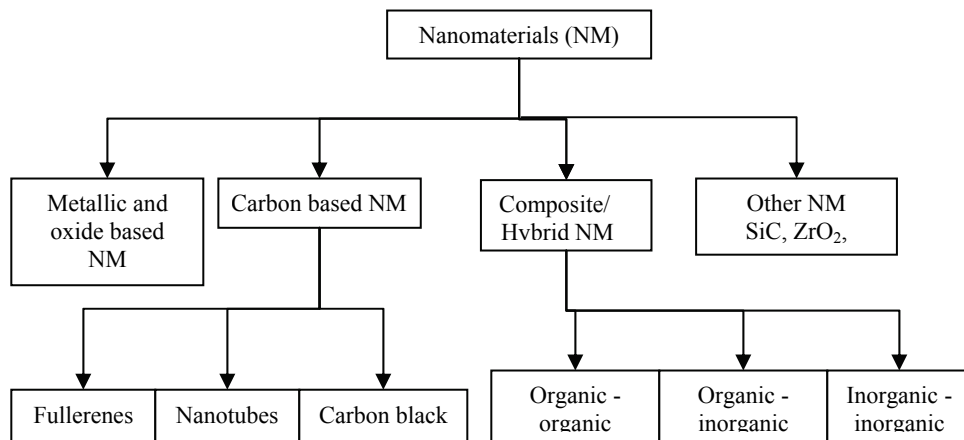


Fig. 1. Nanomaterials classification function of the nature of the components.

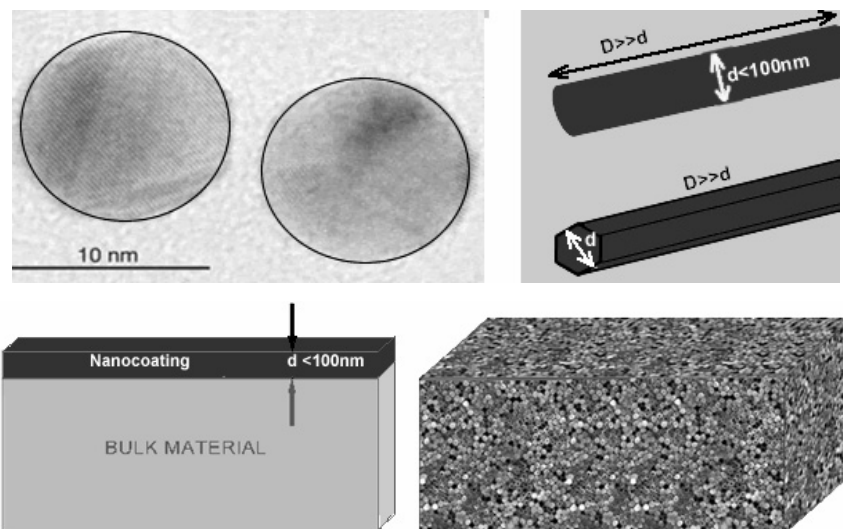


Fig. 2. Nanomaterials classification function of the number of characteristics dimensions (reproduced with permission).

Among carbon-based nanomaterials, depending on the hybridization states we can include: nanodiamonds, fullerenes, carbon onions, single and multi-walled carbon nanotubes and grapheme [8], with different physical, chemical and electronic properties.

Recently, graphene have attracted attention, due to its novel mechanical, thermal and electronic properties [9], material processing being till the last year the rate-limiting step in graphene applications. The scotch tape method [10] or the micro-mechanical cleavage discovery encouraged the research in this field. Other methods include various chemical combinations and reductions, important amounts of graphene for commercial use becoming possible. Graphite nanoplatelets represent also a solution for inexpensive filler substitutes for carbon nanotubes with interesting properties [11]. It is essential to mention that the sorption of organic molecules is improved on a basal plane of graphite where the molecules adsorb laying flat in comparison with the sorption on the curved tube wall, the effect of the carbon nanotubes nanoscale curvature on the surface adsorption being largely explained in [12].

As far as costs, graphene-based materials are cheaper than the carbon nanotube counterpart, displaying similar properties. Furthermore, toxicity issues are reduced because graphene based materials are one nanometer thick, being less likely to cause cancer [13]. Taking into account these advantages, graphene entrapped in biosensors construction prove to be efficient solutions for improving the characteristics of the biosensors such as: the linear range, the detection limit and the correlation coefficient values in comparison with other electroanalytical techniques.

Engineered Carbon-Based Nanomaterials (ECNM) unite the distinctive properties of sp^2 hybridized carbon bonds with the unusual characteristics of physics and chemistry at the nanoscale. From the electrical conductivity of a single nanotube to the adsorptive capacity of bulk nanomaterials, both single molecule and bulk properties offer potential advances in environmental systems. Carbon nanomaterials are generally consistent with traditional physical-chemical models and theories including electrostatics [14], adsorption, hydrophobicity [15]. Molecular modeling has provided an interpretation of physical-chemical processes occurring at the nanoscale that are otherwise inaccessible through experimental techniques, though computational demands limit the range of length-scale, chirality and layers feasible in the molecular modeling of heterogeneous nanotube and graphene samples [16].

The potential energies of interaction between carbon nanomaterials are described by the classic Lennard-Jones continuum model. The Lennard-Jones model accounts for both van der Waals attractive forces (Kessom, Debye and London forces) and Pauli repulsion originating from overlapping electron orbitals at very short separation distances [17]. Geometry-specific empirical constants provide strong correlation to the theory of a universal graphitic potential when geometries are considered.

Functionalization via covalent or supramolecular techniques reduces aggregation through steric hindrance and the introduction of polar functional groups that confer

hydrophilicity to the otherwise hydrophobic nanofillers [18]. Hydrophobicity relates the strength of water-water interactions to water-particle and particle-particle interactions. A hydrophobic molecule will interact less favorably with water than two solute molecules interact with each other, causing the liquid to withdraw from the surface and form a vapor layer. Molecular simulations of CNTs in water suggest that the primary barrier to dissolution is the energy required to disrupt water-water bonds when forming a cavity for the CNT [19].

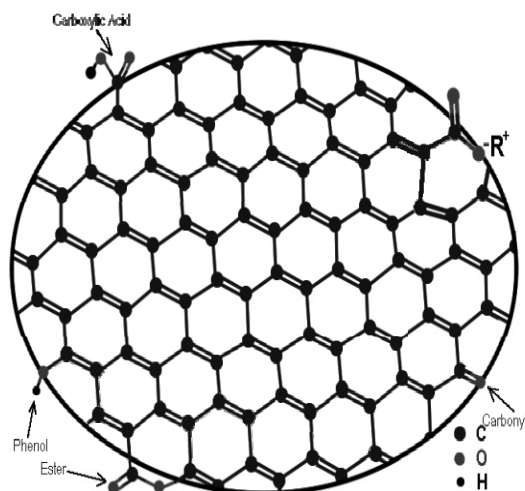


Fig. 3. Functionalization through oxidation of the graphene edges.

Modification of the surface morphology is important in enhancing the capability of graphene, the functional groups being created through chemical functionalization. Usually, the surface characteristics are altered due to the introduction of new functional groups such as: COOH, HO-, lactones, C=O through oxidation, which later on can be further functionalized [20].

In the literature of the last three years, there were published several sensors and biosensors based on graphene. A sensing platform for ultrasensitive determination of cadmium was presented based on the Nafion-graphene nanocomposite film modified electrode [21]. The graphene is dispersed in the Nafion solution, the interfusion of graphene into the Nafion film exhibiting excellent stripping performance for trace analysis of heavy metals, based on the advantages of the graphene nanosheets. The sensor responds on a concentration range from 0.2 to 15 $\mu\text{g L}^{-1}$, with a detection limit of 0.005 $\mu\text{g L}^{-1}$, using a 500 s preconcentration.

Types of Sensors Based on Carbon Nanomaterials. Removal of contaminants from the environment and from agricultural areas should firstly use methods to determine the presence of these chemicals.

Rapid and robust sensors used in the detection of pollutants at the molecular level can enhance the environmental protection. The process control of the industrial production, the ecosystem monitoring and environmental decision will be improved if more sensitive and cheaper techniques for the detection of contaminants would be easily available. Very important will become in these conditions the continuous monitoring devices that can detect pollutants at trace level.

Different sensors are used operating on different principles. Among them it can be mentioned: solid state electrochemical sensors as chemical gas sensors very good in what concerns sensitivity and reproducibility, but with poor selectivity [22].

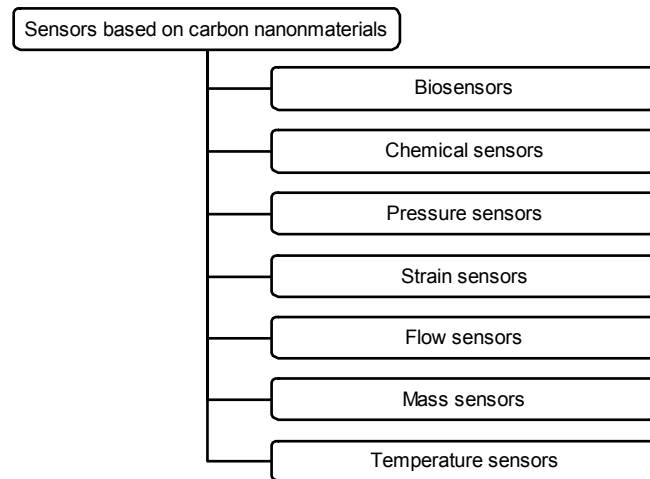


Fig. 4. Types of sensors based on carbon nanomaterials.

Experimental investigations suggest that mechanical deformation can change the electrical conductance of metallic and semiconducting CNTs. [23, 24]. This provides the foundation for the application of CNTs as high-sensitivity **electromechanical sensors**. Reports by Srivastava *et al.* [25] found that the chemical reactivity of SWCNTs can be significantly increased by local strain on SWCNTs. Several researchers have proposed the use of CNTs for measuring **strain** and **pressure** at nanoscale [26, 27].

Flow sensors are devices used for measuring the flow rate or quantity of a moving

liquid or gas. A CNT flow sensor is based on the generation of a current/voltage in a bundle of SWCNTs when the bundle is kept in contact with flowing liquid.

Micromechanical resonators such as microcantilevers are based on the detection principle that the resonant frequency of the cantilever depends on the inverse square root of the cantilever mass. Therefore, a change in the mass of the resonator is detected as a shift in resonant frequency. The small size and extraordinary mechanical properties of CNTs make these nanostructures promising candidates for replacing cantilever structures in a **mass sensor**. The principle of mass sensing is based on the resonant frequency shift of a CNT resonator when it is subjected to changes in attached mass or external loading. The resonant frequency is sensitive to the resonator mass, which includes the self-mass of the resonator and the mass attached on the resonator. The key issue of mass detection is in measuring the change in the resonant frequency due to the added mass.

Biosensors contain biological materials such as proteins (*e.g.*, cell receptors, enzymes, antibodies), oligo- or polynucleotide, microorganisms, or even whole biological tissues [28], and is used to monitor biological processes or for the recognition of biomolecules.

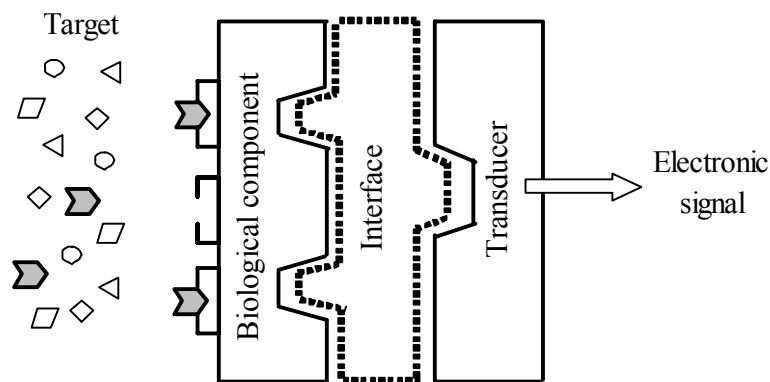


Fig. 5. General schematic representation of biosensors.

The integration of biomolecules with CNTs has resulted in hybrid systems, in which CNTs are used as nanoscale electrode elements (*e.g.*: enzyme electrodes), as electronic elements (*e.g.*: CNT-Field effect transistors) and as platforms upon which biomolecules can be attached.

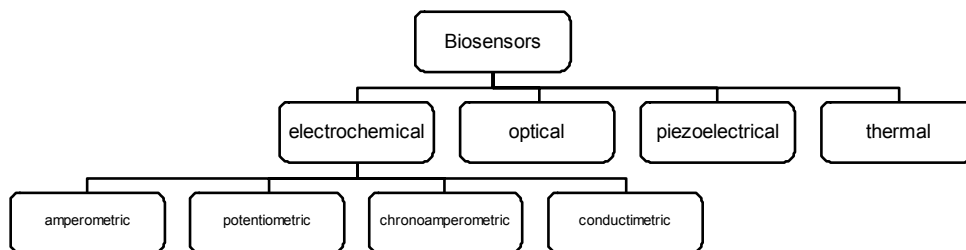


Fig. 6. Types of biosensors using carbon based nanomaterials.

Amperometric Biosensors are based on the measurement of a steady state current produced when a constant potential is applied. The current recorded is related to the oxidation or reduction of an electrochemical species in function of the rate at which it is consumed or produced by a biological element immobilized at the electrode surface.

Potentiometric transducers are based on measurement of a change in potential, the magnitude of which is dependent on the concentration of the analyte.

In **chronoamperometric biosensors**, the enzyme reaction is allowed to proceed for a short period before the potential step is applied.

Conductimetric Biosensors involve a biocomponent immobilized between two closely spaced electrodes and are based on the overall change in conductivity in a solution induced by the consumption or production of ionic species in a reaction.

The basis of **optical biosensors** is the change in optical phenomena such as absorption, fluorescence, luminescence, refractive index or scattering that occurs when light is reflected at a sensing surface.

A **piezoelectric** transducer is a device which transforms one type of energy to another by taking advantage of the piezoelectric properties of certain crystals or other materials (e.g.: quartz crystal microbalance, QCM).

It is important to be noticed that if the electroanalytical values would be compared with the values obtained using chromatographic techniques and values obtained using organic phase enzyme electrodes based biosensors without nanomaterials, carbon-based nanomaterials improved characteristics of the methods and simple real time analysis.

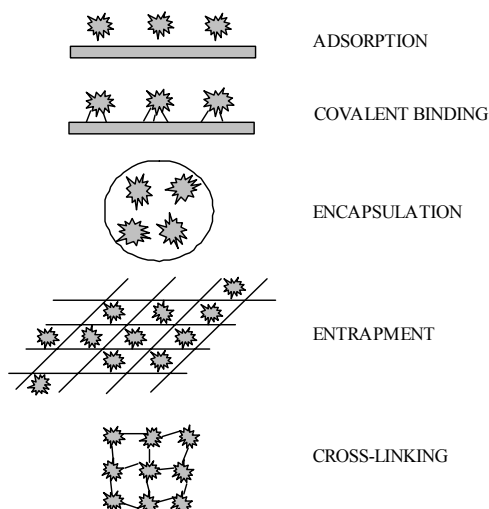


Fig. 7. Principal methods of immobilization.

Immobilization by **adsorption** involves reversible surface interactions between enzyme and support material. The forces involved are mostly electrostatic, as Van der Waals forces, ionic and hydrogen bonds.

Covalent Binding involves the formation of covalent bonds. Functional chemical groups belonging to amino acid residues on the surface of the enzyme may be attached covalently at the chemically activated supports (glasses, cellulose, synthetic polymers).

Encapsulation of receptors can be achieved by enveloping the biological components within various forms of semipermeable membranes. The enzymes are free in solution, but restricted in space.

Immobilization by **entrapment** involves that enzymes are free in solution, but restricted by lattice structure of the entrapment system. There are three general methods: entrapment behind a membrane, entrapment of biological receptors within self assembled monolayers (SAMs) or bi-layer lipid membranes (BLMs), entrapment of biomolecules within polymeric matrix membranes.

Cross-linking procedure is support-free and involves joining the receptor to each other to form a large, three-dimensional complex structure this being achieved by chemical or physical methods.

Applications of biosensors based on carbon nanomaterials in pesticides analysis in agriculture. Pesticides are widely used in agricultural practices as insecticides, fungicides, rodenticides, etc...but the toxicological problems connected to

their persistent residues were noticed after years of use [29]. There are already mentioned health risks due to their accumulation and the increased risk of cancer. Nanotechnologies can offer improved detection using sensor based on nanomaterials as well as complete degradation of many of them.

Carbon nanotubes based enzyme biosensors. Conventional electrochemical biosensors use glassy carbon electrodes (GCE) or metal electrodes (Au, Pt, Cu) for voltammetric or amperometric analyte detection. Carbon based nanomaterials [30, 31] were introduced in the construction of these electrodes for testing their new achieved sensing properties [32]. CNTs can improve some of these electrodes characteristics [33] such as poor sensitivity and high overpotential for electron transfer reactions [34] taking into account their property to undergo fast electron transfer and the resistance of CNTs to surface fouling. The selectivity and sensitivity can be improved using immobilized enzymes, CNTs facilitating the connection between the enzyme and the substrate.

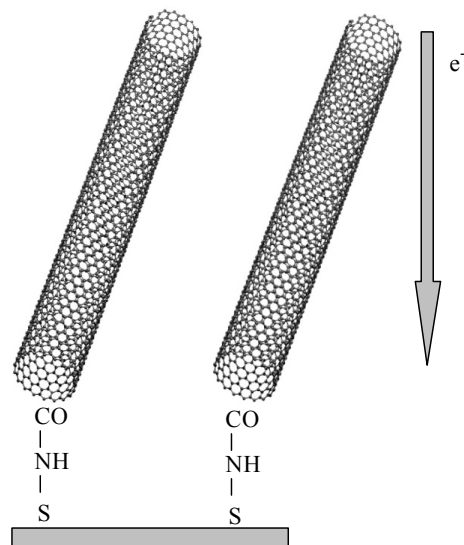


Fig. 8. Scheme of the connection between the enzyme and the substrate on the surface of the CNTs.

Among the examples of **CNT biosensors used for the detection of organophosphate compounds** there can be mentioned: disposable biosensor for organophosphate nerve agents based on carbon nanotubes modified thick film strip electrode was proposed by Joshi *et al.* [35]. Biosensors based on self-assembling

acetylcholinesterase on carbon nanotubes for flow injection/amperometric detection of organophosphate pesticides and nerve agents were designed by Liu *et al.* [36]. andimalla *et al.*, proposed another technique of enzyme immobilization through Binding of acetylcholinesterase to multiwall carbon nanotube-cross-linked chitosan composite for flow-injection amperometric detection of organophosphate insecticide [37] **Amperometric biosensors for organophosphate compounds by absorbing OPH onto a SWCNT- or MWCNT modified GCE** were realized by Deo *et al.* [38].

Table 1. Characteristics of carbon-based nanomaterials acetylcholinesterase biosensors for pesticides analysis

Immobilization method	Electrode type	Technique	Pesticide	Detection limit, M	Ref.
Physical adsorption	MWCNT/SPE	Amperometric	Paraoxon	0.5×10^{-9}	[39]
Covalent immobilization using glutaraldehyde	AChE/MWCNT-Chi/GCE	CV	Triazophos	0.01×10^{-6}	[40]
Physical entrapment	MWCNT/GCE	CV	Triazophos	5.0×10^{-9}	[41]
LBL self assembling technique	PDDA/AChE/MWCNT/GCE	FIA	Paraoxon	0.4×10^{-12}	[36]

CV–cyclic voltammetry; FIA–flow injection analysis; GCE–glassy carbon electrode; AchE–acetylcholinesterase; Chi–chitosan; MWCNT–multiwalled carbon nanotubes

Table 2. AChE inhibition-based biosensors with CNTs for chlorpyriphos (CPF) detection

Inhibition	Enzyme	Technique	Sample	LOD	Ref.
CPF	AChE	Voltammetric	Wine	$< 300 \text{ ng mL}^{-1}$	[42]
CPF	Butyrylcholinesterase (BChE)	Voltammetric	Grape juice	$2 \times 10^{-8} \text{ M}$	[43]
CPF	AChE	Voltammetric	Aqueous sample	$3 \times 10^{-8} \text{ M}$	[44]
CPF	AChE	Voltammetric	Aqueous samples	$1.58 \times 10^{-10} \text{ M}$	[35]

Graphene based biosensors for environmental sensing. New class of sensors were developed after the discovery of carbon based nanomaterials, beginning with 2007, after Geim *et al.* [45] Some of the key factors influencing graphene electrical

and optical properties need to be further studied in order to establish if these really improve the characteristics of graphene based biosensors in comparison with CNTs based ones [46, 47]. This rather new nanomaterial will probably give raise in the future to lots of differently fabricated biosensors and platforms [48] of graphene-based biosensors, but at this moment there are relatively few reports in this area.

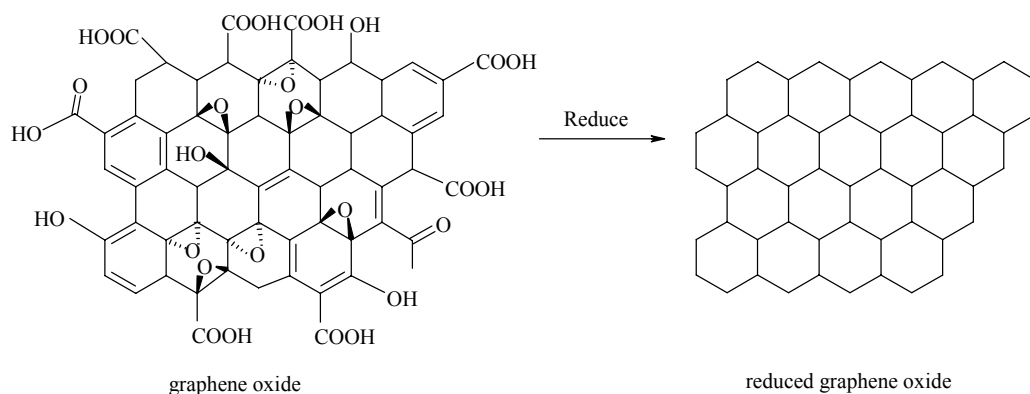


Fig. 9. Scheme of GO reduction process to RGO.

An important observation is that graphene needs to be functionalized [49, 50, 51] to modify its electrical properties [52], stronger adsorption onto graphene involving the role of impurities or vacancies [53]. It is also important how the electrode is constructed and how the signal is built on [54, 55]. When focusing on the construction of graphene-based biosensors, the number of graphene layers plays an important role, opening up the possibility to hone the graphene's electronic properties [56, 57].

Based on the electrocatalytic activity of graphene and the performance for direct electrochemistry of glucose oxidase, graphene proved to be till this moment a good electrode material for oxidase biosensors [58]. There were reported several glucose biosensors in the last two years. Lu *et al.* [59], reported the first example of glucose biosensor based on graphitic nanoplatelets (xGnP) with good properties and these properties were lately improved by introducing metal nanoparticles on the graphitic nanoplatelets and keeping in this way the nanoparticles extremely small and well distributed [60, 61]. Chitosan was used by Kang *et al.* [62] for a better graphene dispersion and a better immobilization of the of the enzyme molecules. Shan *et al.* [63], a composite film on gold electrode with enhanced performances due to the large surface area and good electrical conductivity of graphene.

Table 3. Graphene based biosensors for glucose sensing

Electrode	Method	Sensitivity	Detection limit ($\mu\text{g L}^{-1}$)	Ref.
Exfoliated graphite nanoplatelets/glucose oxidase/Nafion	Voltammetry	$14.17 \mu\text{A}(\text{mM}^{-1}.\text{cm}^{-2})$	$10 \mu\text{M}$ (S/N=3)	[64]
Glucose oxidase/graphene/chitosan	Direct electrochemistry	$37.93 \mu\text{A}(\text{mM}^{-1}.\text{cm}^{-2})$	0.02 mM	[63]
Pt-Au,graphene/glucose oxidase/Nafion	Voltammetry		$1 \mu\text{M}$	[65]
Pt/glucose oxidase/graphene/chitosan	Amperometric sensor		$0.6 \mu\text{M}$	[62]

Based on their distinctive properties, graphene offer potential applications in environmental systems. Size, shape, surface area, sorption and electronic properties play an important role in the sorption of environmental contaminants and in environmental sensing.

A new acetylcholinesterase (AChE) biosensor based on the immobilization of exfoliated graphitic nanoplatelets (xGnPs) in chitosan and glutaraldehyde for organophosphate pesticides was proposed by Ion *et al.* [66], Glutaraldehyde is used as cross-linker to bonded AChE to a composite of cross-linked chitosan and xGnPs leading to a new acetylthiocholine iodide (ATCI) sensor. The presence of xGnPs on the electrode surface leads to enhanced electron transfer rate with reduced surface fouling [67]. xGnPs are highly conductive nanomaterials with interesting possible future application in biochemical sensing. The proposed sensor combines for the first time the highly conductive and electroanalytic behavior of xGnPs with the biocompatibility of chitosan, leading to good stability and increased sensitivity for detection of ATCI. It will be further applied to analysis of organophosphate pesticides for environmental monitoring. The detection limit of this sensor was $1.58 \times 10^{-10} \text{ M}$, with a simple fabrication, a fast response and an acceptable stability.

Networked sensing systems can monitor environmental parameters and providing data maintaining water and soil quality. For example, CNTs based sensors present advantages in sensor platforms in simultaneous determinations of several kinds of on-field contaminants [68, 69, 70]. The improved characteristics of these sensors lie in covalent and supramolecular functionalization with enzymes, metals and chemical groups. The environmental applications of CNTs based biosensors were presented in several reviews [47, 71, 72]. Based on the models offered by CNTs (considered as enrolled graphene), graphene opens the way of ultra-sensitive and ultra-fast electronic sensors due to their low electrical noise materials. Even if CNTs have almost ideal properties for electronic applications, they have one dimensional structure which is not

suitable in electronic devices, but this problem was solved after the discovery of graphene [73] that is 2D structure of one atomic thick carbon. Together with the interesting properties of CNTs, graphene can be considered as very challenging materials for environmental sensors.

Detection of mixtures of pesticides in real samples. The major research into the detection of pesticides took place using mostly chromatographic methods of analysis, where each pesticide in the mixture can be determined. In real environmental samples there are more than one pesticide in one sample, the effect of the sample matrix having an important influence. Where a mixture of pesticide is present, the inhibition of AChE will represent the total anticholinesterase effect, so only using chromatographic methods each pesticide from the mixture will be detected.

Detection of the presence of pesticides in real samples was carried out by several research groups, in the following table a comparison between results obtained using AChE- CNM based biosensors and chromatographic techniques being presented.

Table 4. Characteristics of nanomaterial based AChE sensors with chromatographic techniques

Immobilization method	Electrode type	Techniques [Incubation time]	Organophosphorus pesticide (linear conc. in M)	Detection limit in M [correlation coefficient]	Ref.
Physical adsorption	MWCNTs/SP E	Amperometry [30 min]	Paraoxon (1.0×10^{-9} to 6.9×10^{-9})	0.5×10^{-9} [0.9859]	[74]
LBL self assembling technique	PDDA/AChE/PDDA/MWCNT/GCE	FIA [6 min]	Paraoxon (1×10^{-12} to 0.1×10^{-9})	0.4×10^{-12}	[42]
Covalent immobilization using glutaraldehyde as cross linking agent	AChE/MWCNTs-Chi/GCE	CV [10 min]	Triazophos (0.03×10^{-6} to 7.8×10^{-6} and 7.8×10^{-6} to 32×10^{-6})	0.01×10^{-6} [0.9966, 0.9960]	[75]
Physical entrapment	MWCNTs/SiS G/GCE	CV [12 min]	Triazophos (0.02×10^{-6} to 1×10^{-6} and 5×10^{-6} to 30×10^{-6})	5.0×10^{-9} [0.9957 and 0.9986]	[76]
		Gas chromatography (GC)	Methyl parathion Malathion Triazophos	0.04×10^{-6} 0.03×10^{-6} 0.08×10^{-6}	[77]
		Liquid chromatography – atmospheric pressure chemical ionization-mass spectrometry (LC-APCI-MS)	Malathion Paraoxon Triazophos	0.02×10^{-6} 0.08×10^{-6} 0.02×10^{-6}	[78]
		Matrix Solid-Phase Dispersion (MSPD) and GC	Parathion methyl Malathion	4.0×10^{-9} 9.0×10^{-9}	[79]

In the area of biosensors, stabilized enzymes provide the tools for the development of complex analytical instruments. The most important purpose of the stabilization techniques is to decrease the tendency of enzymes to unfold, by increasing its rigidity. Recent studies using carbon nanoporous materials have shown that it is a stabilization effect when enzymes are introduced into nanosized cages [80, 81]. The improved performances of CNTs based biosensors are attributed to this effect, but their higher price discourages the application at a large scale. The development of inexpensive nano sized graphene sheets may develop affordable biosensors with high sensitivity and fast response.

Legislation onto pesticides. National governments establish regulatory limits to minimize the contamination with pesticide residues of the environment and of the agricultural areas. Hamilton *et al.* [82] give a comprehensive overview of regulatory limits for pesticides in water issued by WHO, Australia, USA, New Zealand, Japan, Canada, the European Union and Taiwan. Only the European Union (EU) has a different approach to regulatory limits a maximum limit of $0.1 \mu\text{g L}^{-1}$ being set for individual pesticides and a combined maximum limit of $0.5 \mu\text{g L}^{-1}$ for total pesticides. These limits can be a problem in the application of enzymatic detection methods, because methods there are not able to detect pesticides at the legal limits will have very limited applications.

Conclusions

The real time analysis in field conditions is much needed for robust performance of carbon-nanomaterials-based electrochemical sensors, but only few sensors based on these materials have reported real sample analysis. Among these few examples where multiwalled carbon nanotubes were used, some of the obtained performances of the sensors are in good agreement and even superior in comparison with chromatographic methods. Taking into account the rapid analysis procedure, these nanomaterials prove to be very promising for real sample analysis and comparing the much lower prices of graphene and their improved characteristics with carbon nanotubes, graphene and graphite nanoplatelets will be probably the materials of the future in sensors for environmental and agriculture real field applications, becoming very clear that nanotechnology can offer fundamentally new technologies in environmental detection, sensing and remediation and in agriculture technology.

References

- [1] J. LI., N. MA, J.P. GIESY, Z. WANG, *Toxicol. Lett.* **183**, 65-71, 2008.

- [2] C.J. SINCLAIR, A.B. BOXALL, Environ. Sci. Technol. 37, 4617–4625, 2003.
- [3] P. KEBLINSKI, S.K. NAYAK, P. ZAPOL, P.M. AJAYAN, Phys. Rev. Lett. **89**, pp. 2555031–2555034, 2002.
- [4] M. ASHBY, P. FERREIRA, D. SCHODEK, eds, Nanomaterials, Nanotechnologies and Design: Elsevier, 2009.
- [5] R. XU, J. MA, X.C. SUN, Z.P. CHEN, X.L. JIANG, Z.R. GUO, Cell Research, **19**, pp. 1031–1034, 2009.
- [6] T.-L. LAI, Y.-L. LAI, C.-C. LEE, Y.-Y. SHU, C.-B. WANG, Catalysis Today, **131**, pp. 105–110, 2008.
- [7] A. BILYK, S. LI, J. MURPHY, S. PETINAKIS, K. ZERDIN, A. SCULLY, Progress in Organic Coatings, **62**, pp. 40–48, 2008.
- [8] M.S. MAUTER, M. ELIMELECH, Environ. Sci. Technol., **42**, pp. 5843–5859, 2008.
- [9] J.C. MEYER, A.K. GEIM, M.I. KATSNELSON, K.S. NOVOSELOV, T.J. BOOTH, S. ROTH, Langmuir, **25**, pp. 6122–6128, 2009.
- [10] A. GEIM, “*The rise of graphene*”, web site:
<http://www.lbl.gov/publicinfo/newscenter/pr/2008/graphene.pdf>
- [11] S. STANKOVICH, R.D. PINER, X. CHEN, N. WU, S.T. NGUYEN, R.S. RUOFF, J. Mater. Chem., **16**, pp. 155–158, 2006.
- [12] S. GOTOVAC, H. HONDA, Y. HATTORI, K. TAKANASHI, H. KANO, K. KANEKO, Nano Lett., **7**, pp. 583–587, 2007.
- [13] P. PATEL, „*Graphene-polymer composite*”, 2008 Review web site:
<http://www.technologyreview.com/computing/20821>
- [14] S. FURMANIAK, A.P. TERZYK, P.A. GAUDEN, G. RYCHLICKI, J. Colloid Interface Sci., **295**, pp. 310–317, 2006.
- [15] J.H. WALTHER, R.L. JAFFE, E.M. KOTSALIS, T. WERDER, T. HALICIOGLU, P. KOUMOUTSAKOS, Carbon **42**, pp. 1185–1194, 2004.
- [16] A. FERNANDEZ, J. Chem. Phys. **119**, pp. 5315–5319, 2003.
- [17] L.A. GIRIFALCO, M. HODAK, R.S. LEE, Phys. Rev. **B62**, pp. 13104–13110, 2000.
- [18] M. TERASHIMA, S. NAGAO, Chem. Lett. 36, pp. 302–303, 2007.
- [19] J.H. WALTHER, R. JAFFE, T. HALICIOGLU, P. KOUMOUTSAKOS, J. Phys. Chem. **B105**, pp. 9980–9987, 2001.
- [20] P. NOVAK, T. JEDNAKAC, G.D. VUKOVIC, M. COLIC, M.D. RISTIC, R. ALEKSIC, A.A. PRIC-GRUJIC, P.S. USKOKOVIC, Croatica Chem. Acta **85**, pp. 451–456, 2012.
- [21] J. LI, S. GUO, Y. ZHAI, E. WANG, Electrochem. Commun. **11**, pp. 1085–1088, 2009.
- [22] G. ERANNA, B.C. JOSHI, D.P. RUNTHALA, R.P. GUPTA, Crit. Rev. Solid State Matter. Sci. 2004, 29.111.doi doi:10.1080/10408430490888977.
- [23] J. CAO, Q. WANG, H. DAI, Phys. Rev. Lett. **90**, pp. 1576011–1576014, 2003.
- [24] M. GRUJICIC, G. CAO, W.N. ROY, Appl. Surf. Sci., **229**, pp. 316–323, 2004.
- [25] D. SRIVASTAVA, D.W. BRENNER, J.D. SCHALL, K.D. AUSMAN, M.F. YU, R.F. RUOFF, J. Phys. Chem. **B103**, pp. 4330–4337, 1999.
- [26] C. STAMPER, T. HEBLING, A. JUNGEN, C. HEIROLD, Phys. Status Solidi **B243**, pp. 3537–3541, 2006.
- [27] I. KANG, M. K. SCHULZ, J. H. KIM, V. SHANOV, D. SHI, Smart Mater. Struct. **15**, pp. 737–748, 2006.
- [28] G.S. WILSON, R. GIFFORD, Biosens. Bioelectron. **20**, pp. 2388–2403, 2005.
- [29] Q. CHAUDHRY, P. SCHROEDER, D. WERCK-REICHART, W. GRAJEK, R. MARECIK, Env. Sci. Pollut. Res., doi: 10.1065/espr2001.09.084.1

- [30] L. WU, X.J. ZHANG, H.X. JU, *Biosens. Bioelectron.* **23**, pp. 479–484, 2007.
- [31] M. ZHOU, L. SHANG, B.L. LI, L.J. HUANG, S.J. DONG, *Biosens. Bioelectron.*, **24**, pp. 442–447, 2008.
- [32] R.L. McCREERY, *Chem. Rev.* **108**, pp. 2646–2687, 2008.
- [33] M.D. RUBIANES, G.A. RIVAS, *Electrochem. Commun.*, **5**, pp. 689–694, 2003.
- [34] R.S. NICHOLSON, *Anal. Chem.*, **37**, pp. 1351–1355, 1965.
- [35] K.A. JOSHI, J. TANG, R. HADDON, J. WANG, W. CHEN, A. MULCHANDANI, *Electroanalysis*, **17**, pp. 54–58, 2005.
- [36] G. LIU, Y. LIN, *Anal. Chem.*, **78**, pp. 835–843, 2006.
- [37] V.B. KANDIMALLA, H. JU, *Chem. Eur. J.*, **12**, pp. 1074–1080, 2006.
- [38] R.P. DEO, J. WANG, I. BLOCK, A. MULCHANDANI, K.A. JOSHI, Y. LIN, *Anal. Chem. Acta*, **530**, pp. 185–189, 2005.
- [39] G. LIU, J. WANG, R. BARRY, C. PETERSEN, C. TIMCHALK, P.L. GASSMAN, Y. LIN, *Chem. Eur. J.* **14**, pp. 9951–9959, 2008.
- [40] D. DU, X. HUANG, J. CAI, A. ZHANG, *Sens. Actuators B* **127**, pp. 531–535, 2007.
- [41] D. DU, J. CAI, D. SONG, A. ZHANG, *J. Appl. Electrochem.* **37**, pp. 893–898, 2007.
- [42] M. Del CARLO, M. MASCINI, A. PEPE, D. COMPAGNONE, *J. Agric. Food Chem.* **50**, pp. 7206–7210, 2002.
- [43] A. IVANOV, G. EVTUGYN, H.G. BUDNIKOV, F. RICCI, D. MOSCONE, G. PALLESCHI, *Anal. Bioanal. Chem.* **377**, pp. 624–629, 2003.
- [44] E.V. SUPRUNS, H.C. BUDNIKOV, G.A. EVTUGYN, KH.Z. BRAININA, *Bioelectrochemistry*, **63**, pp. 281–284, 2004.
- [45] A.K. GEIM, K.S. NOVOSELOV, *Nature Materials*, **6**, pp. 652–655, 2007.
- [46] J. WANG, *Electroanalysis*, **17**, pp. 7–14, 2005.
- [47] J.F. WANG, S.L. YANG, D.Y. GUO, P. YU, D. LI, J.S. YE, L.Q. MAO, *Electrochem. Commun.*, **11**, pp. 1892–1895, 2009.
- [48] C.H. LU, H.H. YANG, C.L. ZHU, X. CHEN, G.N. CHEN, *Angew. Chem.*, **121**, pp. 4879–4881, 2009.
- [49] L.H. TANG, Y. WANG, Y.M. LI, H.B. FENG, J. LU, J.H. LI, *Adv. Funct. Mater.* **19**, pp. 2782–2789, 2009.
- [50] M. ZHOU, Y.M. ZHAI, S.J. DONG, *Anal. Chem.*, **81**, pp. 5603–5613, 2009.
- [51] Z.J. WANG, X.Z. ZHOU, J. ZHANG, F. BOEY, H. ZHANG, *J. Phys. Chem. C* **113**, pp. 14071–14074, 2009.
- [52] H. CHEN, M.B. MULLER, K.J. GILMORE, G.G. WALLACE, D. LI, *Adv. Mater.* **20**, pp. 3557–3561, 2008.
- [53] W.J. LIN, C.S. LIAO, J.H. JHANG, Y.C. TSAI, *Electrochem. Commun.* **11**, pp. 2153–2156, 2009.
- [54] S.L. YANG, D.Y. GUO, L. SU, P. YU, D. LI, J.S. YE, L.Q. MAO, *Electrochem. Commun.*, **11**, pp. 1912–1915, 2009.
- [55] J. JIA, D. KATO, R. KURITA, Y. SATO, K. MARUYAMA, K. SUZUKI, S. HIRONO, T. ANDO, O. NIWA, *Anal. Chem.* **79**, pp. 98–105, 2007.
- [56] N.G. SHANG, P. PAPA-KONSTANTINO, M. MCMULLAN, M. CHU, A. STAMBOULIS, A. POTENZA, S.S. DHESI, H. MARCHETTO, *Adv. Funct. Mater.* **18**, pp. 3506–3514, 2008.
- [57] O. NIWA, J. JIA, Y. SATO, D. KATO, R. KURITA, K. MARUYAMA, K. SUZUKI, S. HIRONO, *J. Am. Chem. Soc.* **128**, pp. 7144–7145, 2006.
- [58] C.S. SHAN, H.F. YANG, J.F. SONG, D.X. HAN, A. IVASKA, L. NIU, *Anal. Chem.* **81**, pp. 2378–2382, 2009.

- [59] J. LU, L. T. DRZAL, R. M. WORDEN, I. LEE, *Chem. Mater.* **19**, pp. 6240–6246, 2007.
- [60] J. LU, I. DO, L.T. DRZAL, R.M. WORDEN, I. LEE, *ACS Nano*, **2**, pp. 1825–1832, 2008.
- [61] H. WU, J. WANG, X.H. KANG, C.M. WANG, D.H. WANG, J. LIU, I.A. AKSAY, Y.H. LIN, *Talanta*, **80**, pp. 403–406, 2009.
- [62] X.H. KANG, J. WANG, H. WU, I.A. AKSAY, J. LIU, Y.H. LIN, *Biosens. Bioelectron.* **25**, pp. 901–905, 2009.
- [63] C.S. SHAN, H.F. YANG, D.X. HAN, Q.X. ZHANG, A. IVASKA, L. NIU, *Biosens. Bioelectron.* **25**, pp. 1070–1074, 2009.
- [64] J. LU, L.T. DRZAL, R.M. WORDEN, I. LEE, *Chem. Mater.* **19**, pp. 624–6246, 2007.
- [65] T.T. BABY, S.S. JYOTHIRMAYEE ARAVIND, T. AROCKIADOSS, R.B. RAKHI, S. RAMAPRABHU, *Sens.&Actuator* **B145**, pp. 71–77, 2010.
- [66] A.C. ION, I. ION, A. CULETU, D. GHERASE, C. MOLDOVAN, R. IOSUB, A. DINESCU, *Mat. Sci. Eng.* **C30**, pp. 817–821, 2010.
- [67] R.T. KACHOOSANGI, M.M. MUSAMEH, I.A. YOUSEF, J.M. YOUSEF, S.M. KANAN, L. XIAO, S.G. DAVIES, A. RUSSEL, R.G. COMPTON, *Anal. Chem.* **81**, pp. 435–442, 2009.
- [68] F. VALENTINI, V. BIAGIOTTI, C. LETE, G. PALESCHI, J. WANG, *Sens. Actuators* **B128**, pp. 326–333, 2007.
- [69] N. CHOPRA, V.G. GAVALAS, B.J. HINDS, L.G. BACHAS, *Anal. Lett.* **40**, pp. 2067–2096, 2007.
- [70] B.L. ALLEN, P.D. KICHAMBARE, A. STAR, *Adv. Mater.* **19**, pp. 1439–1451, 2007.
- [71] Y.H. LIN, W. YANTASEE, J. WANG, *Front. Biosci.* **10**, pp. 492–505, 2005.
- [72] K.R. ROGERS, *Anal. Chim. Acta* **568**, pp. 222–231, 2006.
- [73] K.S. NOVOSELOV, *et al.*, *Science*, **306**, pp. 666–669, 2004.
- [74] K.A. JOSHI, J. TANG, R. HADDON, W. JOSEPH, W. CHEN, A. MULCHANDANI, *Electroanalysis*, **17**, pp. 54–58, 2005.
- [75] D. DU, X. HUANG, J. CAI, A. ZHANG, *Sens. Actuat.* **B127**, pp. 531–535, 2007.
- [76] D. DU, J. CAI, D. SONG, A. ZHANG, *J. Appl. Electrochem.* **37**, pp. 893–898, 2007.
- [77] A.D. MUCCIO, P. PELOSI, I. CAMONI, D.A. BARBINI, R. DOMMARCO, T. GENERALI, A. AUSIL, *J. Chromatogr.* **A754**, pp. 497–506, 1996.
- [78] M. FERNANDEZ, Y. PICO, S. GIROTTI, J. MANES, *J. Agric. Food Chem.* **49**, pp. 3540–3547, 2001.
- [79] B. ALBERO, C.S. BRUNETE, J.L. TADEO, *J. Agric. Food Chem.* **51**, pp. 6915–6921, 2003.
- [80] S. SOTIROPOULOU, V. GAVALAS, V. VAMVAKAKI, N.A. CHANIOTAKIS, *Biosens. Bioelectron.* **18**, pp. 211–215., 2003.
- [81] S. SOTIROPOULOU, N.A. CHANIOTAKIS, *Anal. Bioanal. Chem.* **375**, pp. 103–105, 2003.
- [82] D.J. HAMILTON, A. AMBRUS, R.M. DIETERLE, A.S. FELSOR, C.A. HARRIS, P.T. HOLLAND, *Pure Appl. Chem.* **75**, pp. 1123–1155, 2003.

The Effects of Silica Nanostructures on Halotolerant Microorganisms Isolated from Rock Salt Crystal

Mădălin ENACHE¹, Simona NEAGU¹, Crina ANASTASESCU²,
Roxana COJOC¹, Maria ZAHARESCU²

¹Institute of Biology Bucharest of the Romanian Academy,
296 Splaiul Independenței street, P.O. Box 56-53, Bucharest, 060031, Romania
E-mail: roxana.cojoc@ibiol.ro; simona_trifan@yahoo.com;
madalin.enache@yahoo.com

²Institute of Physical–Chemistry “Ilie Murgulescu” of the Romanian Academy,
202 Splaiul Independenței, Bucharest 060021, Romania
E-mail: mzaharescu2004@yahoo.com; crina.anastasescu@icf.ro

Abstract. This paper deals with the evidentiating of the potential effect both bactericidal and bacteriostatic of some oxidic silica nanostructures towards the halotolerant microorganisms *Bacillus subtilis* and *Virgibacillus halodenitrificans*, isolated from subterranean salt crystal. The studies were focused on the testing of these activities under relatively similar conditions to those observed in several environments, namely highly polluted areas or with nanobiotechnological potential. The as-prepared SiO₂ based microtubes showed a slight inhibitory effect for *Bacillus subtilis* but, on the other hand acted to stimulate the growth of *Virgibacillus halodenitrificans*. In opposite, the thermal treated microtubes at 400°C for one hour stimulated the growth of *Bacillus subtilis* and diminished the growth rate of *Virgibacillus halodenitrificans*. The silica nanostructures with spherical shape and platinum doped silica microtubes had a positive effect on the growth of both tested strains.

Introduction

One of the most important research approaches in the modern sciences is represented by nanobiotechnologies (Klabunde, 2001), an area located at the frontiers between several sciences with a relatively high interdisciplinary degree. The

nanoscience could be considered as the science of the small particles of materials. These small particles are very important since all material properties (i.e. melting point, electrical and optical properties) are modified when the size of constitutive particles is reduced to nanoscale. The new obtained properties resulted in new opportunities for technological development and novel biotechnologies (Kohli and Martin, 2005).

Some of the applications of the micro and nanoparticles in biotechnologies are related to the enzyme's encapsulation (Chang and Prakash, 2001), DNA transformation (Kneuer *et al.*, 2000; Koltover *et al.*, 1998; Radler *et al.*, 1997) biosensors (Cao *et al.*, 2002; Demers *et al.*, 2002; Park *et al.*, 2002) and others like drug delivery (Ulrich *et al.*, 1999; Lee *et al.*, 2002; Murthy *et al.*, 2002).

Nanoparticles with functionalized surfaces could be used for the release of genetic material in viable cell by transformation processes. Silica nanospheres labeled with ammonium groups could be used for binding and transporting DNA in specific cells. The identification of the protein synthesized in the cell following codification of the introduced DNA by silica nanosphere could confirm the successful transformation of the genetic material (Kneuer *et al.*, 2000). Other studies revealed that also nanospheres with a lipid nature (cations) and liposomes could play an important role in the transformation processes (Koltover *et al.*, 1998; Radler *et al.*, 1997).

Apparently, the spherical nanoparticles are easier to be obtained than microtubes and nanotubes. In comparison with the spherical nanoparticles, nanotubes are characterized by an inner space where chemical or biochemical materials with the same size as proteins or small molecules could be inserted (Mitchell *et al.*, 2002; Lee *et al.*, 2002). On the other hand, nanotubes have an internal and external surface which could be functionalized in different ways, either chemically or biochemically (Mitchell *et al.*, 2002). In this way, it appears the possibility of functionalization of nanotubes inner side with biochemical compounds. This functionalization influences the chemical features of the outer side, making it compatible with some biological materials. Another particularity of nanotubes is represented by the presence of the two open ends which could be an advantage for the relatively easy functionalization of the internal surface.

This paper emphasizes the potential effect both bactericidal and bacteriostatic of some oxidic silica nanostructures towards the halotolerant microorganisms *Bacillus subtilis* and *Virgibacillus halodenitrificans*, isolated from underground salt crystal from Slănic Prahova area. The studies were focused on testing these activities in similar conditions as those observed in several environments, namely highly polluted areas or nanobiotechnology fields in which various nanostructures are used. Such kind of nanostructures could be applied in the technologies of obtaining some disinfectants based on photocatalysts, but also in other industrial areas. The bactericidal or

bacteriostatic effect has been observed by monitoring the growth of the halophilic bacterial cultures by recording the optical density and by evaluating the total dehydrogenase activity as an indicator of the biological activity, allowing in this way the monitoring of the biological activity of tested silica nanostructures.

Materials and Methods

Halophilic bacterial strains

The halophilic bacterial strains used in this study were isolated from underground salt crystal taken from Slănic Prahova area and identified in a previous investigation as being *Virgibacillus halodenitrificans* and *Bacillus subtilis*. The strains were cultivated on MH media with the following composition (g/L): yeast extract (10), proteose peptone (5), glucose (1), NaCl (100), MgCl₂ × 6H₂O (7), MgSO₄ × 7H₂O (9.6), CaCl₂ × 2H₂O (0.36), KCl (2), NaHCO₃ (0.06), NaBr (0,026) (Ventosa et al., 1989). The medium pH was 7.0 – 7.2 before autoclaving. When necessary, during the experiments, the medium was supplemented with seven milligrams of each tested nanostructure (spheres, nanotubes, etc. – Table 1). For the solidified form of the medium, agar was added (20 g/L).

Testing of antimicrobial properties – The effect of investigated nanostructures on the growth of the tested halotolerant strains has been estimated as follows: approximately seven milligrams of each tested nanostructure were added in the culture medium in the presence of microbial cells and the resulted mixture was incubated at 28⁰C for 24 hours. The microbial growth was monitored for 24 hours by measuring the optical density at 660 nm.

The bactericidal or bacteriostatic effect of the investigated nanostructures has been evaluated by the following experiment: the investigated nanostructures were put in contact with a known amount of microbial cells in phosphate buffer (0.06 M, pH 6.1) and the resulted mixture was incubated for 48 hours at 28⁰C. In the next step, one milliliter of the mixture was spread in a Petri dish and incorporated in 25–30 ml of molten agar (cooled at around 55⁰C). The total number of colony forming units was counted after 24 hours of incubation at 28⁰C. This number has been correlated with the amount of microbial cells from the mixture.

Tested nanostructures - were SiO₂ microtubes and nanospheres obtained by sol-gel method in the presence of *DL* or *meso*-tartaric acid template. The experimental conditions and some characteristics are summarized in Table 1.

Table 1. The description of the silica microtubes and nanospheres used in the experiments

Sample	Description of the sample
A	As-prepared SiO ₂ microtubes prepared accordingly to sol-gel method in the presence of <i>DL</i> -tartaric acid
B	Previous sample thermally treated at 400°C, 1 hour
C	SiO ₂ nanospheres prepared in similar conditions with sample A, but in the presence of <i>meso</i> -tartaric acid
D	Sample A doped with Pt by impregnation with H ₂ PtCl ₆ and reduced in H ₂ , 300°C (Pt/SiO ₂)

Dehydrogenase activity – as indicator of total biological activity has been evaluated following the Casida method (Casida et al., 1964). Briefly, 0.5 ml 3% TTC (triphenyl-tetrazolium chloride) were added to three milliliters of bacterial cultures and the mixture was incubated at 37°C for 24 hours. The dehydrogenase activity was expressed as mg formazan % (reaction product resulted from transformation of colorless TCC to red formazan).

Results and Discussions

Tested nanostructures

The nanostructures used in this study were SiO₂ tubes and particles obtained by sol-gel method using *DL* or *meso*-tartaric acid as template (Anastasescu et al., 2010). Following synthesis, several post reaction treatments were performed and the resulted nanostructures were analyzed by transmission electron microscopy. The investigation revealed that samples A, B and D (see table 1) had a microtubular structure, while sample C consisted of spherical nanostructures (Fig. 1).

The effect of nanostructures on the tested halotolerant strains

The presence of the investigated nanostructures in the culture medium of the used halotolerant strains revealed a different effect for each tested microbial strain (Fig. 2). Thus, the as-prepared SiO₂ microtubes (sample A) showed a slight inhibitory effect on the growth of *Bacillus subtilis*. On the other hand, the growth of *Virgibacillus halodenitrificans* appeared to be slightly stimulated by the presence of these

microtubes. In the presence of sample B (thermally treated microtubes), the growth of *B. subtilis* was also slightly stimulated, an opposite effect if compared with sample A. The strain of *V. halodenitrificans* has a diminished growth rate in the presence of sample B, which appears to be an opposite effect if compared with sample A (as-prepared SiO_2 microtubes). On the other hand, in the presence of sample C (nanospheres) a positive effect for both tested strains is recorded (growth was stimulated). A similar behavior was also registered also in the presence of the platinum doped sample (D).

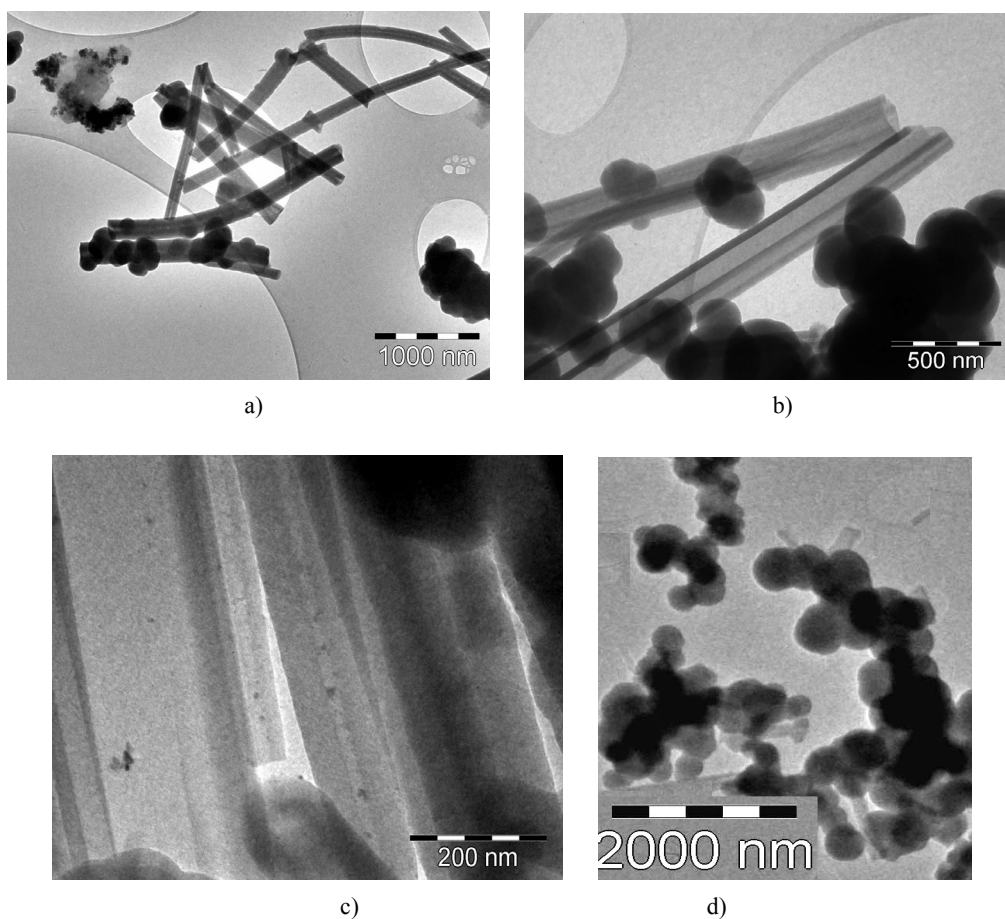


Fig. 1. The microtubular shape of the sample A (a), B (b), D (c) and spherical shape of sample C (d).

This variable response could be due either to the structure and/or morphology of the investigated nanostructures. The dehydrogenase activity recorded at the end of incubation period (24 hours) as indicator of total biological activity supported this variable response (Table 2) mentioned before and revealed either a slight inhibitory effect on the microbial growth or a growth stimulation.

Table 2. Dehydrogenase activity

1 = *Virgibacillus halodenitrificans*; 2 = *Bacillus subtilis*; M = blank (bacterial culture without nanostructures); A, B, C, D = investigated nanostructures described in Table 1; mg formazan growth = dehydrogenase activity in growth of culture as data recorded in Fig. 2; mg formazan viability T_0 = dehydrogenase activity recorded at start of the experiment “*The bactericidal or bacteriostatic effect*” as described in Materials and Methods section; mg formazan viability 24h = dehydrogenase activity recorded at the and (24 hours) of the experiment “*The bactericidal or bacteriostatic effect*” as described in Materials and Methods section

Sample	mg formazan growth		mg formazan viability T_0		mg formazan viability 24 h	
	1	2	1	2	1	2
M	3.89	0.23	0.20	0.17	0.11	0.09
A	0.47	0.21	0.12	0.51	0.09	0.01
B	0.29	0.22	0.10	0.25	0.13	0.10
C	0.52	0.22	0.13	0.23	0.09	0.10
D	0.36	0.22	0.11	0.15	0.10	0.10

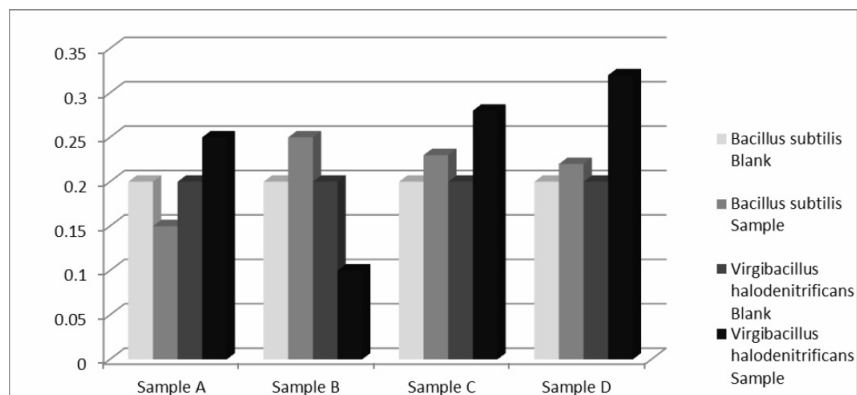


Fig. 2. The growth of tested halotolerant bacterial strains in the presence of nanostructures with various compositions and morphology (Table 1) after 24 hours incubation time; X axis representing D.O. at 660 nm.

The data presented in Fig. 2 revealed that the thermal treatment of the SiO₂ microtubes (sample B) modifies the nanostructures effect on the tested microbial strains. In this way the antibacterial effects towards the strain of *V. halodenitrificans* could be observed, in opposition to the effect of growth stimulation registered in the case of *B. subtilis*. On the other hand, the thermal treatment of the samples C and D conducted to a stimulating growth effect also for *V. halodenitrificans*. This behavior could be also attributed to the mechanisms of interaction established between microbial cells and silica microtubes and nanosphers .

The morphology of investigated nanostructures affected their activity on the tested halotolerant microbial cells. Thus, if the two microbial strains were grown in the presence of microtubules (sample A), the antimicrobial activity was observed only against *B. subtilis*, whereas in the case of cultivation in the presence of silica nanospheres (sample C) both tested strains were able to grow.

The data recorded in Table 3 showed that the viability of the tested strains was affected by the presence of the investigated nanostructures. The bactericidal effect was recorded only in the case of *Virgibacillus halodenitrificans*. The dehydrogenase activities (Table 2) are in accordance with the data recorded in Table 3, both for *V. halodenitrificans* and *B. subtilis*.

Table 3. The bactericidal effect of investigated nanostructures on the microbial cells

	1	2
M	Infinite	1×10^6
A	99×10^6	34×10^6
B	126×10^6	32×10^6
C	163×10^6	22×10^6
D	89×10^6	2×10^6

1 = *Virgibacillus halodenitrificans*; 2 = *Bacillus subtilis*;
 M = blank (bacterial culture without nanostructures);
 A, B, C, D = investigated nanostructures described in Table 1

Concluding Remarks

The as-prepared SiO₂ microtubes (sample A) showed a slight inhibitory effect against *Bacillus subtilis* but, on the other hand, they stimulated the growth of *Virgibacillus halodenitrificans*. In opposition, the microtubes thermally treated at 400°C for one hour (sample B) stimulated the growth of *Bacillus subtilis* and diminished the growth rate of *Virgibacillus halodenitrificans*. The silica nanostructures with spheric shape (sample C) and platinum doped silica microtubes (sample D) showed a positive effect on the growth of both tested strains.

The variable response of the tested halotolerant microbial strains could be attributed to the morphology and composition of the investigated nanostructures as resulted also from the dehydrogenase activity data and the viability data of the strains.

On the other hand, the thermal treatment of the nanostructures conducted to a positive effect towards *Virgibacillus halodenitrificans*, in the case of un-doped microtubes (sample A), silica nanospheres (sample C) and platinum doped microtubes (sample D). In the case of thermally treated microtubes (sample B) the effect towards *Virgibacillus halodenitrificans* was a negative one.

References

- [1] C. ANASTASESCU, M. ANASTASESCU, V.S. TEODORESCU, M. GARTNER, M. ZAHARESCU, “*SiO₂ Nanospheres and Tubes Obtained by Sol-Gel Method*”, J. Non-Cryst. Solids, **356**, pp. 2634–2640, 2010.
- [2] Y.W.C. CAO, R.C. JIN, C.A. MIRKIN, “*Nanoparticles with Raman spectroscopic fingerprints for DNA and RNA detection*”, Science, **297**, pp. 1536–1540, 2002.
- [3] CASIDA J.E. jr., KLEIN D.A., SANTORO T., “*Soil dehydrogenase activity*”, Soil. Sci., **98**, pp. 371–376, 1964.
- [4] T.M.S. CHANG, S. PRAKASH, “*Procedures for microencapsulation of enzymes, cells and genetically engineered microorganisms*”, Molecular Biotech, **17**, pp. 249–260, 2001.
- [5] L.M. DEMERS, D.S. GINGER, S.J. PARK, Z. LI, S.W. CHUNG, C.A. MIRKIN, “*Direct patterning of modified oligonucleotides on metals and insulators by dip-pen nanolithography*”, Science, **296**, pp. 1836–1838, 2002.
- [6] K.J. KLABUNDE, “*Nanoscale Materials in Chemistry*”, Wiley-Interscience, NY, 2001.
- [7] C. KNEUER, M. SAMETI, U. BAKOWSKY, T. SCHIESTEL, H. SCHIRRA, H. SCHMIDT, C.M. LEHR, “*A nonviral DNA delivery system based on surface modified silica-nanoparticles can efficiently transfect cells in vitro*”, Bioconj. Chem., **11**, pp. 926–932, 2000.
- [8] I. KOLTOVER, T. SALDITT, J.O. RADLER, C.R. SAFINYA, “*An inverted hexagonal phase of cationic liposome-DNA complexes related to DNA release and delivery*”, Science, **281**, pp. 78–81 1998.
- [9] P. KOHLI, R.C. MARTIN, “*Smart nanotubes for biotechnology*”, Current Pharma. Biotech, **6**, pp. 35–47, 2005.
- [10] K.E. LEE, B.K. KIM, S.H. YUK, “*Biodegradable polymeric nanospheres formed by temperature-induced phase transition in a mixture of poly(lactide-co-glycolide) and poly(ethylene oxide)-poly(propylene oxide)-poly(ethylene oxide) triblock copolymer*”, Biomacromolecules, **3**, pp. 1115–1119, 2002.
- [11] S.B. LEE, D.T. MITCHELL, L. TROFIN, N. LI, T.K. NEVANEN, H. SÖDERLUND, C.R. MARTIN, “*Antibody-based bio/nanotube membranes for enantiomeric drug separations*”, Science, **296**, pp. 2198–2200, 2002.
- [12] M. LEWIN, N. CARLESSO, C. TUNG, X-W. TANG, D. CORY, D.T. SCADDEN, R. WEISSLEDER, “*Tat peptide-derivatized magnetic nanoparticles allow in vivo tracking and recovery of progenitor cells*”, Nature Biotech., **18**, pp. 410–414, 2000.
- [13] D.T. MITCHELL, S.B. LEE, L. TROFIN, N. LI, T.K. NEVANEN, H. SÖDERLUND, C.R. MARTIN, “*Smart nanotubes for bioseparations and biocatalysis*”, J. Am. Chem. Soc., **124**, pp. 11864–11865, 2002.

- [14] N. MURTHY, Y.X. THNG, S. SCHUCK, M.C. XU, J.M.J. FRECHET, “*A novel strategy for encapsulation and release of proteins: hydrogels and microgels with acid-labile acetal cross-linkers*”, *J. Am. Chem. Soc.*, **124**, pp. 12398–12399, 2002.
- [15] S.J. PARK, T.A. TATON, C.A. MIRKIN, “*Array-based electrical detection with nanoparticles probes*”, *Science*, **295**, pp. 1503–1506, 2002.
- [16] J. RADLER, I. KOLTOVER, T. SALDITT, C.R. SAFINYA, “*Structure of DNA cationic liposome complexes: DNA intercalation in multilamellar membranes in distinct interhelical packing regimes*”, *Science*, **275**, pp. 810–814, 1997.
- [17] K.E. ULRICH, S.M. CANNIZZARO, R.S. LANGER, K.M. SHAKESHELF, “*Polymeric systems for controlled drug release*”, *Chem. Rev.*, **99**, pp. 3181–3198, 1999.
- [18] A. VENTOSA, M.T. GARCIA, M. KAMEKURA, H. ONISHI, F. RUIZ-BERRAQUERO, “*Bacillus halophilus sp. nov., a new moderately halophilic Bacillus species*”, *Syst. Appl. Microbiol.*, **12**, pp. 162–166, 1989.

Pulsed Laser Ablation Synthesis of Carbon Nano-Structures: Effect of Target Composition and Laser Ablation Condition on Their Yield and Morphology

Iulian BOERASU and Marius ENACHESCU

Center for Surface Science and Nanotechnology, University Politehnica of Bucharest,
Splaiul Independentei 313, Bucharest, ROMANIA

E-mail: marius.enachescu@upb.ro

Abstract. This work is organized to provide a snapshot of our approach, achievements and understanding on the topic of carbon nano-particles, specifically carbon nano-onions and carbon nanotubes. The experiments have been performed employing a new and innovative laser ablation chamber design. The conditions for carbon nano-onions deposition, using excimer laser to ablate a commercial pure graphite target, are reviewed and confirmed by transmission electron microscopy analyses. We also reviewed results about UV laser ablation on metal doped carbon-based targets under different temperatures and laser pulse repetition rates to reveal the influence of the temperature and pulse frequency on the single wall carbon nanotubes synthesis and its yield.

1. Introduction

Carbon nano-particles have been intensively studied in the last decade due to their remarkable electronic and structural properties, which make them valuable for nanotechnology, magnetic storage materials, single electron devices, point source field emitters and electrochemical capacitors, and for their potential applications in advanced concepts for lubrication products [1]. Nowadays, carbon has been mimicked in the laboratory with the development of discrete chemical systems, such as fullerenes, carbon nano-onions (CNOs) and carbon nanotubes (CNTs).

Carbon nano-onions, also called onions-like carbon (OLCs), onion-like fullerenes (OLFs), are a unique class of nanomaterials, often referred to as the zero-dimensional pendant to multi-wall carbon nanotubes.

A critical element for CNOs synthesis is to master the fabrication of high quality, reliable CNOs. Two techniques were mainly reported in literature for

fabrication of CNOs. The first of them, also called Kuznetsov method [2], reported the production of extremely pure CNOs in high yields by annealing carbon nanodiamond particles at temperatures above 1200°C. The second one, called Sano method [3], is reporting production of CNOs by arcing between two graphite electrodes under water. There are some drawbacks to these two methods. The main drawback is related to the fact that the CNOs obtained by these methods are quite different: small CNOs with 6-8 shells (5nm) are obtained by Kuznetsov's method as compared with large CNOs of 20-30 shells and about 15-25 nm in the case of Sano's technique. Another drawback of these two methods is related to the apparatus involved in CNOs fabrication, which is very complex and highly specialized.

The recorded reports of carbon nanotubes (CNTs) belong from early '50 when the Russian researchers Radushkevich and Lukyanovich [4] reported first their observation. Later on 1976 the single (or double) walled carbon nanotubes were reported by Oberlin *et al.* [5].

The recent history of the CNTs start by 1991 when Sumio Iijima, from Nippon Electric Corporation (NEC) Research Laboratory in Japan, has been the first scientist who described the multiwalled carbon nanotubes (MWCNTs) preparation process after a random event during the test of a new arc evaporation method for C₆₀ carbon molecule fabrication [6]. Two years later, in 1993, the first reports about the growth process of single walled carbon nanotubes (SWCNTs) are published almost simultaneously in two separate works from Iijima *et al.* and Bethune *et al.* [7, 8]. Since this time, the SWCNTs have been one of the hottest topics in both physics and material science.

The rolling of a single graphene layer, which is a hexagonal network of carbon atoms, led to form a single tube, *i.e.*, a SWCNT (Fig. 1). When two or more concentric tubes are placed one into another, MWCNTs are formed.

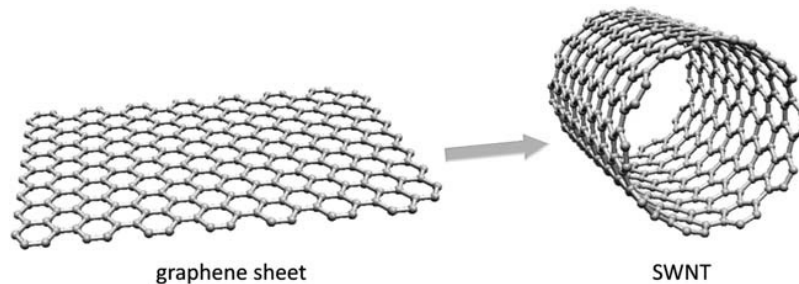


Fig. 1. Wrapping of graphene sheet to form SWCNT [7].

Due to remarkable electronic and structural properties, SWCNTs have started to revolutionize various applications areas, from electronics, electromagnetic devices, to composite materials and optics, to biomaterials and biomedical devices. Studies in biological and pharmaceutical fields were extensively reported by literature,

proving that CNTs can act as a part of biosensors, drug and vaccine delivery vehicles [9, 10, 11, 12, 13, 14, 15, 16].

During the challenge of the wonderful world of CNTs several techniques were examined with the aim to produce high quality CNTs. Nowadays, three main synthesis methods are mastered on the CNTs production field: arc discharge, laser ablation and chemical vapor deposition (CVD).

In between them, the arc discharge and chemical vapor deposition methods are widely applied for the formation of MWCNTs. Many studies were made to improve either the quality or the quantity of the produced material by optimizing the synthesis process. As a result some types of CVD methods were discovered such as plasma-enhanced, microwave-enhanced, radiofrequency-enhanced CVD. Nowadays, the laser vaporization is the best reported method to grow high-quality, high-purity SWCNTs. The laser ablation technique favors the growth of higher purity SWCNTs (about 90% pure) with a better graphitized structure than those produced in the arc process. By this synthesis technique, the MWCNTs are generated only employing special reaction conditions.

Unfortunately, the growth of SWCNTs by laser vaporization is not yet fully controlled or fully understood. Thus, their potential technological applications, which depend on the growth rates and the possibility of large-scale production are affected by this lack of fundamental understanding.

This work is organized to provide a snapshot of our approach, achievements and our understanding on the topic of CNTs. Our approach consists in proposing a new design of the laser vaporization apparatus. The new design aim to eliminate the major drawbacks of the prior-art designs such as complexity and costs. The important role of the synthesis parameters is outlined. The results summarized in this work are essentially the studies from the last few years. While the level of our understanding accumulated during this period is vast, here is presented what are certainly the strongest achievements.

2. Synthesis Apparatus

The pulsed laser-ablation process for the production of single-wall carbon nanotubes was developed by Guo *et al.* [17].

Figure 2 depict a schematic of the oven laser-vaporization apparatus proposed by Guo's group.

Typically, a laser shot is directed to a carbon target (1) and vaporizes a small amount of material inside of an oven heated up to 1200°C [17, 18, 19, 20]. During ablation, an uniform and smooth face for ablation is ensured by laser beam scanning across the target surface under computer control system. The soot produced by the laser vaporization is usually swept by the flowing working gas (Ar, N₂, etc.) from the high-temperature zone, and deposited onto a water-cooled copper collector (2) positioned outside the furnace.

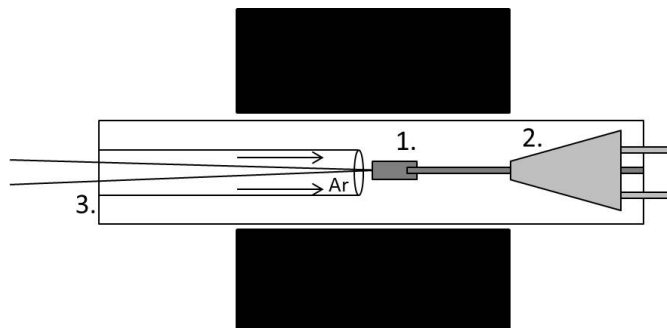


Fig. 2. Schematic of the Guo synthesis apparatus for CNTs by laser ablation technique [17]. The key elements of apparatus are the ablation target (1), the water-cooled copper collector (2) and the quartz tube (3).

On a single laser shot, the vaporized material self-assembles to form a high volume fraction of SWCNTs.

One disadvantage of using this design of laser ablation apparatus is the small carbon deposit. The cause is a complex design of the reaction apparatus that also led to both difficult manipulation and expensive apparatus.

Noticeable improvements of the design for the laser ablation apparatus was recently reported by Enachescu's group [21, 22]. Figure 3 present a cut-away side view of the novel, experimental set-up by Enachescu's group for the laser ablation of the carbon targets. The laser ablation chamber consists of a quartz tube (2), 60mm in diameter, mounted inside a hinged tube furnace (3). The temperature of the furnace can be varied from 30°C up to 1200°C and the quartz tube is O-ring sealed to ensure pressure control from 10^{-3} Torr up to atmospheric pressure.

The ablation gas is entering the chamber just after the quartz window (1), controlled by a flowmeter. The gas flow can be varied from 0 to 300 L/h. As novelty, the length of the oven has been increased to 675 mm compared to prior art reactor designs, of only 305 mm, which would ensure a quite constant temperature zone or a smaller temperature gradient inside the chamber.

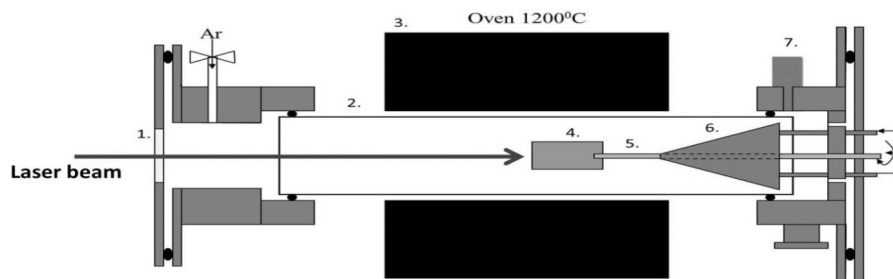


Fig. 3. Chamber schematics: 1) Quartz laser window; 2) Quartz tube; 3) Electrical Oven; 4) Target; 5) Graphite transfer rod; 6) Cold Finger; 7) Vacuum gauge.

Pulsed laser vaporization experiments were carried out using a Compex Pro 205 excimer laser from Coherent, operating with a wavelength of 248 nm, 25 ns pulse length and 10 Hz repetition rate. The laser beam was focused on a 20 mm² spot perpendicularly directed on a pure graphite commercial target surface. The pressure inside the reactor was fixed at 7 Torr while an Argon flow was kept at about 300L/h. The observed plume resulting from the laser interaction with the graphite target (4) was 20-30 mm long and the ablation products condensed on the water-cooled cold finger (6).

3. Target Composition

Already the first Guo's laser ablation experiments has pointed out that the composition of the target material is a crucial factor in the CNTs synthesis. The first used target was made of pure graphite, which was machined to be a cylinder. Previous reported results, including here our reported achievements, has demonstrated that laser ablation on a pure graphite targets yield fullerenes and nano-onions by laser ablation [23, 24, 25].

SWCNTs are obtained when simultaneously with carbon, a small percentage of catalyst transition metal are mixed. There are studies which has evaluated a series of mono- and bi-metal catalysts pointing-out that binary metal mixtures can significantly enhance SWCNTs yields [23, 24, 25].

Isolated SWCNTs were formed when monometallic Co or Ni/graphite target has been used. It was demonstrated that a high amounts of SWCNTs bundles are obtained applying bimetallic graphite catalyst Ni/Y (Yttrium) with the concentration of Ni always higher than that of Y, or Ni/Co in equal concentration [26, 27].

However, previous publications have focused on using targets that have been obtained by hot pressing, using Graphite Cement GC-8010B supplied by Metal Forming Lubricants, Inc. or pressing followed by temperature curing [23, 24, 25]. These methods are time consuming and usually more expensive. We have proposed a novel target preparation method that eliminates the need for pressing or hot-pressing and the associated difficulties related to it. The novel preparation procedure involves mixing mono- and bi-metal catalysts powders (particle size 0.10-0.45µm) with the graphite cement. To our knowledge, carbon cement supplied by Dylon has been used with the addition of graphite powder [24]. Our preparation method did not include any additional graphite. The mixture was placed in a PTFE mold in which the 2 cm in diameter target is formed. The mixture was cured at 130°C for 4 hours. This ensures the reaction of the resin from the graphite cement. Finally, the target was removed from the mold and heated to 800°C for one hour in an inert atmosphere in order to remove the unreacted resin. The mass loss during the temperature treatments was 39%. This new method is very easy and straight forward to implement, with great results for SWCNTs synthesis.

The performance of the novel design for the laser ablation apparatus proposed by Enachescu's group have been highlighted by several experiments in details reported in scientific papers. As comparison, experiments in the same conditions as the ones reported in the literature by using a prior-art apparatus have been performed [28]. As in the Braidy experiments, the ablation setup was including an KrF excimer laser, producing 25ns pulses at 248 nm with 100 to 700 mJ energy. The laser was focuses the laser beam on a 20 mm² rectangle spot on the target.

Two types of targets have been ablated in our new design of ablation reactor without the use of an inner tube: a pure graphite target and a Co/Pt doped cement target prepared by the new procedure proposed by Enachescu's group. It must be emphasized that except the preparation procedure, the Co/Pt doped cement targets used in both experiments have been of the same chemical composition. The ablation parameters for these targets are mentioned in Table 1.

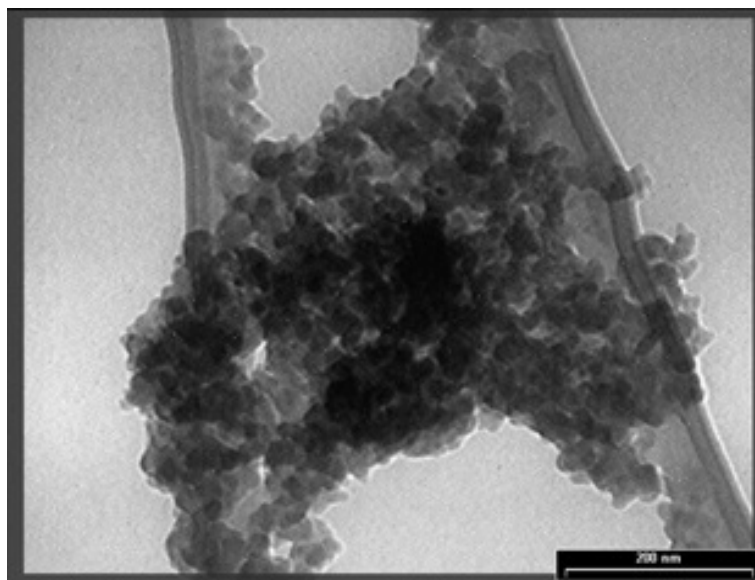
Table 1. Ablation parameters

Parameter	Pure graphite Target	Co/Pt doped cement target
Laser Energy	700mJ	700mJ
Pulse frequency	10 Hz	30 Hz
Temperature	900 °C	1100°C
Argon flow	300 L/h	250L/h
Pressure	10 Torr	500 Torr

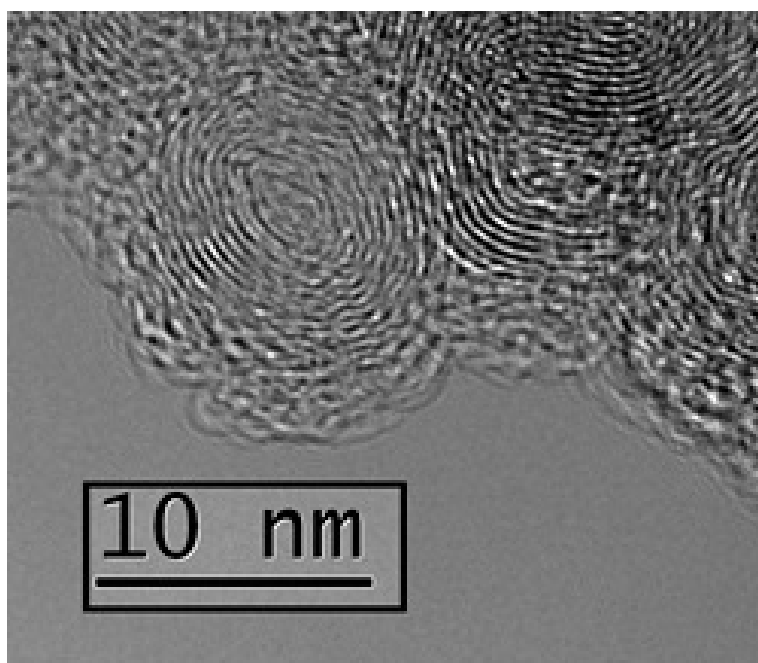
The collected products were studied using transmission electron microscope (TEM) and High Resolution Transmission Electron Microscopy (HRTEM).

As depicted in Fig. 4, the products obtained by ablating the pure graphite, target look like very well-defined nano-particles, both individual and clustered. Isolated CNOs on the TEM experimental grid is a probabilistic difficult to catch due to the fact that many times the individual CNOs are dragged to form a cluster even in the solution deposited on the TEM grids. Statistic measurements show that they have diameters between 6-25 nm. The individual nano-particles are usually spherical and have a concentric shell structure.

On the other hand, as depicted by Fig. 5, the TEM and HRTEM images performed on the ablation products of the target with Co/Pt as catalysts make evidence of the presence of SWCNTs surrounded by amorphous carbon. Moreover, the presence of the catalyst can also be seen as nanoparticles a few nanometer in diameter. The nanotubes are isolated or bundled up. This is in accordance to the findings of Braidy's reported results on SWCNTs obtaining in similar ablation conditions but using a prior-art apparatus.

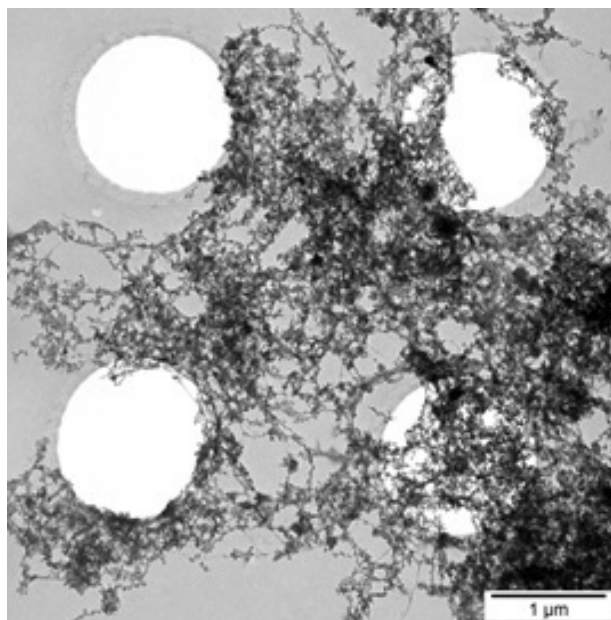


a)

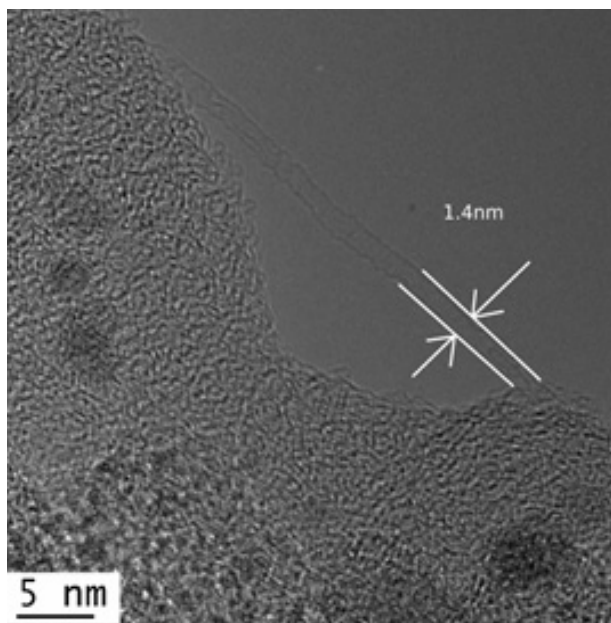


b)

Fig. 4. TEM and HRTEM images of the nano-onions obtained by ablating a pure graphite target at 700mJ and 300L/h.



a)



b)

Fig. 5. HRTEM image on SWCNTs obtained by the ablation of the Pt/Co doped target.

Further structural analysis has been performed by means of micro-Raman spectroscopy. In Fig. 6, a typical Raman spectrum of the products obtained by laser ablation of the pure graphite target is presented.

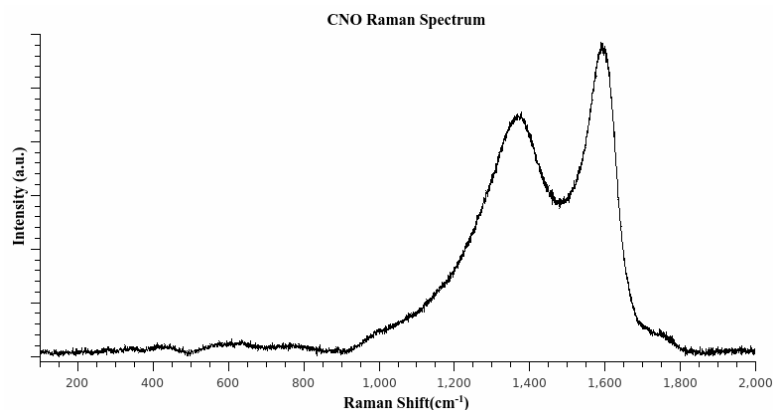


Fig. 6. Micro-Raman spectra of nano-onions obtained by laser ablation of graphite target.

The spectrum shows the presence of the D band centered at 1349 cm^{-1} and the G band with a maximum peak at 1592 cm^{-1} . The presence of the G band in the Raman spectra indicates sp^2 carbon hybridization while the D band is usually attributed to defect-induced Raman features [29].

The micro-Raman spectrum of the products obtained by laser ablation of the Co/Pt doped target is presented in Fig. 7 alongside the Raman spectrum of commercial SWCNTs from Sigma Aldrich, used as reference sample.

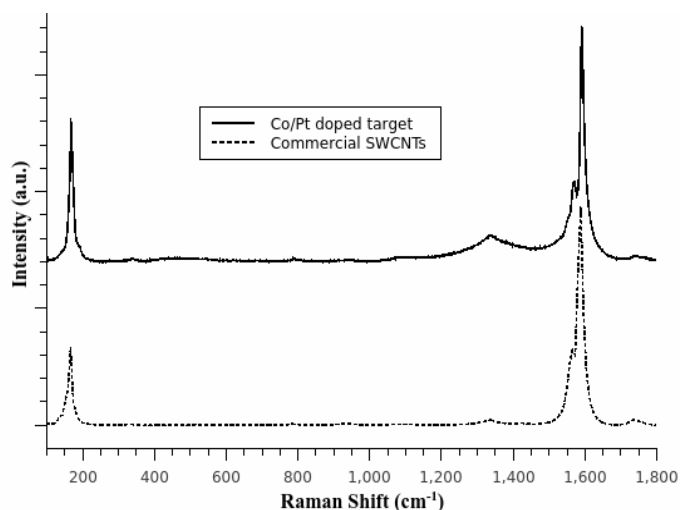


Fig. 7. Micro-Raman spectra of SWCNTs obtained by laser ablation of Co/Pt doped target.

The Raman spectrum shows 3 main bands. The first, centered at 164 cm^{-1} , is attributed to the radial breathing mode (RBM) of the SWCNTs. The RBM corresponds to the vibration of the C atoms from the nanotube in the radial direction²⁸. Another strong feature in the Raman spectrum is the G band with a maximum at 1589 cm^{-1} . The G band is characteristic for sp^2 carbon hybridization. The G band corresponds to the vibration of C atoms in the transversal and longitudinal direction [29]. A broad band centered at 1340 cm^{-1} and usually named the D band is also present in the SWCNTs spectrum. This is characteristic for scattering from defect sites, *i.e.*, sp^3 carbon hybridization. Previous studies show that the RBM peak for MWCNTs is too weak to be observable in the Raman spectra [29]. Thus, the RBM band centered at 164 cm^{-1} confirms that the nanotubes are single walled.

According to these results, the performances of the new laser ablation apparatus design for KrF excimer laser synthesis of carbon nanomaterials, including here nano-onions and carbon nano-tubes, has been well evidenced versus prior-art apparatus [28].

4. Results and Discussions

In our studies, results about the morphologies and microstructure of un-purified ablation products, as collected after ablation of a pure graphite target were obtained by Transmission Electron Microscopy (TEM) and High Resolution Transmission Electron Microscopy (HRTEM) analysis.

As depicted in Fig. 8, the products look like well-defined carbon nano-onions (CNOs), both individual and clustered through an amorphous carbon matrix.

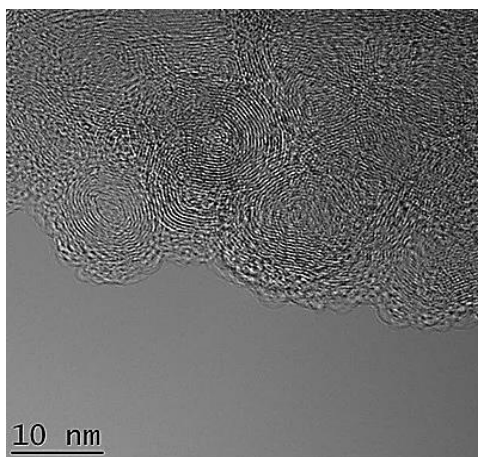
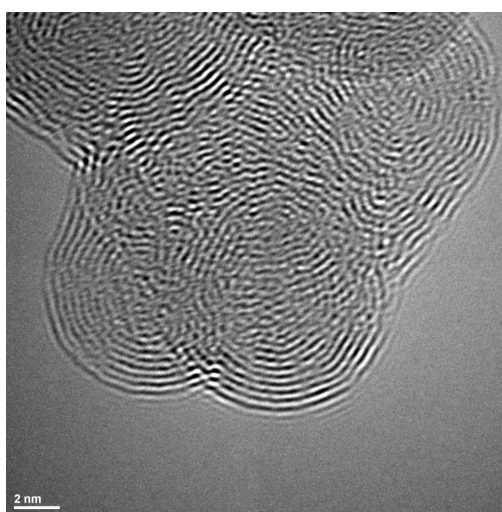
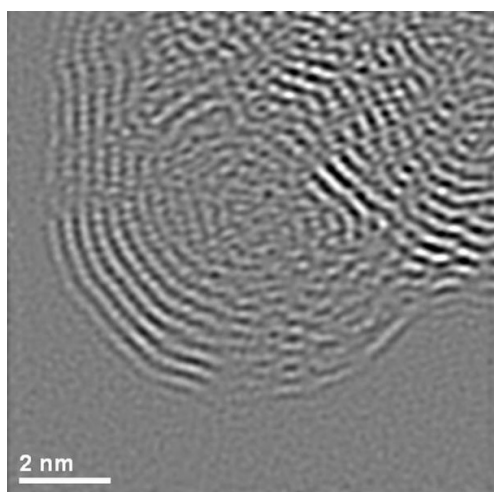


Fig. 8. Characteristic HRTEM micrograph of un-purified ablation products showing nano-onions like structures surrounded by an amorphous matrix.

Figure 9a) is showing a cluster of CNOs while the Fig. 9b) is showing just one CNO. It has to be understood that the CNOs are not bounded in the cluster and they are easy to be dispersed in an ultrasounds baths treatment done in distilled water. However, to catch just isolated CNOs on the TEM experimental grid is a probabilistic difficult process while many times the individual CNOs are dragged to form a cluster even in the solution deposited on the TEM grids. Usually, individual CNOs are obtained after functionalization treatments specially performed to avoid the electrostatically agglomeration of fabricated CNOs.



a)



b)

Fig. 9. HRTEM image of a) clustered CNOs and b) single CNOs.

Statistic measurements of the diameter of the observed CNOs were found in the range of 10 to 25 nm. The individual nano-onions are spherical and formed by 10-20 concentric shells. The graphitic interlayer distance of the CNOs was estimated in 10 different samples and the mean value was found to be 0.35 nm, as evidenced by the inset in Figure 10, which is close to the ideal graphitic interlayer spacing [30].

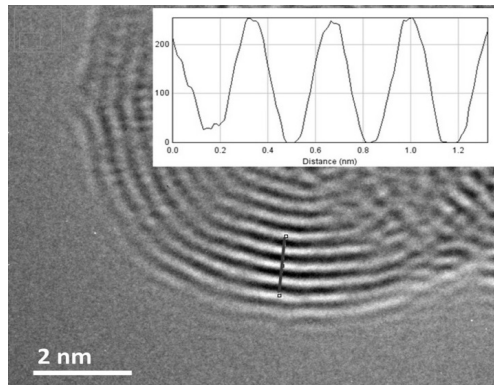


Fig. 10. HRTEM micrograph showing the graphitic interlayer of the CNOs. The measurement of the interlayer distance is coming from the insert.

However, the structures that are observed in the HRTEM look like carbon onions with hollow core. As observed, no amorphous carbon can be found inside of the shell; thus pure carbon nano-onions have been obtained. As seen, the hollow core of the onion is regular and very small (less than 5 nm). The inter-atomic distance in between the carbon atoms was also measured in 10 different samples and the mean value was found to be 0.24 nm as evidenced by the inset in Fig. 11.

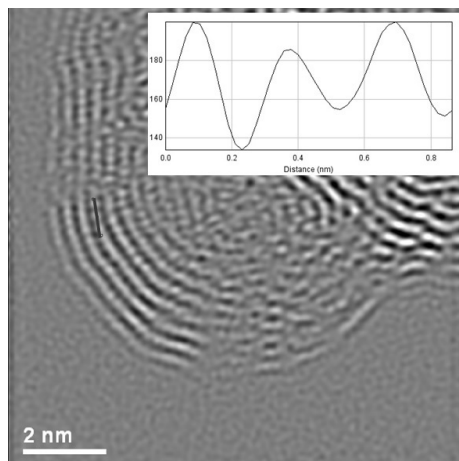


Fig. 11. HRTEM micrograph of a CNO used for calculation of the interatomic distance. The result of the measurement for the interatomic distance is presented in the insert.

TEM and HRTEM analysis have been performed on the ablation products obtained from graphite target doped with bi-component catalysts by Enachescu's group [31] (see Fig. 12). The SWCNTs are embedded within the amorphous carbon. The presence of the catalyst can also be seen as nanoparticles a few nanometer in diameter. The nanotubes are isolated or bundled up. This is in accordance to the findings of other groups on SWCNTs obtained by laser ablation [32, 33, 34].

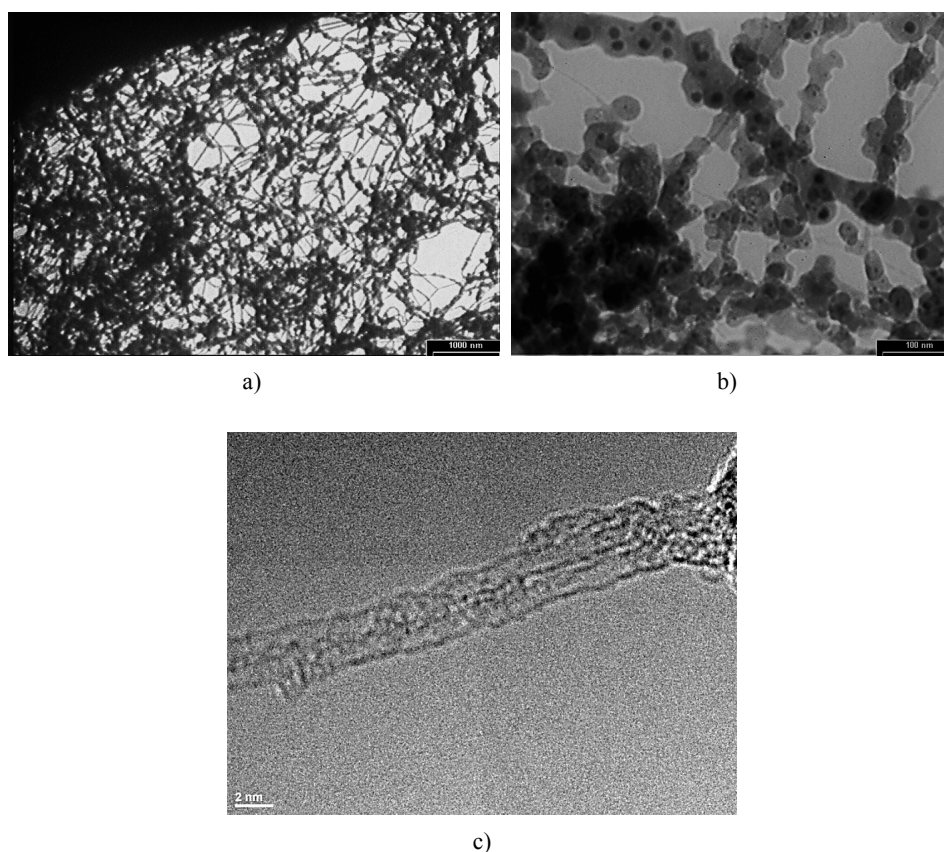


Fig. 12. TEM a), b) and c) HRTEM image on SWCNTs obtained by the ablation of the bi-component doped target.

Thermo-gravimetric analysis (TGA) was used to measure the purity of the SWCNTs obtained. The weight loss of the collected products has been measured. The temperature was gradually increased by 5°C/min under furnace 21% Oxygen atmosphere at normal pressure. The mass loss versus temperature curve is presented in Fig. 13.

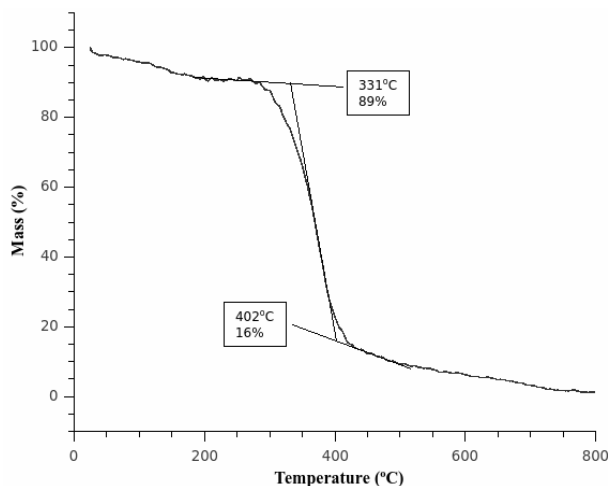


Fig. 13. Thermo-gravimetric analysis used to estimate the purity of synthesized SWCNTs.

The mass loss between 300°C and 450°C can be attributed to the oxidation of SWCNTs. The purity of the ablation can be estimated to be about 70%. The ablation byproducts are amorphous carbon that oxidizes at lower temperatures and catalyst nanoparticles covered in graphitic layers of carbon.

4. The Effect of the laser Parameters

Generally, the effect of laser intensity and furnace temperature on diameter distribution, yield and physical characteristics of SWCNTs was extensively studied and documented in the literature [35, 36, 37].

One of the ablation parameters that has not been thoroughly documented is the laser pulse frequency, or repetition rate. Few attempts are reporting about the influence of the laser repetition rate and concluding that an increase from 1 to 30 Hz of a Nd:YAG laser pulse leads to a small decrease in the mean SWCNTs diameter: from 1.25 nm to 1.21 nm [38]. Similar results are reported when a laser ablation was performed using a KrF excimer laser (248 nm wavelength) and the repetition rate was increased from 30 Hz to 150 Hz [39]. According to these reported studies, the increase in repetition rate has led to an increase in the ratio of nanotubes with diameter 1.49nm compared to SWCNTs with a diameter of 1.22nm.

We compared TEM images of recorded ablation products obtained at 1100°C using a 248 nm wavelength KrF excimer laser operating at and 10, 30 and 50 Hz. The ablated target used for this studies was a Co/Ni doped target. The ablation environment inside the ablation reactor was consisting in an Argon flux of 250L/h at a pressure of 500Torr.

Characteristic TEM and HRTEM micrographs of our ablation products obtained at 50 Hz show similar morphology with those for the ablation products at 10Hz and 30Hz respectively (see Fig. 14).

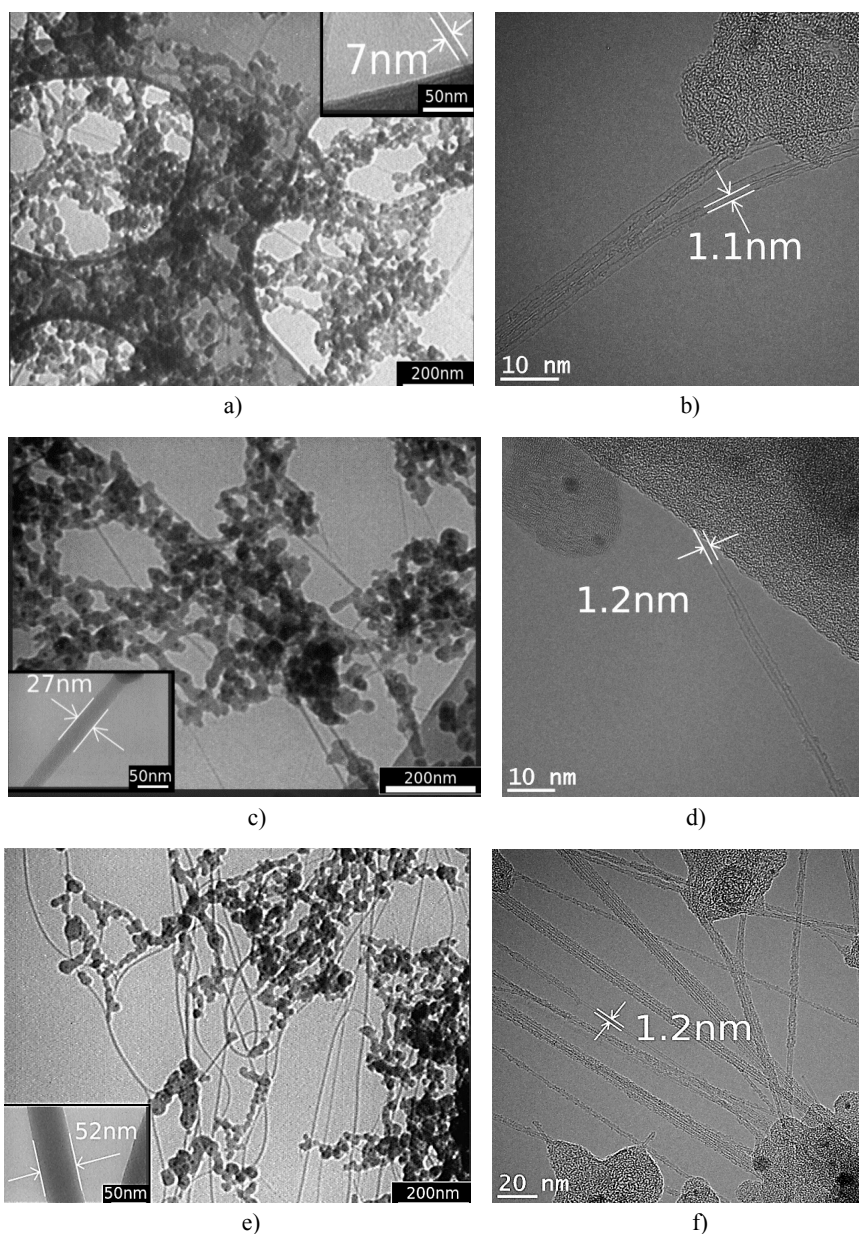


Fig. 14. TEM micrographs of the ablation products at 1100°C and a) 10Hz, c) 30 Hz and e) 50 Hz. The b), d) and f) images shows corresponding HRTEM micrograph on an individual SWCNT growth at 10Hz, 30 Hz and 50 Hz respectively.

The ablation products consist of SWCNTs bundles, amorphous carbon and catalyst nanoparticles. The obvious difference observable when comparing the three characteristic morphologies is the bundle size of the SWCNTs. At 50 Hz, the measured diameters of the bundles of SWCNTs are generally higher, ranging from a few nanometers up to 55 nm, triple in size as compared to the bundles found in the products obtained by laser ablation at 10 Hz and doubled compared to the bundles obtained by laser ablation at 30 Hz. It is obvious that a higher repetition rate enhances further the formation of larger bundles of nanotubes having a narrower diameter distribution. Such an enhancement is thought to be a consequence of the extra local heating of the target surface under high repetition rate conditions.

The micro-Raman spectroscopy analysis performed on ablations products from 10, 30 and 50 Hz repetition rate have shown that a higher repetition rate enhances further the formation of larger bundles of nanotubes having a narrower diameter distribution.

All the recorded spectra of the SWCNTs present in the ablation products presents two regions of interest. Fig. 15 shows the Raman spectra of the products obtained by the ablation at 10, 30 and 50 Hz.

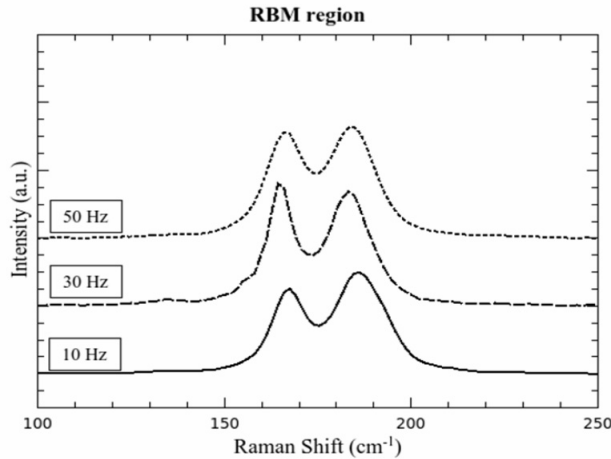


Fig. 15. Low frequency Raman spectra on ablation products at 10, 30 and 50Hz using 532 nm excitation wavelength.

At low wavenumbers, 100 to 300 cm^{-1} a band entitled the Radial Breathing Mode (RBM) is characteristic for SWCNTs. The Raman frequency in this region is inversely proportional to the SWCNTs diameter by the following equation:

$$\omega_{\text{RBM}} = \frac{c_1}{d} + c_2 \quad (1)$$

where ω_{RBM} is the radial breathing mode frequency (in cm^{-1}), d is the SWNT

diameter (in nm), c_1 and c_2 are constants with values of $c_1=215 \text{ cm}^{-1}$ and $c_2=18 \text{ cm}^{-1}$ respectively[40].

According to quotation (1) there are small variations between the products obtained at these three repetition rates pointing-out that the nanotube diameters are not influenced by the repetition rate used. The diameters calculated with the above equations are in the 1.3 to 1.5 nm range.

Figure 16 shows the high frequency region of the Raman spectra, 1200 to 1700 cm^{-1} , of the products obtained by ablation at 10, 30 and 50Hz, and the D band centered at 1340 cm^{-1} is observed. The second characteristic band present in the Raman spectra is centered on around 1600 cm^{-1} . This is the G band and its split can be observed. The lower frequency component of the G band is ascribed to vibrations along the circumferential direction of the nanotubes (G^-) and it is attributed to resonance effect in metallic nanotubes. The other one, at higher frequency, is associated to vibrations along the direction of the nanotube axis (G^+) and is associated with semiconducting nanotubes[41]. The high similarity of the G bands from the Raman spectra indicates that the electronic character of the SWCNTs in the sample was not influence by the laser repetition rate.

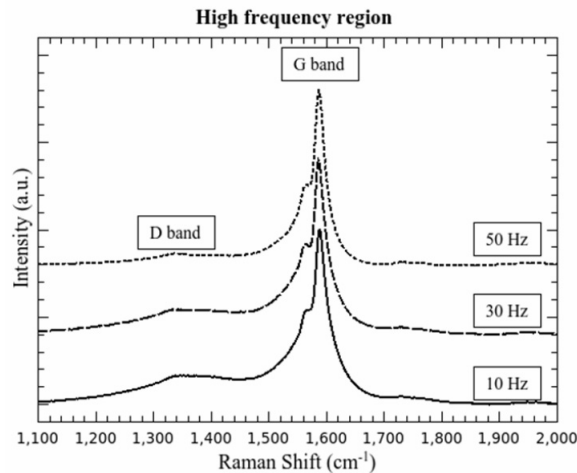


Fig. 16. High frequency Raman spectra on ablation products at 10, 30 and 50Hz using 532nm excitation wavelength.

5. The Effect of Temperature

It is a fact that all the work reported to date on the laser vaporization based synthesis of SWCNTs was carried out using lasers emitting either in the visible or in the infrared domains. There are not so many studies reported on the use of lasers emitting in the UV domain for the growth of SWCNTs. Braidy *et al.* have reported that for UV laser synthesis of SWCNTs the growth temperature is a key parameter

that strongly favors the formation of the SWCNTs. According to their results, increasing the growth temperature from 550 to 1150 °C is leading to higher yield of SWCNTs and an increase of the diameter distribution [32].

Our results, already published elsewhere [24], are confirming the Braidly findings: the increase in ablation temperature has led to an increase in SWCNTs productivity. This was visible from both the TEM and HRTEM micrographs and from Raman micro-spectroscopy.

Morphological characterizations of the products obtained consisting of TEM and HRTEM micrographs were obtained with a Phillips EM410 operating at 80kV and a Jeol-ARM200F with a resolution of 0.2nm and 0.11nm respectively. In Fig. 17 characteristic TEM micrographs of the ablation products at 700, 900 and 1100°C are presented.

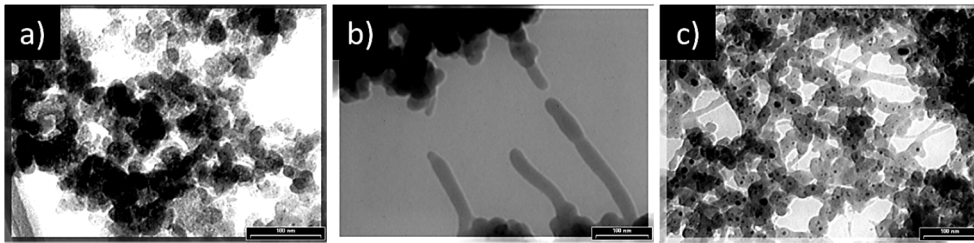


Fig. 17. TEM micrographs of the ablation products obtained at a) 700°C; b) 900°C; c) 1100°C.

In Fig. 17 a) can be seen that the products resulted from the ablation carried out at 700°C consists mainly of amorphous carbon and catalyst particles. At 900°C (Fig. 17b), the TEM micrographs reveals the presence of small amounts of SWCNTs together to amorphous carbon and catalyst particles. At the highest used growing temperature, *e.g.*, 1100°C, the ablation yielded the highest purity of SWCNTs as visible from the TEM micrographs (see Fig. 17c). Micro-Raman spectra of the ablation products have been performed and characteristic spectra are presented in Fig. 18.

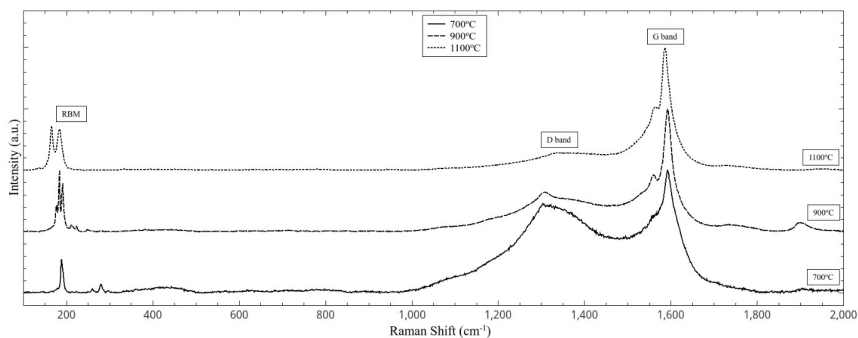


Fig. 18. Raman spectra of the ablation products obtained at 700, 900 and 1100°C with 532 nm excitation wavelength.

All the acquired spectra depict a maximum in the RBM band at around 188cm^{-1} . A low intensity peak at 279cm^{-1} peak can also be seen in the spectrum from 700°C . Using equation (1), the SWCNTs diameters are calculated and the obtained values are ranging from 1.26 nm to 0.82 nm respectively. The spectrum of the products of the 900°C ablation presents three maximums in the RBM region, at 176, 183 and 190cm^{-1} . The estimated diameter range for this interval would be between 1.25 and 1.36 nm. The RBM region from the Raman spectrum of the 1100°C ablation products presents two maximums at 164cm^{-1} and 183cm^{-1} which represents a diameter distribution from 1.3 nm to 1.5 nm.

As depicted by Fig. 18, two bands are visible at high frequency. The first one is the D band centered at around 1340cm^{-1} . This band is usually attributed to the scattering on sp^3 hybridized carbon atoms from defect sites and amorphous carbon. The second one, centered at around 1587cm^{-1} is named G band and is characteristic for scattering on sp^2 hybridized carbon atoms. The ratio of the normalized intensity of these two bands is a good indication of the quality of the sample, *i.e.*, the higher D band intensity indicating more amorphous carbon or defects in the sample [41]. The I_G/I_D ratios for the 700, 900 and 1100°C samples are 1.5, 2.0 and 7.7, indicating a decrease in the amorphous carbon and/or defects in the ablation products obtained at higher temperatures. This is in good accordance with the TEM and HRTEM micrographs that show an increase in SWCNTs production with increasing the growing temperature.

6. Conclusions

Some of the most critical topics about the synthesis of carbon nano-structures by UV laser ablation process have been discussed. It was described in details how the target composition is influencing the type of nano-structures growth.

Synthesis of carbon nano-onions by UV laser vaporization technique on a pure graphite target, in a new laser ablation chamber design, using a KrF excimer laser have been discussed. HRTEM analysis shows that the synthesized CNOs were typically 25-30 nm in diameter. The observed individual nano-onions were spherically shaped and have a concentric shell structure, formed by 10-20 shells with a hollow core. The HRTEM images recorded on obtained ablation products look like well-defined nano-onions, both individual and clustered through an amorphous carbon matrix. Isolated CNOs on the TEM experimental grid is probabilistic difficult to catch due to the fact that many times the individual CNOs are dragged to form a cluster even in the solution deposited on the TEM grids.

The ablation of metal doped target has yielded SWCNTs, documented via TEM, micro-Raman spectroscopy, as well as TGA measurements. The new chamber demonstrated production up to 70% purity of the SWCNTs, showing that the new design of the ablation apparatus is suitable for SWCNTs production. The ablation of catalyst doped carbonaceous targets has been carried out at various

temperatures: 700, 900 and 1100°C, and repetition rates: 10, 30 and 50Hz. The influence of the temperature and repetition rate on the ablation products has been investigated with TEM and Raman-confocal micro-spectroscopy.

The increase in ablation temperature has led to an increase in SWCNTs productivity of about 70%.

This was visible from both the TEM and HRTEM micrographs and micro-Raman spectroscopy has been used to depict the way in which the target composition and the ablation conditions affects the carbon nanotubes formation and yield. TEM micrographs have made evidence of the fact that the amount of amorphous carbon decreases with increasing ablation temperature. Raman spectra of the ablation products have also shown that the average diameter of the obtained SWCNTs increases with increasing ablation temperature.

The SWCNTs bundle diameter has been shown to increase with the increase in laser repetition rate. The laser pulse frequency did not have an observable impact on the nanotube diameter under the ablation conditions used. The I_G/I_D ratios for the 700, 900 and 1100°C samples are 1.5, 2.0 and 7.7, indicating a decrease in the amorphous carbon and/or defects in the ablation products obtained at higher temperatures.

The purity of the SWCNTs in the ablation products has been shown to increase with increasing the laser pulse repetition rate.

Acknowledgements. This work was supported by the Ministry of National Education, Romania and by the European Union through the European Regional Development Fund and by Romanian National Authority for Scientific Research (POSCCE-O 2.1.2-2009-2/12689/717) as well as by the Romanian Executive Agency for Higher Education, Research, Development and Innovation Funding (UEFISCDI) through the program PN-II "Capacitati" under contract No. 686/22.04.2013.

References

- [1] K.W. STREET, M. MARCHETTI, R.L. VANDER WAL, A.J. TOMASEK, *Tribol Lett*, **16**, pp. 143, 2004.
- [2] V.L. KUZNETSOV, A.L. CHUVILIN, Y.V. BUTENKO, I.Y. V.M. MALKOV, *Titov, Chem. Phys. Lett.*, **222**, pp. 343, 1994.
- [3] N. SANO, H. WANG, M. CHLOWALLA, I. ALEXANDROU, G.A.J. AMARATUNGA, *Nature*, **414**, pp. 506, 2001.
- [4] L.V. RADUSHKEVICH and V.M. LUKYANOVICH, *Zh. Fiz. Khim.*, **26**, pp. 88, 1952.
- [5] A. OBERLIN, M. ENDO and T. KOYAMA, *J. Cryst. Growth*, **32**, pp. 335, 1976.
- [6] S. IIJIMA, *Nature*, **354**, pp. 56, 1991.
- [7] S. IIJIMA and T. ICHIHASHI, *Nature*, **363**, pp. 603, 1993.
- [8] D.S. BETHUNE, C.H. KIANG, M.S. DEVRIES, G. GORMAN, R. SAVOY, J. VAZQUEZ and R. BEYERS, *Nature*, **363**, pp. 605, 1993.
- [9] B.T. YAKOBSON, R.E. SMALLEY, *Am. Sci.*, **85**, pp. 324, 1997.
- [10] V.N. POPOV, *Mat. Sci. Eng. R: Reports*, **43**, pp. 61, 2004.

- [11] M. PARADISE, T. GOSWAMI, *Mat. Design*, **28**, pp. 1477, 2007.
- [12] J.C. GRUNLUM, A.R. MEHRABI, M.V. BANNON, J.L. BAHR, *Adv. Mat.*, **16**, pp. 150, 2004.
- [13] P.R. SUPRONOWICZ, P.M. AJAYAN, K.R. ULLMAN, B.P. ARULANANDAM, D.W. METZGER, R. BIZIOS, *J. Biomed. Mat. Res.* **A59**, pp. 499, 2002.
- [14] H. KOERNER, G. PRICE, N.A. PEARCE, M. ALEXANDER, R.A. VARIA, *Nature Mater.*, **3**, pp. 115, 2004.
- [15] R. SEN, B. ZHAO, D. PEREA, M.E. ITKIS, H. HU, J. LOVE, E. BEKYAROVA, *NanoLett.*, **4**, 459, 2004.
- [16] Y. LIN, S. TAYLOR, H. LI, S.K.A. FERNANDO, L. QU, W. WANG, L. GU, B. ZHOU, Y.P. SUN, *J. Mater. Chem.*, **14**, pp. 527, 2004.
- [17] T. GUO, P. NIKOLAEV, A. THESS, D.T. COLBERT and R.E. SMALLEY, *Chem. Phys. Lett.*, **236**, pp. 419, 1995.
- [18] A. THESS, R. LEE, P. NIKOLAEV, H. DAI, P. PETIT, J. ROBERT, C. XU, Y.H. LEE, S.G. KIM, A.G. RINZLER, D.T. COLBERT, G.E. SCUSERIA, D. TOMANEK, J.E. FISHER, R.E. SMALLEY, *Science*, **273**, pp. 483, 1996.
- [19] M. YUDASAKA, T. ICHIHASHI, T. KOMATSU and S. IJIMA, *Chem. Phys. Lett.*, **299**, 91, 1999.
- [20] A.G. RINZLER, J. LIU, H. DAI, P. NIKOLAEV, C.B. HUFFMAN, F.J. RODRIGUEZ-MACIAS, P.J. BOUL, A.H. LU, D. HEYMANN, D.T. COLBERT, R.S. LEE, J.E. FISHER, A.M. RAO, P.C. EKLUND, R.E. SMALLEY, *Appl. Phys. A: Mater. Sci. Process.*, **67**, pp. 29, 1998.
- [21] P.M. BOTA, D. DOROBANTU, I. BOERASU, D. BOJIN, M. ENACHESCU, *Surface Engineering and Applied Electrochemistry*, **50**(2), 2014, (in press).
- [22] P.M. BOTA, D. DOROBANTU, D. BOJIN, M. ENACHESCU, accepted for publication in *Materials Research Innovations*, 2014.
- [23] S. IJIMA, *J. Cryst. Growth*, **50**, pp. 675, 1980.
- [24] T.W. EBBESEN, P.M. AJAYAN, *Nature*, **358**, pp. 220, 1992.
- [25] D. DOROBANTU, P.M. BOTA, I. BOERASU, D. BOJIN, M. ENACHESCU, *Surface Engineering and Applied Electrochemistry*, **50**(3), 2014 (in press).
- [26] W.K. MASER, E. MUNOZ, A.M. BENITO, M.T. MARTÍNEZ, G.F. de la FUENTE, Y. MANIETTE, E. ANGLARET, J.-L. SAUVAJOL, *Chem. Phys. Lett.*, **292**, pp. 587, 1998.
- [27] W.K. MASER, A.M. BENITO, E. MUOZ, G.M. de VAL, M.T. MARTINEZ, A. LARREA, G.F. de la FUENTE, *Nanotechnology*, **12**, pp. 147, 2001.
- [28] N. BRAIDY, M.A. EL KHAKANI, G.A. BOTTON, *Chemical Physics Letters*, **354**, pp. 88, 2002.
- [29] D. ROY, M. CHHOWALLA, H. WANG, N. SANO, I. ALEXANDROU, T.W. CLYNE, G.A.J. AMARATUNGA, *Chem. Phys. Lett.*, **373**, pp. 52, 2003.
- [30] G. RADHAKRISHNAN, P.M. ADAMS, F.D. ROSS, *Journal of Physics: Conference Series*, **59**, pp. 424, 2007.
- [31] P.M. BOTA, D. DOROBANTU, I. BOERASU, D. BOJIN, M. ENACHESCU, *Journal of Experimental Nanoscience*, accepted for publication 2014.
- [32] G. RADHAKRISHNAN, P.M. ADAMS, L.S. BERNSTEIN, *Appl. Surf. Sci.*, **253**, pp. 7651, 2007.
- [33] A.A. PURETZKY, D.B. GEOHEGAN, X. FAN, S.J. PENNYCOOK, *Appl. Phys.* **A70**, pp. 153, 2000.
- [34] S. AREPALLI, P. NIKOLAEV, W. HOLMES, S. BRADLEY, *Appl. Phys. Lett.*, **78**, pp. 11, 2001.
- [35] V. Le BORGNE, B. AISSA, M. MOHAMEDI, Y.A. KIM, MORINOBU ENDO, M.A. EL KHAKANI, *J Nanopart Res*, **13**, pp. 5759, 2011.
- [36] S. BACHILO, S. STRANO, C. KITTEL, R.E. SMALLEY, R.B. WEISMAN, *Carbon. Nanotub Sci.*, **298**, pp. 2361, 2002.

- [37] S. BANDOW, S. ASAKA, Y. SAITO, A.M. RAO, L. GRIGORIAN, E. RICHTER, P.C. EKLUND, *Phys Rev Lett.*, **80**, pp. 3779, 1998.
- [38] O. JOST, A. GORBUNOV, L.C. CIACCHI, W. POMPE, X. LIU, T. PICHLER, L. DUNSCH, M.S. GOLDEN, J. FINK, in H. Kuzmany *et al.* (Ed.) *AIP Conference Proceedings*, **591**, 341, 2001.
- [39] N. BRAIDY, M.A. EL KHAKANI, G.A. BOTTON, *Chemical Physics Letters*, **354**, pp. 88, 2002.
- [40] S.S. HARILAL, C.V. BINDHU, R.C. ISSAC, V.P.N. NAMPOORI, C.P.G. VALLABHAN, *J. App. Phys.*, **82**, pp. 2140, 1997.
- [41] A. JORIO, M.A. PIMENTA, A.G. SOUZA FILHO, R. SAITO, G. DRESSELHAUS, M.S. DRESSELHAUS, *New Journal of Physics*, **5**, pp. 1391, 2003.

Strategies for the Structure and Morphology Control of BaTiO₃ Nanoparticles

Florentina MAXIM¹, Paula FERREIRA², Paula VILARINHO²

¹Department of Chemical Thermodynamics, “Ilie Murgulescu” Institute of Physical Chemistry of the Romanian Academy, Splaiul Independentei 202, 060021 Bucharest, Romania
E-mail: fmaxim@icf.ro

²Department of Materials and Ceramic Engineering, CICECO, University of Aveiro, Campus de Santiago, 3810-193 Aveiro, Portugal
E-mail: paula.vilarinho@ua.pt, pcferreira@ua.pt

Abstract. This review provides insights regarding synthesis strategies for simultaneous control of tetragonality, size and shape in barium titanate. Details concerning the understanding of structure, size and shape effect on BaTiO₃ properties will be considered in the first part. Then a revision of the most reported BaTiO₃ particles solution-based synthesis approaches for the control of its structure and morphology will be presented. In the final section, a description of the contribution of the authors to the topic is presented and demonstrates that low-temperature hydrothermal synthesis using suitable titanium precursors is a suitable approach to simultaneously control structure and morphology in BaTiO₃.

1. Introduction

Control of the shape and size in multifunctional materials is a great interest because they play very important roles in determining magnetic, electrical, and optical properties due to the spatial geometry effect.[1] [1] In this view, notable advancement has been made for the controlled synthesis and self-organization of inorganic materials with regular geometrical shapes, whether in the dimensions of nanoscale or micrometer scale.[2] [2]

The ferroelectric materials with perovskite structure have found widespread applications as sensors, microactuators, infrared detectors, microwave phase filters and

non-volatile memories, for which their functional properties such as switchable polarization, piezoelectricity, high non-linear optical activity, pyroelectricity, and non-linear dielectric behavior are indispensable. [3-7] [3-7]

BaTiO₃ is a typical ferroelectric material, subject to fundamental research since WWII due to its high permittivity and low losses properties suitable for many applications. According to Haertling [8] [8] the discovery of non-linear dielectric properties in barium titanate associated with very high values of the dielectric permittivity, was crucial for the development of the new generation of materials for electronic and microelectronic devices. Hence, BaTiO₃ is among the most systematically studied and widely used ferroelectrics and considered as the prototype lead-free ferroelectric ceramic. BaTiO₃ was firstly used as piezoelectric ceramic transducers. However, due to the discovery of better piezoelectric properties in other materials, namely the solid solution between lead titanate and lead zirconate, BaTiO₃ found its main use as high permittivity dielectric in multilayer ceramic capacitors (MLCC). [9] [9] Barium titanate based ceramics show dielectric constant values as high as 15,000 as compared to 5 or 10 for common ceramic and polymer materials. The high dielectric constant BaTiO₃ ceramic based disk capacitors are simple to be manufactured and have captured more than 50% of the ceramic capacitor market. [10] [10] The advances in tape casting technology have made it possible to make dielectric layers < 20 μm thick. This combined with the use of a high dielectric constant ceramic like BaTiO₃ allows large capacitance values to be achieved in relatively small volume capacitor devices. Good reviews have been written on the state of the art of the MLCC technology and the technical challenges it faces. [10-12] [10-12]

Devices miniaturization or scaling down, in one word the nanotechnology, is the strategy for improved resources efficiency in energy devices, as has been highlighted in the FP7 Observatory NANO report, European Nanotechnology Landscape, released in November 2011 [13] [13]. In nanotechnology the concept “smaller” means greater performance in less space. A performing capacitor is the one that can store a large amount of electrical charge (high capacitance density) and then discharge that charge to give a significant amount of power (high operating voltage) with maximum efficiency (low losses as leakage current or power dissipation). In order to guarantee the good performance of a capacitor high surface area electrodes and high dielectric constant materials are required. In 2006 the International Technology Roadmap for Semiconductors (ITRS) suggested that the capacitors structure must become three-dimensional (3D) by 2010 to accommodate requisite storage density. [14] [14] The 3D architecture capacitors refer to vertically stackable cell arrays in monolithic integration, with acceptable yield and performance. Their use is a requirement for the dynamic

random access memories (DRAM) scaling down, as has been highlighted in the last report of ITRS. [15] [15]

The present review is divided in three parts. In the first section the explanation regarding the necessity of understanding the size and shape effect on the barium titanate properties is provided. The second part is a revision of the most common barium titanate particles synthesis approaches for the control of its structure, size and morphology. Finally, some original results reported by the authors during the last 8 years are presented and discussed. It is demonstrated that the low temperature hydrothermal synthesis using suitable titanium precursors is a very good strategy for the simultaneous control of structure, size and shape in BaTiO₃.

2. Effect of Structure, Size and Shape on the Barium Titanate Application

This section will answer the following questions:

- Why is needed tetragonal structured barium titanate?
- Why small size of BaTiO₃ particles is required?
- Why are looked-for different BaTiO₃ particles shapes?

BaTiO₃ is one of the complex oxides within the perovskite family and a typical ferroelectric material. The ideal perovskite structure adopted by many oxides has the general formula ABO_3 . [16][16] Based on the tolerance factor (t) [17][17], which takes into account the sizes of the O , A and B ions, the ideal perovskite structure adopts the cubic space group $Pm3m$. But factors other than the ionic size, *e.g.* degree of covalency, metal-metal interactions, Jahn-Teller and ion pair effects play a role in determining the space group. [18][18] At room temperature and atmospheric pressure barium titanate BaTiO₃ adopts a tetragonal structure with a space group $P4mm$ [19][19]. For pure barium titanate, the tolerance factor equals 1.06. Here the tolerance factor is greater than 1 (ideal) because Ti⁴⁺ is smaller than its cavity and/or Ba²⁺ is larger than its cavity. During several years the room temperature tetragonal structure of barium titanate was controversial. Based on the studies of Evans [19-20][19, 20] and Megaw [21][21], the structure of barium titanate is now well known and the room temperature tetragonal structure of the BaTiO₃ is explained by ionic displacement of the Ti ions regarding to the oxygen ions. This structural feature induces a spontaneous electric polarization that can be reversed by the application of an external electric field, the fingerprint of the ferroelectric materials.

It was observed that the ferroelectricity of BaTiO₃ disappears in particles smaller than 120 nm [22][22]. Further, the dielectric constant, although it increases with decreasing size, reaches a maximum at a grain size near the nanometer scale below

which it rapidly decreases [23][23]. These observations have stimulated an exponential growth on research aiming to understand the phenomena [24-28][24-28]. By then, one of the explanations was related to the stabilization of the cubic paraelectric polymorph of BaTiO₃ at room temperature, rather than the ferroelectric tetragonal structure for particles with size in the nanoscale [25][25]. Besides the size it has been theoretical demonstrated that the shape of the BaTiO₃ nanoparticles can also influence its tetragonality [29][29]. According to Morozovska BaTiO₃ ferroelectricity seems to be independent of the particle size in the case of anisotropic “cylindrical” shaped nanoferroelectrics or one-dimension (1D) nanostructures, such as nanotubes, nanorods and nanowires. It was theoretically demonstrated that 1D BaTiO₃ particles preserve the tetragonality even at very low dimensions (2.5 nm) and an enhancement of the ferroelectricity is expected due to the effective surface tensions and minimal depolarization field influence in the cylindrical nanoparticles [29][29]. This theoretical prediction of the absence of a critical size for 1D nanoferroelectrics introduced a new variable in the discussion of dimensionality in ferroelectrics, and, besides the size, the dependence on the shape gained importance [30][30]. It is therefore important to establish from the experimental point of view the relations between synthesis–structure–morphology–properties in ferroelectric nanostructures, namely in BaTiO₃.

3. Solution-Based Methods for Simultaneous Control of Structure, Size and Shape in BaTiO₃

The ferroelectric tetragonal structure of BaTiO₃ is mostly reported for materials synthesized at relatively high temperatures, above 600°C [31-33][31-33], where grain growth and aggregation are inevitable. On the other hand, syntheses at lower temperatures mostly led to the formation of BaTiO₃ non-ferroelectric cubic structure [34-35][34, 35]. With the need of preparing materials at very low temperatures that could be compatible with polymeric materials of low melting point, as required by the microelectronic industry, hydrothermal and related methods have been gaining importance.[36][36] The common BaTiO₃ structure obtained by hydrothermal synthesis is cubic. However several reports describe the hydrothermal synthesis of tetragonal BaTiO₃ powders. Asiaie *et al.* obtained tetragonal BaTiO₃ nanopowders of 90, 300 and 500 nm particle sizes by hydrothermal crystallization at 240°C starting from BaCl₂ and hydrated titanium oxide with a varying concentration of NaOH in the reaction medium [37] [37]. In this work only the larger particles were pure barium titanate, whereas the powder with smallest particle sizes (90 nm) contained unreacted titanium dioxide [37][37]. At the same hydrothermal treatment temperature, 240°C, Xu *et al.* prepared tetragonal BT powders with an average particle size of 80 nm [38][38].

At even lower temperature, 220°C, Jung *et al.* obtained tetragonal BaTiO₃ particles through glycothermal reaction for 12 h using Ba(OH)₂ and amorphous titanium hydrous gel as precursors and 1,4-butanediol and water as solvent [39][39]. High purity tetragonal BaTiO₃ powders with an average size of 150 nm in diameter were synthesized by a hydrothermal reaction at temperatures of around 200°C by Xie *et al.* [40][40]. Tetragonal BaTiO₃ was hydrothermally obtained at 200°C [41][41] or higher than this temperature [42][42] from titanium butoxide and Ba(OH)₂ [41][41] or Ba(NO₃)₂ in the presence of KOH [42][42]. The influence of the particles shape on the BaTiO₃ tetragonality has also been verified by hydrothermal synthesis. Cube-shaped and highly crystalline tetragonal BaTiO₃ was obtained from amorphous peroxo-precursor prepared by mixing BaCl₂, TiCl₄, H₂O₂, NH₄OH which was hydrothermally treated in a 10 M NaOH solution at 200°C for 24 h [43][43]. BaTiO₃ nanowires obtained at 170°C hydrothermal temperature [44][44] present high tetragonality and, in consequence, good ferroelectric and dielectric properties [45][45].

4. Structure and Morphology Control of BaTiO₃ by Hydrothermal Synthesis

The present authors demonstrated that tetragonal BaTiO₃ particles can be obtained at temperatures lower than 170°C by hydrothermal synthesis [46, 47][46, 47]. We established the relations between the precursor chemistry and the final structure of barium titanate compound. In this section our results obtained using different titanium precursors for the hydrothermal synthesis of barium titanate are revised and discussed in terms of structural and morphological characterization of the obtained powder.

(a) The first approach consists in a chemical template method. For this we used dry powder of layered sodium titanate nanotubes (TiNTs), prepared by hydrothermal synthesis [48][48], as both titanium precursors and growth directing agents. [49, 50][49, 50] The structural analysis was conducted by X-ray diffraction (XRD) and Raman spectroscopy (Fig. 1) and the morphological evaluation was done by scanning and transmission electron microscopy (SEM and TEM) (Fig. 2 and Fig. 3).

It was observed that when dry TiNTs powder was hydrothermal treated with aqueous solution of Ba(OH)₂ at various temperatures (90, 110 and 200°C) for different reaction times, the structure and the morphology of the barium titanate product is changing as follows:

➤ At low temperature and low time pseudo-cubic structured (Fig. 1) ‘wild’ type dendritic (Fig. 2a and 3a) BaTiO₃ particles have been formed by a phase boundary topotactic reaction on the TiNTs surface.[49, 50]

➤ At intermediate temperature and time of reaction round shaped particles of BaTiO_3 (Fig. 2b) were formed. [49]

➤ Finally, at high temperature and longer time ‘seaweed’ type dendrites with predominately tetragonal structure were obtained, the BaTiO_3 crystallization process being controlled by a dissolution precipitation mechanism.[49, 50]

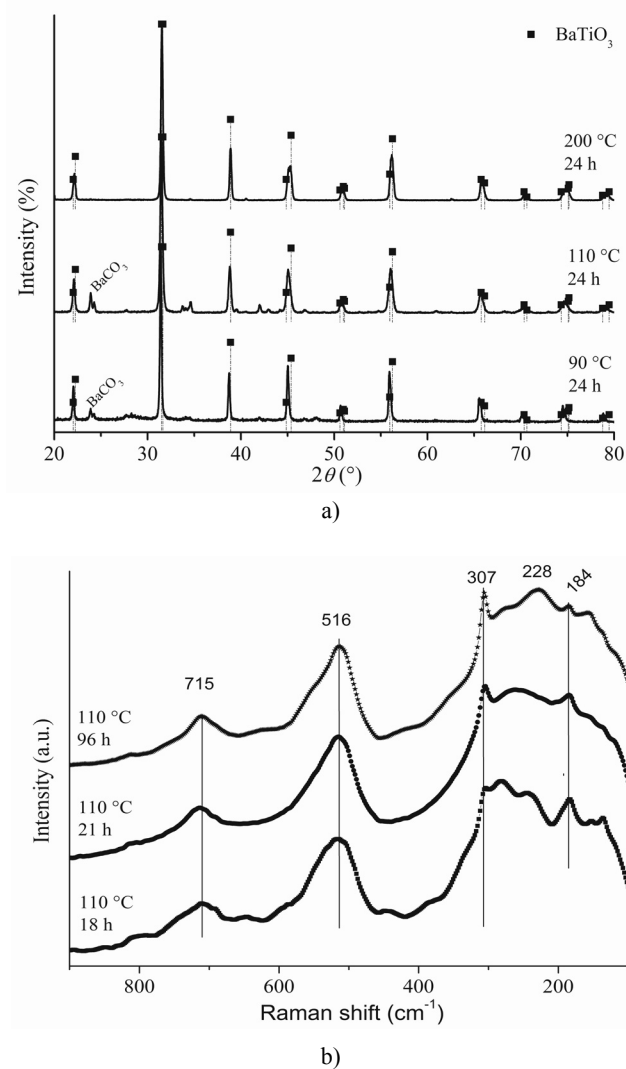


Fig. 1. XRD and Raman spectra of samples obtained from dry TiNTs and $\text{Ba}(\text{OH})_2$.

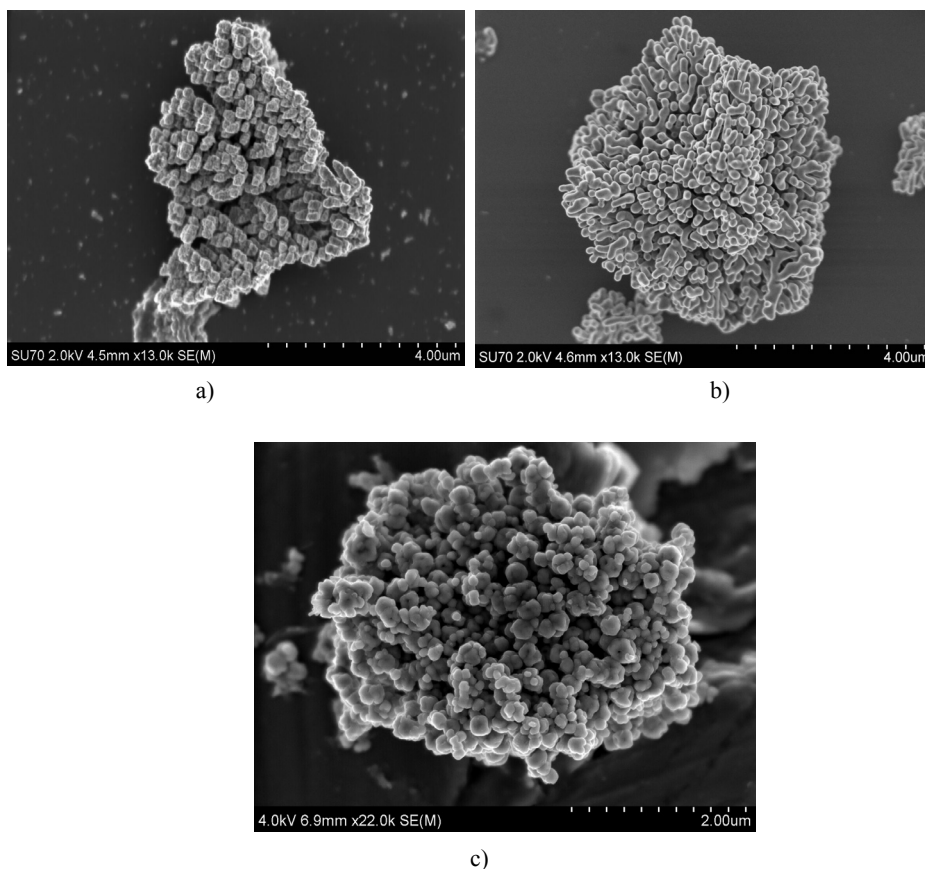


Fig. 2. SEM images of BaTiO₃ powders obtained starting from dry TiNTs and Ba(OH)₂; the images are presented in the order of reaction stages showing the formation of “wild”-type dendrites to round shaped particles and “seaweed” dendrites

The gradual transition from pseudocubic to tetragonal barium titanate with the reaction temperature and time is indicated by the reflections around 2θ of 45° [(200) and (002)] in the X-Ray patterns which became broader as the temperature (Fig. 1a) and time of reaction increases [49, 50][49, 50]. The splitting of the reflection at $2\theta \approx 45^\circ$ is characteristic of the tetragonal distortion of the BaTiO₃ structure. This cell distortion is reflected also in the Raman spectra [49, 50][49, 50] by the appearance of the sharp band at $\sim 307 \text{ cm}^{-1}$ (Fig. 1b). We postulate therefore, that at the early stages of crystallization cubic BaTiO₃ is more likely to form, whereas at later stages predominately tetragonal BaTiO₃ particles are obtained [49, 50][49, 50]. In SEM (Fig.

2) and TEM (Fig. 3) micrographs, we observed that the transition from pseudocubic to tetragonal is accompanied by a change in the particle morphology from “wild”-type dendrites to round shaped particles and “seaweed” dendrites. At low synthesis temperature (90°C) and short reaction times “wild” type dendrites with a rough defective surface are formed (Fig. 2a and 3a). As the crystallized BaTiO₃ fraction increases with the temperature and time, round shaped particles are observed (Fig. 2b) followed by defect free dendritic particles with smooth surface called “seaweed” type (Fig. 2c and 3b).

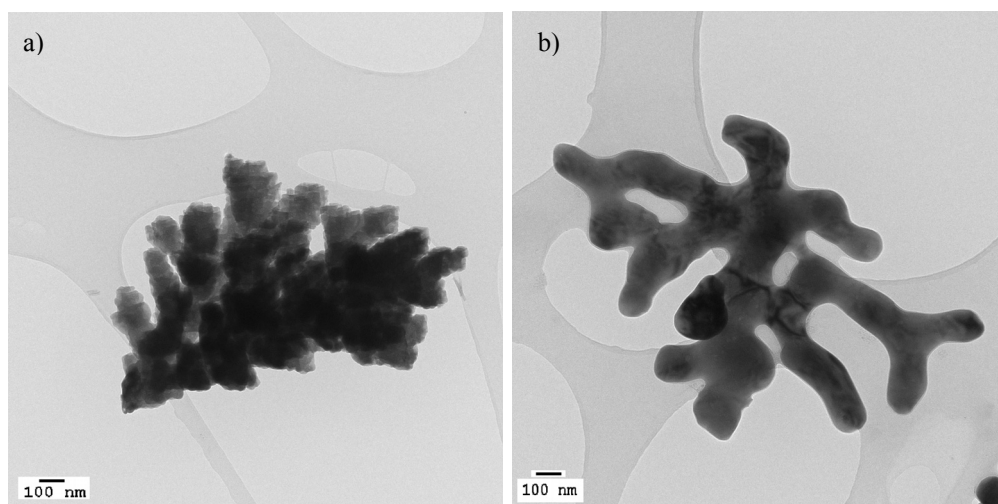


Fig. 3. TEM micrographs of a) wild-type and b) seaweed dendrites.

Our previously work [49, 50][49, 50] clearly shows that dry TiNTs can not easily act as directing growth agents for hydrothermal synthesis of BaTiO₃ but influence the anisotropic growth of this perovskite compound.

(b) In our subsequent investigations, the effect of titanium alkoxides as titanium precursors on the hydrothermal synthesis of BaTiO₃ was assessed.[46, 51][46, 51] This approach is based on sol-gel processes knowing that the sol-gel based methods have the advantage of good mixing of the reagents which induce a controllable structure, stoichiometry, size and shape of the final product. The sol-gel process is a versatile, solution-based process for producing various ceramic and glass materials in the form of nanoparticles, thin-film coatings, or fibers and involves the transition of a liquid, colloidal “sol” into a solid “gel” phase.[52][52] It is, furthermore, a cheap technique that allows fine control of chemical composition. Typical starting materials for the

preparation of the sol include metal salts or metal organic compounds, such as metal alkoxides, which undergo a series of hydrolysis and condensation reactions to form a colloidal or polymeric sol. One of the major drawbacks is that the product typically consists of an amorphous phase rather than defined crystals and, thus, requires crystallization and postannealing steps at high temperatures. Therefore in our study the sol-gel processes were combined with hydrothermal synthesis methods. The hydrothermal method enables the formation of crystalline particles or films without the need for postannealing and calcinations.[49-51, 53][49-51, 53]

For this approach titanium butoxide [Ti(OBu)₄] and titanium iso-propoxide [Ti(OⁱPr)₄] were used as titanium sources. The barium and titanium reagents sol was precipitated in aqueous solution of NaOH and hydrothermally treated at various temperatures for different times.[46, 51][46, 51]

The structural analysis by XRD and Raman (Fig. 4) of the samples prepared from different titanium alkoxides revealed that tetragonal in average but orthorhombic at local scale BaTiO₃ is obtained from Ti(OⁱPr)₄. Cubic in average but tetragonal at local scale barium titanate was obtained instead with Ti(OBu)₄ as titanium precursor.

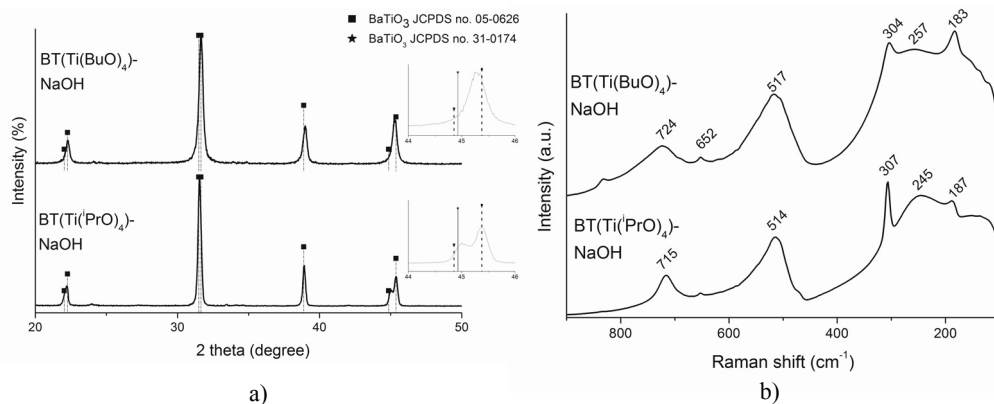


Fig. 4. XRD and Raman spectra of the samples obtained from different titanium alkoxides.

It was considered that the stabilization of different BaTiO₃ phases under hydrothermal conditions is depending on the Ti coordination in the titanium aqueous species [54][54], but this speculation has not been experimentally proved before our work. In our experimental conditions, Ti(OⁱPr)₄ is likely to form monomeric species in which the titanium atom is 4-fold coordinated (tetrahedric). Differently the Ti(OBu)₄ forms oligomers in the same experimental conditions in which each titanium atom is in

5-fold coordination. [55][55] This difference can be responsible for the formation of distinct barium titanate structures when starting from different titanium alkoxides precursors.[46][46]

The effect of some additives on the hydrothermal synthesis of BaTiO₃ starting from Ti(OBu)₄ was studied.[51][51] There are syntheses procedures in which the modification of the crystal growth may occur if the growth on some of the crystal faces will be restricted. This may be achieved by reducing the supply of material to a particular crystal face or by modifying the specific surface energy, that is, in the presence of some additives, named crystal habit modifiers [56][56] and classified as additive-assisted syntheses.

We reported that although the tested additives influenced the growth of BaTiO₃, their behaviour varied.[51][51] For instance, the poly(acrylic acid) (PAA) adsorbed on specific crystallographic faces changing the growth kinetics. PAA influences BaTiO₃ nucleation by modifying the quantity of the Ba²⁺ in solution. The direct aggregation observed when PAA is used (Fig. 5b) indicates that this additive also influences the growth of BaTiO₃. These results suggest that the growth process is controlled by an aggregation mechanism called oriented attachment.[57, 58][57, 58] It is then suggested that in the present study PAA could preferentially adsorb on high energy BaTiO₃ crystallographic faces, decreasing the growth rate of these faces and inducing the oriented attachment of BaTiO₃ particles. It can be therefore stated that PAA limits the growth kinetics of BaTiO₃ by decreasing the surface energy and so decreasing the growth rates of specific crystallographic faces. So PAA both adsorbs onto high energy surfaces and is trapped during the precipitation. [51][51]

The hydroxypropylmethylcellulose (HPMC) is growth inhibitor and also crystal habit modifier (Fig. 5c). [51][51] HPMC is a polysaccharide chemically derived from cellulose by insertion of hydrophobic moieties such as hydroxypropyl and methyl. Despite the introduction of these hydrophobic groups, HPMC presents a linear polymeric chain with a high hydrophilic character due to the presence of polyhydroxy groups on the molecular chains, which make the polymer water-soluble.[59][59] The hydrophobic parts of HPMC are important for its surface activity (as in a polysoap) and unique hydration-dehydration characteristics.

In our experimental conditions [51][51] HPMC acts as both growth inhibitor and crystal growth modifier. HPMC can act as a growth inhibitor as the crystal growth can be regulated and restricted by the three-dimensional network structure of HPMC gel formed when increasing the synthesis temperature and additive concentration.[51][51]

When using titanium isopropoxide Ti(OⁱPr)₄ as titanium source, the obtained results lead to the following key aspects [46][46]:

- At the hydrothermal synthesis temperature as low as 110°C tetragonal cube like (Fig. 6a) BaTiO₃ nanoparticles are formed;
- When increasing the NaOH concentration the tetragonal BaTiO₃ faceted cuboids-shaped (Fig. 6b) particle size increases. Moreover, at high concentrations of the NaOH barium titanate (111) twins growth appear (Fig. 6c);
- Monophasic crystalline BT is formed when using NaOH as mineralizer, compared to the sample obtained in the presence of N(CH₃)₄OH in which amorphous TiO₂ NRs are formed as a secondary product.

It was reported that the (111) crystallographic plane twins of barium titanate can only be formed at high temperatures (higher than 1300°C) and in samples containing an excess amount of TiO₂ [60, 61][60, 61]. They play an important role in the abnormal grain growth in BaTiO₃ ceramics due to the singular grain boundaries formed along the {111} flat faces of the BaTiO₃ grains [62, 63][62, 63]. Although well-documented the role of (111) twins in the abnormal grain growth of ceramics, their formation mechanism in BaTiO₃ powders is still under debate. We demonstrated that the formation of (111) BaTiO₃ growth twins is influenced by the increased concentration of sodium ions, which act as growth modifiers [46][46], and it is not influenced by the titanium surplus as reported before [64, 65][64, 65].

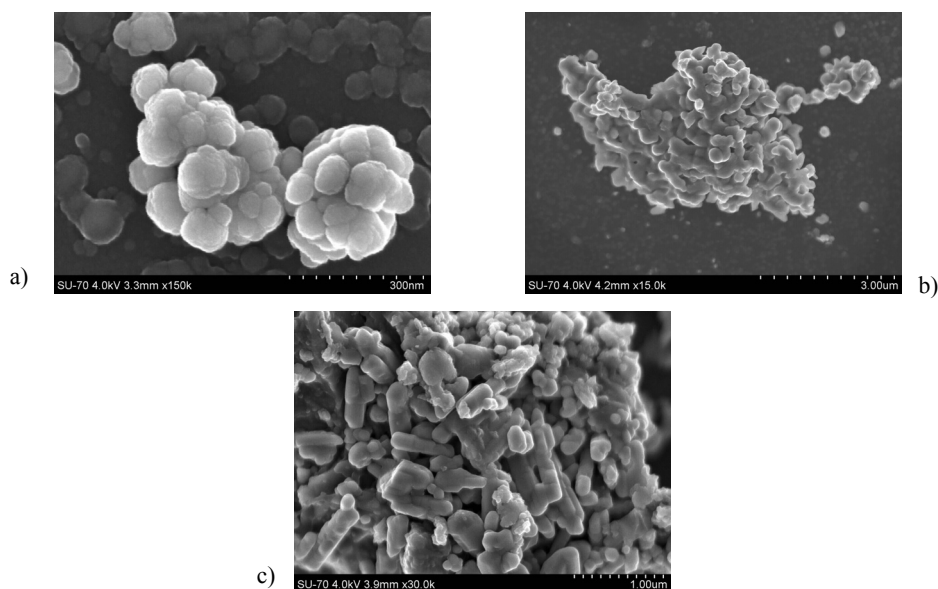


Fig. 1. SEM images of the samples obtained from Ti(BuO)₄ in the presence of additives: a) blank; b) PAA; c) HPMC.

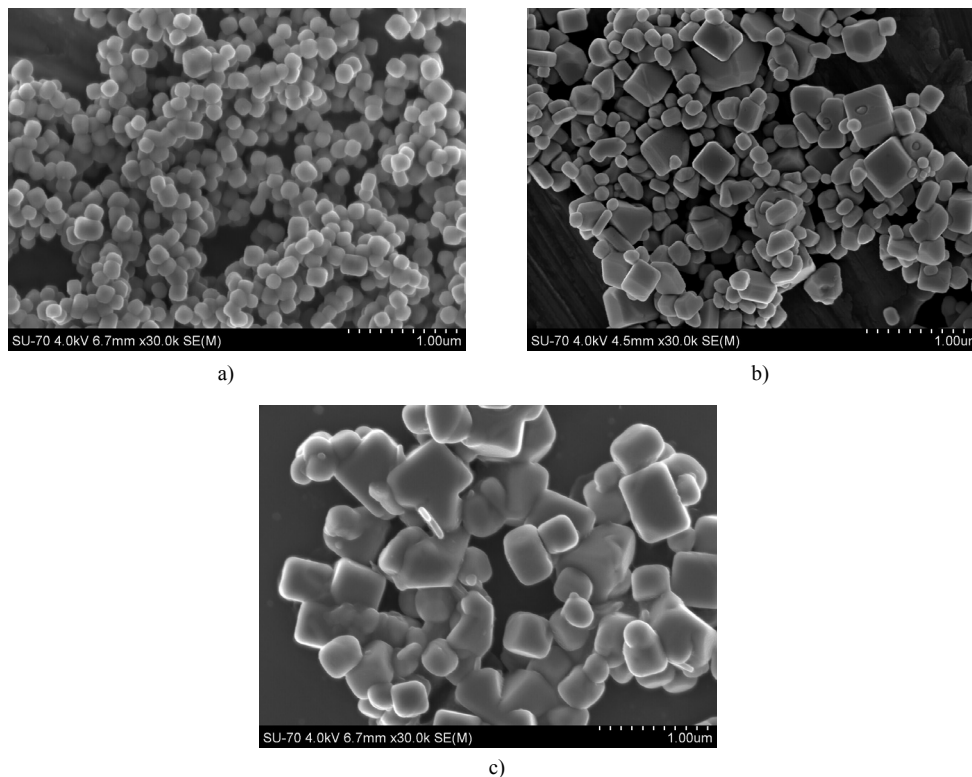


Fig. 6. SEM micrographs of the BaTiO₃ samples obtained from Ti(O'Pr)₄

5. Conclusions

The present revision provides good insights of finding low temperature synthesis strategies for structure and morphology control of BaTiO₃ nanoparticles. It is demonstrated that the structural transformation of barium titanate is accompanied by morphological changing in accordance with the characteristics of the titanium precursor. In the reported studies we confirmed that the hydrothermal synthesis, at temperatures not higher than 200°C, is suitable for the preparation of:

- Tetragonal structured BaTiO₃ with “seaweed” dendritic morphology which was obtained at late stage reaction of dry TiNTs powders hydrothermally treated with Ba(OH)₂. At early stages of barium titanate crystallization, “wild” type dendritic particles with cubic structure were obtained by a phase-boundary mechanism using dry TiNTs as titanium precursors.

➤ Tetragonal cube-shaped with uniform size distribution and dimension of ~ 70 nm BaTiO₃ obtained starting from titanium isopropoxide and barium acetate in the presence of NaOH. Instead, round shape barium titanate particles with predominantly cubic structure were formed when titanium butoxide was used as titanium precursor. This result is the first experimental proof that the stabilization of different barium titanate phases under hydrothermal conditions is depending on the Ti coordination in the titanium aqueous species.

This work is an unquestionable experimental proof of the barium titanate structural and morphological control obtained by tuning the titanium precursor's chemistry at low temperature hydrothermal crystallization.

Acknowledgement. Acknowledgements are addressed to the Portuguese Foundation for Science and Technology (FCT) and FEDER, the European Network of Excellence FAME, under the Contracts FP6-500159-1 and PTC/CTM/100468/2008 and to the Portuguese Electron Microscopy Network - RNME - Pole University of Aveiro, FCT Project REDE/ 1509/RME/2005. Florentina Maxim is thankful to FCT for the fellowship SFRH/ BD/23375/2005. Dr. Florentina Maxim is thankful to the Romanian National Authority for Scientific Research, CNCS – UEFISCDI, for the grant PN-II-RU-TE-2011-3-0160.

References

- [1] J. WANG, A.K. TAGANTSEV, N. SETTER, *Physical Review* **B83**, pp. 014104, 2011.
- [2] L. MANNA, D.J. MILLIRON, A. MEISEL, E.C. SCHER, A.P. ALIVISATOS, *Nature Materials* **2**, pp. 382–385, 2003.
- [3] Y. XU, "*Ferroelectric Materials and their Applications*", North-Holland Elsevier Amsterdam, 1991.
- [4] K. UCHINO, *Ferroelectric devices*, Marcel Dekker, New York, 2000.
- [5] J.W. WAANDERS, "*Piezoelectric Ceramics: Properties and Applications*", Philips Components, Eindhoven-The Netherlands 1991.
- [6] B. JAFFE, W.R. COOK Jr, H. JAFFE, "*Piezoelectric ceramics*", Academic Press, London, 1971.
- [7] M.E. LINES, A.M. GLASS, "*Principles and applications of ferroelectrics and related materials*", Clarendon Press, Oxford, 1977.
- [8] G.H. HAERTLING, *Journal of the American Ceramic Society* **82**, pp. 797–818, 1999.
- [9] P.M. VILARINHO, *Scanning Probe Microscopy: Characterization, Nanofabrication and Device Application of Functional Materials* **186**, pp. 3–33, 488, 2005.
- [10] D. HENNINGS, M. KLEE, R. WASER, *Advanced Materials* **3**, pp. 334–340, 1991.
- [11] R. WASER, *Advanced Materials* **4**, pp. 311–311, 1992.
- [12] K. BREDER, A.A. WERESZCZAK, L. RIESTER, T.P. KIRKLAND, R.J. BRIDGE, 23rd Annual Conference on Composites, Advanced Ceramics, Materials, and Structures: A: Ceramic Engineering and Science Proceedings, John Wiley & Sons, Inc., pp. 565–572, 2008.
- [13] B. Willems, Institute of Nanotechnology- FP7 Observatory NANO, 2011, pp. 109.

- [14] in: <http://www.itrs.net/Links/2006Update/2006UpdateFinal.htm>, (Ed.), 2006.
- [15] in: <http://www.itrs.net/Links/2011ITRS/Home2011.htm>, (Ed.), 2011.
- [16] R.H. MITCHELL, "Perovskites: Modern and Ancient", Almaz Press, Thunder Bay, Canada, 2002.
- [17] V.M. GOLDSCHMIDT, *Naturwissenschaften* **14**, pp. 477–485, 1926.
- [18] A.S. BHALLA, R.Y. GUO, R. ROY, *Materials Research Innovations* **4**, pp. 3–26, 2000.
- [19] H.T. EVANS, Massachusetts Institute of Technology, 1953.
- [20] H.T. EVANS, *Acta Crystallographica* **14**, pp. 1019–&, 1961.
- [21] H.D. MEGAW, *Acta Crystallographica* **15**, pp. 972–&, 1962.
- [22] K. UCHINO, E. SADANAGA, T. HIROSE, *Journal of the American Ceramic Society* **72**, pp. 1555–1558, 1989.
- [23] G. ARLT, D. HENNINGS, G. DEWITH, *Journal of Applied Physics* **58**, pp. 1619–1625, 1985.
- [24] K. ISHIKAWA, K. YOSHIKAWA, N. OKADA, *Physical Review* **B37**, pp. 5852–5855, 1988.
- [25] M.H. FREY, D.A. PAYNE, *Physical Review* **B54**, pp. 3158–3168, 1996.
- [26] Z. ZHAO, V. BUSCAGLIA, M. VIVIANI, M.T. BUSCAGLIA, L. MITOSERIU, A. TESTINO, M. NYGREN, M. JOHNSON, P. NANNI, *Physical Review* **B70**, 2004.
- [27] J. PETZELT, T. OSTAPCHUK, I. GREGORA, D. NUZHNYI, I. RYCHETSKY, K. MACA, Z. SHEN, *Ferroelectrics* **363**, pp. 227–244, 2008.
- [28] N.J. JOSHI, G.S. GREWAL, V. SHRINET, T.P. GOVINDAN, A. PRATAP, *Ieee Transactions on Dielectrics and Electrical Insulation* **19**, pp. 83–90, 2012.
- [29] A. MOROZOVSKA, E. ELISEEV, M. GLINCHUK, *Physica B: Condensed Matter* **387**, pp. 358–366, 2007.
- [30] P.M. RORVIK, T. GRANDE, M.A. EINARSRUD, *Advanced Materials* **23**, pp. 4007–4034, 2011.
- [31] T.K. MANDAL, *Materials Letters* **61**, pp. 850–854, 2007.
- [32] I. TSUYUMOTO, M. KOBAYASHI, T. ARE, N. YAMAZAKI, *Chemistry of Materials* **22**, pp. 3015–3020, 2010.
- [33] P.R. REN, H.Q. FAN, X. WANG, K. LIU, *Materials Letters* **65**, pp. 212–214, 2011.
- [34] Y. KOBAYASHI, A. NISHIKATA, T. TANASE, M. KONNO, *Journal of Sol-Gel Science and Technology* **29**, pp. 49–55, 2004.
- [35] J. MOON, E. SUVACI, T. LI, S.A. COSTANTINO, J.H. ADAIR, *Journal of the European Ceramic Society* **22**, pp. 809–815, 2002.
- [36] M.M. VIJATOVIC, J.D. BOBIC, B.A. STOJANOVIC, *Science of Sintering* **40**, pp. 155–165, 2008.
- [37] R. ASIAIE, W.D. ZHU, S.A. AKBAR, P.K. DUTTA, *Chemistry of Materials* **8**, pp. 226–234, 1996.
- [38] H.R. XU, L. GAO, J.K. GUO, *Journal of the European Ceramic Society* **22**, pp. 1163–1170, 2002.
- [39] Y. JUNG, D. LIM, J. NHO, S. CHO, R. RIMAN, B. WOOLEE, *Journal of Crystal Growth* **274**, pp. 638–652, 2005.
- [40] Y. XIE, S. YIN, T. HASHIMOTO, Y. TOKANO, A. SASAKI, T. SATO, *Journal of the European Ceramic Society* **30**, pp. 699–704, 2010.
- [41] S. MOON, H.W. LEE, C.H. CHOI, D.K. KIM, *Journal of the American Ceramic Society* **95**, pp. 2248–2253, 2012.
- [42] R.J. LI, W.X. WEI, J.L. HAI, L.X. GAO, Z.W. GAO, Y.Y. FAN, *Journal of Alloys and Compounds* **574**, pp. 212–216, 2013.
- [43] M. ÖZEN, M. MERTENS, J. LUYTEN, F. SNIJKERS, H. D'HONDT, P. COOL, *Ceramics International* **38**, pp. 619–625, 2012.
- [44] U.A. JOSHI, S.H. YOON, S.G. BAIK, J.S. LEE, *Journal of Physical Chemistry* **B110**, pp. 12249–12256, 2006.

- [45] N.J. JOSHI, G.S. GREWAL, V. SHRINET, A. PRATAP, N.J. BUCH, *Integrated Ferroelectrics* **115**, pp. 142–148, 2010.
- [46] F. MAXIM, P. FERREIRA, M. WILLINGER, P. VILARINHO, submitted to *Chemistry of Materials*, 2014.
- [47] F.V. MAXIM, PhD Thesis - Department of Ceramics and Glass Eng., University of Aveiro, Aveiro, 2010.
- [48] F. MAXIM, P. FERREIRA, P.M. VILARINHO, *Journal of Porous Materials* **18**, pp. 37–45, 2011.
- [49] F. MAXIM, P. FERREIRA, P.M. VILARINHO, I. REANEY, *Crystal Growth & Design* **8**, pp. 3309–3315, 2008.
- [50] F. MAXIM, P.M. VILARINHO, P. FERREIRA, I.M. REANEY, I. LEVIN, *Crystal Growth & Design* **11**, pp. 3358–3365, 2011.
- [51] F. MAXIM, P. FERREIRA, P.M. VILARINHO, A. AIMABLE, P. BOWEN, *Crystal Growth & Design* **10**, pp. 3996–4004, 2010.
- [52] C.J. BRINKER, G.W. SCHERER, "*Sol-gel science the physics and chemistry of sol-gel processing*", Academic Press, San Diego (CA), 1990.
- [53] K. BYRAPPA, A.S. DAYANANDA, C.P. SAJAN, B. BASAVALINGU, M.B. SHAYAN, K. SOGA, M. YOSHIMURA, *Journal of Materials Science* **43**, pp. 2348–2355, 2008.
- [54] M.M.R. LENCKA, R.E., *Chemistry of Materials* **5**, 1993.
- [55] F. BABONNEAU, S. DOEUFF, A. LEAUSTIC, C. SANCHEZ, C. CARTIER, M. VERDAGUER, *Inorganic Chemistry* **27**, pp. 3166–3172, 1988.
- [56] J.A. DIRKSEN, T.A. RING, *Chemical Engineering Science* **46**, pp. 2389–2427, 1991.
- [57] J.F. BANFIELD, S.A. WELCH, H.Z. ZHANG, T.T. EBERT, R.L. PENN, *Science* **289**, pp. 751–754, 2000.
- [58] R.L. PENN, J.F. BANFIELD, *Science* **281**, pp. 969–971, 1998.
- [59] A. RENDLEMAN, *J. Carbohydrates in Solution*, American Chemical Society, pp. 51–69, 1973.
- [60] V. KRASEVEC, M. DROFENIK, D. KOLAR, *Journal of the American Ceramic Society* **73**, pp. 856–860, 1990.
- [61] B.K. LEE, S.Y. CHUNG, S.J.L. KANG, *Acta Materialia* **48**, pp. 1575–1580, 2000.
- [62] M.-G. LEE, S.-Y. CHUNG, S.-J.L. KANG, *Acta Materialia* **59**, pp. 692–698, 2011.
- [63] Y.K. CHO, S.J.L. KANG, D.Y. YOON, *Journal of the American Ceramic Society* **87**, pp. 119–124, 2004.
- [64] T. YAMAMOTO, *British Ceramic Transactions* **94**, pp. 196–200, 1995.
- [65] S.B. QIN, D. LIU, F.F. ZHENG, Z.Y. ZUO, H. LIU, X.G. XU, *Crystengcomm* **12**, pp. 3003–3007, 2010.

Nanomaterials for Restoration and Conservation of Historical Monuments

Rodica-Mariana ION

ICECHIM, Bucuresti, Romania

Universitatea VALAHIA, Facultatea de Ingineria Materialelor si Mecanica, Targoviste, Romania

E-mail: rodica_ion2000@yahoo.co.uk

Abstract. The nanomaterials are known as consolidating compatible materials that obey the principle of authenticity historical monuments where they are used. In this paper, hydroxyapatite nanoparticles (HAp) as consolidating nanomaterial, is applied to the chalk samples (without historical value) prelevated from Basarabi historical monument. Some physico-chemical (Infrared spectroscopy Fourier-Transformed (FTIR), Dynamic Light Scattering (DLS), differential thermal analysis (DSC), X-ray diffraction (XRD), scanning electron microscopy (SEM), microscopy atomic force (AFM), relative kinetic stability parameter for the chalk samples treated with HAp, and mechanical properties (compressive strength and capillary water uptake test), have been evaluated and discussed, too, for chalk stone and HAp.

1. Introduction

The materials from the architectural monuments are prone to degradation phenomena, aesthetic, and functional. Historical monuments suffer various forms of degradation, the most common being capillary moisture infiltration combined with migration and crystallization of salts, improper works on architecture structure, vibrations caused by blasting, traffic, cracks in the substrate, corresponding dislocations facing and contraction cracks as a fine network of cracks, due to the contraction of unsuitable materials introduced into the original substrate, technical flaws, the inadequate restoration (refurbishment), the phenomenon of freeze-thaw, air pollution in the presence of humidity and temperature variations, technical defects may result to a friable mortar, resulting in a powdery surface of the plaster, not resistant to

mechanical action, deposits adhering impurities (dust, smoke, soot, cobwebs - and adhesion (smoke, tar, bird droppings), due to air pollution, improper maintenance of the monument, soluble efflorescence, poorly soluble or insoluble - are due salts (nitrate, sulfate, chloride, carbonate) which crystallizes in certain conditions of temperature and humidity on architectural surfaces, and not in the last time, degradations due to the action of microorganisms that thrive in conditions of microclimate: humidity, temperature, light, air pollution [1].

Through their superior properties, the nanomaterials, which became most popular and used materials in architecture conservation, show improved mechanical properties due to the small physical size and a large surface area, known for their compatibility as consolidating materials that obey the principle of authenticity historical monuments that were used [2, 3]. Some nanomaterials as Ca and Mg hydroxides or carbonates, have been applied in the conservation of paper, wood and stone [4, 5].

In this paper, it is studied hydroxyapatite nanoparticles powder (HAp) as an alternative to the above-mentioned hydroxides. HAp is applied to the samples (without historical value) taken from Basarabi historical monument - the first medieval religious monument in Dobrogea. Discovered in 1957, the ensemble Basarabi - Murfatlar is one of the most impressive archaeological sites in Europe. Will be analyzed the size and density of the HAp particles by means of Dynamic Light Scattering (DLS), differential thermal analysis in order to determine the glass transition temperature and the crystallization temperature, X -ray diffraction (XRD) and scanning electron microscopy (SEM) and microscopy atomic force (AFM) to identify the phases and microstructures present. Also, the petrographic and physico -chemical (X-ray fluorescence energy dispersive (EDXRF), relative kinetic stability parameter for chalk samples treated with hydroxyapatite compared to those treated $\text{Ca}(\text{OH})_2$ and $\text{Mg}(\text{OH})_2$, are discussed in this paper. Mechanical properties as compressive strength and capillary water uptake test, have been evaluated and discussed, treated as shown above.

2. Experimental Part

Specimens Samples Preparation

The samples prelevated from Basarabi Church (samples collected from the exterior of the monument, without any value for this church. Samples were obtained by taking a minimum part of the archaeological object, with the aid of a scalpel with diamond tip, to minimize any damage and contamination. Being detached from the Church's wall, all the samples, have the same constitution as the wall and the same composition.

Consolidants

Hydroxyapatite was obtained by chemical precipitation method from calcium nitrate tetrahydrate $\text{Ca}(\text{NO}_3)_2 \cdot 4\text{H}_2\text{O}$ and dibasic ammonium phosphate $(\text{NH}_4)_2\text{HPO}_4$, at room temperature [6]. The powder was dry mortar in a mortar and pestle and then calcined in alumina crucible at 1200°C for 1h.

Application of Consolidants

The application of all types of consolidant was carried out by spraying, 5 times. After the each treatment the samples were covered for one day by a slightly opened cover to avoid quick evaporation of solvent. Next day the cover was removed and the specimens were exposed to laboratory conditions to get dry. The following application cycle was done when the specimens became completely dry. After drying the specimens were obviously covered by white layer of nanomaterial suspension.

Characterization Techniques

The samples were analyzed by using the following techniques:

Ion Chromatography, performed on a DIONEX DX-500 Chromatograph, was used to identify the soluble salts as cations and anions present in the samples. The eluent was sodium carbonate and sodium bicarbonate with a flow rate of 2 ml/min, and a 4 mm column for the separation of anions.

The diffraction analysis has been carried out in a DRON UM1 diffractometer using an iron filter for the CoK_α radiation (1.79021\AA) and also, with a XRD, Philips Diffractometer PW 1840, 40kV/20mA, $\text{Cu K}\alpha$ radiation).

DSC was performed on a Mettler-Toledo Instrument DSC 823^o. Samples (1-2 mg) were loaded into sealed aluminum pans with lids and heated to 600°C at a heating rate of $10^\circ\text{C min}^{-1}$ in oxygen flux (100 ml min^{-1}).

The phases were also characterized by **Fourier transformed infrared spectroscopy** (FT-IR, Perkin-Elmer Spectrum One FT-IR Spectrometer), using the KBr pellets method.

For evaluating the effectiveness of the consolidating treatments, the **relative kinetic stability** of the dispersion of nanomaterials, was defined as ξ , which is calculated after [7].

The particles size and theirs size distribution have been measured by **Dynamic Light Scattering** (DLS) technique.

Scanning electron microscopy (SEM) produces high resolution images of a sample surface. The Quanta 200 Scanning Electron Microscope (SEM) was used to

produce enlarged images of a variety of specimens, achieving magnifications of over 100000x providing high resolution imaging in a digital format.

Atomic force microscopy (AFM) investigations were carried out with an Agilent 5500 SPM system, described by PicoSPM controlled by a MAC Mode module and interfaced with a PicoScan controller from Agilent Technologies, Tempe, AZ, USA (formally Molecular Imaging). The original images for the samples, the 3D topographical images and section analysis over the articles were performed using the PicoView SPM Software, version 1.6.2, Molecular Imaging. Height image data obtained by the AFM is three-dimensional.

The conservation efficiency of the consolidant was estimated:

- by compressive strength, with Silver Schmidt Hammer L, with a compressive range 5-30 N/mm² and 0.735 Nmm impact energy (EN 12 504-2).
- by capillary water uptake tests, determined according to the method according to EN ISO 15148 .

3. Results and Discussion

Stone Characterization

Stone materials are characterized by a mineral-inorganic nature, and by hydrophilic properties, both these aspects being very important when choosing the treatments for their conservation. Two main causes for stone deterioration have to be mentioned: acid attack (caused by rains and humidity condense in polluted urban atmospheres) and soluble salts cyclic crystallization [8]. The first mechanism (acids) induces corrosion to carbonatic materials such as calcium and/or magnesium carbonates based stones while silicatic stones are only poorly affected. The second mechanism (salts) is mainly active towards porous stones, independently of their nature. Also, important is the effect on low porosity stones. This is important for the consolidation of natural stone such as limestone, marble or sandstone as well as for mortar and plaster [9].

It should take into account that decay agents can reach the surface both from outside (acid attack and salts deposits) and inside (soluble salts), in case of porous materials [10]. Some studies on environmental influences on degradation stone monuments, considering the factors such as temperature (average, minimum, maximum), number of days of frost and sunny days, humidity annual average rainfall amount and chemical composition, currents air, will be evaluated, too, knowing that carbonates have been detected as the predominant in the body of the church with sulphates impurities [11].

Usually, calcium carbonate is occurring as limestone, chalk and biomaterials. It is known that some nonaqueous dispersions of calcium, barium or magnesium hydroxide nanoparticles started to be tested and used as new possible consolidants for calcareous

material [12]. Gypsum is, as lime, one of the important component used as binder alone or together with lime for the production of plaster and mortars [13,14]. In order to evaluate the efficiency of the new treatment method, based on nanomaterials, first of all the characteristics of the substrates and chalk wall, have been evaluated.

Many literature sources rank magnesium sulfate among the most damaging salts [15] The alteration of stone is a natural and irreversible process. Crystallization of soluble salts in the construction materials, is considered today one of the most important decay process. These soluble salts induce the rock fabric, when efflorescence appear, especially, and induce crystallization within the pores causing the stone damage. All the damage processes from the stone surface is due to high level of sulphates, chlorides, nitrates, detected by ion chromatography and Ca, Na, K and Mg. Deterioration of mortar can be rarely attributed to the presence of only one salt. The most abundant salts are chlorides, sulphates or nitrates, of calcium, sodium, potassium, magnesium and sometimes also ammonium cations. Source of chlorides are usually deicing agents, nitrates are of organic origin. Sulphates are usually rising from groundwater but may be also a product of calcium carbonate corrosion reaction with sulphur oxides. By ICP-MS all the metals constituents of the chalk sample, have been identified, Table 1.

Table 1. The metal composition of the chalk stone sample [20].

Metal	Concentration (ppm)	Metal	Concentration (ppm)
Ti	75.19	Cu	42.69
Sr	857.69	K	2600
Ba	136.92	Al	8100
Mn	272.115	Fe	4800
Bi	191.69	Mg	2300
Sn	152.115	Na	8600
Si	14400	Li	34.61
Ca	241200	Zr	10.77

Divalent metal ions of similar ionic radius as Ca^{2+} may be incorporated as impurities into calcite during mineral precipitation. In agreement with the literature data, these results indicate the presence of Sr, which is favouring the calcite stability by precipitation/adsorption of SrCO_3 and the dissolution of CaCO_3 is occurring at these sites [16]. On the other hand, Gutjahr and co-workers have shown that Sr^{2+} causes a significant reduction in the growth and dissolution rates of aragonite. This was

attributed to reversible adsorption of Sr^{2+} ions at growth sites (kinks) [17]. Cu^{2+} and Zn^{2+} could form soluble oxides and carbonated over the calcite surface [18].

Magnesium sulfate tends to precipitate within a wider crystallization front and in pores of different size, while sodium sulfate is mainly concentrated close to the surface and in large pores. The goal of the DSC experiments was to determine the composition of the salt mixture that forms by drying a magnesium sulfate solution [19-21]. By DSC techniques is important to detect the soluble salts arising from the degradation, because the soluble salts are usually hydrated, so they undergo changes at low temperatures, less than 100°C , Figure 1. Hydrated or anhydrous Mg and Na sulphates are visible in all chalk samples.

Table 2. Decomposition temperature of the salts which appear as products of the monument chalk stone

Soluble salts/ $T(^{\circ}\text{C})$	Phase transition
Na_2SO_4	275
$\text{Na}_2\text{SO}_4 \cdot 10\text{H}_2\text{O}$	90; 271
K_2SO_4	583
MgSO_4	352
$\text{MgSO}_4 \cdot 7\text{H}_2\text{O}$	135; 200; 360
$\text{MgSO}_4 \cdot 6\text{H}_2\text{O}$	110; 156; 200; 275; 360
$\text{MgSO}_4 \cdot \text{H}_2\text{O}$	345
$(\text{NH}_4)_2\text{SO}_4$	355
KNO_3	133

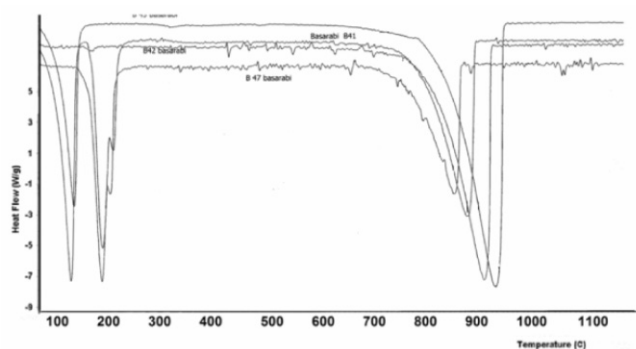


Fig. 1. The DSC diagrammes for different church walls (left ordinate, mg; right ordinate, mg/Celsius degree). [B41 = stone dislocated from inside West wall; B42 = wall efflorescence dislocated from the inside wall surface; B45 = wall sample from inside East wall; B47 = dust from the dome surface].

The FTIR spectra of HAp put into evidence the specific absorption bands:

- two bands at 3432cm^{-1} and 622cm^{-1} due to the stretching mode of hydrogen-bonded OH- ions and hydrogen-bonded OH- ions, respectively
- the bands from $600\text{-}601\text{cm}^{-1}$ and 571cm^{-1} , 1090cm^{-1} , $1050\text{-}1044\text{cm}^{-1}$ arises from $-\text{PO}_4^{3-}$,
- the bands at 632cm^{-1} attributed to OH- group.

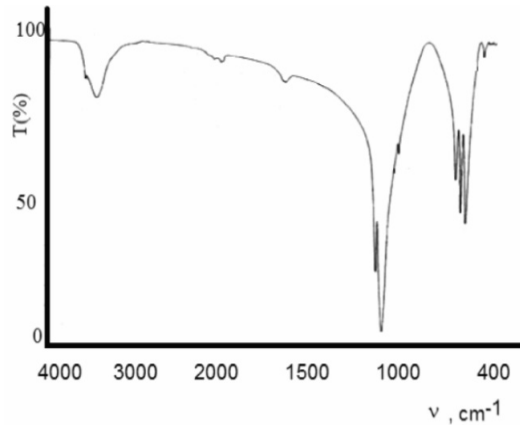


Fig. 2. FTIR spectrum of HAp.

The SEM images put into evidence the crystalites and only few spherical agglomerations of $0.1\mu\text{m}$, Fig. 3.

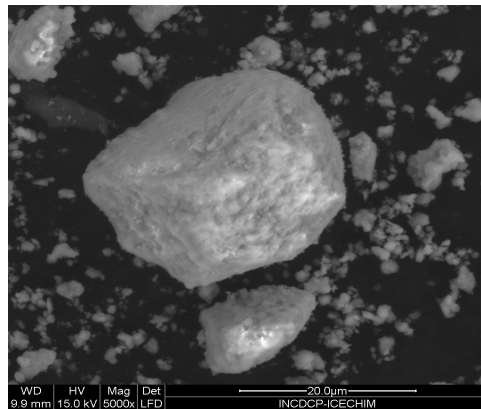


Fig. 3. SEM of HAp.

From AFM topography is easy to observe a good distribution around 100 nm, Fig. 4.

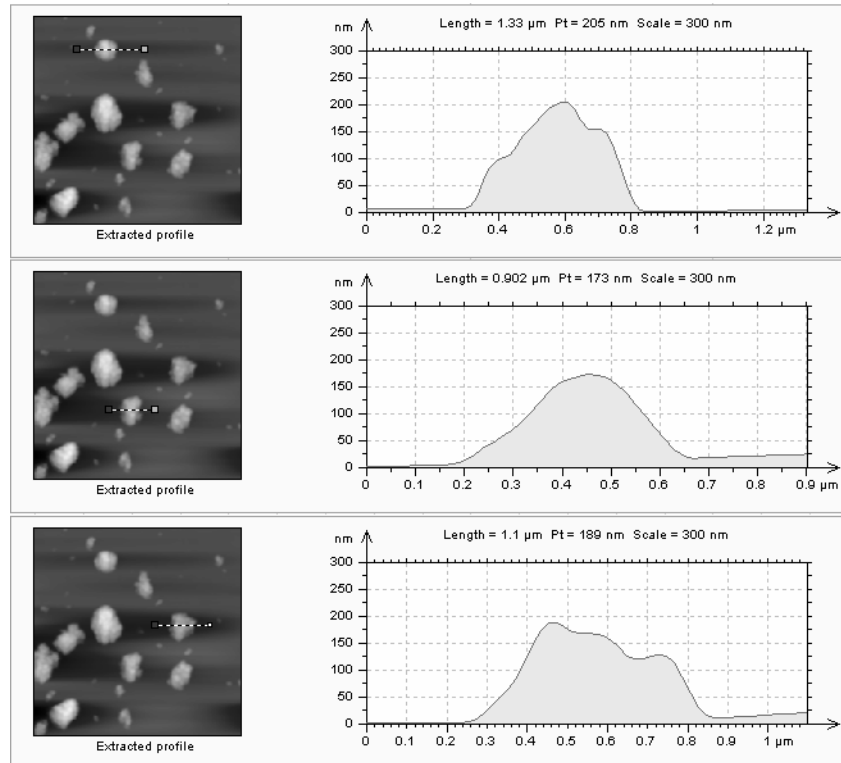


Fig. 4. AFM for Hap.

Consolidation Options

Nanotechnology applied to building materials represents an example of nanotechnologies application based on the design of material properties in order to obtain the increased performances, developing new products for specific architectural applications. Historically, limestone objects, lime-based renders and wall paintings have been treated with solutions that resulted ultimately in the deposition of calcium carbonate [22]. A saturated solution of calcium hydroxide in water was one of the earliest treatments for building materials and was well documented in the classical literature by authors such as Vitruvius (c. 70-25 BC) [23,24]. For chalk consolidation, HAP has been used, due to the similarities with calcite of the lattice parameters, Table 3.

Table 3. Lattice parameters of calcite and calcium hydroxide [14]

Mineral	a (Å)	b (Å)	c (Å)
Calcite	9.98	9.98	33.82
Hydroxyapatite	9.45	9.44	6.90

In order to avoid the long time of consolidation, a new nanomaterial has been used, selected from its similarity of lattice parameters with those of calcite and proper to consolidate carbonate stones [25]. The relative kinetic stability of HAp has a low value (30 nm, Fig. 5), by comparison with calcium hydroxide which has a bigger size (408.9 nm), Figs. 6.

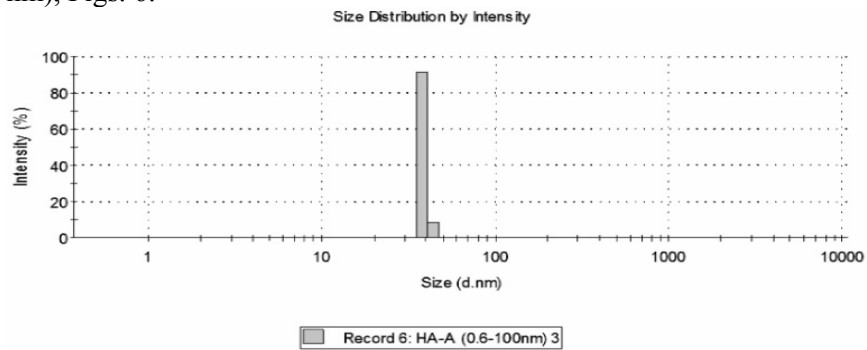


Fig. 5. Size distribution for HAp nanoparticles dispersed in 2-propanol.

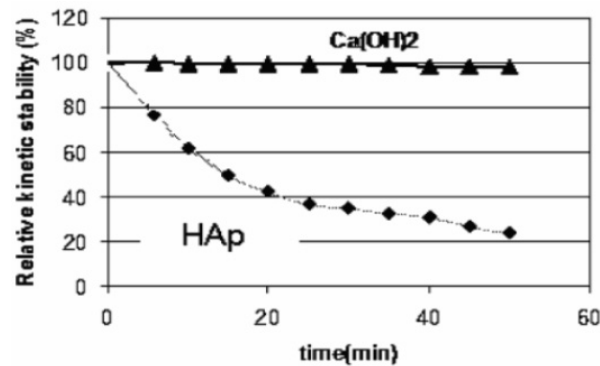


Fig. 6. The relative kinetic stability of nanomaterials.

Scanning electron microscopy research was performed to investigate microstructure characteristic of the samples, Fig. 7. An encapsulation and covering of acicular chalk

crystals with size around 8 microns could be observed, and also, is visible a good consolidation capacity.

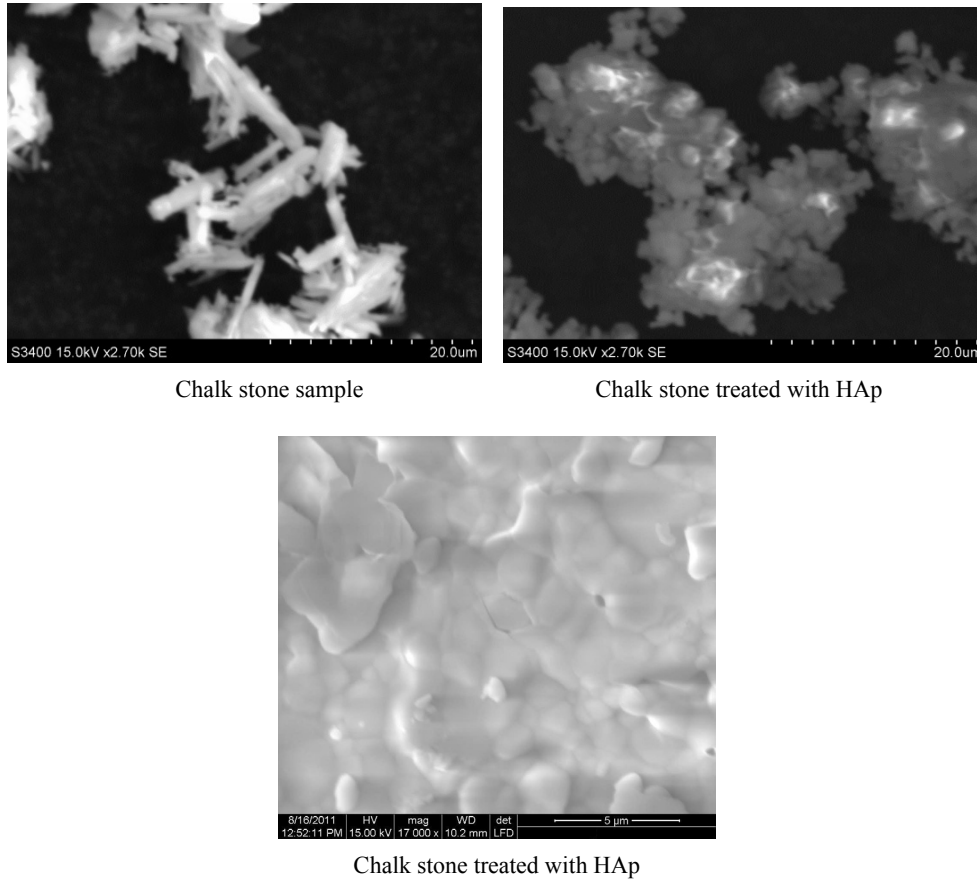


Fig. 7. SEM of chalk stone, HAp and chalk treated with HAp.

Similar results have been obtained by AFM, Figs. 8. AFM revealed a rough surface architecture for HAp, the predominant size of grains being in the range of 90-100nm. The light part of the image can be the consequence of the presence of a thick part of sizing material, possibly to an aggregate form [27]. By spraying on a cubic piece, whiter colour is evident, Fig. 9.

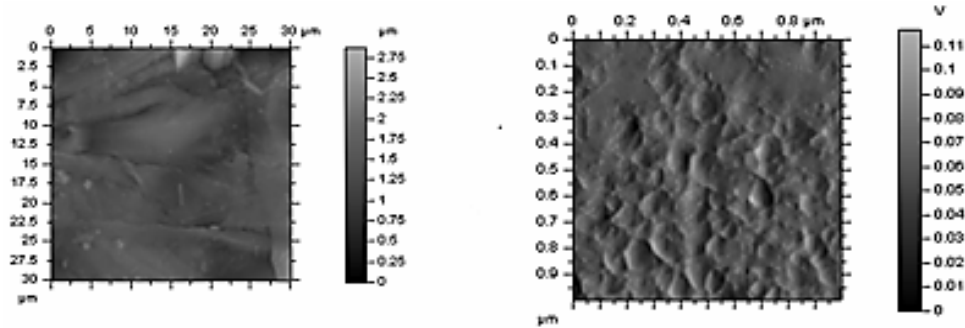


Fig. 8. AFM image of $\text{Ca}(\text{OH})_2$ on chalk surface (left), and HAp on chalk surface (right).

Three specimens of cube shape ($4 \times 4 \times 4 \text{ cm}^3$) of chalk samples were used for measurement. Before testing, all samples were dried up to constant weight at 80°C in a drying chamber for 24 hours. After the drying process the substrates were left to get cold for two hours in a dessicator and their aspect was measured, Fig. 9. Despite of its relatively low stability, HAp is uniform layer, and induce a high white colour of the treated surface.

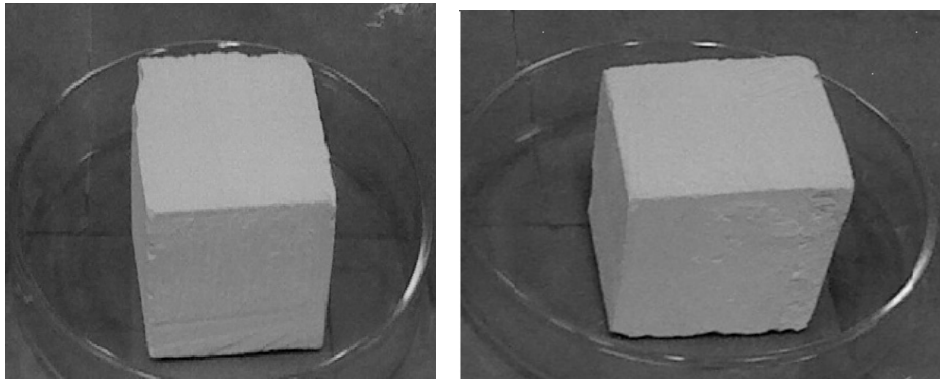


Fig. 9. The aspect of chalk sample before (left) and after treatment (right) with nanomaterial HAp.

For the chalk samples, the compressive strength determined with Silver-Schmidt Hammer, indicated that the most effective treated sample has a compressive strength of 40 MPa and is that treated with $\text{Ca}(\text{OH})_2$. In the case of $\text{Ca}(\text{OH})_2$, we have to take into account the non-uniform thickness of the consolidant, due to the aggregation tendency of $\text{Ca}(\text{OH})_2$. The results are shown in Table 4. For the chalk samples, the treatment with $\text{Ca}(\text{OH})_2$ do not cause any increase in cohesion, rather a decrease. Also, to explain the

low values obtained with HAp, we should take into account the considerable moisture from this area, which lowered the average value of compressive strength of this area.

Table 4. Mechanical tests for the studied samples

Sample	Treatment	Compressive strength (Silver Schmidt) (MPa)(5 mm)	Water absorbed (cc/cm ² s)
Chalk sample	Not treated	20±3.2	2.22±0.10
	Ca(OH) ₂	40±2.3	2.25±0.22
	HAp	25±2.5	2.05±0.084

The capillary water uptake of the test blocks is decreased after the treatment with consolidants, concluding that the treatment makes the stone samples more compact and less permeable to water, Table 4. Low capillary action can protect the stone against erosion by water and soluble salts or bases [28]. The area treated with Ca(OH)₂ shows an absorption capacity bigger to the untreated zone. A possible explanation of this behaviour is the inhomogeneity of the chalk and the high capacity of Ca(OH)₂ to aggregate.

4. Conclusions

In this paper has been treated the structural, morphological and compositional aspects of chalk stone sample prelevated from Basarabi Chalk Church (Romania), for which a new restoration method based on nanoparticles HAp has been tested. A complex collection of analytical techniques DLS, SEM, AFM, DSC, XRD, ξ , have been used in order to identify the major constituents of chalk stone, useful for subsequently method of restoration. The mechanical parameter compressive strength and capillary water uptake, concluded the efficiency of HAp by comparison with Ca(OH)₂.

Acknowledgements. This work was supported by a grant of the Romanian National Authority for Scientific Research, CNDS-UEFISCDI, project number 222/2012.

References

- [1] J. ASHURST, *Conservations of ruins*, Oxford: Elsevier/Butterworth-Heinemann, pp. 3-9, 2007.
- [2] G. ZIEGENBALG, „*Colloidal calcium hydroxide: A New Material for Consolidation and Conservation of Carbonatic Stones*”, 11th International Congress on Deterioration and Conservation of Stone, Torun, Poland, pp. 1109–1115, 2008.

- [3] G. ZIEGENBALG, K. BRÜMMER and J. PIANSKI, „Nano-Lime - a New Material for the Consolidation and Conservation of Historic Mortars”, 2nd Historic Mortars Conference HMC2010 and RILEM TC 203-RHM Final Workshop, Prague, Czech Republic, pp. 1301–1309, 2010.
- [4] S.M. DONCEA, R.M. ION, R.C. FIERASCU, E. BACALUM, A.A. BUNACIU and H.Y. ABOUL-ENEIN, „Spectral methods for historical paper analysis: composition and age approximation”, *Instrum Sci Technol.*, **38**, pp. 96–106, 2009.
- [5] R.M. ION, S.M. DONCEA, M. L. ION, V. RĂDIȚOIU, V. AMĂRIUȚEI, „Surface investigations of old book paper treated with hydroxyapatite nanoparticles”, *Applied Surface Science*, **285A**, pp. 27–32, 2013.
- [6] A.A. POINESCU, R.M. ION, R.I. VAN STADEN, J.F. VAN STADEN, M. GHIUREA, „Different microscopic characterization techniques on hydroxyapatite powder”, *Journal of Optoelectronics and Advanced Materials*, **13**(4), pp. 416–421, 2011.
- [7] G. GABRIELLI, F. CANTALE and G.G.T. GUARINI, „Adsorption of amphiphilic mixtures and stabilization of suspension of hydrophobic solids in water”, *Colloid Surface* **A119**, pp. 163–174, 1996.
- [8] E. BORRELLI, „Conservation of Architectural Heritage, Historic structures and materials: ARC Laboratory handbook. **3**, ICCROM, pp. 5–7. 1988.
- [9] B.L. CLARKE and J. ASHURST, „Stone Preservation Experiments”, Building Research Establishment, , pp. 78, 1972.
- [10] G. CULTRONE, E. SEBASTIÁN and M. ORTEGA HUERTAS, „Forced and natural carbonation of lime-based mortars with and without additives: Mineralogical and textural changes”, *Cement and Concrete Research.*, **35**, pp. 2278–2289, 2005.
- [11] S.Z. LEWIN, „The Preservation of Natural Stone”, *Art and Archaeology Technical Abstracts*, **6**(1), pp. 185–188, 1966.
- [12] F. LIPMANN, „Sedimentary Carbonate Minerals”, Springer Verlag, Berlin, 1973.
- [13] CA. PRICE, „Stone Conservation: An Overview of Current Research.”, Getty conservation Institute., pp. 73, 1996.
- [14] A. GOUDIE, R. COOKE and A. EVANS, „Experimental investigation of rock weathering by salts”, *Area*, **2**, pp. 42–48, 1970.
- [15] A.E. CHAROLA, “Salts in the Deterioration of Porous Materials: An Overview”, *J. American Institute for Conservation (JAIC)*, **39**(3), pp. 327–343, 2000.
- [16] R.M. ION, I.R. BUNGHEZ, S.F. POP, R.C. FIERASCU, M.L. ION and M. LEAHU, „Chemical Weathering of chalk stone materials from Basarbi Churches”, *Metalurgia International.*, **2**, pp. 89–93, 2013.
- [17] A. GUTJAHR, H. DABRINGHAUS and R. LACMANN, „Studies of the growth and dissolution kinetics of the CaCO₃ polymorphs calcite and aragonite II. The influence of divalent cation additives on the growth and dissolution rates”, *Journal of Crystal Growth*. **158**, pp. 310–315, 1996.
- [18] C.A. PRICE, „The use of the sodium sulphate crystallization test for determining the weathering resistance of untreated stone”, *Proc. Int. Symp. On the Deterioration and Protection of Stone Monuments*, Paris, pp. 23, 1978.
- [19] S.F. POP, R.M. ION, „Thermal analysis of the chemical weathering of chalk stone materials”, *Journal of Optoelectronics and Advanced Materials*, **15**(7-8), pp. 888–892, 2013.
- [20] R.M. ION, R.C. FIERASCU, M. LEAHU, M.L. ION, D. TURCANU-CARUTIU, „Nanomaterials for conservation and preservation of historical monuments”, *Proc. EWCHP*, pp. 97–104, 2013.

- [21] BARCINA, L.M. ESPINA, A. SUFIREZ, M. GARCIA, J.R., RODRIGUEZ, J. Characterization of monumental carbonate stones by thermal analysis (TG, DTG and DSC), *Thermochimica Acta* **290**, pp. 181–189, 1971.
- [22] E. RUIZ-AGUDO, F. MEES, P. JACOBS, C. RODRIGUEZ-NAVARRO, „*The role of saline solution properties on porous limestone salt weathering by magnesium and sodium sulfates*”, *Environ Geol* **52**, pp. 269–281, 2007.
- [23] Vitruvius, Pollio, *Vitruvius On Architecture*, trans. F.Granger, Harvard University Press, Cambridge, 1970.
- [24] M. DRDÁČKÝ, Z. SLÍŽKOVÁ, and G. ZIEGENBALG, „*A Nano Approach to Consolidation of Degraded Historic Lime Mortars*”, *Journal of Nano Research.*, **8**, pp. 13–22, 2009.
- [25] E. CANER, E.N. CANER-SALTIK, G. ORIAL and J.D. MERTZ, „*Deterioration Mechanisms of Historic Limestone and Development of Its Conservation Treatments with Nanodispersive Ca(OH)₂ Solutions*”, 8th International Symposium on the Conservation of Monuments in the Mediterranean Basin, Book of Abstracts, Ed. M.Koui, F. Zezza, National Technical University of Athens, pp. 183, 2010.
- [26] E. CANER, E.N. CANER-SALTIK, G. ORIAL and J.D. MERTZ, „*Deterioration Mechanisms of Historic Limestone and Development of Its Conservation Treatments with Nanodispersive Ca(OH)₂ Solutions*”, 8th International Symposium on the Conservation of Monuments in the Mediterranean Basin, Book of Abstracts, Ed. M.Koui, F. Zezza, National Technical University of Athens, pp.183, 2010.
- [27] L. DEI and B. SALVADORI, „*Nanotechnology in cultural heritage conservation: nanometric slaked lime saves architectonic and artistic surfaces from decay*”, *Journal of Cultural Heritage*, **7**, pp. 110-115, 2006.
- [28] A.S. LEA, J.E. AMONETTE, D.R. BAER, Y. LIANG and N.G. COLTON, „*Microscopic Effects of Carbonate, Manganese and Strontium Ions on Calcite Dissolution*”, *Geochim. Cosmochim. Acta* **65**, pp. 369–379, 2001.

Nanoscale Diodes Without p-n Junctions

Mircea DRAGOMAN

National Institute for Research and Development in Microtechnology (IMT),
P.O. Box 38-160, 023573 Bucharest, Romania
E-mail: mircea.dragoman@imt.ro

Abstract. The *p-n* junction cannot be implemented at the nanoscale because the doping is very often a detrimental effect. The doping could change dramatically the properties of a nanomaterial such as graphene or single-walled carbon nanotubes. Therefore, we will present two graphene diodes without a *p-n* junction. The first is based on the dissimilar metals having workfunction below and above the graphene workfunction and playing the role of a Schottky diode. The second diode is a ballistic graphene diode having a trapezoidal-shape where the rectification is achieved only by the geometry of the device.

1. Graphene Schottky Diodes Based on Graphene

The Schottky diode is the second electronic device as importance after transistors. The Schottky diodes due to their abrupt nonlinear I - V characteristics are used in any electronic circuit where nonlinearities are needed *i.e.* in multipliers, mixers, detectors. Schottky diodes are well-known in semiconductors where metal such as Mo, Pt, or Au or metallic alloys and a semiconductor (*e.g.* Si, GaAs), are producing a Schottky barrier [1]. When new nanomaterials have attained a certain degree of maturity new Schottky diodes were developed using nanoparticles, nanowires, and nanotubes. Also geometrical diode via carving parallel channels in 2DEG devices are used to detect THz waves at room temperature [2].

In principle, the CNT Schottky diodes are implemented with the help of asymmetric contacts [3] and this principle is used even to diodes operating at THz frequencies[4]. However, the impedance of a single CNT is greater than 6.5 k Ω which is a huge mismatch since 50 Ω is used for RF instrumentation. This is a problem for all nanomaterials enumerated above and there are not straightway methods to solve this. In the case of CNTs, many parallel CNTs could reach 50 Ω , but the process is not fully reproducible.

The aim of this first part of the paper is to use the metal contact asymmetry for a Schottky diode based on a graphene monolayer. The work is motivated by the previous work on Schottky diodes graphene displaying poor performances *i.e.* the current does not exceed more than 100-200 μA and poor high frequency performances.[5], [6].

Our graphene diode is fabricated using a coplanar line (CPW), where the central conductor is the central conductor and the outer electrodes are grounds.

The Schottky diodes formed by dissimilar electrodes were deposited on a graphene monolayer which is deposited on Si/SiO₂. We have used a high-resistivity Si substrate, with resistivity greater than 8 k Ω , which has on the top a 300 nm of SiO₂ thermally deposited. Outside Schottky diode area, RF pads were patterned on SiO₂. Fig. 1 is a SEM of our Schottky diode:

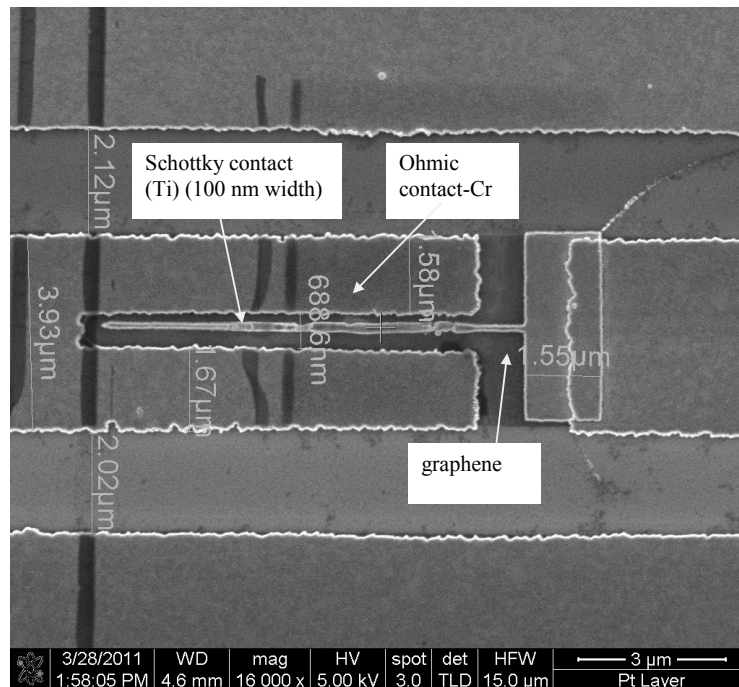


Fig. 1. The Schottky diode (from [7]).

We see that that the central conductor is formed by the two dissimilar electrodes on graphene. The fabrication which implies the utilization of e-beam lithography several times to define in PMMA first the Cr electrodes and then the Ti electrodes, is described in [7]. However, a typical technological flow scheme of fabricating graphene device is depicted in Fig. 2 In the case of the above diode the technological flow scheme is repeated two times for each metal.

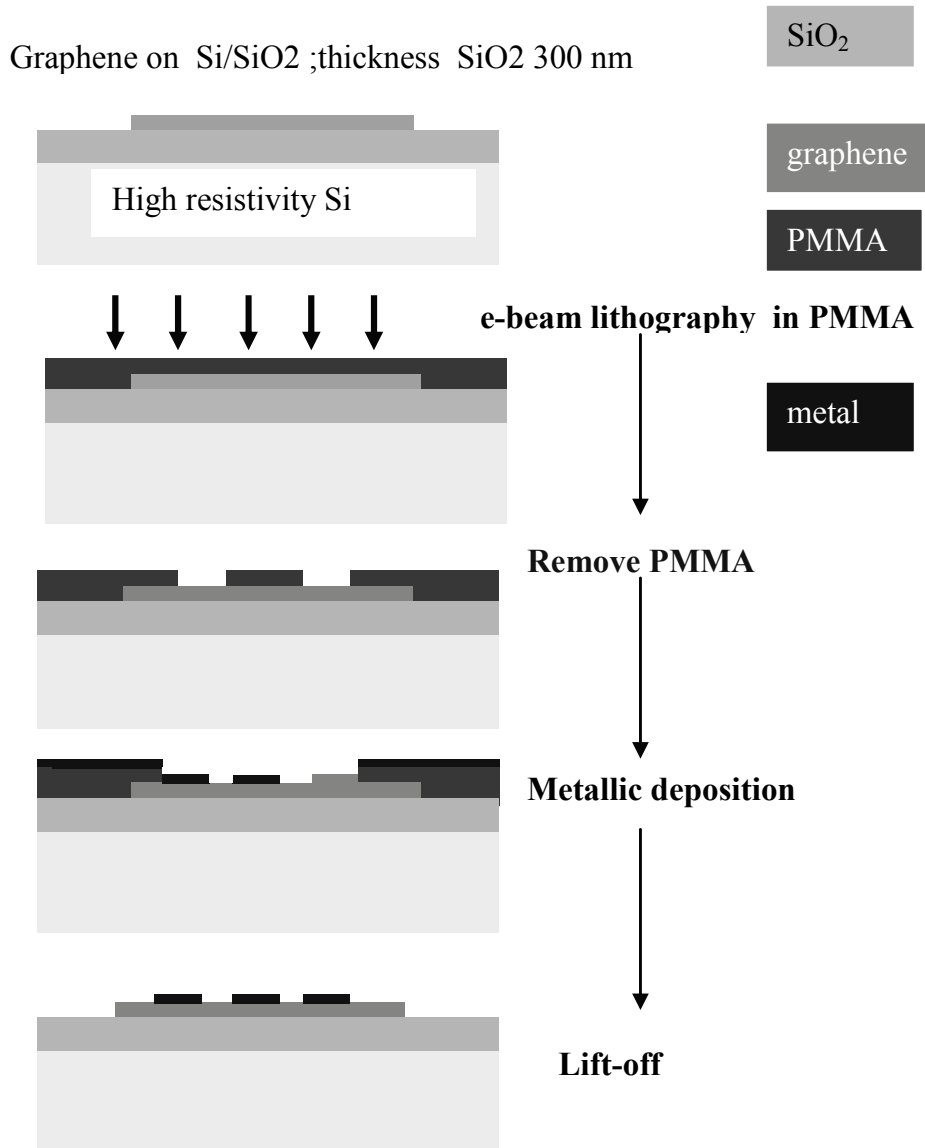


Fig. 2. The typical technological scheme for fabrication RF graphene devices.

In the following table we show the metals which are resistive or make a Schottky contact on graphene taking into account that the graphene workfunction is around -4.5 eV.

Table 1.

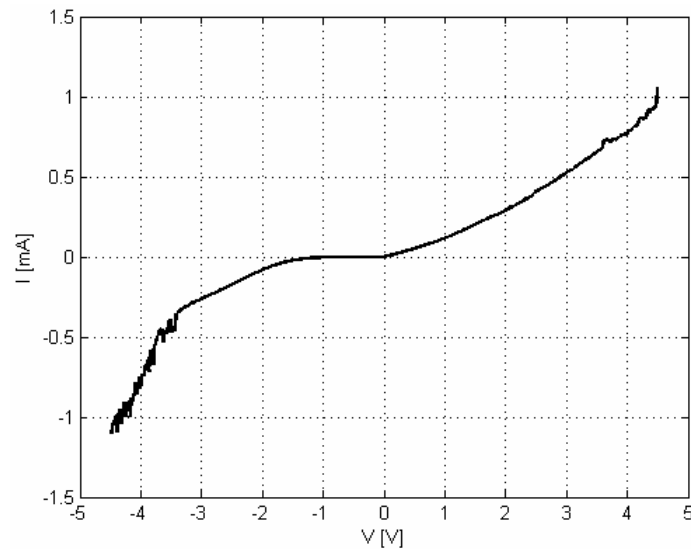
Schottky contact:

Metal	Work function (eV)
Al	-4.27 eV
Ti	-4.33 eV

Ohmic contact:

Metal	Work function (eV)
Pd	-5.12 eV
Cr	-4.5 eV

This Ti/Cr Schottky diode on graphene based on dissimilar metallic contact has an I-V dependence represented in Fig. 3.

**Fig. 3.** The I-V dependence of graphene Schottky [7].

We see that in Fig. 3 all the characteristics of a Schottky diode *i.e.*(i) a rectifying region where the current is very low and two conduction regions. In the positive bias region we see that the current is increasing very fast and at 4.5 V we have 1 mA. We have measured the all the S parameters of the diode in the range 0.04 -65 GHz. Based on them we have elaborated an equivalent circuit represented in Fig. 4.

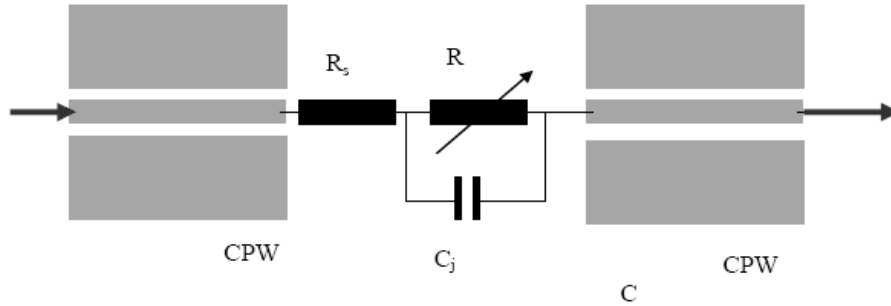


Fig. 4. Equivalent circuit model.

Based on DC and microwave measurement we have extracted the parameters of the diode *i.e.* the series resistance R_s and the junction capacitance, C_j and having the following values:

Table 2.

Bias voltage (V)	RS [Ω]	CJ [fF]
0V	60	3.5
1V	60	3.5
2V	60	3.5
3V	60	3.5
4V	60	3.5

These values allow us to calculate the conversion loss of a graphene mixer with two antiparallel Schottky diodes (see Fig. 5):

$$CL(dB) = 3.9 + 1.7 f / f_c + 9R_s / Z_0$$

At 10 GHz and $Z_0 = 100 \Omega$ we have a CL of 9.2 dB.

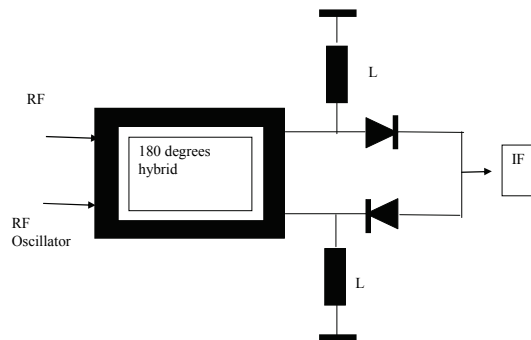


Fig. 5. A graphene Schottky mixer.

This approach has emerged after various works based on graphene FET resistive mixers. Here the drain-source resistance ratio $R_{ds}(\max)/R_{ds}(V_g=0)$ must be greater than 10 which is difficult to be obtained even when nanoindentations are done in the graphene channel.[8]. The reason is that graphene monolayers have no bandgap. Moreover, these nanoindentations mean a lot of work using e-beam nanolithography and the results are hardly reproducible, So, a graphene bilayer will be more suitable, but here very high dc fields are applied to open the gap which could destroy the entire transistor.

2. A ballistic Graphene Diode on Graphene

A geometric diode is a diode which rectifies signals only due its shape. Such a diode is represented in Fig. 6.

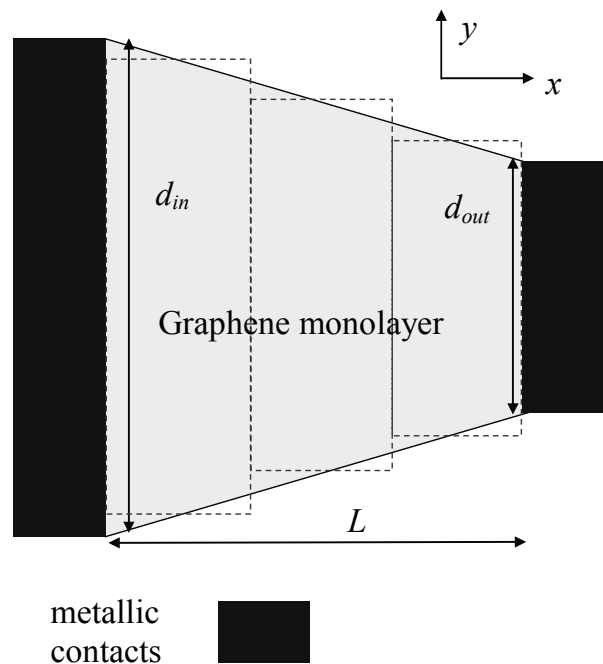


Fig. 6. A geometric diode on graphene.

The graphene diode is designed to have a ballistic transport. The theory of this diode is explained in [9], while in [10] it is described the fabrication on a graphene monolayer wafer. The length of the diode is 100 nm while the graphene monolayer has a mean-free-path at room temperature of 300-400 nm. The diode shoulder is also 100 nm while its neck is only 30 nm. The diode is represented in Fig. 7.

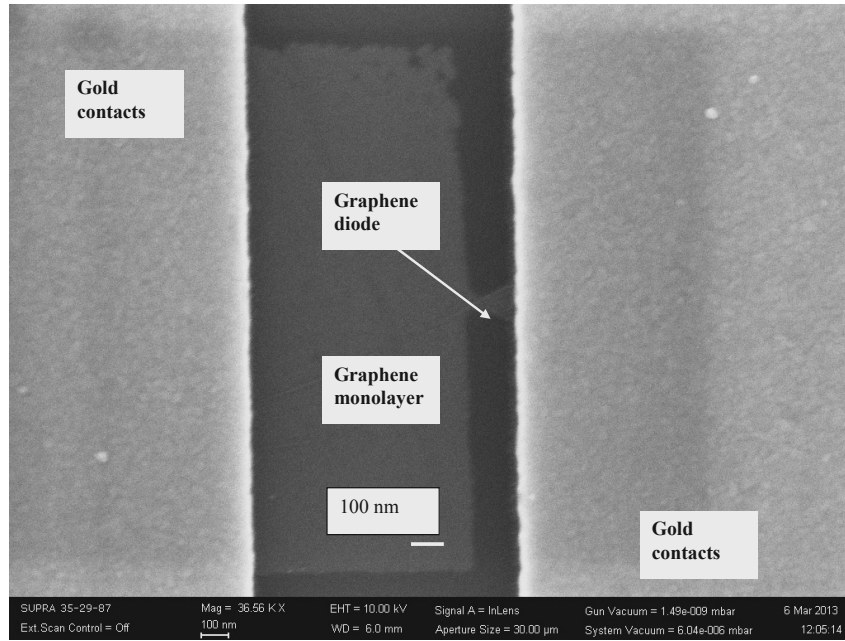


Fig. 7. The graphene geometric diode (SEM) [10].

The I-V characteristics of the diode is represented in Fig. 8

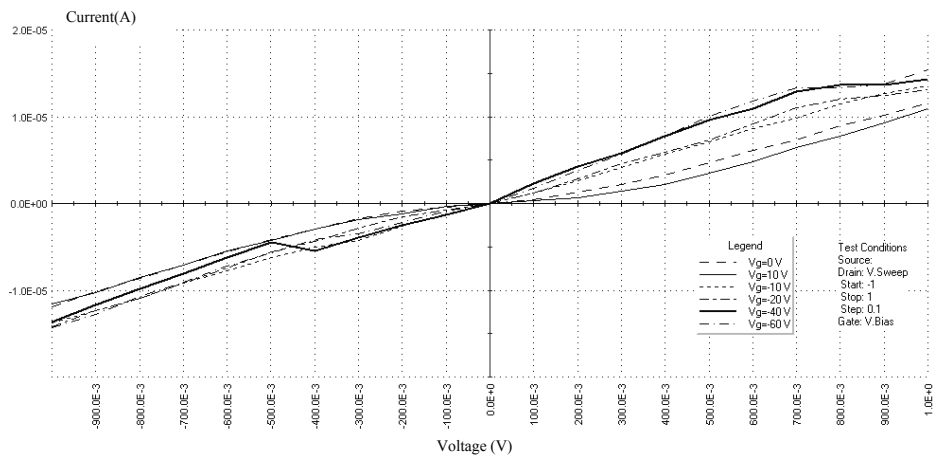


Fig. 8. The I-V dependence of the geometric diode

The diode was measured using a Keithley 4200 SCS we can see that at small back -gate voltages (-10 – -30V), a zero current region of about 0.7 V is present However, at the high back-gate voltages of -60 V, there are too many electrons and

the ballistic transport is lost. Therefore, the zero current region is vanishing and we see a linear dependence of I - V followed by a current saturation. The cutoff frequency of these diode is about 15 THz.

3. Conclusions

We have reported two different types of graphene diodes which are junctionless. Both shows good performances and work at high frequencies.

Acknowledgements. I would like to thank to many scientists which helped me in the quest in the area of carbon nanoelectronics, most of them being co-authors of many papers published in the last period of time. My wife Daniela has helped me with her deep knowledge in the area of quantum mechanics , solid state physics and graphene physics. My colleagues from IMT Bucharest (Alex Muller, Dan Neculoiu, Adrian Dinescu, Alina Cismaru, Antonio Radoi,), Dr. George Konstantinidis from FORTH Heraklion, Dr. George Deligeorgis from LAAS. This work was supported by a grant of Romanian National Authority for Scientific Research, CNCS-UEFISCDI, project number PN-II-ID-PCE-2011-3-0071, and the the European Commission for the financial support via the FP 7 NANO RF (grant agreement 318352).

References

- [1] S.M. SZE, Kwok K. NG, *Physics of Semiconductor Devices*, Wiley 2006.
- [2] C. BALOCCO, S.R. KASJOO, X.F. LU, L.Q. ZHANG, Y. ALIMI, S. WINNERL and M. SONG, “*Room-temperature operation of a unipolar nanodiode at terahertz frequencies*”, *Appl. Phys. Lett.* **98**, 223501, 2011.
- [3] H.M. MANOHARA, E.W. WONG, E. SCHLECHT, B.D. HUNT and P.H. SIEGEL, “*Carbon Nanotube Schottky Diodes Using Ti–Schottky and Pt–Ohmic Contacts for High Frequency Applications*”, *Nano Lett.* **5**(7), pp. 1469–1474, 2005.
- [4] C. LU, L. AN, Q. FU and J. LIU, “*Schottky diodes from asymmetric metal-nanotube contacts*”, *Appl. Phys. Lett.* **88**, pp. 133501, 2006.
- [5] C.-C. CHEN, M. AYKOL, C.-C. CHANG, A.F.J. LEVI and S.B. CRONIN, “*Graphene-silicon Schottky diode*”, *Nano Lett.* **11**, pp. 1863, 2011.
- [6] M.R. ISLAM, D. JOUNG and S.I. KHONDAKER, “*Schottky diode via dielectrophoretic assembly of reduced graphene oxide sheets between dissimilar metal contacts*”, *New J. Phys.* **13**, pp. 035021, 2011.
- [7] M. DRAGOMAN, G. DELIGEORGIS, A. MULLER, A. CIMARU, D. NECULOIU, G. KONSTANTINIDIS, D. DRAGOMAN, A. DINESCU and F. COMANESCU, “*Millimeter wave Schottky diode on graphene monolayer via symmetric metal contacts*”, *J. Appl. Phys.* **112**, pp. 084302, 2012.
- [8] O. HABIBPO J. VUKUSIC, J. STAKE, “*A 30-GHz Integrated Subharmonic Mixer based on a multichannel graphene FET*”, *IEEE MTT*, pp. 841–847, 2013.
- [9] D. DRAGOMAN, M. DRAGOMAN, “*Geometrically induced rectification in two-dimensional ballistic nanodevices*”, *J. Phys.* **D46**, pp. 055306 9, 2013.

- [10] M. DRAGOMAN, A. DINESCU, D. DRAGOMAN, “*On-Wafer Graphene Diodes for High-frequency Applications*”, European Solid State Device Research Conference (ESSDERC), pp. 322–324, September, Bucharest, 2013.

Preparation of Porous Calcium Alginate Beads and Their Use for Adsorption of O-Nitrophenol from Aqueous Solutions

Sandu PERETZ¹, Manuela FLOREA-SPIROIU², Dan-Florin ANGHEL¹,
Daniela BALA², Cristina STOIAN³ and Gheorghe ZGHEREA³

¹ Institute of Physical Chemistry "Ilie Murgulescu", Romanian Academy, Department of Colloids, 202 Spl. Independentei, 060021 Bucharest, Romania
E-mail: sanduperetz@gmail.com

² University of Bucharest, Faculty of Chemistry, Department of Physical Chemistry, 4-12 Regina Elisabeta Blvd., 030018, Bucharest, Romania
E-mail: manu.spiroiu@gmail.com

³ University "Dunarea de Jos" of Galati, Faculty of Sciences and Environment, Department of Chemistry, 111 Domneasca St., 800201, Galati, Romania
E-mail: stoianc@yahoo.com

Abstract. To increase their adsorbent surface, calcium alginate (Ca-Alg)/sodium lauryl sulfate (SLS) beads were synthesized from sodium alginate with SLS as foaming agent, NaCl as porogen agent, and CaCl₂ as cross-linker. The properties of dried Ca-Alg/SLS beads were studied by FTIR and their size by SEM. The adsorption of o-nitrophenol (NP) is dependent of pH, and their adsorption on porous Ca-Alg/SLS beads reaches a maximum for pH = 7. The adsorption experiments indicated that the removal efficiency increases with the quantity of Ca-Alg/SLS beads, and decreases with increasing the initial pollutant concentration. Adsorption isotherms showed that NP adsorption on porous Ca-Alg beads occurs in accordance with Freundlich model.

1. Introduction

Adsorption is one of the most effective and simplest methods to remove pollutants from aqueous wastes, which using polymeric adsorbent that effectively trap many organic pollutants such as phenol derivatives [1-6]. Nitrophenols are the most common organic water pollutants and have adverse health effects on humans because they are toxic even at low concentrations [7]. The o-nitrophenol is used in the production of azo- and sulfur-dyes, insecticides, wood preservatives, rubber, explosives, processing of leather being present in the resulted wastewaters. Up to

some threshold concentrations the nitrophenols can cause the irritation of nose, skin, eyes or throat. The phenol is widely used in various industries and exposure to this contaminant can lead human beings to serious health problems, including symptoms such as diarrhea, dark urine and hemolytic anemia [8].

Nowadays, the use of natural polymers like polyglycolide, polylactide, gelatin, collagen, alginate, chitosan or hyaluronate as absorbents or cleaners for wastewater has received in recent year's considerable attention. Due to the low cost of production and excellent selectivity, the biopolymers are a better alternative to conventional materials for removal cationic and anionic pollutants [9, 10]. Previous studies have shown that nitrophenolic pollutants from wastewaters can be successfully retained by alginate gel complex [11, 12]. Alginate is one of the most extensively used biopolymer for removing the anionic and cationic pollutants from aqueous solutions [13-15]. It is a hydrophilic, biocompatible and inexpensive biopolymer that forms an interconnected open pore network by cross-linking with calcium ions [16, 17].

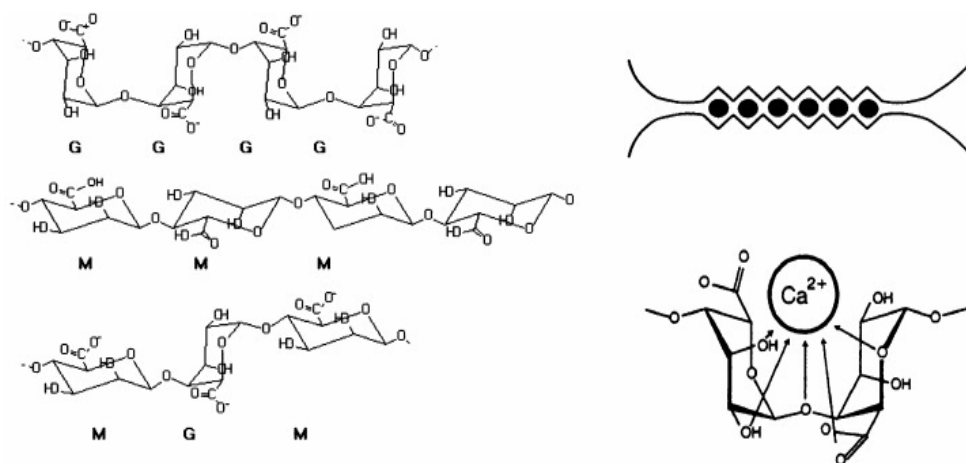


Fig. 1. Calcium alginate – Egg-box structure [22].

Alginate is composed of (1→4)-β-D-mannuronic acid (M) and α-L-guluronic acid (G) units in the form of a homopolymeric (MM- or GG-blocks) and heteropolymeric sequences (MG- or GM-blocks) [18, 19]. The blocks can be homogeneous GGGG or MMMM or alternate MGMG. Studies by partial hydrolysis and investigations by ^{13}C -NMR spectroscopy method unveiled that the monomer residues are not randomly distributed, occurring in blocks of about twenty units. The D-mannuronic acid is connected in the β-configuration through the 1- and 4- positions and the L-guluronic acid is α-1, 4- linked in the polymer. Because of the particular shape of the monomers and of their linkage in the polymer, the geometries of the G-block, M-block, and the alternating regions are substantially different. Specifically, the G-blocks are buckled while the M-blocks

have a shape referred to as an extended ribbon. If two G-block regions are aligned side by side, a diamond shaped hole results. This hole has dimensions that are ideal for the cooperative binding of calcium ions [20].

Sodium alginate forms gels with interconnected pores by ionotropic gellation in the presence of bi- or trivalent cations [21]. The bivalent calcium cation has the ability to fit into the guluronate structures like eggs in an egg-box [22].

Consequently, this binds the alginate chains together by junction zones, sequentially leading to gelling of the solution.

The purpose of this study is to obtain porous calcium alginate beads, which presents superior performance for adsorption of cationic pollutants, by using sodium lauryl sulfate as foaming agent, sodium chloride as porogen agent, and calcium chloride as cross-linker.

2. Experimental

2.1. Materials

Alginic acid sodium salt and sodium lauryl sulfate (SLS) were purchased from Fluka (Switzerland). Sodium and calcium chlorides (NaCl, CaCl₂), and o-nitrophenol (NP) were from Merck (Germany). The water used in the experiments was Milli-Q water (MILLIPORE Simplicity UV Lab System – France).

2.2. Synthesis of Alginate/SLS Beads

Aqueous sodium alginate and SLS mixed solution was prepared by dissolving the components in NaCl 1M solution at 60°C under continuous stirring at 2000 rpm for 30 minutes. The aqueous mixture of 2% (wt/v) sodium alginate and SLS 0.2% (wt/v) in form of drops was dried by lyophilization using a ALPHA 1-2 LD plus (Christ) freeze-dryer. Afterwards, the beads were cross-linked by 1,5, and 10 wt % CaCl₂ solutions for 4 hours, and denoted by Alg-1, Alg-2 and Alg-3. They were thoroughly washed with Milli Q water, and after were dried by lyophilization (pressure = 0.021 mbar, temperature = -55°C, for 48 hours).

The calcium alginate/SLS beads (without using NaCl) were obtained by dropping through a needle of a syringe the mixed sodium alginate/SLS solution into a 1 wt % calcium chloride solution; the system was magnetically stirred at 60 rpm. The beads were dried by lyophilization to be analyzed their surface morphology by scanning electron microscopy (SEM).

2.3. Characterization Techniques

The calcium alginate/SLS lyophilized beads were characterized by Fourier Transform Infrared (FTIR-ATR) Spectroscopy using a Nicolet iN10 FTIR spectrometer (Thermo Scientific), in the 550-4000 cm⁻¹ wavenumber range, at a

spectral resolution of 4 cm^{-1} . The pore sizes and the morphology of the dry beads were determined from the SEM images obtained by using a Quanta 3D FEG 200/400 microscope.

The adsorption of *o*-nitrophenol by the calcium alginate/SLS beads was spectrophotometrically assessed at 282 nm using a Varian Cary 100 Bio UV-Vis spectrophotometer. The concentration of removed NP was calculated at 45 h after reaching the equilibrium, as the difference between the initial concentration and the concentration of non-adsorbed NP remained in the solution. The kinetics regarding the *o*-nitrophenol uptake by porous calcium alginate (Ca-Alg) beads was obtained by analyzing the samples at determined time intervals. The temperature was maintained at 25°C for all the experiments.

3. Results and discussions

3.1. Beads Morphology

The factors affecting the porosity of the polymeric beads were investigated and corroborated with their mutual effects on the morphology. A porous structure of beads is obtained by using SLS as foaming agent and NaCl as porogen compound.

The SEM image shows that dry alginate beads are relatively spherical, presenting a porous surface, and have micrometrical size (Fig. 2).

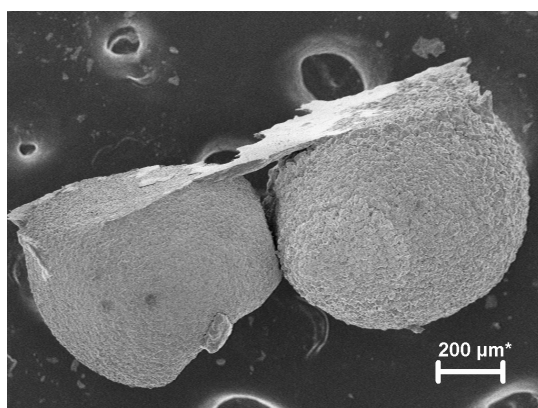


Fig. 2. SEM photo of porous calcium alginate/SLS beads.

SEM photos of the surface of alginate beads (see Fig. 3a) does not show an interconnected pore structure because the beads are not prepared in presence of NaCl, and the sodium alginate solution was not frozen. The freezing in presence of NaCl prevents the large ice crystals formation and results in polymeric structures with uniform dimension of the small pores.

The surface of beads is regular showing structures with 3-D interconnected pores. The NaCl porogen, added prior to formation of the three-dimensional

polymer matrices favors pores connection. The presence of anionic surfactant maintains the shape of the pores by repulsion between the micelles and the carboxylate groups of the polymer chain. Addition of CaCl_2 cross-linker to the sodium alginate solution entails the alignment of the G-blocks and the calcium ions are bound between the two chains like eggs in an egg box [22]. The reactivity of calcium ions to alginates is the result of calcium-induced dimer association of the G-block regions. The pore size depends on the amount of calcium present in the system. The higher the concentration of CaCl_2 leads to more junction zones and increases the number of small pores.

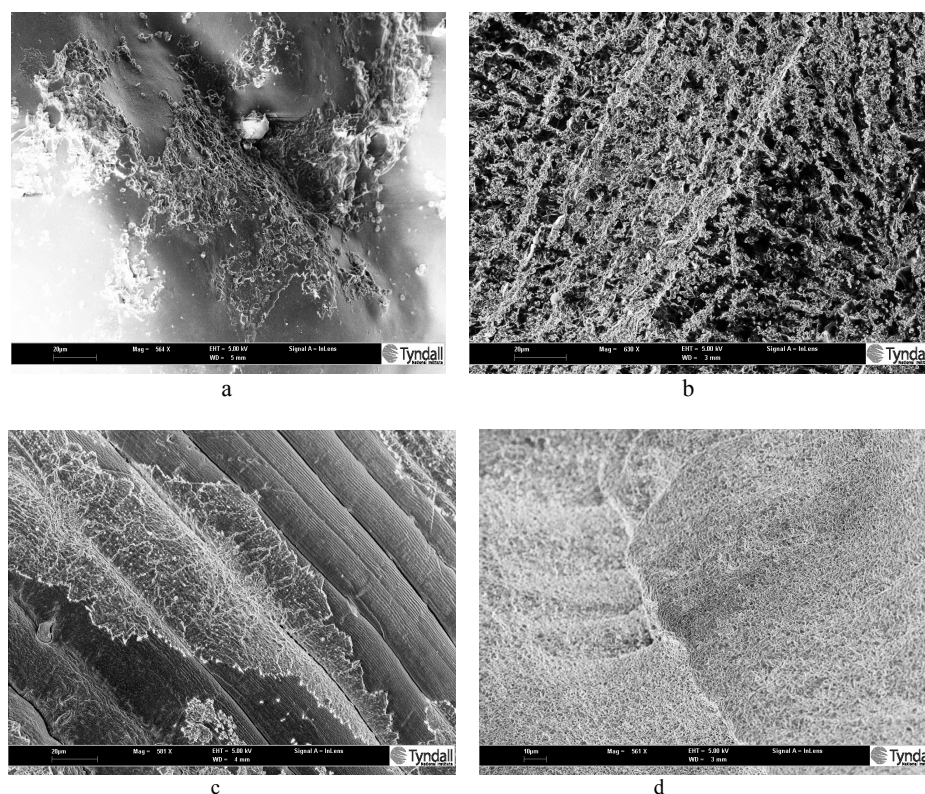


Fig. 3. SEM photos of Ca-Alg/SLS beads surface: Alg-without NaCl (a), Alg-1 (b), Alg-2 (c) and Alg-3 (d).

The size of pores varies from 5 to 10 μm in the cross-linked matrices with 1 wt % CaCl_2 (Fig. 3b). However, the pores are smaller ranging from 0.75 to 1.75 μm when the beads are treated with 5wt % CaCl_2 (Fig. 3c). In presence of high concentration of bivalent cations SLS self-assembles, and forms lamellar micelles. At 10 wt % CaCl_2 , the lamellar micelles bind together the alginate chains by electrostatic bonds with calcium ions. This is revealed by the SEM image of

sample Alg-3 (Fig. 3d) and by the FTIR spectrum (Fig. 4d) that indicates a negative effect on the intermolecular hydrogen bonds.

3.2. Evidence of Alginate Cross-Linking - the FTIR Spectrum

The different morphologies of the obtained biopolymeric beads can be explained taking into account the changes in the intermolecular bonds evidenced by FTIR spectrum (Fig. 4).

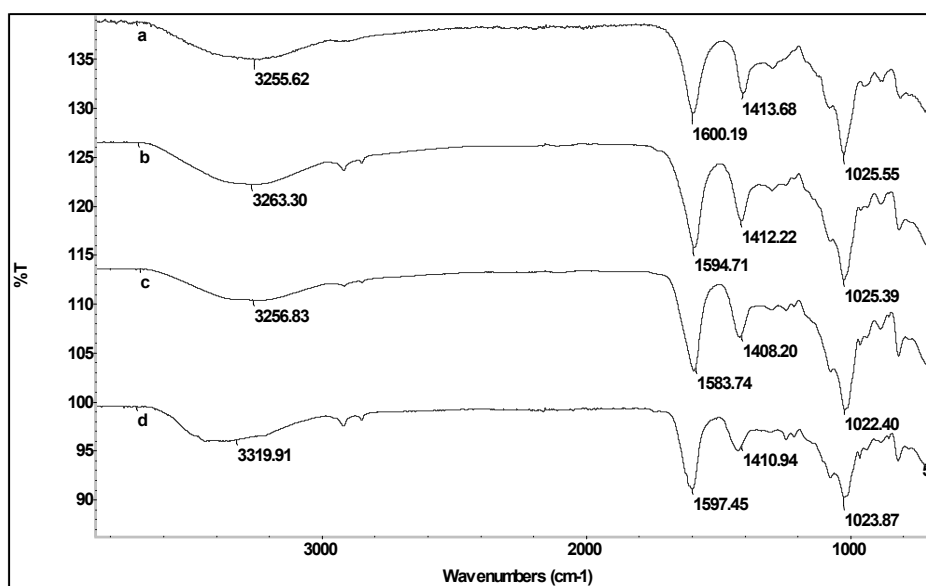


Fig. 4. FTIR spectrum: Na-Alg (a); Ca-Alg/SLS beads cross-linked with CaCl_2 : (b) 1 wt % (Alg-1), (c) 5 wt % (Alg-2), and (d) 10 wt % (Alg-3).

The spectrum of sodium alginate powder shows distinct peaks of hydroxyl (-OH) at 3255 cm^{-1} , carboxyl (-COO) at 1600 cm^{-1} , (-CH) at 1413 cm^{-1} and (C-O-C) at 1025 cm^{-1} (Fig. 4a).

Depending on the calcium chloride concentration, the characteristic peaks of alginate are shifted in the cross-linked samples in the presence of anionic surfactant.

Cross-linking decreases the wavenumber of the carboxyl peak from 1600 to 1594 cm^{-1} for Alg-1, to 1583 cm^{-1} for Alg-2, and 1597 cm^{-1} for Alg-3. The highest shift of the carboxyl absorption band (approximate 17 cm^{-1}) corresponds to Alg-2 sample. We can assume that the optimum CaCl_2 concentration for cross-linking of alginate/SLS mixture is an intermediate value between 1 wt % and 10 wt %, more precisely 5 wt%.

The band (-CH) at 1413 cm^{-1} is also shifted to lower wavenumbers for all the samples.

The characteristic peaks of SLS from 1085 cm^{-1} , 1250 cm^{-1} and 1220 cm^{-1} (SO_4) are masked by the absorption bands of alginate [23].

We found also that the peaks of (C-O-C) are shifted from 1025 cm^{-1} to 1022 cm^{-1} and 1023 cm^{-1} for Alg-2 and respectively Alg-3 samples.

The hydroxyl peak of porous calcium alginate/SLS has a higher wavenumber than that of the sodium alginate. They are shifted from 3255 to 3263 cm^{-1} for Alg-1, and respectively 3256 cm^{-1} for Alg-2 sample. In the case of Alg-3 sample (having a lamellar structure) the shifting of hydroxyl peak significantly increase from 3255 to 3319 cm^{-1} , due to a negative effect of intermolecular bond formation involving adjacent hydroxyl groups. It is probably the result of alginate conformational changes by reacting with CaCl_2 in the presence of an anionic surfactant.

3.3. Mechanism of Pollutant Adsorption

In the present study the affinity and the adsorption capacity of calcium porous alginate beads for o-nitrophenol was investigated. The beads used for the organic pollutant sorption had diameters of 700 to $900\text{ }\mu\text{m}$.

The ionic exchange takes place in the channels of alginate beads between guluronate blocks charges and the counter ions substrate. Because of this positive charge of the investigated pollutants, we suppose that the sorption process is similar to the metal ion uptake [10].

A schematic diagram of the o-nitrophenol adsorption is shown in the Fig. 5. According to the “egg-box” model of gelation mechanism [18] each “cavity” formed in the alginate gel can trap the cationic contaminant (NP) by involving the carboxyl groups from participating uronate residues. The hydroxyl groups, not shown in the figure, serve to stabilize the formed contaminant-alginate complex.

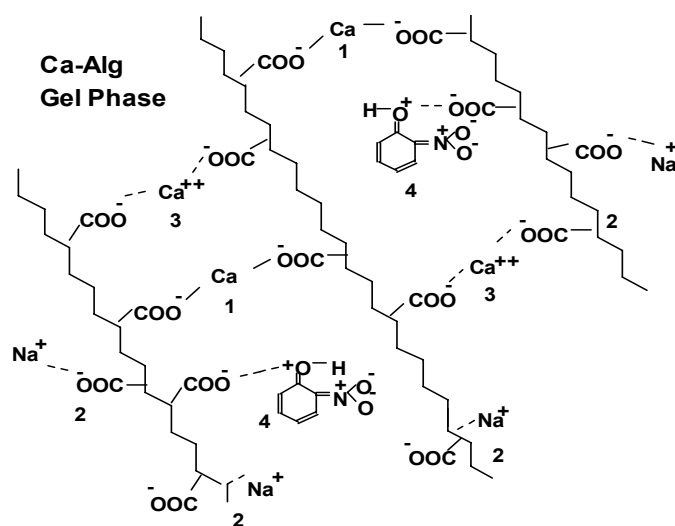


Fig. 5. Schematic diagram of the contaminant adsorption by calcium alginate beads. (1) calcium bound; (2) Na^+ ions that remains in the gel to balance the unoccupied carboxyl groups; (3) free, unbound Ca^{+2} ions in the gel phase; (4) free, unbound cationic contaminants in the gel phase; dashed lines represent electrostatic interaction between NP and unoccupied carboxyl groups.

3.4. Effect of pH on Pollutant Adsorption

The experimental data obtained at various pH values of the medium, at 45 hours after the reaching the equilibrium, are shown in the Fig. 6. The effect of the pH on the removal efficiency was studied in the pH range of 1.5 to 7.5. The uptake of contaminants shows reduced values at low pH, and increases with increasing pH in the range of 4 to 7. The data show that the efficiency for all the removal process of the cationic contaminants is strongly dependent of the pH value. The sorption of o-nitrophenol is low (between 5-15%) in the range of pH = 1.5-3, for all the samples. A significant increase of the contaminant adsorption (about 40-45%) appears at pH above 4, and the maximum value is reached at pH=7. For further increase of pH value the curve show a slight decrease. The results are consistent with the explanation that increasing of pH, the charged sites of the Ca-Alg porous beads becomes more negative.

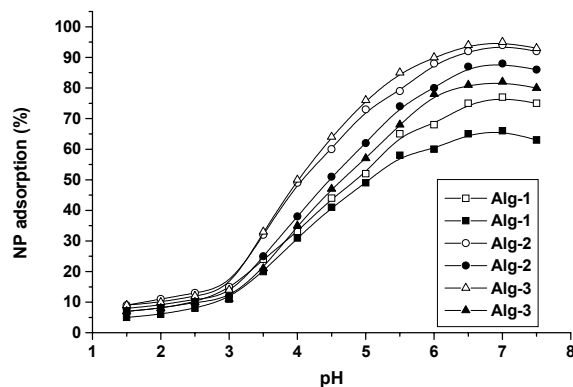
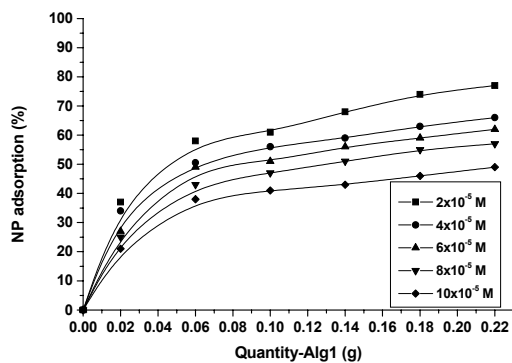


Fig. 6. Influence of pH on NP adsorption for different types of porous Ca-Alg beads, at two contaminant initial concentrations: $2 \times 10^{-5} \text{M}$ (empty symbols) and $10 \times 10^{-5} \text{M}$ (black symbols).

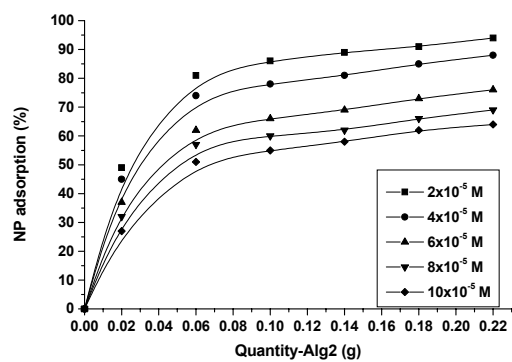
3.5. Influence of Adsorbent Dosage on the Efficiency of NP Removal

The adsorption experiments were conducted to obtain information of NP adsorption efficiency by dry porous calcium alginate beads varying the pollutant initial concentration from 2×10^{-5} to $10 \times 10^{-5} \text{M}$, and the amount of the Ca-Alg beads (samples Alg-1, Alg-2 and Alg-3). The obtained results are presented in the Figs. 7a, b, and c.

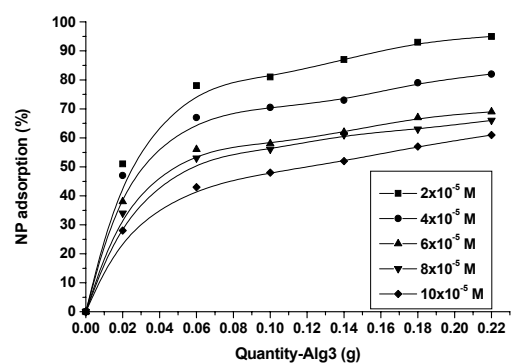
We observe that the NP retention increases with the quantity of beads, and it is dependent of the initial pollutant concentration. By using a quantity of 0.22 g of Alg-2 and Alg-3 porous calcium alginate beads, the pollutant removal is significant, reaching 94-95%. These results are good enough compared to previous adsorption experiments performed on non-porous Ca-Alg gel beads, when maximum removal reached was only 55-59% [12].



a



b



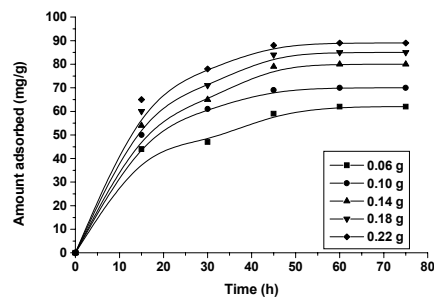
c

Fig. 7. Effect of Alg-1(a) Alg-2 (b) Alg-3 (c) quantity on the efficiency of NP adsorption, for different initial contaminant concentrations, at pH=7.

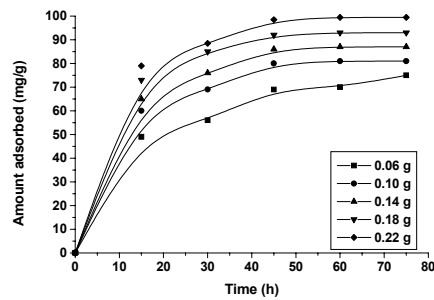
3.6. Kinetics Experiments

The kinetics of adsorption is important in order to evaluate the qualities of the adsorbent and its efficiency of pollutant removal. The NP adsorption versus time was determined for various amounts of dried porous alginate beads (Fig. 8).

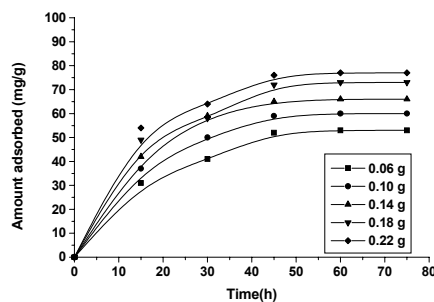
The biggest amounts of adsorbed pollutant were obtained for quantities of 0.22 g porous calcium alginate beads, and for the Alg-2 samples.



a)



b)



c)

Fig. 8. Adsorption of NP versus time, for different quantities of porous Ca-Alg beads. Samples: (a) Alg-1, (b) Alg-2, (c) Alg-3.

The Fig. 8 depicts the kinetics of the NP adsorption, which has three different stages. In the initial stage, occurring in the first 15 hours, a sharp increase of the adsorption is observed. It indicates that the pollutant is adsorbed at the exterior of the beads. In the second stage, from 15 to 45 hours, a slow adsorption process is noticed, and is probably due to the diffusion of the pollutant into the beads pores, when reaching the equilibrium. In the last stage, beyond 70 hours, the uptake of the NP is very small or remains constant. It is the result of solid biopolymer sorbent saturation by the solute.

3.7. Adsorption Isotherms

The adsorption at equilibrium is usually described by an isotherm equation characterized by specific parameters, which express their surface property and the affinity of the sorbent. In the case of o-nitrophenol adsorption onto porous calcium alginate beads, we have investigated which of the two classical models, Langmuir or Freundlich can be applied to our system.

3.7.1. Langmuir adsorption

The Langmuir model is expressed according to the equation [24]:

$$Q_e = \frac{K_L Q_m C_e}{1 + K_L C_e} \quad (1)$$

where:

Q_e (mg/g) - the amount of adsorbed on beads at the equilibrium;

C_e (mg/L) - the concentration of sorbate in solution;

Q_m (mg/g) - the maximum sorption capacity corresponding to complete monolayer coverage;

K_L (L/mg) - the Langmuir constant related to energy of adsorption

The above equation can be rearranged to the following linear form:

$$\frac{C_e}{Q_e} = \frac{1}{K_L Q_m} + \frac{C_e}{Q_m} \quad (2)$$

A plot of C_e/Q_e versus C_e with linear shape, confirm the applicability of the Langmuir adsorption model. The Langmuir constants Q_m and K_L can be evaluated from the slope and intercept of linear equation. The Langmuir model assumes monolayer adsorption on a surface with a finite number of identical adsorption sites [25].

The isotherm was found to be linear over concentration range from 2×10^{-5} to 10×10^{-5} M, and the correlation coefficient was $R^2 = 0.948$. Estimated values for the Langmuir constant was $Q_m = 93.45$ mg/g.

The value of the correlation coefficient is satisfactory and shows that the adsorption of NP onto porous alginate beads is not so precisely described by Langmuir equation, probably due to the heterogeneity of the adsorption sites of the calcium alginate.

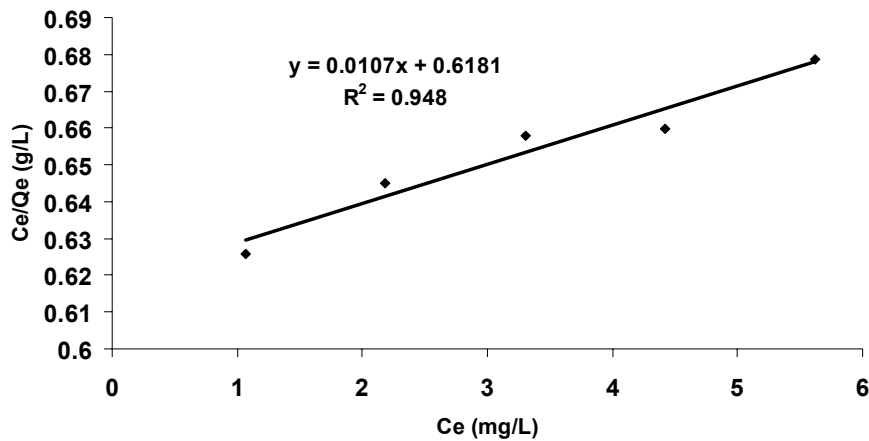


Fig. 9. Langmuir isotherm for NP adsorbed onto porous Ca-Alg beads.

3.7.2. Freundlich adsorption

The Freundlich model is an empirical equation, based on the sorption onto heterogeneous surface [26]:

$$q_e = K_F C_e^{1/n} \quad (3)$$

where:

K_F (L/g) - the Freundlich constant related to the adsorbent capacity;

n - a constant that depends on the adsorption intensity.

If the n value is greater than 1, represent favorable sorption conditions, and it may be attributed to molecular interactions between sorbent and sorbate.

This equation can be represented as:

$$\log q_e = \log K_F + \frac{1}{n} \log C_e \quad (4)$$

The Freundlich constant (K_F) and the exponent (n) are calculated from the intercept and slope of the plot of $\log q_e$ versus $\log C_e$.

The experimental data shows that the correlation coefficient is good ($R^2=0.998$), indicating that the adsorption isotherm of NP can be described by Freundlich equation.

The sorption isotherms parameters for the two models are presented in the Table 1.

Table 1. Isotherm constants and correlation coefficients

Langmuir model			Freundlich model		
Q_m (mg/g)	K_L (L/mg)	R^2	K_F (L/g)	n	R^2
93.45	0.173	0.948	1.605	1.047	0.998

The isotherms parameters show that there is a better correlation of the adsorption with Freundlich model than Langmuir model.

4. Conclusions

Porous beads with a 3-D interconnected pores and lamellar structures were obtained from sodium alginate in the presence of SLS as foaming agent, NaCl as porogen agent and CaCl_2 as cross-linker.

The size of the pores and the structure of alginate beads are influenced by the concentration of calcium ions. By changing the calcium ions concentration, a variation of pore dimension and morphology was evidenced by SEM.

The FTIR and SEM analysis reveal that the optimum concentration of CaCl_2 for cross-linking the alginate/SLS mixtures (to obtain the largest adsorption surface) is of 5 wt %. We found that the matrix of calcium alginate/SLS is lamellar for 10 wt% CaCl_2 .

The increasing of calcium alginate/SLS porous beads quantity leads to increased adsorption efficiency of the pollutant.

The o-nitrophenol was adsorbed onto calcium alginate beads in three stages. In the first stage reveals a sharp increase in the adsorption process up to 60%. Although in the second and third stage of the process is slow, it is adsorbed 95% of the contaminant.

The kinetic experiments show that NP adsorption onto porous calcium alginate/SLS beads obeys the Freundlich equation.

Acknowledgement. This research was supported by Romanian Academy, "Ilie Murgulescu" Institute of Physical Chemistry. The support of EU (ERDF) and Romanian Government (POS-CCE O2.2.1 project INFRANANOCHEM, No. 19/2009.03.01) and of (UEFISCDI) (Project PN-II-ID-PCE-2011-3-0916, Contract No. 177/2011) is gratefully acknowledged.

References

- [1] B.C. PAN, Y. XIONG, Q. SU, A.M. LI, J.L. CHEN, Q.X. ZHANG, *Chemosphere*, **51**, pp. 953–962, 2003.
- [2] J. HUANG, K. HUANG, C. YAN, *J. Hazard Mater.* **167**, pp. 69–74, 2009.

- [3] A. LI, Q. ZHANG, G. ZHANG, J. CHEN, Z. FEI, F. LIU, *Chemosphere*, **47**, pp. 981–989, 2002.
- [4] B.C. PAN, X. ZHANG, W.M. ZHANG, J.Z. ZHENG, B.J. PAN, J.L. CHEN, Q.X. ZHANG, *J. Hazard Mater.*, **121**, pp.233–41, 2005.
- [5] K. YAMADA, T. TAMURA, Y. AZAKI, A. KASHIWADA, Y. HATA, K. HIGASHIDA, Y. NAKAMURA, *J. Polym. Environ.*, **17**, pp. 95–102, 2009.
- [6] S.H. LIN, R.S. JUANG, *J. Environ. Management*, **90**, pp. 1336–1349, 2009.
- [7] S. PALIWAL, M. WALES, T. GOOD, J. GRIMSLEY, J. WILD, A. SIMONIAN, *Anal. Chim. Acta*, **596**, pp. 9–15, 2007.
- [8] ATSDR, 1998- Toxicological profile for phenol. U.S. Department of Health and Human Services CAS # 108-95-2, Public Health Service, Atlanta, GA.
- [9] J.M. LI, X.G. MENG, C.W. HU, J. DU, *Bioresource Technol.*, **100**, pp. 1168–1173, 2009.
- [10] S. BABEL, T.A. KURNIAWAN, *J. Hazard. Mater.*, **97**, pp. 219–43, 2003.
- [11] A. ELY, M. BAUDU, J.P. BASLY, M. KANKOU, *J. Hazard. Mater.*, **171**, pp. 405–409, 2009.
- [12] S. PERETZ, O. CINTEZA, *Rev. Chim.*, **58**, pp. 1129–1133, 2007.
- [13] D. ZENG, D. HU, J. CHENG, *J. Environ. Protection*, **2**, pp. 1370–1374, 2011.
- [14] L.K. JANG, D. NGUYEN, G.G. GEESEY, *Water Res.*, **29**, pp. 307–313, 1995.
- [15] M. IORGULESCU, M. FLOREA-SPIROIU, O. CINTEZA, C. PETCU, I. NITA, *Annals Univ. Bucharest*, **XVI**, pp. 59–67, 2007.
- [16] G. KLOCK, A. PFEFFRMANN, C. RYSER, P. GROHN, B. KUTTLER, H.J. HAHN, U. ZIMMERMANN, *Biomaterials*, **18**, pp. 707–713, 1997.
- [17] R.J. SCHMIDT, L.Y. CHUNG, A.M. ANDREWS, O. SPYRATOU, T.D. TIRNER, *J. Pharm. Pharmacol.*, **45**, pp. 508–513, 1992.
- [18] A. HAUG, B. LARSEN, O. SMIDSROD, *Acta Chem. Scand.*, **20**, pp. 183–190, 1966.
- [19] A. HAUG, B. LARSEN, O. SMIDSROD, T. PAINTER, *Acta Chem. Scand.*, **23**, pp. 2955–2962, 1969.
- [20] H. GRASDALEN, B. LARSEN, O. SMIDSROD, *Carbohydr. Res.*, **56**, pp. 11–15, 1977.
- [21] Z. WANG, Q. ZHANG, M. KONNO, S. SAITO, *Biopolymers*, **33**, pp. 703–711, 1993.
- [22] E. SCHETTINIA, G. SANTAGATA, M. MALINCONICO, B. IMMIRZI, G.S. MUGNOZZA, G. VOX, *Resources, Conservation and Recycling*, **70**, pp. 9–19, 2013.
- [23] R.B. VIANA, A.B.F. DA SILVA, A.S. PIMENTEL, *Adv. Physical Chem.*, **1**, DOI:10.1155/2012/903272, 2012.
- [24] E. TORRES, Y.N. MATA, M.L. BLAZQUEZ, J.A. MUNOZ, F. GONZALEZ, A. BALLESTER, *Langmuir*, **21**, pp. 7951–7958, 2005.
- [25] W. HAN, C. LIU, R.J. BAI *Membr. Sci.*, **302**, pp. 150–159, 2007.
- [26] C. MAHAMADI, B. MADOCHA, *Am. J. Anal. Chem.*, **4**, pp. 373–378, 2013.

Comparative Thermodynamic Study on Exfoliated Graphite Nanoplatelets Systems Dispersed in Dimethylformamide and water at T= (293.15, 298.15 and 303.15) K

Florinela SIRBU^a, Ion ION^b, Alina Catrinel ION^b

^a”Ilie Murgulescu” Institute of Physical Chemistry of Romanian Academy,
202 Splaiul Independentei str., 060021, Bucharest, Romania
E-mail: sflorinela@yahoo.com

^b”Politehnica” University of Bucharest, Faculty of Applied Chemistry and
Material Science, 1-7 Polizu str., 011061, Bucharest, Romania
E-mail: i_ion@chim.upb.ro, ac_ion@yahoo.com

Abstract. The density, speed of sound and refractive index of diluted binary mixtures of exfoliated graphite nanoplatelets dispersed in water, and N,N-dimethylformamide, respectively, at different concentrations of solvate and at different temperatures have been measured. From the experimental data obtained, acoustic parameters such as the acoustic impedance, isentropic compressibility, specific refraction, space-filling factor, and relaxation strength were calculated for all compositions and temperatures. The results have been used to identify molecular interactions in the mixtures, including structural changes of exfoliated graphite nanoplatelets in polar solvents.

Keywords: thermodynamic study; exfoliated graphite nanoplatelets (xGnP); aqueous binary mixtures; optical properties; acoustical properties.

1. Introduction

The thermodynamic study of binary systems containing exfoliated graphite nanoplatelets (xGnP) dispersed in water (H₂O), and N,N-dimethylformamide (DMF) respectively is important for understanding the physical-chemical behavior of liquid mixtures containing carbon-based nanomaterials. The acoustic and optical properties present considerable interest in extending the temperature range of thermodynamic data for systems containing exfoliated graphite nanoplatelets systems dispersed in dimethylformamide and water, respectively [1-4].

There is a variety of intermolecular interactions among graphene sheets in particular colloidal ones in solution [5-7]. The interactions between two colloid

particles in liquids are assumed to be the sum of two contributions: London – Van der Waals forces and electrical double layer (EDL) forces. In addition, solvation forces, hydrophilic forces and sterical forces are also present in many colloidal systems and affect their colloidal behavior. The simulations revealed that the adsorption of the polar, organic solvent molecules such as NMP, particularly the single layer of solvent molecules confined on the graphene sheets form an energy barrier and prevent the approaching of the graphene sheets from a complete recombination. As the magnitude of the energy barrier is directly dependent on the affinity of the solvent to graphene, the scale of solvation forces is strongly affected by the chemistry of the solvents. The simulations suggest the following order for the ability to stabilize pristine graphene in suspensions: NMP>DMSO>DMF [8, 9].

Adsorption of water on carbon surfaces has been studied since 1968 by Kiselev *et al.* [10] Several simulations proved that water can be strongly adsorbed at low relative pressures by carbon adsorbents due to the potential overlap in small pores [11, 12].

Water is found to behave very differently while interacting with hydrophobic pristine graphene [13]. There are very few experimental studies of water interactions with the carbon-based nanomaterials flat surfaces, such as graphene or exfoliated graphite nanoplatelets [14, 15] even if these nanomaterials can be used as sorbents in environmental applications [16, 17].

When water is in contact with graphene, the hydrophobic graphene surface would disrupt the dynamic hydrogen bonds of water, resulting in significant translational and rotational entropy loss of water molecules [18]. In aqueous medium, attractive forces arise between hydrated graphene sheets [19]. Such forces are often referred as hydrophobic forces and explain why water is not a good solvent to disperse pristine graphene. Nevertheless, the electrostatic repulsion is among the most exploited, because it can be readily tuned by chemical modifications of the graphene surface [20]. In this way, the properties of graphene-based dispersions can be easily controlled by adjusting a variety of factors such as: pH, ionic strength and surface chemistry [21, 22].

As part of a our project on the thermodynamic properties of liquid mixtures, [23-25] a comparison between the new measurements of density, speed of sound and refractive indices of the binary system $x\text{GnP} + \text{H}_2\text{O}$ with $x\text{GnP} + \text{DMF}$ [26] at various concentrations of $x\text{GnP}$ and different volumes of the solvents at $T = (293.15, 298.15, \text{ and } 303.15) \text{ K}$ are presented.

From the measured data, the optical and acoustical properties such as acoustic impedance, isentropic compressibility, specific refraction, space-filling factor and relaxation strength calculated through different equations.

This study reports new experimental data for density, speed of sound and refractive indices of the binary system $x\text{GnP} + \text{H}_2\text{O}$ at various concentrations of $x\text{GnP}$ and different volumes of the solvents at $T = (293.15, 298.15, \text{ and } 303.15) \text{ K}$; studies the influence of the solvents on the physical-chemical behavior of $x\text{GnP}$;

calculates acoustic and optical parameters such as acoustic impedance, adiabatic compressibility, specific refraction, space-filling factor and relaxation strength calculated through different equations from experimental density, speed of sound and refractive index results.

2. Experimental Section

2.1. Materials and methods

xGnP containing a mass fraction more than 0.95 carbon was provided from XG Sciences, Lansing, MI, USA and was characterised in our laboratory. KBr, and N,N-dimethylformamide (DMF) have been supplied by Merck.

Exfoliated graphite nanoplatelets were used without any pretreatment because of their mass fraction purity higher than 0.99. The details of the chemicals used for samples preparation are given in the Table 1.

Table 1. Comparison of Experimental Densities (ρ), Speed of Sound (c), Refractive Indices (n_D) of Water with Literature Values at Temperatures of (293.15, 298.15 and 303.15) K

T/K	$\rho/\text{kg}\cdot\text{m}^{-3}$		$c/\text{m}\cdot\text{s}^{-1}$			n_D		
	Expt.	Lit.	Expt.	Lit.	Expt.	Lit.		
water								
293.15	998.22	998.220	[27]	1484.26	1483.1	[27]	1.33300	[27]
		998.206	[28]		1482.36	[29]	1.33297	[30]
298.15	997.04	997.043	[31]	1498.35	1497.40	[32]	1.33249	[33]
		997.040	[34]		1496.20	[35]	1.33250	[36]
303.15	995.63	995.650	[28]	1510.61	1509.00	[36]	1.33187	[37]
		995.600	[37]		1509.14	[38]	1.32500	[39]

Working solutions of different compositions xGnP + H₂O were prepared at 298.15 K using deionized and doubly distilled water. The aqueous mixtures were prepared by mixing known compositions of stock and water solutions in narrow-mouth, ground glasses. The binary solutions were kept in special airtight glass bottles to avoid evaporation. A volume of 100 cm³ stock solution of exfoliated graphite nanoplatelets (solute) of 0.001 g·cm⁻³ at 293.15 K was prepared by directly weighing the materials using an A&D GH-252 (Japan) analytical balance with an accuracy of ± 0.0001 g. The dispersion of solute + water was improved by addition of pure ethanol 0.1 cm³ to 15 cm³ stock solution. The initial composition of the solutions was prepared with a precision of ± 0.0002 g·cm⁻³. For each solute, six

samples with different specific compositions domain from (0 to 100) $\text{kg}\cdot\text{m}^{-3}$ in increments of $20 \text{ kg}\cdot\text{m}^{-3}$. For uniformity, all of the aqueous mixtures were dispersed using an ultrasonic bath. The uncertainty in the composition at samples preparation was estimated to be less than $\pm 0.0001 \text{ g}\cdot\text{cm}^{-3}$. Each sample was sonicated for 30 minutes at 303.15 K and measured immediately.

The density and speed of sound of stock binary mixtures were measured with an Anton Paar DSA 5000 digital (Austria) analyser with a precision of $\pm 0.000001 \text{ g}\cdot\text{cm}^{-3}$. During the measurements of the density the temperature was controlled at a precision of $\pm 0.001 \text{ K}$, and several Peltier units have been used. The internal calibration of the instrument was confirmed by measuring the density and speed of sound in atmospheric air and doubly distilled deionised water, according to the recommendations of the manufacturer. Similar to the results described in the literature, the density of water was measured as $0.99704 \text{ g}\cdot\text{cm}^{-3}$ at 298.15 K [31, 34]. The values of ρ and c were reproducible within $\pm 0.000005 \text{ g}\cdot\text{cm}^{-3}$ and $\pm 0.05 \text{ m}\cdot\text{s}^{-1}$, respectively. The refractive indices were measured using an Anton Paar GmbH Abbe automatic refractometer with an accuracy of ± 0.000001 , and the temperature of the samples was controlled within $\pm 0.01 \text{ K}$. The refractometer was calibrated by measuring the refractive index of doubly distilled and deionized water. The refractive index of water was measured as 1.33249 at 298.15 K, which is similar to the value mentioned in the literature of 1.33250 [33, 34]. The samples were introduced into the cell (prism assembly) using a syringe. At least three independent measurements were done for each sample at each temperature to assure the effectiveness of the measurement. All the measurements were repeated at least three times and were repeatable within the level of precision quoted for the apparatus. Uncertainties associated with the experimentally data such as density, ultrasonic speed and refractive index were estimated based on the uncertainty of the measurement [40] and presented together with the experimental results in the tables.

2.2. Theory and Calculation

The following thermodynamic acoustical and optical parameters have been estimated using the standard relations employed in previous studies [41-46]. The acoustic impedance (Z) has been calculated using the following relation [41]:

$$Z = \rho c \quad (1)$$

where ρ is the density ($\text{kg}\cdot\text{m}^{-3}$), and c is the speed of sound ($\text{m}\cdot\text{s}^{-1}$) in the mixture.

The isentropic compressibility coefficient k_s for the pure solvent and liquid mixtures have been estimated from the density ρ and the speed of sound c using the Laplace equation [42].

$$k_S = \frac{1}{K} = \frac{1}{\rho c^2} \quad (2)$$

where, K is the bulk modulus of the solution.

According to the method of Gerecse [43] and Lorentz-Lorenz [44], the space-filling factor (S) has been computed from refractive index (sodium D line) data using the following relation [45]:

$$S = \frac{B}{V} = \frac{n_D^2 - 1}{n_D^2 + 2} \quad (3)$$

where, B is the effective volume occupied by molecules per mole, V is the molecular volume and n_D is the refractive index of the aqueous solution.

The specific refraction (r_D) has been estimated from the density (ρ) and space-filling factor (S) using the Lorentz and Lorenz equation, which is based on the electromagnetic theory of light, whereas the other equations are of empirical origin [46]:

$$r_D = \frac{n_D^2 - 1}{n_D^2 + 2} \frac{1}{\rho} \quad (4)$$

The relaxation strength (r) has been calculated using the following equation [45]:

$$r = 1 - \frac{c^2}{c_{ct}^2} \quad (5)$$

where, c is the speed of sound in the experimental solution, and c_{ct} is a constant with a value of $1600 \text{ m}\cdot\text{s}^{-1}$ [46].

The specific concentration dependence on density and on ultrasound speed obtained in the two systems was correlated by a polynomial type equation:

$$F(Y) = \sum_{i=1}^n A_i C^{i-1} \quad (6)$$

where, Y represents the properties measured in general (ρ , c) and C represents the specific concentration.

Correlations of ρ , c , k_S and r as a function of concentration (Eq. 7) along with the absolute average percentage deviation (AAD) were analyzed. The absolute average percentage deviation (AAD %) was determined using the following relationship:

$$AAD(Y) = \frac{100}{N} \sum_i^n \left| \frac{Y_{Expt.} - Y_{Calc.}}{Y_{Expt.}} \right| \quad (7)$$

where N is the number of experimental data points. The subscripts “Expt.” and “Calc.” represent the values of the experimental and calculated property, respectively.

3. Results and Discussion

In order to characterize the interactions between solvent molecules and graphene we experimentally determined the thermodynamic parameters: density, ultrasound speed and refractive indices for xGnP dissolved in two solvents: DMF and H₂O, observing that DMF was a more effective solvent in comparison with H₂O.

The carbon based nanoparticles (xGnP) dispersed in DMF solvent were characterized previously [26] and discussed there. The experimental data of densities, ultrasound speed and refractive indices as a function of the specific concentration of xGnP in DMF and in water are presented in Table 2.

Table 2. Experimental Values of the Density ρ , Ultrasound Speed c and Refractive Index n_D at Various Temperatures T and Specific Concentrations C of xGnP, for the Binary xGnP + H₂O^a Mixture

T/K	$\rho/kg \cdot m^{-3}$	$c/m \cdot s^{-1}$	n_D	$\rho/kg \cdot m^{-3}$	$c/m \cdot s^{-1}$	n_D
	$C/kg \cdot m^{-3} = 0$			$C/kg \cdot m^{-3} = 20$		
293.15	998.22	1484.26	1.33300	997.50	1486.97	1.33327
298.15	997.04	1498.35	1.33249	996.35	1500.73	1.3328
303.15	995.63	1510.61	1.33187	994.95	1512.76	1.33223
	$C/kg \cdot m^{-3} = 40$			$C/kg \cdot m^{-3} = 60$		
293.15	996.81	1489.82	1.33343	996.18	1492.69	1.333597
298.15	995.66	1503.31	1.33294	995.04	1505.86	1.33305
303.15	994.27	1515.07	1.33238	993.64	1517.35	1.33244
	$C/kg \cdot m^{-3} = 80$			$C/kg \cdot m^{-3} = 100$		
293.15	995.44	1494.97	1.33366	995.05	1497.56	1.33399
298.15	994.31	1507.87	1.33317	993.90	1510.25	1.33350
303.15	992.88	1519.43	1.33260	992.50	1521.3	1.33292

^a $C/kg \cdot m^{-3}$ is the specific concentration of xGnP in the H₂O solvent. Standard uncertainties u are $u(T) = 0.001$ K for ρ and c ; $u(T) = 0.01$ K for n_D and the combined expanded uncertainties U_c are $U_c(\rho) = 0.01$ kg·m⁻³, $U_c(c) = 0.05$ m·s⁻¹; (level of confidence = 0.95, $k = 2$) and $U_c(n_D) = 0.00001$.

Based on the values of the measured properties, the derived thermophysical parameters as a function of the specific concentration fraction at three different

temperatures between (293.15 and 303.15) K were calculated and presented in Table 3.

Table 3. Calculated Values of the Acoustic Impedance Z , Adiabatic Compressibility k_S , Space Filling Factor S , Specific Refraction r_D , and Relaxation Strength r at Various Temperatures T , Specific Concentration C of (xGnP), for the System xGnP+ H₂O

T/K	$\frac{Z}{10^5 \cdot \text{kg} \cdot \text{m}^{-2} \cdot \text{s}^{-1}}$	$\frac{k_S}{10^{-10} \cdot \text{m}^2 \cdot \text{N}^{-1}}$	S	$\frac{r_D}{10^{-3} \cdot \text{m}^3 \cdot \text{kg}^{-1}}$	r
$C/\text{kg}\cdot\text{m}^{-3} = 0$					
293.15	14.81617	4.54731	0.20569	0.20606	0.13944
298.15	14.93907	4.46748	0.20541	0.20602	0.12303
303.15	15.04015	4.40145	0.20506	0.20596	0.10862
$C/\text{kg}\cdot\text{m}^{-3} = 20$					
293.15	14.83247	4.53403	0.20584	0.20636	0.13630
298.15	14.95246	4.45641	0.20558	0.20633	0.12024
303.15	15.05124	4.39195	0.20527	0.20631	0.10608
$C/\text{kg}\cdot\text{m}^{-3} = 40$					
293.15	14.85069	4.51980	0.20594	0.20666	0.13298
298.15	14.96790	4.44417	0.20566	0.20656	0.11721
303.15	15.06389	4.38158	0.20535	0.20653	0.10334
$C/\text{kg}\cdot\text{m}^{-3} = 60$					
293.15	14.86989	4.50529	0.20603	0.20682	0.12964
298.15	14.98385	4.43192	0.20572	0.20675	0.11421
303.15	15.07703	4.37118	0.20538	0.20670	0.10064
$C/\text{kg}\cdot\text{m}^{-3} = 80$					
293.15	14.88146	4.49492	0.20607	0.20701	0.12697
298.15	14.99290	4.42334	0.20579	0.20697	0.11184
303.15	15.08616	4.36255	0.20547	0.20695	0.09817
$C/\text{kg}\cdot\text{m}^{-3} = 100$					
293.15	14.90147	4.48112	0.20625	0.20727	0.12395
298.15	15.01039	4.41122	0.20597	0.20724	0.10904
303.15	15.09896	4.35349	0.20565	0.20721	0.09596

The density, ultrasound speed and refractive index values as a function of specific concentration of exfoliated graphite nanoplatelets (xGnP) are shown in Figs. 1, 2 and 3, respectively, by comparison between both binary xGnP + DMF [26] and xGnP + H₂O systems, along of polynomial correlated values (ρ , c).

Fitting parameters A_i and absolute average percentage deviation results are reported in Table 4 for binary AC in DMF mixtures at all temperatures studied.

Table 4. Fitting Parameters A_i , Correlation Coefficient (R^2) Obtained for Density ρ , Ultrasonic Speed c , Isentropic Compressibility k_s and Relaxation Strength r Along with the Absolute Average Percentage Deviation (AAD %) for Binary xGnP + H₂O Mixture.^a

T/K	$C/kg\cdot m^{-3}$	$A_1/kg\cdot m^{-3}$	$A_2/kg^0\cdot m^0$	$A_3/kg^1\cdot m^3$	A_4	R^2	AAD %
$\rho/kg\cdot m^{-3}$							
293.15	0-100	998.24	- 0.038815	0.000065	-	0.99771	0.004
298.15	0-100	997.06	- 0.037489	0.000055	-	0.99809	0.004
303.15	0-100	995.66	- 0.037510	0.000054	-	0.99711	0.005
T/K	$C/kg\cdot m^{-3}$	$A_1/kg^0\cdot m^{-1}\cdot s$	$A_2/kg\cdot m^{-4}\cdot s$	$A_3/kg^2\cdot m^{-7}\cdot s$	A_4	R^2	AAD %
$c/m\cdot s^{-1}$							
293.15	0-100	1484.20	0.1462429	-0.0001286	-	0.99953	0.005
298.15	0-100	1498.30	0.1294214	-0.0001018	-	0.99939	0.004
303.15	0-100	1510.53	0.1185571	-0.0001036	-	0.99960	0.004
T/K	$C/kg\cdot m^{-3}$	A_1	A_2	A_3	$A_4\cdot 10^{-9}$	R^2	AAD %
n_D							
293.15	0-100	1.332991	0.000019086	- 0.000000266	2	0.99306	0.006
298.15	0-100	1.332485	0.000018383	- 0.000000254	2	0.99838	0.007
303.15	0-100	1.331875	0.000025157	- 0.000000425	3	0.99952	0.005
T/K	$C/kg\cdot m^{-3}$	$A_1/10^{-10}\cdot kg^0\cdot m^{-2}\cdot N^{-1}$	$A_2/10^{-10}\cdot kg^{-1}\cdot m^{-5}\cdot N^{-1}$	$A_3/10^{-10}\cdot kg^{-2}\cdot m^{-8}\cdot N^{-1}$	A_4	R^2	AAD %
$k_s/10^{-10}\cdot m^2\cdot N^{-1}$							
293.15	0-100	4.5475657	- 0.0007185	0.0000006	-	0.99889	0.014
298.15	0-100	4.4677032	- 0.0006030	0.0000004	-	0.99854	0.013
303.15	0-100	4.4017500	- 0.0005243	0.0000004	-	0.99954	0.007
T/K	$C/kg\cdot m^{-3}$	$A_1/kg^0\cdot m^0$	$A_2/kg^1\cdot m^3$	$A_3/kg^2\cdot m^{-6}$	A_4	R^2	AAD %
r							
293.15	0-100	0.1395071	- 0.0001697	0.0000001	-	0.99954	0.152
298.15	0-100	0.1230932	- 0.0001518	0.0000001	-	0.99940	0.109
303.15	0-100	0.1087068	- 0.0001404	0.0000001	-	0.99959	0.111

^a A_i and R^2 were obtained from Eq. 7; AAD %: $AAD(Y) = \frac{100}{N} \sum_i^n \left| \frac{Y_{Expt.} - Y_{Calc.}}{Y_{Expt.}} \right|$, where N = 6 number of experimental data at each temperature.

Figure 1 presents the density as a function of the solute concentration of the binary mixtures xGnP + DMF [26] and xGnP + H₂O at various temperatures.

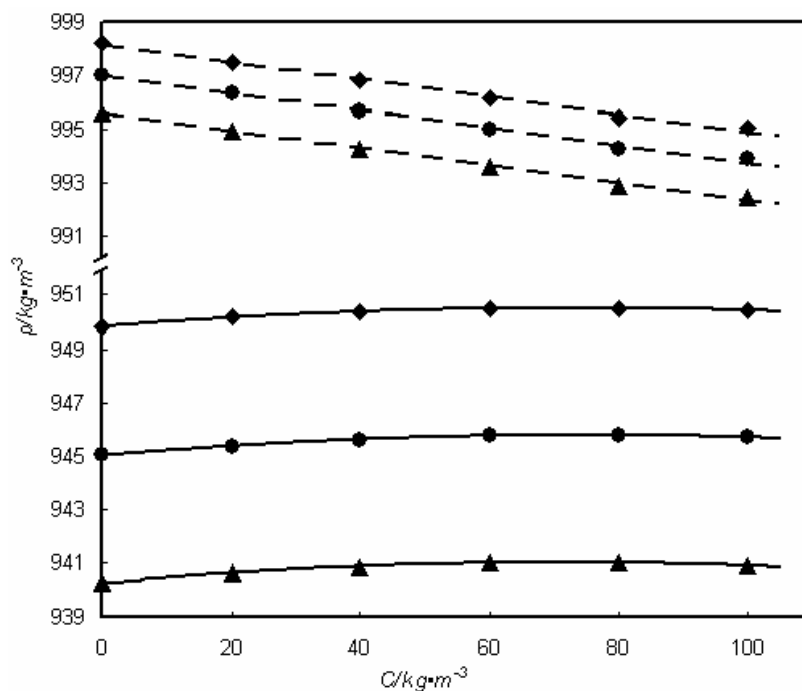


Fig. 1. Comparative representation of the density of binary xGnP + H₂O and xGnP + DMF [26] systems versus concentration of solute at various temperatures, T/K: ◆, 293.15; ●, 298.15; ▲, 303.15; --, for H₂O; —, for DMF; polynomial correlated values.

Good dispersion of graphene is influenced by the solubility parameters and surface tensions of the solvents, being found that an efficient solvent has a surface tension equivalent to that of graphene [47]. Good solvents for graphene provide stable colloidal dispersions for nanosized graphene.

Solvent molecules alone cannot exfoliate graphene, ultrasonic treatment being necessary. When the graphene sheets achieve certain separation by the ultrasonic treatment, the solvent molecules can insert between the graphite layers providing a colloidal stability.

The density of the binary system xGnP + DMF decreases by increasing the temperature and increases by increasing the concentration of the solute. Slight differences were observed between the two systems, indicating that DMF changes the structure of xGnP more strongly than water. These differences may be due to the number and position of oxygen-containing groups at the edges of xGnP, which improves the dispersion of the nanomaterial in DMF. These results support the

conclusion that a π - π interaction [48] occurs between carbon-based nanomaterials and DMF, which increases the density by increasing the mole fraction of the mixture.

The density profiles for the organic solvents suggest stronger interaction between the graphene surface and the DMF molecules, no clear isolated solvent layer being observed near the graphene surface in H_2O . There exists an enrichment of solvent layer near the graphene surface in both solvents, but the average interactions energies between the surrounding solvent molecules and the graphene is different. The dependence of the velocity of ultrasound on the concentration of $xGnP + DMF/H_2O$ is presented in Fig. 2.

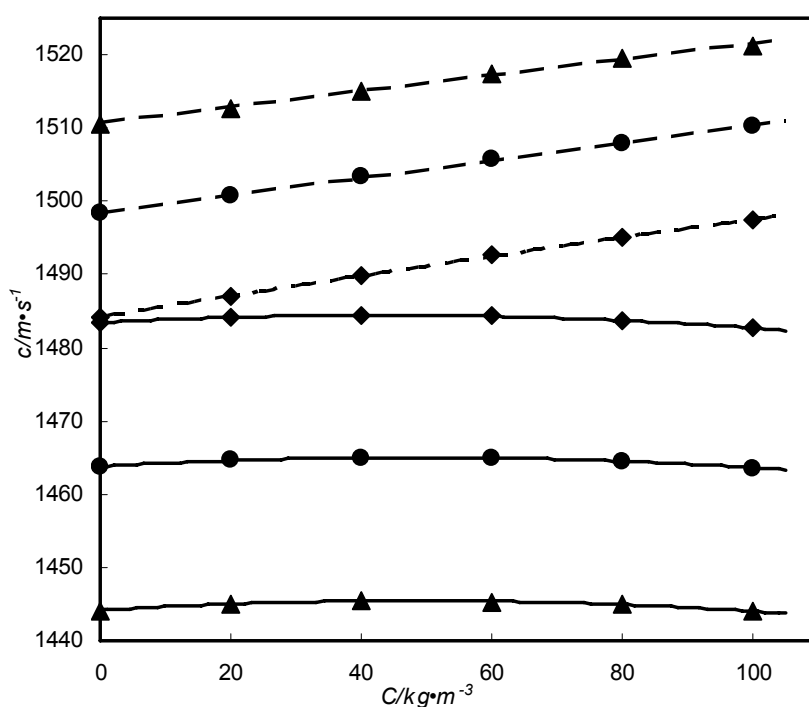


Fig. 2. Comparative representation of the ultrasound speed of binary $xGnP + H_2O$ and $xGnP + DMF$ [26] systems versus concentration of solute at various temperatures, T/K : \blacklozenge , 293.15; \bullet , 298.15; \blacktriangle , 303.15; $-\cdot-$, for H_2O ; $—$, for DMF ; polynomial correlated values.

As shown in Fig. 2, the ultrasound speed slightly increased with an increase in the concentration of the solute, indicating the presence of solute-solvent interactions via hydrogen bonding, which can produce displacements of electrons and nuclei in this range of concentrations. It slightly decreases with the temperature, much more for the $xGnP + DMF$ system. As the temperature

increased, the thermal energy leads to the breaking of the bonds and it weakens the molecular forces which decreases the ultrasound speed.

After the equilibrium, it can be presumed that DMF molecules can spread over the graphene surfaces, forming a complete solvent layer, this demonstrating that the graphene surface is solvophilic for the organic solvents [49]. The interaction between the organic molecules and graphene is larger than the inherent intermolecular interactions between the solvent molecules. Meanwhile, the water solvent just shows a hydrophobic dispersion interaction with the graphene surface. It is interesting to note that the attraction forces are approximately the same in different solvent media, which is determined by the attractive interaction between graphene sheets, being clear that the initial exfoliation is less dependent upon the solvent medium and the ultrasound speed will not have a significant variation in different solvents. The dependence of the refractive indices on the concentration of the solute (active carbon and exfoliated graphite nanoplatelets) in DMF is presented in Fig. 3.

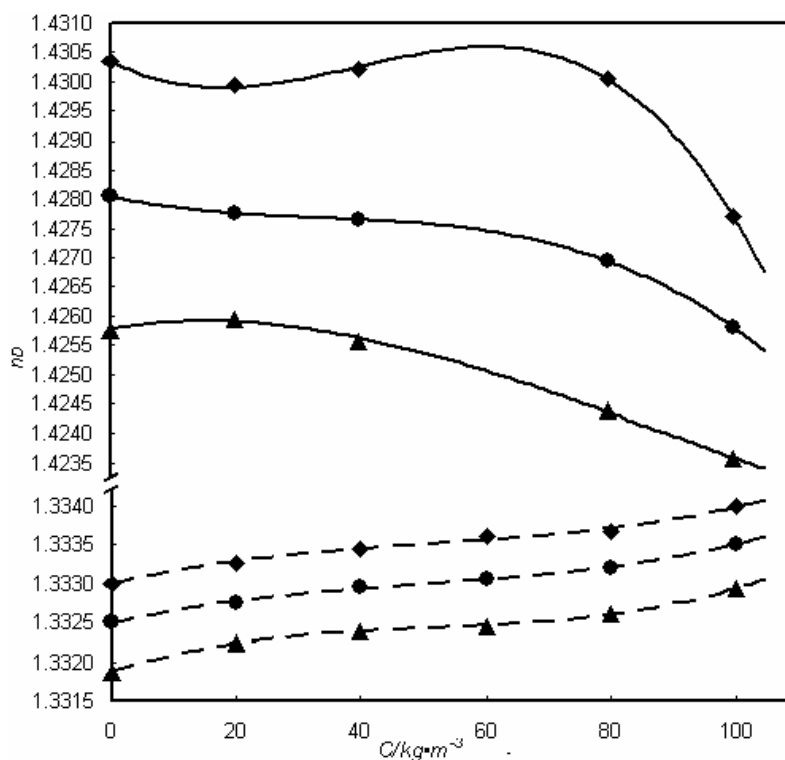


Fig. 3. Comparative representation of the refractive index of binary xGnP + H₂O and xGnP + DMF systems versus concentration of solute at various temperatures,

T/K: ◆, 293.15; ●, 298.15; ▲, 303.15; ---, for H₂O; —, for DMF [26];
polynomial correlated values.

Regardless of the temperature, at a concentration of 0.08 g mL^{-1} , the value of the refractive index and the space-filling factor increased, suggesting that dispersion improves for a specific concentration of xGnP in DMF. In comparison, variations in the refractive indices were not detected in water at the same concentration.

The repulsive forces which appear originate from the solvent-induced interactions. These forces are favourable to promote exfoliation and prevent aggregation. At very large separation, the force approaches to zero, indicating a complete detachment, this suggesting that in the exfoliation process the interfacial resistance at the beginning of graphene exfoliation is from the attractive interaction between graphene layers and then the solvent-induced force dominantly influence the subsequent exfoliation process. The repulsive force in organic solvent is higher than in the water solvent, this consisting with the enhanced interaction strength between the organic solvent and the graphene surface. The repulsive forces play a role in the attractive interaction between graphene sheets. In the water solvents, the solvent-induced forces present a weak interaction, blocking the parallel exfoliation.

The total resisting force is originating from the attractive interaction between the graphene sheets. In organic solvents, the solvent-induced force can give rise to the repulsive force to aid the exfoliation process, because of the stable confined solvent layer accommodated in the gap between the shifted graphene sheet and the fixed graphite.

In the water solvent, the confined solvent layer is not well accommodated because of the weak surface affinity. The water-induced force from the outer solvent molecules is the main controlling factor of the resisting action of the sheet moving [47].

The dependence of the isentropic compressibility on the concentration of the solute is presented in Fig. 4.

As shown in Fig. 4, the isentropic compressibility of the two binary systems increases with an increase in temperature. In the xGnP + DMF system, the isentropic compressibility decreases by increasing the concentration up to $0.06 \text{ g}\cdot\text{mL}^{-1}$, then increased for $C = 0.1 \text{ g}\cdot\text{mL}^{-1}$. The observed increase and decrease in the isentropic compressibility as a function of the concentration in the xGnP + DMF binary mixture were indicative of interactions between component molecules.

Isentropic compressibility is varies in a reversed dependence to the square of the ultrasound of speed, and its deviation can be attributed to the loss of di-polar association between the solvent molecules and differences in the size and shape of xGnP molecules, which reduces the velocity and increases the compressibility.

Dipole-dipole interactions or hydrogen-bonded complex formation between unlike molecules increased the velocity of ultrasound and decreased the compressibility. In the xGnP + H_2O system, the first mode of adsorption is characterized by water interactions within the graphene layers that are stacked to form graphitic microstructures of carbogenic materials [50].

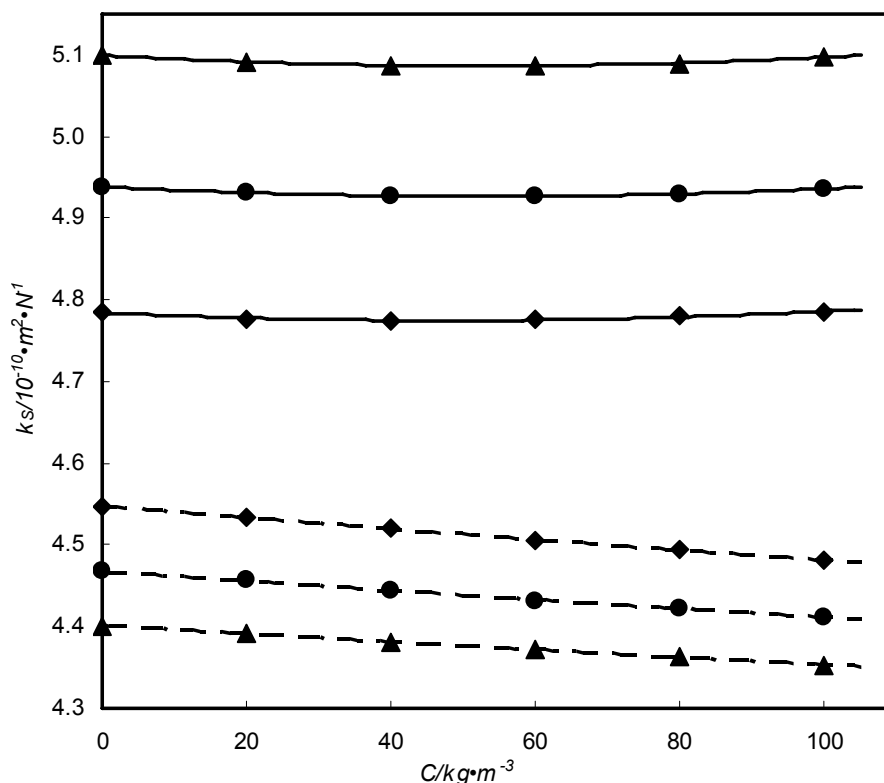


Fig. 4. Comparative representation of the isentropic compressibility of binary xGnP + H₂O and xGnP + DMF systems versus concentration of solute at various temperatures, T/K: ◆, 293.15; ◻, 298.15; ▲, 303.15; --, for H₂O; —, for DMF [26]; polynomial correlated values.

The graphene layers offer a small attraction for water molecules, the micropores will adsorb water, the adsorption being followed by cooperative interactions of the adsorbed water with the other water molecules until filling of the graphitic microstructures occurs. The second mode of adsorption occurs via interaction of water with oxygenated functional groups that are present outside the graphitic microstructures. This interaction is characterized by a high degree of attraction, affected by pore size and site density. The dependence of the relaxation strength on the temperature of both systems shows differences, as evidenced in Fig. 5.

In the xGnP + DMF binary mixture, the relaxation strength decreased up to a solute concentration of 0.06 g·mL⁻¹ and increased after by increasing the solute concentration, suggesting the predominance of molecular interactions [51].

In the xGnP + H₂O binary mixture, the relaxation strength increased with an increase in the temperature and decreased with an increase in the concentration over the concentration range. As the concentration of water gradually increased, various

interactions such as H-bonding, dipole-dipole and dipole induced dipole interactions occurred between molecules.

The possible presence of carboxylic, carbonyl and hydroxyl groups appears to prevent the water molecules from filling the graphene layers, whereas the removal of these groups allows water to adsorb between the layers.

The presence of oxygenated functional groups reduces the micropore volume accessible to water molecules and does not affect the micropore volume accessible to DMF molecules.

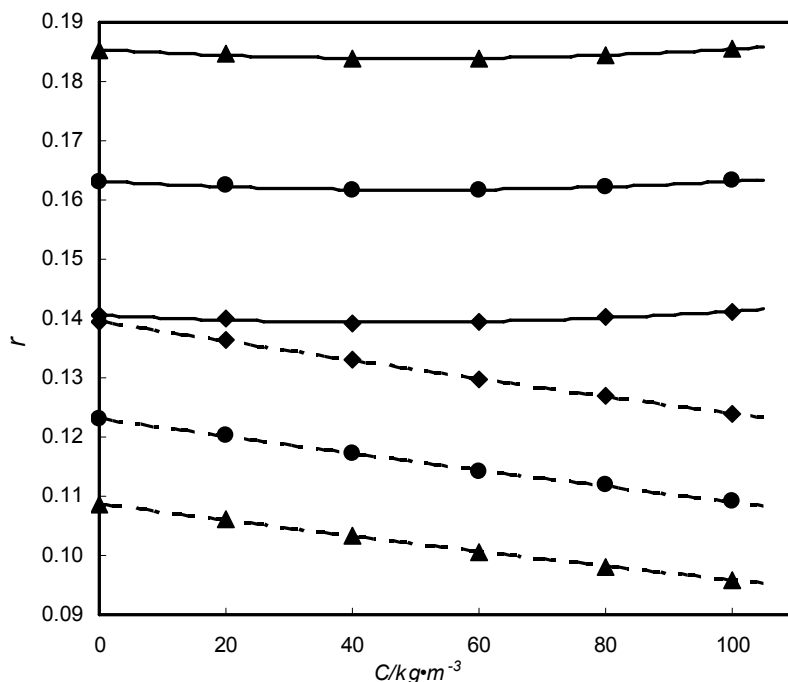


Fig. 5. Comparative representation of the relaxation strength of binary xGnP + H₂O and xGnP + DMF [19] systems versus concentration of solute at various temperatures, T/K: ◆, 293.15; ●, 298.15; ▲, 303.15; ---, for H₂O; —, for DMF; polynomial correlated values.

Conclusions

In summary we developed a novel approach of characterization for the graphene-based nanomaterials in organic and in aqueous solvents, base on the experimental determination of some thermodynamic parameters.

Considering the importance of surface chemistry in the adsorption of water, further characterization of the nature of water bonding with the functional groups is necessary. Additional thermodynamic information can be obtained by examining

the multi-temperature equilibrium data. This work renders it possible to achieve important opportunities of to use the carbon-nanostructure of graphene in composite nanomaterials for low-cost and environmental – friendly decontamination adsorbents for organic and inorganic contaminants.

Acknowledgments. The present study was carried out within the research programme Chemical Thermodynamics of “Ilie Murgulescu” Institute of Physical Chemistry, which was financed by the Romanian Academy of Sciences. Support from the EU (ERDF) and Romanian Government, which allowed for the acquisition of the research infrastructure under POS-CCE O 2.2.1 project INFRANANOCHEM - Nr. 19/01.03.2009 is gratefully acknowledged.

References

- [1] A.B. BOURLINOS, V. GEORGAKILAS, R. ZBORIL, T.A. STEROTIS, A.K. STUBOS, *Small* **5**, pp.1841–1845, 2009.
- [2] A.O. NEILL, U. KHAN, P.N. NIRMALAJ, J. BOLAND, J.N. COLEMAN, *J. Phys. Chem. C*. **115**, pp. 5422–5428, 2011.
- [3] C.E. HAMILTON, J.R. LOMEDA, Z.Z. SUN, J.M. TOUR, A.R. BARRON, *Nano Lett.* **9**, 3460–3462, 2009.
- [4] Y. HERNANDEZ, M. LOTYA, D. RICKARD, S.D. BERGIN, J.N. COLEMAN, *Langmuir* **26**, pp. 3208–3213, 2010.
- [5] J.N. COLEMAN, *Adv. Funct. Mater.* **19**, pp. 3680–3695, 2009.
- [6] C.J. SHIH, S.C. LIN, M.S. STRANO, D. BLANKSCHTEIN, *J. Am. Chem. Soc.* **132**, (), pp. 14638–14648, 2010.
- [7] M.S. STRANO, V.C. MOORE, M.K. MILLER, M.J. ALLEN, E.H. HAROZ, C. KITRELL, *NanoSci. Nanotechnol.* **39**, pp. 81–86, 2003.
- [8] Y. HERNANDEZ, V. NICOLOSI, M. LOTYA, F.M. BLIGHE, Z.Y. SUN, S. De, *NAT. Nanotechnol.* **3**, pp. 563–568, 2008.
- [9] C. FU, X. YANG, *Carbon* **55**, pp. 350–360, 2013.
- [10] L.D. BELYAKOVA, A.V. KISELEV, N.V. KOVALEVA, *Russ. J. Phys. Chem., Ussr.* **42**, 1204–1208, 1968.
- [11] A. STRIOLO, A.A. CHAILVO, P.T. CUMMINGS, K.E. GUBBINS, *Langmuir*, **19**, pp. 8583–8591, 2003.
- [12] J.C. LIU, P.A. MONSON, *Langmuir*, **21**, pp. 10219–10225, 2005.
- [13] C. RODRÍGUEZ-GONZÁLEZ, O.V. KHARISSOVA, A.L. MARTÍNEZ-HERNÁNDEZ, V.M. CASTAÑO, C. VELASCO- SANTOS, *Dig. J. Nanomater. Bios.* **8**, pp. 127–138, 2013.
- [14] V.T. NGUYEN, D.D. Do, D. NICHOLSON, *Carbon* **66**, pp. 629–636, 2014.
- [15] X. LI, L. LI, Y. WANG, H. LI, X. BIAN, *J. Phys. Chem. C***117**, pp. 14106–14112, 2013.
- [16] A.C. ION, A. ALPATOVA, I. ION, A. CULETU, *Materials Science and Engineering B* **176**, pp. 588–585, 2011.
- [17] A.C. ION, I. ION, A. CULETU, *Materials Science and Engineering B***176**, pp. 504–509, 2011.
- [18] F. ROUQUEROL, J. ROUQUEROL, K.S.W. SING, *Adsorption by powders and Porous Solids*, Academic Press, London, 1999.
- [19] J.Y. BRENNAN, T.J. BANDOSZ, K.T. THOMPSON, K.E. GUBBINS, *Colloids Surf.* **A539**, pp. 187–188, 2001.
- [20] L. ZHOU, Y. SUN, Y.P. ZHOU, *AIChEJ* **48**, pp. 2412–2416, 2002.

- [21] M. TAGAWA, M. IKEMURA, Y. NAKAYAMA, Y. OHMAE, *Tribol. Lett.* **17**, pp. 575–580, 2004.
- [22] C.M. WHITE, D.H. SMITH, K.L. JONES, A.L. GOODMAN, S.A. JIKICH, R.B. LAKOUNT, S.B. DU BOSE, E. OZDEMIR, B.I. MORSI, K.T. SCHROEDER, *Energy Fuels* **19**, pp. 659–724, 2005.
- [23] O. IULIAN, F. SIRBU, C. STOICESCU, *Rev. Roum. Chim.* **53**, pp. 1125–1129, 2008.
- [24] F. SIRBU, O. IULIAN, *J. Chem. Eng. Data* **55**, pp. 3853–3858, 2010.
- [25] F. SIRBU, O. IULIAN, A.C. ION, I. ION, *J. Chem. Eng. Data* **56**, pp. 4935–4943, 2011.
- [26] I. ION, F. SIRBU, A.C. ION, *J. Chem. Eng. Data* **58**, pp. 1212–1222, 2013.
- [27] M.M. PALAIOLOGOU, G.K. ARIANAS, N.G. TSIERKEZOS, *J. Solution Chem.* **35**, pp. 1551–1565, 2006.
- [28] W. WAGNER, A. PRUSS, *J. Phys. Chem. Ref. Data* **31**, pp. 387–535, 2002.
- [29] A.F.S.S. MENDONÇA, F.A. DIAS, I.M.S. LAMPREIA, *J. Solution Chem.* **36**, pp. 13–26, 2007.
- [30] A.V. RAYER, K.Z. SUMON, A. HENNI, P. TONTIWACHWUTHIKUL, *J. Chem. Thermodyn.* **43**, pp. 1897–1905, 2011.
- [31] I.B. MALHAM, M. TURMINE, *J. Chem. Thermodyn.* **40**, pp. 718–723, 2008.
- [32] D.R. LIDE, *CSIR Handbook of Chemistry and Physics*, 7th ed., 1990–1991.
- [33] A. ARCE, A. BLANCO, A. SOTO, I. VIDAL, *J. Chem. Eng. Data* **38**, pp. 336–340, 1993.
- [34] J.A. RIDDICK, W.B. BUNGER, T.K. SAKANO, *Organic Solvents: Physical Properties and Methods of Purification*. 4th edn. Wiley, New York, 1988.
- [35] M.N. ROY, R. CHANDA, G. GHOSH, *Russ. J. Phys. Chem.* **A83**, pp. 1331–1341, 2009.
- [36] B.R. SHINDE, S.S. JADHAV, S.U. SHINDE, D.R. SHENGULE, K.M. JADHAV, *Arch. Phy. Res.* **2**, pp. 107–113, 2011.
- [37] A. TOUMI, M. BOUANZ, *J. Mol. Liq.* **139**, pp. 55–60, 2008.
- [38] I.M.S. LAMPREIA, Â.F.S. SANTOS, *J. Sol. Chem.* **39**, pp. 808–819, 2010.
- [39] U.S. VURAL, V. MURADOGLU, S. VURAL, *Bull. Chem. Soc. Ethiop.* **25**, pp. 111–118, 2011.
- [40] Evaluation of measurement data-guide to the expression of uncertainty in measurement. Report of Working Group 1 of the Joint Committee for Guides in Metrology, 2008.
- [41] C. GONZALEZ, J.M. RESA, J. LANZ, M. IGLESIAS, *J. Food Eng.* **77**, pp. 152–161, 2006.
- [42] J.S. ROWLINSON, F.L. SWINTON, *Liquid and Liquid Mixtures*, Butterworths, London, 3rd ed., 1982.
- [43] N.G. GERECZE, *Acoustica* **38**, pp. 51–57, 1977.
- [44] G.A.C.M. SPIERINGS, G.P. MELIS, *J. Mater. Sci.* **16**, pp. 1059–1062, 1981.
- [45] V.N. REDDY, K.S.W.K. RAO, M.C.S. SUBHA, K.C. RAO, presented at International Conference on Advances in Polymer Technology, 356, Feb. 26-27, India, 2010.
- [46] R.D. ALLEN, *Am. Mineralogist* **41**, pp. 245–257, 1956.
- [47] Y. LIANG, D. WU, X. FENG, K. MULLER, *Adv. Mater.* **21**, pp. 1679–1683, 2009.
- [48] D. CHEN, H. FENG, *J. Li, Chem. Rev.* **112**, pp. 6027–6053, 2012.
- [49] K. YANG, B. XING, *Chem. Rev.* **110**, pp. 5989–6008, 2010.
- [50] S.W. RUTHERFORD, *Langmuir* **22**, pp. 9967–9975, 2006.
- [51] D.R. DREYER, S. PARK, C.W. BIELAWSKI, R.S. RUOFF, *Chem. Soc. Rev.* **39**, pp. 228–240, 2010.

Nanostructured Titanosilicate Microspheres with Gallium and Lanthanum Based Nanocrystals

O. PONTA, S. SIMON

Babes-Bolyai University, Faculty of Physics & Institute for Interdisciplinary Research in
Bio-Nano-Science 400084 Cluj-Napoca, Romania

E-mail: oponta@phys.ubbcluj.ro

E-mail: simons@phys.ubbcluj.ro

Abstract. The aim of this study was to synthesize by sol-gel and spray drying amorphous titanosilicate microspheres gallium/lanthanum oxides, and to develop nanocrystalline phases by thermal treatments. Microspheres size was less than 5 μ m. The samples were slightly doped with Gd₂O₃ in order to receive EPR information on the surrounding of Gd³⁺ ions usually disposed in similar sites to that occupied by gallium or lanthanum. The changes induced in samples structure and morphology by Ga₂O₃ or La₂O₃ addition and by thermal treatments were investigated by XRD and SEM, FTIR, Raman and EPR spectroscopies. Beside anatase and rutile, Ga₂O₃ and La₂Ti₂SiO₉ nanocrystals were developed, all these crystalline phases being desired concerning their applications.

Keywords: microspheres, titanosilicate, nanocrystals, sol-gel, spray drying

1. Introduction

Silica-titania mixed oxides have been of large interest [1-3], especially as catalysts and catalyst support materials, due to the fact that silica-titania nanocomposites have higher photoactivity than pure TiO₂. The presence of TiO₂-SiO₂ binary system compounds in photocatalytic field [4-6] is related to the advantages from both TiO₂, an n-type semiconductor with catalytic activity, and SiO₂, with high thermal stability and good mechanical strength, but some more by generation of new photoactive sites due to the interaction of TiO₂ and SiO₂ [7-9]. Not as extensive as in the field of photocatalysis, there is also a promising interest for titanosilicates in the field of biomaterials [10-14]. Nanosized titanium dioxide polymorphs (anatase and rutile) have wide applications ranging from a substance for white pigment to photocatalysts and nanoscale electronic devices, and they play also a role in the biocompatibility of bone implants. The performance of TiO₂ polymorphs in the mentioned applications strongly relies on their physicochemical

characteristics such as crystallinity, crystal size, specific area and surface characteristics [15]. Bulk and surface defects have an important role in many processes occurring at oxide surfaces, *e.g.* vacancies may serve as active sites facilitating adsorption of different species [16, 17].

The addition of rare earths (RE) may change the physical and chemical properties of titanosilicate systems. The doping with RE ions can change the particle morphology, and retard the crystalline grain growth during heat treatments [18], that is an important aspect in photocatalytic applications. The catalytic activity of $\text{TiO}_2\text{-SiO}_2$ generally increases with the addition of rare earth promoters [18]. The effect of rare earths addition on hydrophilicity of $\text{TiO}_2/\text{SiO}_2$ films was also reported, namely the hydrophilicity of pure TiO_2 film is enhanced by both SiO_2 and La_2O_3 [19]. In low concentration range of La_2O_3 this materials has applicability in both optical glass and biomaterials fields. It was reported that lanthanum enhances *in vitro* osteoblast differentiation but has no effect on type I collagen [20]. Interestingly, lanthanum is rapidly emerging as a major player in the management of multiple other systemic diseases especially in the field of oncology [21-23].

Taking into consideration the good catalytic activity of gallium sites [24] this study aims to investigate the $\text{SiO}_2\text{-Ti}_2\text{O}$ system both with lanthanum oxide and with gallium oxide. The study is focussed on the effect of lanthanum and gallium as well as of the thermal treatment influence on the surface composition and structure of these titanosilicate systems because their physical and chemical surface properties are of major interest in different applications. A small amount of gadolinium was added, considering that the Gd^{3+} ($4f^7, {}^8\text{S}_{7/2}$) is a paramagnetic ion in the S state, frequently used as EPR sensors for structural investigations of noncrystalline and ceramic materials [25-27].

Specific thermal treatments were applied in order to develop controlled nanocrystals, oxygen vacancies and thermally stabilize the synthesized materials. It was chosen for the synthesis the sol-gel method combined with spray drying process because sol-gel method offers a good chemical homogeneity, low-temperature processing and allows the control of pore size distribution, while spray-drying is widely employed to solidify sols into fine powders, being a single-step process which can readily be scaled up [28]. Various complementary characterization techniques were used: X-ray diffraction (XRD), scanning and electron microscopy (SEM), electron paramagnetic resonance (EPR), Fourier transform infrared (FTIR) and Raman spectroscopies in order to obtain a clearer picture of the physico-chemical properties.

2. Experimental

Synthesis

$\text{TiO}_2\text{-SiO}_2$ microspheres with 5 mol % lanthanum or gallium oxide doped with gadolinium, hereinafter noted as 5Ga and 5La, have been prepared by a combined

sol-gel with spray drying methods. The spray dried microspheres were less than 5 μm in diameter. The sol was obtained by the hydrolysis and polycondensation of tetraethoxysilane-TEOS (98%, Aldrich) and titanium isopropoxide-TIP (98%, Merck) and is schematically presented in Fig. 1. Titanium isopropoxide $\text{C}_{12}\text{H}_{28}\text{O}_4\text{Ti}$ (TIP), tetraethoxysilane $\text{Si}(\text{OC}_2\text{H}_5)_4$ (TEOS), gadolinium nitrate $\text{Gd}(\text{NO}_3)_3 \cdot 6\text{H}_2\text{O}$, gallium nitrate $\text{Ga}(\text{NO}_3)_3 \cdot 6\text{H}_2\text{O}$, lanthanum nitrate $\text{La}(\text{NO}_3)_3 \cdot 6\text{H}_2\text{O}$ of p.a. purity were used as starting materials and 2-methoxyethanol as solvent (Table 1). The starting materials TEOS, TIP, gadolinium, gallium/lanthanum nitrates were mixed with 2-methoxyethanol in 1:2 mass ratio for the first two precursors, and 1:10 mass ratio for the last three, subsequently being stirred for 30 minutes in order to get a clear solution with high homogeneity. All these preparation steps were accomplished in air at room temperature. The solutions, in ratios accordingly to the desired composition, were mixed together for 15 minutes and the final solution was sprayed using a Buchi-290 Mini Spray-dryer device in order to obtain microspheres, according to the schematic representation given in Fig. 1. In spray drying, a solution or suspension is fed to an atomizer and the droplets formed are mixed with a hot gas. This causes the solvent of the droplets to evaporate, leaving a dry powder product. Using this technique the number of unit operations is reduced, improving production efficiency and reducing costs, especially since spray drying is a technique that can be easily automated and equipped for in-line product analysis.

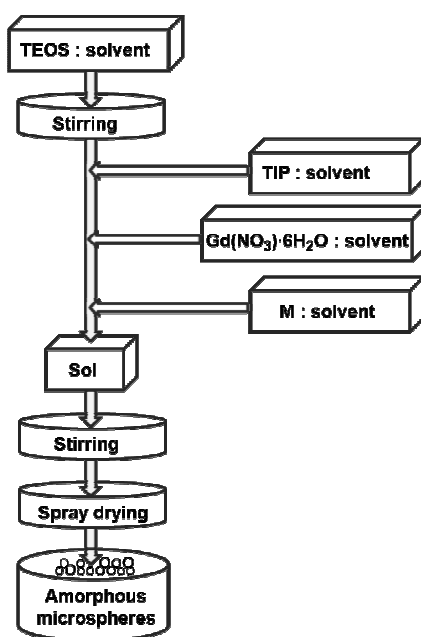


Fig. 1. Schematic representation of the samples synthesis (M = $\text{Ga}(\text{NO}_3)_3 \cdot 6\text{H}_2\text{O}$, $\text{La}(\text{NO}_3)_3 \cdot 6\text{H}_2\text{O}$).

Table 1. Precursors - solvent weight ratio.

Starting materials		Ratio (weight %)
Precursors	Solvent	
TEOS	2-methoxyethanol	1:2
TIP		
Gd(NO ₃) ₃ ·6H ₂ O		1:10
Ga(NO ₃) ₃ ·xH ₂ O		
La(NO ₃) ₃ ·6H ₂ O		

For spray-drying we used an accessory Inert Loop B-295 and a 1.4 mm nozzle tip. The flow type was co-current with mixing of air and liquid at the nozzle head. The powder was collected using a cyclone. The air spray flow rate was 600 l/h and the aspirator rate was kept constant at 95%. The inlet temperature was controlled at 120°C. The outlet temperature (70°C) was determined by the inlet temperature and relative factors such as air and liquid flow rates. All processing parameters for the spray drying procedure were the same for both SiO₂–Ti₂O–La₂O₃ (5La) and SiO₂–Ti₂O–Ga₂O₃ (5Ga) samples. The resulted powders were white microsphere particles.

Three different thermal treatments, at 700, 900 and 1100°C, for 30 minutes, have been applied on samples in order to remove the remained precursors from synthesis process, to stabilize the sample and to develop the desired crystalline phases.

Experimental Techniques

The XRD patterns were recorded with a Shimadzu XRD–6000 diffractometer using Cu Ka ($\lambda = 1.5405 \text{ \AA}$) radiation, at a scan speed of 2°/min. Crystallographic identification was accomplished by comparing the experimental XRD patterns with those of JCPDS (Joint Committee on Powder Diffraction Standards: JCPDS#PDF) database for standard inorganic crystal structures. The average crystallite sizes were estimated based on Scherrer's formula [29]: $D = k\lambda/\beta \cos\theta$, where D is the average particle size, k is a constant equal to 0.89, λ is the wavelength of X-rays equal to 0.1542 nm (*i.e.* Cu Ka) and β is the full width at half maximum (FWHM) of the representative peak.

The morphology of the samples was explored by scanning electron microscopy (SEM) using a FEI QUANTA 3D FEG dual beam and Jeol JSM 5510LV scanning electron microscopes in high vacuum work mode. In order to amplify the secondary electrons signal a conductive Pt-Pd coating of 3 nm thickness was applied to the specimen into an Agar Automatic Sputter Coater, in Ar atmosphere.

FTIR spectroscopic analyses were realized with a JASCO 6200 FTIR spectrometer in the 4000 to 400 cm⁻¹ range with a spectral resolution of 4 cm⁻¹. The

FTIR spectra were recorded from the mixture of the powder samples with KBr pressed into pellets. In order to compare the infrared absorption band intensities, we used the same sample amount (0.8 g) for all KBr pellets.

The Raman measurements were performed using a Raman Systems R3000 CN spectrometer equipped with a 785 nm diode laser coupled to a fiber optic probe. The spectra were recorded in one acquisition, 10 s integration time. The laser power on the sample was 150 mW.

Room temperature cw-EPR spectra were recorded in the magnetic field range of 700–4700 G, with ADANI 6400 EPR spectrometer, operating in X band (9.1–9.6 GHz). EPR glass capillaries of the same diameter were filled with samples of equal quantities. The spectrometer settings were: modulation frequency at 100 kHz, modulation amplitude at 1 G and power attenuation of 6 dB.

3. Results and Discussion

X-Ray Diffraction Analysis

The X-ray diffraction patterns of the obtained samples presented in the Figs. 2 and 3, evidence the presence of nanocrystals in both systems. One can observe that lanthanum and gallium addition lead to different phase developments after 30 minutes heat treatments. After a calcination at 700°C, the sample with lanthanum (5La) remains amorphous (as revealed by the broad characteristic diffraction peak between $2\theta \sim 20^\circ$ and 30° , Fig. 3a), while the one with gallium develops anatase nanocrystals, identified by the diffraction lines at $2\theta \sim 25.3^\circ$ (101) and $2\theta \sim 48.0^\circ$ (200) (JCPD#PDF card No. 21-1272), of 4 nm in size. By increasing the thermal treatment up to 900°C beside the anatase nanocrystals the rutile phase have been observed in the 5 Ga sample (JCPD#PDF card No. 21-1276). In this sample the average crystallites size was found to be 5.5 and 9 nm for anatase and rutile, respectively (Table 1). If we take out the sample from the oven immediately after the temperature is reaching 900°C, only anatase phase is developed (see inset of the Fig. 2). After 30 minutes at 1100°C, the anatase phase disappeared and, beside rutile, nanocrystals of Ga_2O_3 have been developed.

Table 2. Mean crystallite size of the crystalline phases developed after heat treatment as derived from Scherrer formula.

Samples	Heat treatment temperature (°C)	Phase	Crystallites size (nm)
5Ga	700	Anatase	4
	900	Anatase	5.5
		Rutile	9
	1100	Rutile	25
		Ga_2O_3	20
5La	700	amorphous	-
	900	Rutile	-
	1100	Rutile	27
		$\text{La}_2\text{Ti}_2\text{SiO}_9$	29

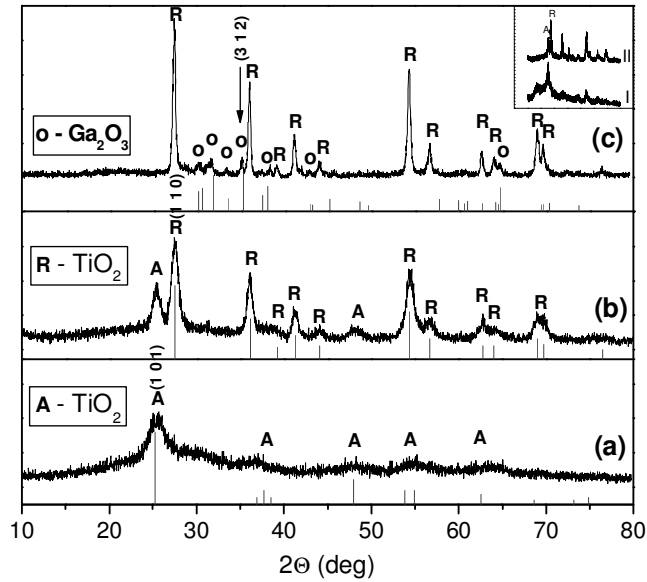


Fig. 2. The XRD patterns of 5Ga microspheres after 30 minutes calcination at 700 (a), 900 (b) and 1100°C (c). Inset: the XRD patterns of 5Ga microspheres (I) calcined at $900^\circ C$ for 30 minutes, (II) removed from the oven once $900^\circ C$ temperature was reached.

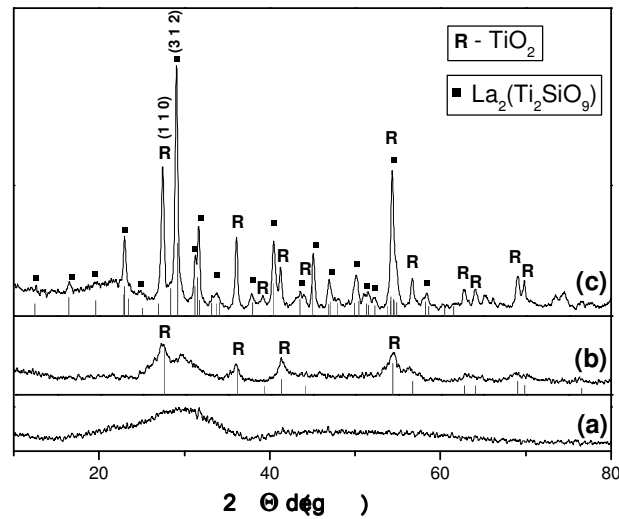


Fig. 3. The XRD patterns of 5La microspheres after 30 minutes calcination at 700 (a), 900 (b) and 1100 °C (c).

For the sample with lanthanum the transition from amorphous state is directly to the rutile phase, but only at $900^\circ C$, the nanocrystalites being too small for fair size

estimation. Moreover at this temperature, starts the $\text{La}_2\text{Ti}_2\text{SiO}_9$ (JCPD#PDF card No. 82-1490) nucleation process (Fig. 3). At a higher temperature both crystalline phases are now well developed, the crystals size being larger for the $\text{La}_2\text{Ti}_2\text{SiO}_9$ phase (Table 2).

Scanning Electron Microscopy

The SEM results show that the obtained particles after 30 minutes heat treatment at 700°C are well defined and have a spherical shape of less than $5\ \mu\text{m}$ in diameter without visible pores on the surface (Figs. 4 and 5). In the case of gallium containing samples it can be observed, after all thermal treatments the presence of some nanocrystals on the surface. On the 700°C calcined 5Ga microspheres the formed nanocrystalites must be, accordantly with XRD pattern, of anatase type, while after 900°C thermal treatment the well evidenced crystals are of rutile type. The 1100°C heat treatment leads to an increase of the rutile nanocrystals, but also new nanocrystals, of different shape, appear. The crystals of acicular shape on these microspheres can be of Ga_2O_3 phase, according to XRD pattern of this sample.

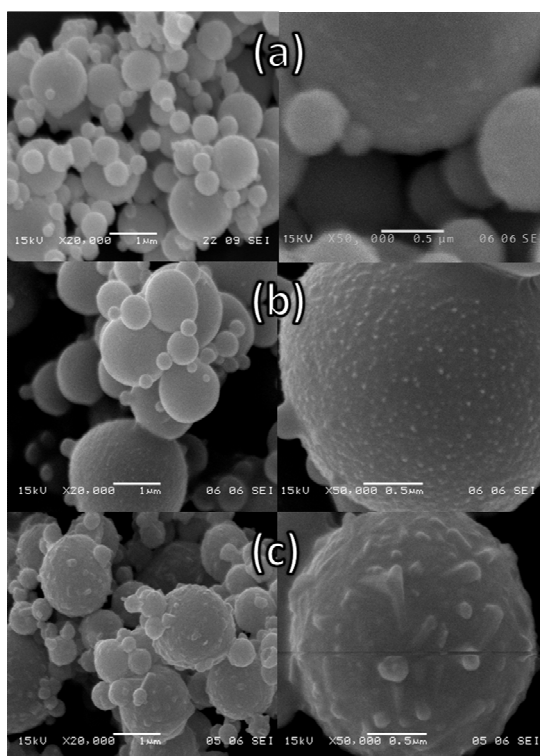


Fig. 4. SEM image of 5Ga samples at two different magnifications after 30 minutes heat treatment at 700°C (a), 900°C (b) and 1100°C (c).

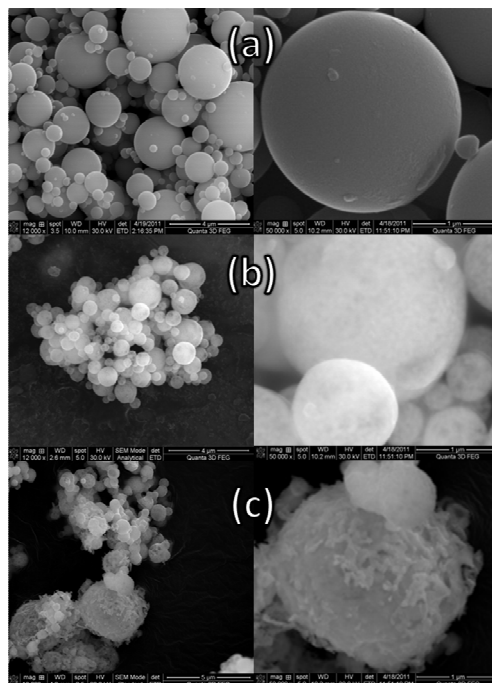


Fig. 5. SEM image of 5La sample at two different magnifications for 700 (a), 900 (b) and 1100°C (c) thermal treatment.

The SEM images for lanthanum containing samples are presented in the Fig. 5 for all three heat treatments. The 5La microspheres heat treated at 700°C that present an amorphous structure according to XRD pattern emphasized a smooth surface. At higher thermal treatments some changes occur on the 5La microspheres' surface, thereby it can be noticed a roughness of these microspheres surface compared with those annealed at 700°C. A different morphology can be observed at the highest calcination temperature (1100°C) (Fig. 5c). Related to XRD pattern (Fig. 3c) two types of nanocrystals, rutile and $\text{La}_2\text{Ti}_2\text{SiO}_9$ phase, are developing after 1100°C heat treatment temperature, the last one being the dominant one. The nanocrystals emphasized on the 5La microspheres surface can be related to $\text{La}_2\text{Ti}_2\text{SiO}_9$ phase, because the rutile crystals have different shape (Fig. 4.).

Fourier Transform Infrared Spectroscopy

The Figs. 6 and 7 present the FTIR spectra for the 5Ga and 5La microspheres, respectively. All these spectra are dominated by two broad absorption bands. First one is located in the intermediate region ($1000\text{-}1300\text{ cm}^{-1}$), while the second one in

the low wavenumber region (400-900 cm^{-1}). These broad bands are better resolved by increasing the thermal treatment due to the development of crystalline phases according to XRD patterns.

The broad absorption band located in the intermediate region has the maximum value in the 1000-1150 cm^{-1} spectral range and a shoulder (around 1200 cm^{-1}) whose contribution increases with the heat treatment applied. This band is assigned to asymmetric stretching mode of Si-O-Si group involving mainly oxygen motion along the Si-Si direction [30] (ASTO1 mode) of the tetrahedral SiO_4 co-ordination unit, while the shoulder can be ascribed to the longitudinal optical Si-O-Si stretching vibration (ASLO1 mode) [31-34]. The corresponding symmetric motion STO1 can be detected at 797 cm^{-1} [34-38] as a component of broad absorption band located in the low wavenumber region. In the 1000-1150 cm^{-1} wavenumber region is repeated also the Ti-O-Si vibration [4, 37] around 1080 cm^{-1} that can overlay with the Si-O-Si vibration band above mentioned.

In the 900-1000 cm^{-1} spectral region can be observed a broad vibration band of low intensity. This band decrease in intensity for the sample with gallium content (5Ga), while for the 5La sample is better resolved (Figs. 6 and 7). The band can be assigned to the stretching of the Si-O species of Si-O-Ti or Si-O defects sites which are formed by the inclusion of Ti^{3+} ions into the SiO_2 matrices [38]. The existence of this absorption feature indicates that during the synthesis a process of linkages between the two networks, *i.e.* SiO_4 and TiO_6 , occurs. The presence of oxygen vacancies is also evidenced in the EPR spectra presented in Figs. 10 and 11. Should be notice here that this broad band contains also the contribution of the silanol groups, (Si-OH) whose vibrations are usually present in FTIR spectra in this wavenumber region. For the sample with gallium content (5Ga) can be observed that the intensity of this band monotonically decreases by calcination. For this sample a segregation of silica take place by increasing the thermal treatment and only Ga_2O_3 and TiO_2 cristaline phases are developed according to XRD data (Fig. 2). Thus can be assume that the main contribution for this band are the silanol groups (Si-OH) stretching vibrations. In the FTIR spectra of the sample with lanthanum content (5La) the broad band is better resolved for the 1100°C calcination temperature (Fig. 7). For 5La sample beside TiO_2 nanocrystals, $\text{La}_2\text{Ti}_2\text{SiO}_9$ phase is developed with increasing the thermal treatment temperature, phase that involves both silicon and titanium (Fig. 3). Therefore, it can be concluded that this well resolved band around 955 cm^{-1} observed in the FTIR spectrum of the 1100°C thermal treated 5La sample is related to vibrations of Si-O-Ti bridges [34, 35, 39, 40].

In the low wavenumber region (400-900 cm^{-1}) of the sample with gallium content (5Ga) can be observed a band around 415 cm^{-1} for the microspheres thermal treated at 1100°C. For the 700°C calcined sample, this band is not present in the FTIR spectrum, but a weak shoulder is visible at 900°C thermal treatment. This band is representative for rutile structure and the FTIR data are in good

agreement with the XRD results. The FTIR vibration band around 500 cm^{-1} are related to six-fold coordinated octahedral Ga [41]. This band increases in intensity by increasing the thermal treatment, being better resolved for 1100°C calcination temperature where the Ga_2O_3 nanocrystals are developed, according to XRD pattern (Fig. 2c). In the $570\text{-}800\text{ cm}^{-1}$ wavenumber region is present a broad absorption band with a shoulder around 830 cm^{-1} . This band is a convolution of the vibration mode of four-fold coordinated $[\text{GaO}_4]^-$ structures (reported around 745 cm^{-1} [41]) and TiO_2 rutile vibrations (reported at $800\text{-}650\text{ cm}^{-1}$ [42, 43]), while the shoulder is related to Si-O in SiO_2 structure[44].

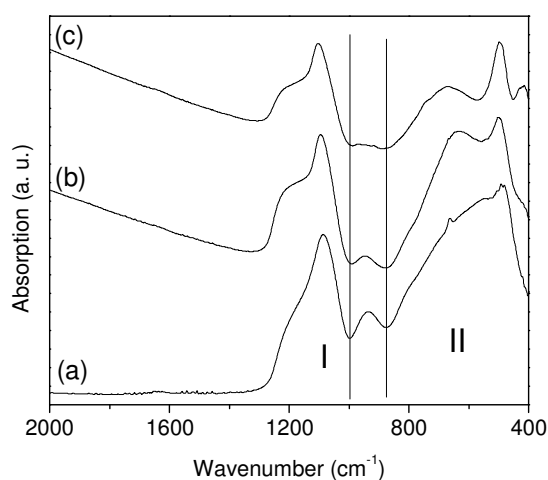


Fig. 6. FTIR spectra of the 5Ga sample thermal treated at 700 (a), 900 (b) and 1100°C (c).

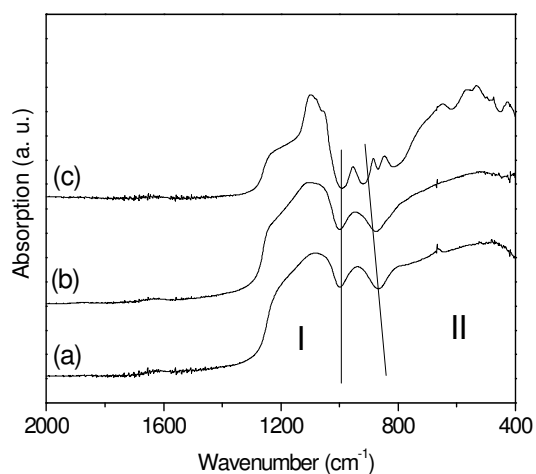


Fig. 7. FTIR spectra of the 5La sample thermal treated at 700 (a), 900 (b) and 1100°C (c).

The 5La FTIR spectra have characteristic shape of amorphous structures for the 700 and 900°C calcined microspheres. For the 1100°C thermal treatment the spectrum is better resolved due to the development of TiO₂ rutile and La₂Ti₂SiO₉ nanocrystals. The band located in the 1000-1300cm⁻¹ spectral region is broader for the 5La microspheres compared with the 5Ga ones because it can contain also the contribution of La-O-Si vibration that is reported around 1065 cm⁻¹ [45]. Moreover the La-O vibration can be evidenced in the low spectral region around 515 and 475 cm⁻¹ [46, 47].

In the FTIR spectra of the both 5Ga and 5La samples (Figs. 6 and 7), the vibration bands at around 1640 cm⁻¹ are associated with the presence of molecular water. By increasing the heat treatment temperature, this band become weaker suggesting the gradual evaporation of OH groups [48].

Raman Spectroscopy

In the Figs. 8 and 9 are presented the Raman spectra of the microspheres with gallium (5Ga) and lanthanum (5La) content, respectively. Only the microspheres thermal treated at 1100°C for the both gallium and lanthanum containing samples and the ones calcined at 900°C for 5La evidenced Raman bands, for the rest the fluorescence phenomena covered the Raman signal. The Fig. 8 presents the Raman spectrum of the 5Ga microspheres thermal treated at 1100°C in comparison with the Raman spectrum of pure TiO₂ rutile (RRUFF ID: R050031) and can be observed three vibration bands around 235, 445 and 610 cm⁻¹ and a shoulder at 700 cm⁻¹. All these Raman vibration bands are related to TiO₂ rutile nanocrystals, the results being in agreement with XRD results where the rutile diffraction lines dominate the pattern.

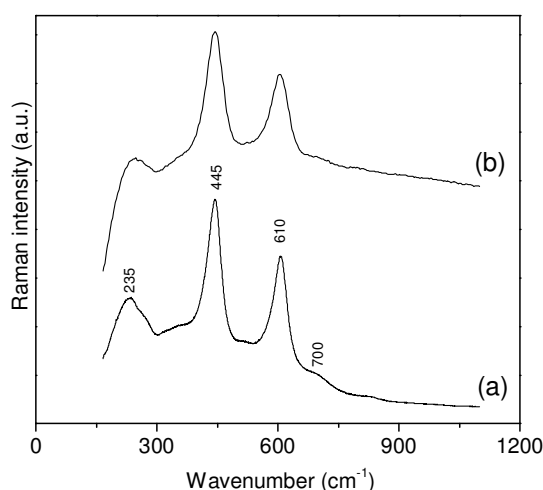


Fig. 8. Raman spectra of the (a) 1100°C heat treated 5Ga microspheres and (b) pure TiO₂ rutile (RRUFF ID: R050031).

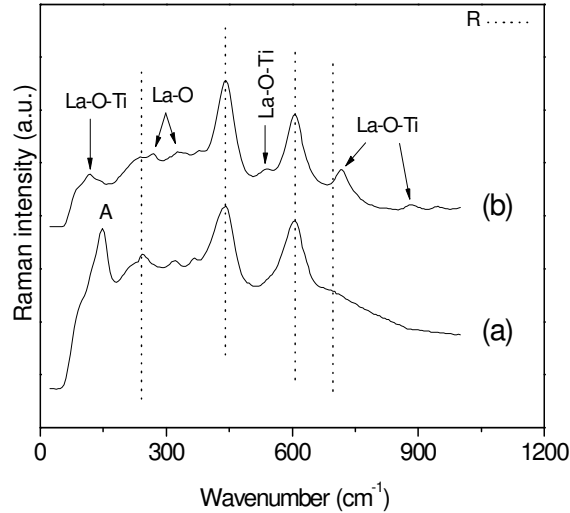


Fig. 9. Raman spectra of the (a) 900 and (b) 1100°C heat treated 5La microspheres.

The characteristic Raman bands of TiO_2 rutile are also evidenced in the Raman spectra of the microspheres with lanthanum content for both thermal treatments presented in Fig. 9. Beside the specific bands for rutile there is visible some other features around: 120, 150, 270, 335, 530, 710 and 885 cm^{-1} . The Raman bands around 270 and 335 cm^{-1} are related with La-O vibration [49], while the 120, 530, 710 and 885 cm^{-1} are characteristic to La-O-Ti vibrations [50].

Moreover the 900°C calcined microspheres (5La) present in the low wavenumber region a Raman band around 150 cm^{-1} , which is the characteristic peak of anatase crystalline phase. In the XRD pattern (Fig. 3b) cannot be evidenced the anatase diffraction lines, thus can be concluded that the crystallite size for anatase phase is under XRD resolution.

Electron Paramagnetic Resonance Spectroscopy

The gadolinium doping is allowing to obtain additional information about the structure and local order. The Gd^{3+} ions are paramagnetic resonance centres sensitive to their surrounding that can give details about the structural changes occurred in their vicinity [51-55]. These changes can occur due to the different composition of the microspheres (addition of gallium or lanthanum oxide) and the crystallinity degree induced by the thermal treatments. The Figs. 10 and 11 are presented the EPR spectra of the microspheres with gallium and lanthanum content, respectively at 700, 900 and 1100°C temperature. For the microspheres heat treated up to 900°C is evidenced in the both systems three EPR signals at $g \sim 5.9, 2.8$ and 2.0. These are typical signals of Gd^{3+} ions located at sites with

intermediate and weak crystal fields respectively, a characteristic of so called U-spectrum of Gd^{3+} ions in disordered matrices. This is the most frequent signature of S-state rare earth ions in such materials [52, 55-57].

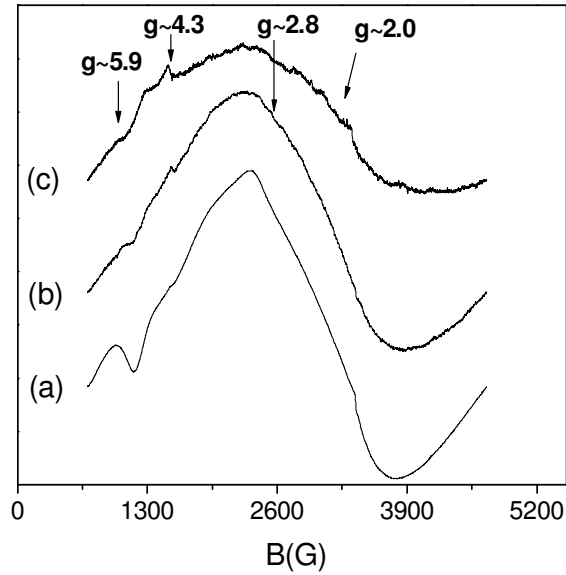


Fig. 10. EPR spectra of the 5Ga microspheres thermal treated at 700 (a), 900 (b) and 1100°C (c).

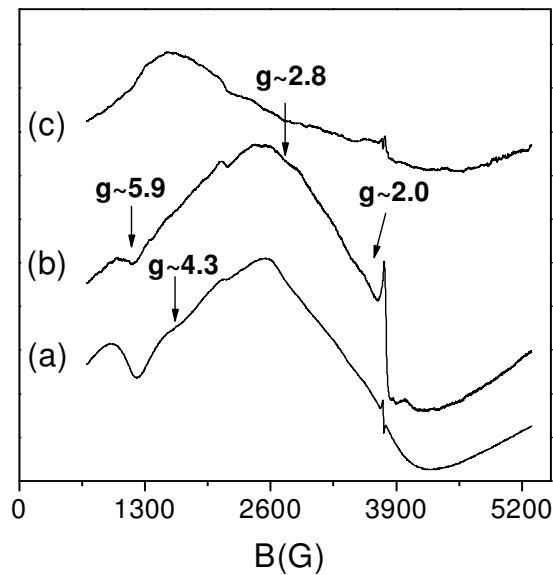


Fig. 11. EPR spectra of the 5La microspheres thermal treated at 700 (a), 900 (b) and 1100°C (c).

The structural changes induced by the calcination are well reflected in the EPR spectra of the both systems (Figs. 10 and 11). One can observe that the large EPR line at $g \sim 2.0$ dominates the spectra. This signal directly reflects the changes in the spin-lattice relaxation rate and most importantly the structural disorder around Gd^{3+} ions. Except the $1100^{\circ}C$ annealed sample with lanthanum can be assumed that Gd^{3+} ions are preponderantly disposed in the residual non-crystalline phase, experiencing weak crystal fields, resulting from structural relaxation, but with still a high degree of disorder around them [52-55]. Moreover the small features at $g \sim 5.9$ and 2.8 indicate that there are sites in the non-crystalline matrices where the Gd^{3+} ions are experiencing intermediate field. The EPR spectrum of the $1100^{\circ}C$ thermal treated sample with lanthanum is assigned to Gd^{3+} ions distributed in lanthanum site from the $La_2Ti_2SiO_9$ developed phase. The line at $g \sim 4.3$ is assigned to iron (III) that appears because of iron impurities.

All the spectra have a sharp signal overlapped on the large EPR line at $g \sim 2.0$ that dominates the spectra. This signal is more pronounced in the microspheres with lanthanum and can be attributed to oxygen vacancies, a bulk defect, probably an electron trapped on an oxygen vacancy. Can be observed in the EPR spectra that the samples with lanthanum content have larger amount of oxygen vacancies compared with the gallium content samples.

4. Conclusions

$SiO_2-Ti_2O-M_2O_3$ ($M = Ga, La$) microspheres of less than $5 \mu m$ in diameter with active surface were synthesized by sol-gel process combined with spray drying method titanosilicate. Activation was realized by nanocrystals development on surface after heat treatments.

TiO_2 rutile phase was induced by $1100^{\circ}C$ heat treatment as confirmed by XRD and FTIR and Raman spectroscopies. Beside rutile, $La_2Ti_2SiO_9$ phase was developed in the lanthanum containing sample, and Ga_2O_3 in the sample with gallium. Anatase phase was evidenced by X-ray diffraction in lanthanum containing sample up to $900^{\circ}C$, but not in gallium containing sample, even Raman analysis highlighted a band characteristic for anatase, and suggests that the crystallites size is under the XRD detection limit. The developed nanocrystals were clearly shown by SEM analysis. While the gallium is postponing the transition temperature of anatase to rutile, so that microspheres can be of interest for catalytic reactions, supported by anatase, at quite high temperatures (up to $900^{\circ}C$), the lanthanum is not favorable for anatase phase formation, but is postponing the microspheres crystallization. After heat treatment at higher temperature ($1100^{\circ}C$), both samples are presenting on their surface rutile nanocrystals but together with gallium oxide nanocrystals or of $La_2Ti_2SiO_9$ phase. These microspheres taped with such mixtures of nanocrystals are candidates for different applications in the fields like catalysis and biomedical applications.

References

- [1] A.A. ISMAIL, I.A. IBRAHIM, M.S. AHMED, R.M. MOHAMED, H. ELL-SHALL, *J. Photochem. Photobiol. A* **163**, pp. 445, 2004.
- [2] M.S. VOHRA, K. TANAKA, *Wat. Res.* **37**, pp. 3992, 2003.
- [3] Z. FENG, L. KAIMING, W. GUOLIANG, S. HUA, H. ANMIN, *J. Cryst. Growth* **264**, pp. 297, 2004.
- [4] Y. ZANG, Y. WU, M. CHEN, L. WU, *Colloid Surface A* **353**, 216, 2010.
- [5] W. DONG, C.W. LEE, X. LU, Y. SUN, W. HUA, G. ZHUANG, S. ZHANG, J. CHEN, H. HOU, D. ZHAO, *Appl. Catal. B* **95**, pp. 197, 2010
- [6] X. GAO, I.E. WACHS, *Catal. Today* **51**, pp. 233, 1999.
- [7] T.V. NGUYEN, O.B. YANG, *Catal. Today* **87**, pp. 69, 2003.
- [8] F. MEI, C. LIU, L. ZHANG, F. REN, L. ZHOU, W.K. ZHAO, Y.L. FANG, *J. Cryst. Growth.* **292**, pp. 87, 2006.
- [9] V. PĂRVULESCU, V.I. PARVULESCU, G. POPESCU, A. JULBE, C. GUIZARD, L. COT, *Catal. Today* **25**, pp. 385, 1995.
- [10] M.S. DADASH, S. KARBASI, M.N. ESFAHANI, M.R. EBRAHIMI, H. VALI, *J. Mater. Sci. Mater. Med.* **22**, pp. 829, 2011.
- [11] S. AREVA, V. AARITALO, S. TUUSA, M. JOKINEN, M. LINDEN, T. PELTOLA, *J. Mater. Sci. Mater. Med.* **18**, pp. 1633, 2007.
- [12] A. CHENITI, O. PONTA, L. TIRLE, T. RADU, S. SIMON, *J. Optoelectron. Adv. Mat.* **6**, pp. 560, 2012.
- [13] O. PONTA, E. VANEA, A. CHENITI, P. BERCE, S. SIMON, *Mater. Chem. Phys.* **135**, pp. 863, 2012.
- [14] O. PONTA, C. GRUIAN, E. VANEA, B. OPREA, H.-J. STEINHOFF, S. SIMON, *J. Mol. Struct.* **1044**, pp. 2, 2013.
- [15] J. Matthiesen, The influence of point defects on TiO₂(110) surface properties; A scanning tunneling microscopy study: PhD thesis, Editor: Interdisciplinary Nanoscience Center (iNANO), 2007.
- [16] U. DIEBOLD, *Surf. Sci. Rep.* **48**, pp. 53, 2003.
- [17] M.V. GANDUGLIA-PIROVANO, M. HOFFMAN, J. SAUER, *Surf. Sci. Rep.* **62**, pp. 219, 2007.
- [18] R.M. MOHAMED, I.A. MKHALID, *J. Alloy. Compd.* **501**, pp. 143, 2010.
- [19] K. GUAN, Y. YIN, *Mater. Chem. Phys.* **92**, pp. 10, 2005.
- [20] X. WANG, L. YUAN, J. HUANG, T.-L. ZHANG, K. WANG, *J. Cell. Biochem.* **105**, pp. 1307, 2008.
- [21] S. KAPOOR, *J. Cell. Biochem.* **106**, pp. 193, 2009.
- [22] L. Feng, H. Xiao, X. He, Z. Li, F. Li, N. Liu, Z. Chai, Y. Zhao, Z. Zhang, *Neurotoxicol. Teratol.* **28**, pp. 119, 2006.
- [23] G. FEI, L. YUANLEI, W. YANG, X. AN, L. GUOHUI, *J. Rare Earths* **25**, pp. 359, 2007.
- [24] J.R. MOWRY, R.F. ANDERSON, J.A. JONSON, *J. Oil Gas* **83**, pp. 128, 1985.
- [25] D.L. GRISCOM, *J. Non-Cryst. Solids* **67**, pp. 81, 1984.
- [26] L.E. ITON, C.M. BRODBECK, S.L. SUIB, G.D. STUCKY, *J. Chem. Phys.* **79**, pp. 1185, 1983.
- [27] C. LEGEIN, J.Y. BUZARE, G. SILLY, C. JACOBONI, *J. Phys.:Cond. Matter* **8**, pp.4339, 1996.
- [28] P. KORTESUO, M. AHOLA, M. KANGAS, I. KANGASNIEMI, A. YLI-URPO, *J. KIESVAARA, Int. J. Pharm.* **200**, pp. 223, 2000.
- [29] J.I. LANGFORD, A.J.C. WILSON, *J. Appl. Cryst.* **11**, pp. 102, 1978.
- [30] A.G. KALAMPOUNIAS, *Bull. Mater. Sci.* **34**, pp. 299, 2011.
- [31] A. VULPOI, L. BAIA, S. SIMON, V. SIMON, *Mater Sci Eng C* **32**, pp. 178, 2012.

- [32] A. CHRISANTHOPOULOS, N. BOUROPOULOS, S.N. YANNOPOULOS, *Vib. Spectrosc.* **48**, pp. 118, 2008.
- [33] O. PONTA, R. CICEO-LUCACEL, A. VULPOI, T. RADU, S. SIMON, *J. Biomed. Mater. Res. A* DOI:10.1002/jbma.34989.
- [34] R.F.S. LENZA, W. L. VASCONCELOS, *Mater. Res.* **5** 4, pp. 497, 2002.
- [35] M. SCHRAMM-MARTH, K.L. WALTHER, A. WOKAN, B.E. HANDY, A. BAIKER, *J. Non. Cryst. Solids* **143**, pp. 93, 1992.
- [36] W.T. MINEHAN, G.L. MESSING, C.G. PANTANO, *J. Non. Cryst. Solids* **108**, pp. 163, 1989.
- [37] V. ZELENAK, V. HORNEBECQ, S. MORNET, O. SCHAEF, P. LLEWELLYN, *Chem. Mater.* **18** 14, pp. 3184, 2006.
- [38] Y. Kotani, A. Matsuda, M. Tatsumisago, T. Minami, *J. Sol-Gel Sci. Technol.* **19** (2000) 585.
- [39] S. KLEIN, S. THORIMBERT, W.F. MAIER, *J. Catal.* **163**, pp. 476, 1996.
- [40] P. YAO, W. HU, Y. BAO, C. ZHANG, B. ZHU, W. LIU, Y. BAI, *J. Ceram. Process. Res.* **12**(3) 289, 2011.
- [41] L.G. HWA, Y.R. CHANG, W.C. CHAO, *Mater Chem Phys* **85**, pp. 158, 2004.
- [42] W. HAITAO, S. MENG, P. XU, W. ZHONG, Q. DU, Published online in Wiley DOI: 10.1002/pen.20708.
- [43] A. PIRSON, A. MOHSINE, P. MARCHOT, B. MICHAUX, O.V. CANTFORT, J.P. PIRARD, A.J. LECLoux, *J. Sol-Gel Sci. Technol.* **4**, pp. 179, 1995.
- [44] G. TZVETKOV, N. MINKOVA, *J. Mater. Sci.* **35**, pp. 2435, 2000.
- [45] S. CELERIER, C. LBERTY, F. ASART, P. LENORMAND, P. STEVENS, *Ceram. Int.* **32**, pp. 271, 2006.
- [46] E. RODRIGUEZ-REYNA, A.F. FYENTS, M. MCZKA, J. HANUZA, K. BOULAHYA, U. AMADOR, *J. Solid State Chem.* **197**, pp. 522, 2006.
- [47] Y. IMANAKA, T. MASUI, Y. KATO, *J. Solid State Chem.* **178**, pp. 395, 2005.
- [48] A. JENTYS, G. WARECKA, M. DEREWINSKI, J.A. LERCHER, *J. Phys. Chem.* **93**, pp. 4837, 1989.
- [49] Z.L. ZHANG, C.T. AU, K.R. TSAI, *Appl. Catal.* **62**, pp. L29, 1990.
- [50] K. KRISHNANKUTTY, K.R. DAYAS, *Bull. Mater. Sci.* **31**(6), pp. 907, 2008.
- [51] D.L. GRISCOM, *J. Non. Cryst. Solids* **40** 211, pp. 272, 1980.
- [52] S. SIMION, A.D. UDVAR, *J. Am. Ceram. Soc.* **93**, pp. 2760, 2010.
- [53] S. SIMON, R. POP, V. SIMON, M. COLDEA, *J. Non-Cryst. Solids* **331**, pp. 1, 2003.
- [54] E. CULEA, L. POP, S. SIMON, *Mater. Sci. Eng. B* **112**, pp. 59, 2004.
- [55] O. PONTA, H. MOCUTA, M. VASILESCU, S. SIMON, *J Sol-Gel Sci Technol.* **58**(2), pp. 530, 2011.
- [56] N.S. HUSSAIN, Y. PRABHAKARA REDDY, S. BUDDHUDU, *Mater. Res. Bull.* **36**, pp. 1813, 2001.
- [57] J. KLIAVA, A. MALAKHOVSKII, I. EDELMAN, A. POTSELUYKO, E.A. PETRAKOVSKAJA, S. MELNIKOVA, T. ZARUBINA, G. PETROVSKII, Y. BRUCKENTAL, Y. YESHURUN, *Phys. Rev.* **B 71**, pp. 104406, 2005.

This volume is promoted by the Commission: “Science and Technology of Microsystems” of the Romanian Academy with the technical and financial support of the National Institute for Research and Development in Microtechnologies (IMT Bucharest, <http://www.imt.ro>). The volume is part of the “Micro and Nanoengineering series”, (coordinator – Professor Dan Dascalu, member of the Romanian Academy).

